The Optical and Electronic Properties of $Ge_{1-y}Sn_y$ and $Ge_{1-x-y}Si_xSn_y$ Materials and Devices for Silicon-Integrated Optoelectronics

by

James Dennis Gallagher

A Dissertation Presented in Partial Fulfillment
of the Requirements for the Degree
Doctor of Philosophy

Approved November 2015 by the
Graduate Supervisory Committee:

José Menéndez, Co-Chair
John Kouvetakis, Co-Chair
Fernando Ponce
Andrew Chizmeshya

ARIZONA STATE UNIVERSITY

December 2015

ABSTRACT

Group-IV semiconductor alloys are of interest for Si-integrated optoelectronic applications due to the band gap tunability and enhanced optical capabilities that can be achieved through compositional tuning. This work advances the field by presenting a systematic study of the optical and electronic properties of $Ge_{1-y}Sn_y$ and analogous $Ge_{1-x-y}Si_xSn_y$ alloys.

The fundamental direct and indirect band gaps of $Ge_{1-y}Sn_y$ materials are measured by room temperature photoluminescence in samples containing $0 \leq y \leq 0.11$ and a transition to direct gap materials is found to occur at $y_c = 0.087$. This result is enabled by the development of sample growth and processing protocols that produce high-quality materials epitaxially on Ge-buffered Si(100) substrates. Strategies to optimize the optical performance are explored by varying the film thickness, thermal and surface treatments, and *n*-type doping. The electrical and optical properties of diodes based on these materials are characterized by current-voltage, optical responsivity, and electroluminescence measurements. These show improved optical performance near y_c with tunable emission out to 2500 nm. Measuring the carrier lifetimes in devices with strain relaxed and fully strained interfaces show significantly longer lifetimes in the fully strained case.

The direct and indirect band gaps of Sn-rich ($y > x$) $Ge_{1-x-y}Si_xSn_y$ materials are measured by room temperature photoluminescence on optimized samples. These data confirm a transition to direct gap materials occurs for the ternary alloy as well. Devices based on compositions $0.02 \leq x \leq 0.10$ and $0.03 \leq y \leq 0.11$ are characterized by current-

voltage, optical responsivity, and electroluminescence measurements and show competitive performance with analogous devices based on $Ge_{1-y}Sn_y$ materials. A detailed study of the direct gap in $Ge_{1-x}Si_x$ alloys gives parameters crucial *en route* to a global description of the $Ge_{1-x-y}Si_xSn_y$ fundamental band gaps.

Archetypal laser device designs on Si are explored by fabricating degenerate *pn* junction diodes and highly doped waveguide devices based on high-quality $Ge_{1-y}Sn_y$ materials. The diodes showed tunnel-like current-voltage characteristics and tailored electroluminescence based on the doping profile. The waveguides demonstrate emission under optical stimulation.

ACKNOWLEDGMENTS

The document that lays before the reader was made possible by the guidance and help of many people. Chiefly I am evermore grateful to my advisors Prof. José Menéndez and Prof. John Kouvetakis for the education, resources, and opportunities they have provided. Without them these results and discoveries would not have been made. I am grateful to Dr. Richard Beeler, Dr. Gordon Grzybowski, and Dr. Jay Mathews for the training they provided and for passing down their knowledge of device processing and measurements, equipment management and troubleshooting, chemical handling, and semiconductor growth and characterization. I thank Dr. Chi (Seth) Xu and Charutha (Lasitha) Senaratne for their expertise and skill in sample growth. I also thank Patrick Sims for his expertise in TEM sample preparation and electron microscopy skills.

I am also grateful for the resources at Arizona State University. I gratefully acknowledge the use of the facilities and equipment of the Ira. A. Fulton Center for Solid State Electronics Research (CSSER), the Goldwater Center for Solid State Science (CSSS), and the LeRoy Eyring Center for High Resolution Electron Microscopy (CHREM) at Arizona State University.

This research was funded in part by the U. S. Air Force Office of Scientific Research (AFOSR) under contract numbers FA9550-12-1-0208 and FA9550-13-1-0022.

Lastly I am grateful for the love, support, and inspiration provided by my parents, siblings, grandparents, and partner-in-crime, Sara Draeger.

TABLE OF CONTENTS

Page

LIST OF TABLES…………………………………………………………………....viii

LIST OF FIGURES…………………………………………………………………... ix

CHAPTER

I. INTRODUCTION, BACKGROUND, AND MOTIVATION FOR GE-BASED GROUP-IV ALLOYS…………………………………………………………..1

A. Introduction……………………………………………………………………1

B. Background and Motivation for Ge as a Technological Material………......3

1. History…………………………………………………………....3

2. Electrical and Optical Properties of Ge………………………………..6

3. Epitaxy of Ge for Applications……………………………............13

C. Background and Motivation for $Ge_{1-y}Sn_y$ Materials………………………… 17

D. Background and Motivation for $Ge_{1-x-y}Si_xSn_y$ Materials…………………… 20

II. OPTICAL AND ELECTRONIC PROPERTIES OF GE-SN MATERIALS AND DEVICES..23

A. Optical Properties of $Ge_{1-y}Sn_y$ Materials……………………………......23

1. Introduction……………………………………………………..23

2. Growth and Materials Properties of $Ge_{1-y}Sn_y$ on Ge/Si(100)………... 25

3. Optical Properties of $Ge_{1-y}Sn_y$ Materials on Ge/Si(100)……………...27

4. Enhancing $Ge_{1-y}Sn_y$ Light Emission…………………………………42

5. Conclusion………………………………………………………....52

B. Optical and Electronic Properties of $Ge_{1-y}Sn_y$ *pin* Diodes……………………52

CHAPTER Page

1. Introduction……………………………………………………………..52
2. Growth and Materials Properties of $Ge_{1-y}Sn_y$ *pin* Devices…………...54
3. Theoretical Model of $Ge_{1-y}Sn_y$ *pin* Diode Electroluminescence Spectra for Carrier Lifetime Analysis………………………………………...63
4. Optical and Electronic Properties of $Ge_{1-y}Sn_y$ *pin* Devices…………..67
5. Conclusion…………………………………………………………....85

III. OPTICAL AND ELECTRONIC PROPERTIES OF GE-SI-SN MATERIALS AND DEVICES……………………………………………………………86

A. Optical Properties of Sn-Rich $Ge_{1-x-y}Sn_xSn_y$ Materials……………………… 86
1. Introduction……………………………………………………………..86
2. Growth and Materials Properties of Sn-Rich $Ge_{1-x-y}Sn_xSn_y$ on Ge/Si(100) Substrates……………………………………………...87
3. Optical Properties of Sn-Rich $Ge_{1-x-y}Sn_xSn_y$ Materials on Ge/Si(100) Substrates………………………………………………………… 91
4. Conclusion…………………………………………………………..…..97

B. Optical and Electronic Properties of Sn-Rich $Ge_{1-x-y}Sn_xSn_y$ *pin* Diodes…......97
1. Introduction……………………………………………………………..97
2. Growth and Materials Properties of Sn-Rich $Ge_{1-x-y}Sn_xSn_y$ *pin* Devices on *n*-Ge/Si(100) Substrates……………………………………….100
3. Optical and Electronic Properties of Sn-Rich $Ge_{1-x-y}Sn_xSn_y$ *pin* Devices on *n*-Ge/Si(100) Substrates………………………………………… 106

4. Optical and Electronic Properties of Si and Sn-Rich $Ge_{1-x-y}Sn_xSn_y$ *pin* Devices on *n*-Ge/Si(100) Substrates……………………………...109

5. Conclusion……………………………………………………….…111

C. Compositional Dependence of the $Ge_{1-x-y}Sn_xSn_y$ Fundamental Band Gaps...112

1. Introduction…………………………………………………………112

2. Motivation to Investigate Ge-Rich $Ge_{1-x}Si_x$ Alloys………………... 112

3. Growth and Materials Properties of Ge-Rich $Ge_{1-x}Si_x$ Alloys……... 114

4. Optical Properties and the Compositional Dependence of Ge-Rich $Ge_{1-x}Si_x$ Fundamental Band Gaps……………………………………….…118

5. A Global Descrcription of $Ge_{1-x-y}Sn_xSn_y$ Band Gaps………………..129

6. Conclusion………………………………………………………. 134

IV. STEPS TO A DIRECT GAP GROUP-IV LASER ON SI: DEGENERATE GE-SN JUNCTIONS AND WAVEGUIDES……………………………………… 136

A. Degenerate *pn* Junction Devices……………………………………………136

1. Introduction…………………………………………………………136

2. Growth and Materials Properties of $Ge_{1-y}Sn_y$ Degenerate *pn* Junctions on Ge/Si(100) Substrates………………………………………... 137

3. Optical and Electronic Properties of $Ge_{1-y}Sn_y$ Degenerate *pn* Junctions on Ge/Si(100) Substrates………………………………………... 140

4. Conclusion…………………………………………………..…... 144

B. Optically Pumped Waveguides…………………………………………......144

1. Introduction…………………………………………………………144

CHAPTER Page

2. Growth and Materials Properties of n-$Ge_{1-y}Sn_y$ Waveguides……….146

3. Optical Properties of n-$Ge_{1-y}Sn_y$ Waveguides……………………… 147

4. Conclusion………………………………………………………. 149

V. CONCLUSIONS AND PROPOSAL FOR FUTURE WORK…………………150

REFERENCES……………………………………………………………………… 157

APPENDIX

A MICROELECTRONIC DEVICE PROCESSING PROCEDURE…………...170

B OPERATION OF PHOTOLUMINESCENCE AND ELECTROLUMINESCENCE SYSTEMS…………………………………...189

C OPERATION OF GOLDWATER AND ERC MICROPROBE STATIONS..199

D CATALOUGE OF GE-SN AND GE-SI-SN DEVICES……………………..205

E FITTING AND MODELING PHOTOLUMINESCENCE AND ELECTROLUMINESCENCE DATA BY LINE SHAPES………………… 220

F PERMISSIONS FOR REPRINTED MATERIALS…………………………..228

LIST OF TABLES

Table Page

I. Materials Properties of $Ge_{1-y}Sn_y$ Samples Before Treatments…………………...45

II. Materials Properties of $Ge_{1-y}Sn_y$ Samples After RTA Annealing……………….. 45

III. Materials Properties of $Ge_{1-y}Sn_y$ Samples After CVD Furnace Annealing………46

IV. Materials Properties of $Ge_{1-y}Sn_y$ Samples After Hydrogen Plasma Treatment…..47

V. $Ge_{1-y}Sn_y$ *pin* Diode Sample Parameters…………………………………………..71

VI. $Ge_{1-y}Sn_y$ *pn* Junction Diode Sample Parameters………………………………...137

VII. Peak Wavelengths of $Ge_{1-y}Sn_y$ Materials……………………………………….192

LIST OF FIGURES

Figure Page

1. Ge Band Structure and Density of States……………………………………………6

2. Ge Absorption Coefficient at Room and Low Temperature………………………8

3. PL Properties of Bulk and Thin Film Ge………………………………………... 10

4. XRD and RBS of $Ge_{1-y}Sn_y$/Ge/Si(100) Samples…………………………………25

5. PL of $Ge_{1-y}Sn_y$/Ge/Si(100) vs $Ge_{1-y}Sn_y$/Si(100) Samples………………………...27

6. PL Spectra of $Ge_{1-y}Sn_y$ for $0 \leq y \leq 0.11$ Materials………………………………. 29

7. Compositional Dependence of $Ge_{1-y}Sn_y$ Band Gaps…………………………….. 32

8. Density of States and Level Repulsion in $Ge_{1-y}Sn_y$………………………………36

9. PL Intensity Dependence on Sample Thickness for $Ge_{0.955}Sn_{0.045}$……………… 41

10. PL of n-$Ge_{1-y}Sn_y$ and Band Gap Renormalization………………………………. 42

11. PL Intensity of RTA Annealed $Ge_{1-y}Sn_y$ Samples………………………………..44

12. PL Intensity of CVD Furnace Annealed Samples………………………………. 46

13. PL Intensity of Hydrogen Plasma Treated Samples…………………………….. 48

14. PL Intensity Comparison Between Plasma Treated, CVD Furnace Annealed, and RTA Annealed $Ge_{1-y}Sn_y$ Samples…………………………………………………...49

15. AFM Before and After Hydrogen Plasma Treatment of $Ge_{1-y}Sn_y$………………. 50

16. Schematic Design of $Ge_{1-y}Sn_y$ *pin* Diodes………………………………………..53

17. SIMS Profile of $Ge_{0.93}Sn_{0.07}$ Device with a n-$Ge_{0.93}Sn_{0.07}$ Contact……………… 55

18. XRD Maps of $Ge_{1-y}Sn_y$ *pin* Diodes on n-Ge/Si(100) Substrates…………………57

19. XTEM Micrographs of $Ge_{1-y}Sn_y$ *pin* Diodes on n-Ge/Si(100) Substrates………. 60

Figure Page

20. XSTEM High Resolution Images of $Ge_{1-y}Sn_y$ *pin* Diodes on *n*-Ge/Si(100) Substrates………………………………………………………………... 62

21. Relative Population of the Γ and L Conduction Band Valleys in Relaxed $Ge_{1-y}Sn_y$ Alloys…………………………………………………………………65

22. I-V Plots and Optical Responsivity of $Ge_{1-y}Sn_y$ *pin* Diodes……………………...68

23. Activation Energies and -1V Currents of $Ge_{1-y}Sn_y$ *pin* Diodes………………….. 70

24. Microstructure of the *n*-Ge/*i*-$Ge_{0.98}Sn_{0.02}$ Interface and the EL Intensity Dependence on Injection Current for a $Ge_{0.98}Sn_{0.02}$ *pin* Diode………………….. 72

25. EL of Strain Relaxed $Ge_{1-y}Sn_y$ *pin* Diodes with a *n*-Ge/*i*-$Ge_{1-y}Sn_y$ Interface……..73

26. EL of all $Ge_{1-y}Sn_y$ *pin* Diodes with a *n*-Ge/*i*-$Ge_{1-y}Sn_y$ Interface…………………75

27. Relative Carrier Lifetimes with a *n*-Ge/*i*-$Ge_{1-y}Sn_y$ Interface……………………..77

28. EL of Strain Relaxed and Unrelaxed $Ge_{0.93}Sn_{0.07}$ Devices……………………… 78

29. EMGs of $Ge_{1-y}Sn_y$ *pin* Diodes with a *n*-Ge/*i*-$Ge_{1-y}Sn_y$ Interface…………………79

30. Modeling the EL Intensity as a Function of Injection Current………………….. 81

31. Carrier Lifetimes in $Ge_{1-y}Sn_y$ *pin* Diodes………………………………………... 83

32. XRD and Microscopy of Sn-Rich $Ge_{1-x-y}Si_xSn_y$/Ge/Si(100) Samples…………... 88

33. PL Spectra of Sn-Rich $Ge_{1-x-y}Si_xSn_y$/Ge/Si(100) Samples………………………90

34. Compositional Dependence of the Indirect Gap of Sn-Rich $Ge_{1-x-y}Si_xSn_y$……… 92

35. Compositional Dependence of the Direct and Indirect Band Gaps in Ge-Lattice Matched $Ge_{1-x-y}Si_xSn_y$……………………………………………………………95

36. Schematic Design and RBS of Sn-Rich $Ge_{1-x-y}Si_xSn_y$ *pin* Diodes………………..98

37. XRD Maps of Sn-Rich $Ge_{1-x-y}Si_xSn_y$ *pin* Diodes……………………………..…101

Figure Page

38. High Resolution XSTEM of Sn-Rich $Ge_{1-x-y}Si_xSn_y$ *pin* Diodes..................... 104

39. I-V, Optical Responsivity, and Intensity Dependence of EL on Current Injection in Sn-Rich $Ge_{1-x-y}Si_xSn_y$ *pin* Diodes... 106

40. EL Properties and Band Gaps of Sn-Rich $Ge_{1-x-y}Si_xSn_y$ *pin* Diodes............... 108

41. I-V and EL Properties of Si and Sn-Rich $Ge_{1-x-y}Si_xSn_y$ *pin* Diodes................ 110

42. RBS and XRD Maps of Ge-Rich $Ge_{1-x}Si_x$ Alloys.................................. 114

43. AFM of Ge-Rich $Ge_{1-x}Si_x$ Alloys... 116

44. Compositional Dependence of the Direct and Indirect Band Gaps in Ge-Rich $Ge_{1-x}Si_x$ Alloys Measured by Ellipsometry.. 120

45. PL Spectra of Ge-Rich $Ge_{1-x}Si_x$ Alloys... 124

46. Ge-Rich $Ge_{1-x}Si_x$ Band Gaps from PL Compared with Ellipsometry Values..... 126

47. Degree of Directness in $Ge_{1-x-y}Si_xSn_y$ Alloys.. 130

48. $Ge_{1-x-y}Si_xSn_y$ Global Band Gaps.. 133

49. Schematic Design and XSTEM Images of $Ge_{1-y}Sn_y$ *pn* Junctions................. 138

50. EL from Asymmetrically Doped $Ge_{0.935}Sn_{0.065}$ and $Ge_{0.877}Sn_{0.123}$ *pn* Junctions.. 140

51. Design and EL from Symmetrically Doped $Ge_{1-y}Sn_y$ *pn* Junctions................ 142

52. EL and I-V Characteristics of Asymmetrically Doped *pn* Junctions.............. 143

53. Design and Image of *n*-$Ge_{1-y}Sn_y$ Waveguides... 145

54. Emission Spectra of Optically Pumped *n*-$Ge_{1-y}Sn_y$ Waveguides................... 147

55. EL of All $Ge_{0.93}Sn_{0.07}$ Devices... 152

56. Proposed Layer Design for an Electrically Injected $Ge_{1-y}Sn_y$ Laser on Si......... 155

57. PL and EL Data Correction Flow.. 222

Figure	Page

58. Fitting Corrected PL and EL Data by Gaussian and EMG Functions…………. 225

59. Example Fit of Spontaneous Emission to an EMG Function…………………...226

I. INTRODUCTION, BACKGROUND, AND MOTIVATION FOR GE-BASED GROUP-IV ALLOYS

A. Introduction

Semiconductors play a vital role in modern civilization. Without them there would be no computers, cell phones, or high-definition TVs. The internet, which all of these modern marvels use to communicate vast quantities of data containing emails, webpages, and personal navigation, would not possess its high-speed capabilities without the light-emitting semiconductors that drive all telecommunications. Despite these great achievements owed to the development of semiconductor technology, our current infrastructure is struggling to keep pace with the demand for even faster communication systems, greater data storing, and more powerful computation capabilities. An elegant solution to many of these problems is to integrate new semiconductor materials with conventional Si-based platforms, in hope that the extended capabilities of these new semiconductors can be rapidly utilized without major and costly disruptions to the existing fabrication infrastructure.

Novel photonic materials such as $Ge_{1-y}Sn_y$ and $Ge_{1-x-y}Si_xSn_y$ have been shown to exhibit qualities that make them attractive candidates to meet these modern demands. By alloying Si-Ge materials with Sn they become direct gap semiconductors that efficiently emit and absorb light. This is advantageous because these materials exclusively contain group-IV, elements making them compatible with industry-standard Si substrates. This provides the opportunity to realize optical-based logic and communication components on a chip as well as improve the efficiencies of next generation solar cells.

This dissertation presents a set of parallel studies on the electrical and optical properties of $Ge_{1-y}Sn_y$ and Sn-rich ($y > x$) $Ge_{1-x-y}Si_xSn_y$ materials and devices integrated with Si(100) substrates. Photoluminescence (PL), electroluminescence (EL), and spectral responsivity measurements are used to investigate the optical properties of both material systems. Applying physically motivated lineshape models to the PL and EL spectra yield the fundamental direct (E_0) and indirect (E_{ind}) band gaps across the composition space. The results of these experiments are correlated with the sample materials properties to elucidate the relationships between sample composition, microstructure, and optical performance. The knowledge gained from the materials/performance relationships ultimately provide the basis for the development of prototype group-IV laser devices on Si.

The first chapter of this dissertation will introduce Ge as a photonic material by briefly detailing its history, technologically advantageous properties, and its limitations. This chapter will then proceed to and introduce $Ge_{1-y}Sn_y$ and $Ge_{1-x-y}Si_xSn_y$ alloys and discuss how these offer solutions to the limitations inherent to Ge by expanding its capabilities via compositional tuning with Si and Sn. Chapter II will discuss the optical and electronic properties of $Ge_{1-y}Sn_y$ materials and devices. PL studies of these materials examine the optical properties of intrinsic, doped, and processed samples, while the EL portion will focus on the optical performance of *pin* light emitting diodes (LEDs) based on these materials as a function of composition and microstructure. Chapter III will discuss the optical and electronic properties of Sn-rich ($y > x$) $Ge_{1-x-y}Si_xSn_y$ materials and devices. The first portion covers a PL study of the materials that demonstrates the ternary alloy reproduces optical properties analogous to the binary $Ge_{1-y}Sn_y$ materials. Next, the

optical performance of LEDs fabricated from Sn-rich $Ge_{1-x-y}Si_xSn_y$ materials are investigated by EL experiments. At this point the chapter digresses into a PL study of Ge-rich $Ge_{1-x}Si_x$ materials. The results of this PL study are incorporated with the PL and EL results of the $Ge_{1-x-y}Si_xSn_y$ materials previously discussed to build a global model that describes the ternary fundamental band gaps. Chapter IV will discuss progress made towards a direct gap group-IV laser on Si through the development of light-emitting waveguides and LEDs built from degenerate *pn* junctions. Chapter V will conclude the work with a summary of the dissertation and a proposal of future work to be done in order to build upon and advance the work presented.

B. Background and Motivation for Ge as a Technological Material

1. History

Ge was predicted by Dmitri Mendeleev in 1869,[1] and isolated for the first time by Clemens Winkler in 1886 from the mineral argyrodite.[2] With the advent of quantum mechanics and the classification of material crystal structures in the first quarter of the twentieth century, Felix Bloch in 1928 developed the fundamental theory that showed the energy states of electrons in a periodic potential, such as that in a crystal lattice, can be treated as a continuous band that depend on the reciprocal lattice wave-vector **k**.[3] This preliminary development was used to describe the conduction properties of metals. The early theoretical work by Bloch and others opened the door to the notion that many materials previously thought to be poorly conducting metals, such as Si and Ge, may have a range of energy levels with no available electronic states in the dispersion bands $E_n(\mathbf{k})$. This would create a gap between the set of bonding (insulating) electron states and the set of free (conducting) electron states. In order for a material with this kind of

electronic structure to carry an electrical current the insulating electrons must acquire enough energy to cross the gap to access the conducting states.[4]

At the onset of World War II, British scientists and engineers were developing and implementing radar detection devices by exploiting the rectifying current-voltage (I-V) properties produced between Si and metals.[5] When the United States entered the conflict in 1940, the National Defense Research Committee (NDRC) founded Radiation Laboratories (Rad Labs) with MIT. Research contracts were made between Rad Labs and the universities of Pennsylvania and Purdue to conduct research on Si and Ge-based radar detectors, respectively.[5] The results of the research conducted by the Purdue team were presented to the NDRC.[6] Among their achievements was the development of Ge purification from commercially available oxides, the ability to dope the material both *n* and *p*-type, and the demonstration of photo-electronic effects.[5]

In 1944, in view of the success demonstrated by the Purdue team, the manufacturing of Ge devices was passed along to Bell Labs and Western Electric for mass production.[5] By 1947, Walter Brattain and John Bardeen of Bell Labs produced the first solid-state device capable of signal amplification, the first transistor, by placing a set of three Au point contacts on a block of *n*-type Ge.[7] Up until this point, only vacuum tube triodes had this capability and these suffered from parasitic performance issues at the high frequencies required for radar and radio applications.[5]

Over the next few years much fundamental research was conducted to better understand the electronic and carrier transport properties of Ge. Major breakthroughs included the initial determination of the electronic band structure around 1953,[8,9] measurement of the Ge carrier mobilities[10] and lifetimes,[11] and the understanding of

electron and hole generation and recombination processes.[12,13] As these developments in solid state physics proceeded, William Shockley promoted the idea of creating bipolar junction transistors to circumvent the instability of the initial point-contact devices. These would consist of semiconductor layer sandwiches with a sequence of *pnp* and *npn* layers. Researchers at Bell Labs developed a process to obtain single-crystal Ge by 1950,[14] and within the following year demonstrated rectifying Ge *pn* junctions[15] on the way to fulfilling Shockley's vision of *pnp* and *npn* transistors by the end of 1951.[16] Finally in 1958, Jack Kilby made the first integrated circuit incorporating a bipolar transistor with resistors and capacitors all made from the same piece of Ge.[17]

While the researchers at Bell Labs were developing the solid-state diodes and transistors so fundamental to modern day electronics using Ge, the academic researchers at Purdue and other institutions continued their investigations on Ge after the war by studying its intriguing optical properties that had been initially reported to the NDRC.[6] In 1947 Seymour Benzer studied the photocurrent produced as a function of light intensity on Ge point-contact devices.[18] A few years later as the device technology of Ge matured to bulk junction devices, the spectral dependence of the photocurrent produced in Ge *pn* junctions was reported.[19] Based on these results, the fundamental theories describing the photon-semiconductor interactions of absorption and emission that are required to understand the operation of solar cells, light emitting diodes, and solid-state lasers, were developed.[20,21]

In 1959, Fairchild Semiconductor developed the first Si planar processing technology that eventually precipitated the end of germanium's domination of the microelectronics industry. Jean Hoerni made the first Si transistors that utilized the native

oxide as a protective and insulating barrier between the individual components in the circuit.[22] Si planar processing utilized SiO_2 to mask the device features which was advantageous over then current Ge processing because, unlike GeO_2, SiO_2 is stable under ambient conditions and the semiconductor/oxide interface is electrically passivated due to the high insulating properties of SiO_2.

2. Electrical and Optical Properties of Ge

Bulk, relaxed Ge has a diamond cubic crystal lattice structure which consists of a face-centered cubic unit cell with half of the tetrahedral sites occupied as described by the famous diamond glide plane. Figure 1 plots the electronic band structure of Ge in the panel on the left and the density of states in the panel on the right.[23] There are several

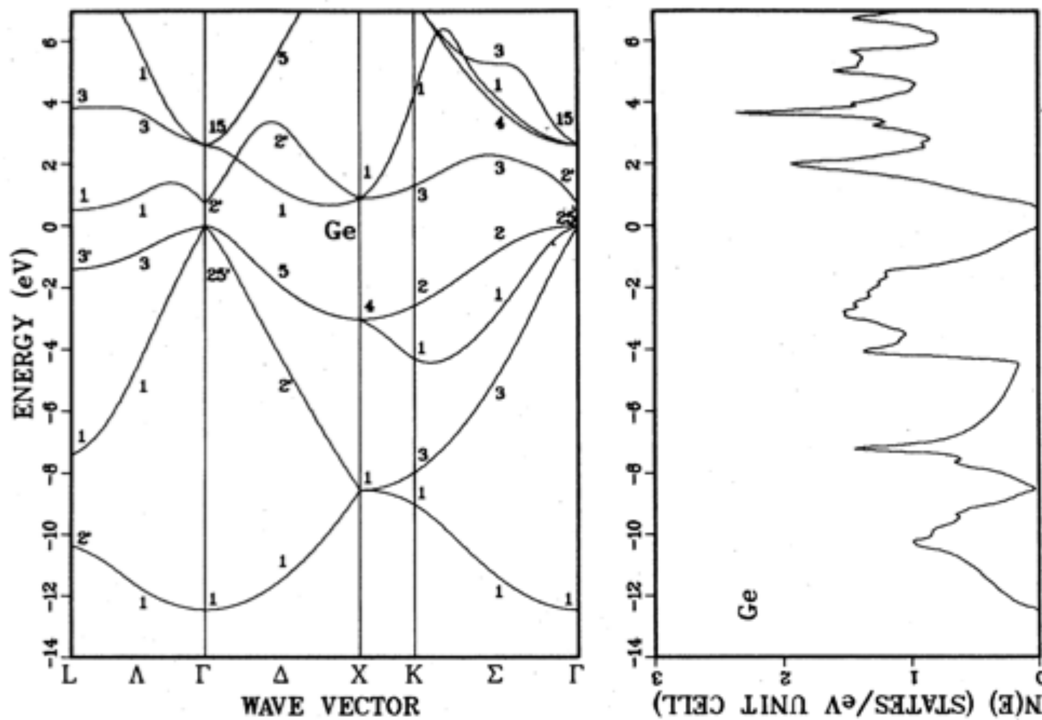

Figure 1: (Left) Energy vs wave vector for relaxed, bulk Ge. (Right) Ge density of states. Reprinted, with permission, from C. S. Wang and B. M. Klein, *Physical Review B*, 24(6), pg. 3393 (1981) (http://dx.doi.org/10.1103/PhysRevB.24.3393).

striking features about the band structure of Ge. The absolute minimum of the conduction band occurs at the L-point, $\mathbf{k} = \frac{\pi}{a}[111]$, of the 1st Brillouin Zone (BZ), where a = 5.6580 Å, the lattice constant of Ge.[24] At room temperature, this valley is only ~140 meV below the local minimum at the Γ-point, $\mathbf{k} = 0$, of the conduction band. The next local minimum of the conduction band in Ge occurs along the Δ-line near the X-point, $\mathbf{k} = \frac{\pi}{a}[100]$. The minimum of this band is an additional ~70 meV above the Γ-point.[25,26,27] The top edge of the valence band is located at the Γ-point, which implies Ge is an indirect gap semiconductor.[28] There are 2 degenerate valence bands at the Γ-point, which are referred to as the heavy hole (HH) and light hole (LH) bands. A third nearby valence band is the split-off (SO) band, separated from the HH and LH bands by the spin-orbit splitting Δ_0 = 0.30 eV.[29] These bands are named hole bands because the absence of electron from one of these bands behaves as a positively charged particle, or hole, with an effective mass inversely proportional to the curvature of the band. The effective mass of holes in the HH band is $0.347m_e$ and the mass of holes in the LH band are $0.042m_e$, where m_e is the electron free mass.[23,30] These effective masses and corresponding densities of states become important when considering the application of Ge to next-generation electronics in state-of-the-art transistors that utilize the high mobilities of electrons and holes in Ge.

The fundamental optical properties of Ge can be understood in terms of the possible electron energy transitions between the conduction band valleys and the valence band maxima across various band gaps observed in the left panel of Figure 1. The gap between the conduction band L-point minimum and the valence band Γ-point maximum is the fundamental indirect gap (E_{ind}) and the corresponding gap between the conduction band minimum and valence band maximum at the Γ-point is the direct gap (E_0). In bulk

Ge near room temperature these gaps are 0.664 eV and 0.805 eV, respectively.[31,32] In order for an electron to cross the E_{ind} gap, both the energy and momentum of the particle must change, with both quantities being conserved in the process through combined interactions involving photon absorption/emission and phonon absorption/emission.

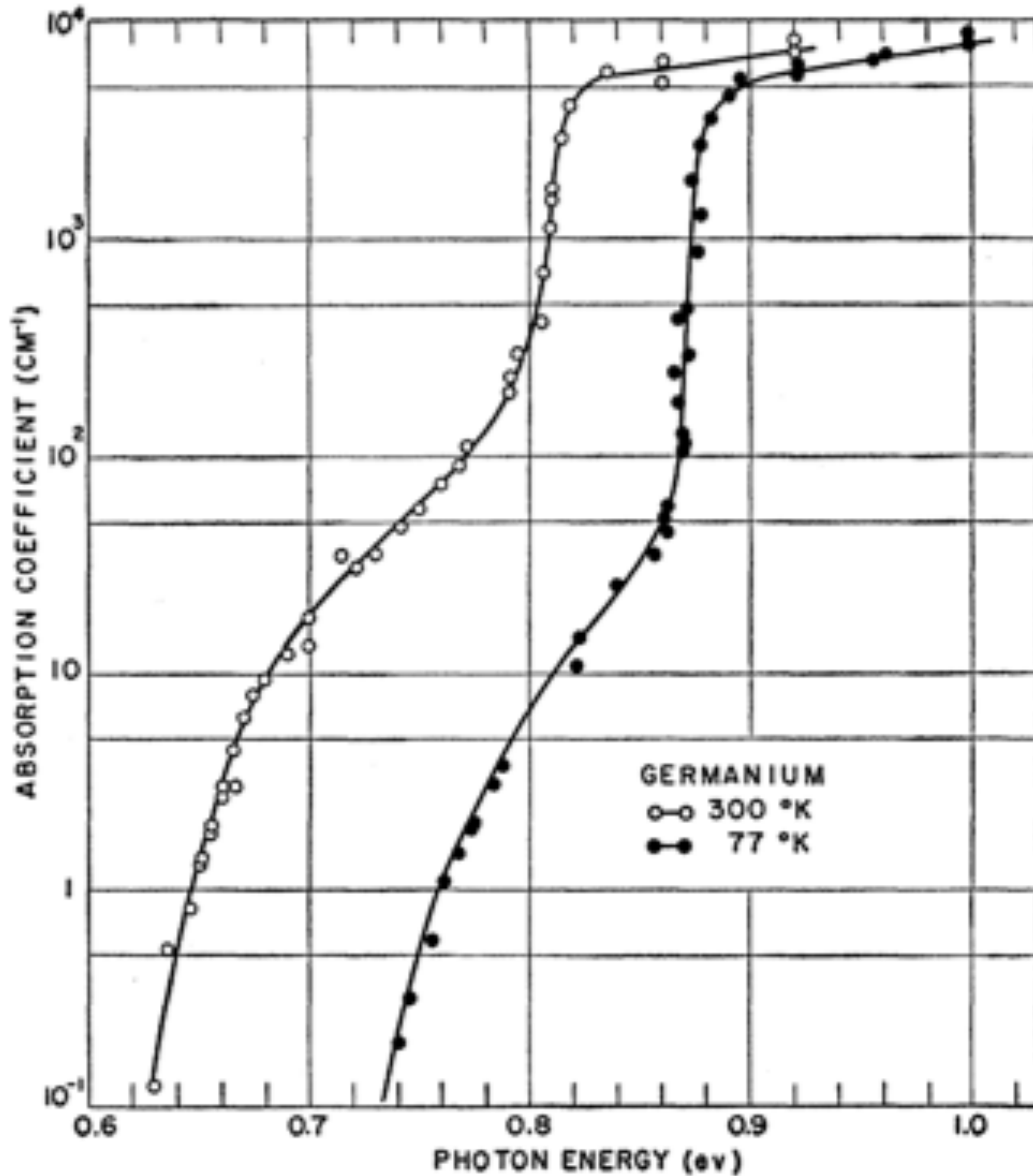

Figure 2: Absorption coefficient of single crystal Ge at 300K and 77K. Reprinted, with permission, from W. C. Dash and R. Newman, *Physical Review*, 99(4), pg. 1151 (1955) (http://dx.doi.org/10.1103/PhysRev.99.1151).

However to cross the E_0, gap only the energy of the electron changes, so these interactions require just the absorption/emission of a photon. This makes the transition across E_0 at the Γ-point much more efficient for optical applications relative to transitions across E_{ind}. As mentioned above, the lowest band gap in Ge is not the direct transition. This makes Ge much more inefficient at emitting light than many III-V semiconductors which do possess a direct fundamental band gap. Additionally, the density of states in the L-valley of the conduction band is much higher than in the Γ-valley,[33] so even if Ge were to be made into a direct gap material, there would still exist significant inefficiencies because a vast majority of the carriers would populate the L-valley once quasi-thermal equilibrium in the conduction band is reached.

Figure 2 plots the room temperature (300 K) and liquid nitrogen (77 K) absorption coefficient of Ge measured by transmission over an energy range straddling the fundamental E_{ind} and E_0 band gaps.[34] The data taken at 300 K shows that the material begins to absorb light for photons with energy ~0.63 eV. The absorption is gradual and not very strong initially since the photoexcited electrons near the top of the valence band at the Γ-point must also change wave vector in order to populate the L-valley. It is worth noting that in recent years the consideration of excitonic effects on the absorption of Ge has been found to be significant in describing the band-edge absorption of Ge-like materials, even at room temperature.[35] When light with energy nearly equal to E_0 is incident on the sample, ~0.80 eV, the absorption increases by almost an order of magnitude as access to the unoccupied states in the Γ-valley become available. This demonstrates qualitatively the much higher efficiency of optical transitions across E_0 relative to E_{ind}. The data also shows that the band gaps shift to higher energies as the

material is cooled to lower temperatures due to thermal expansion/compression and the electron-phonon interaction.[36] This phenomenon is well described by a mathematical

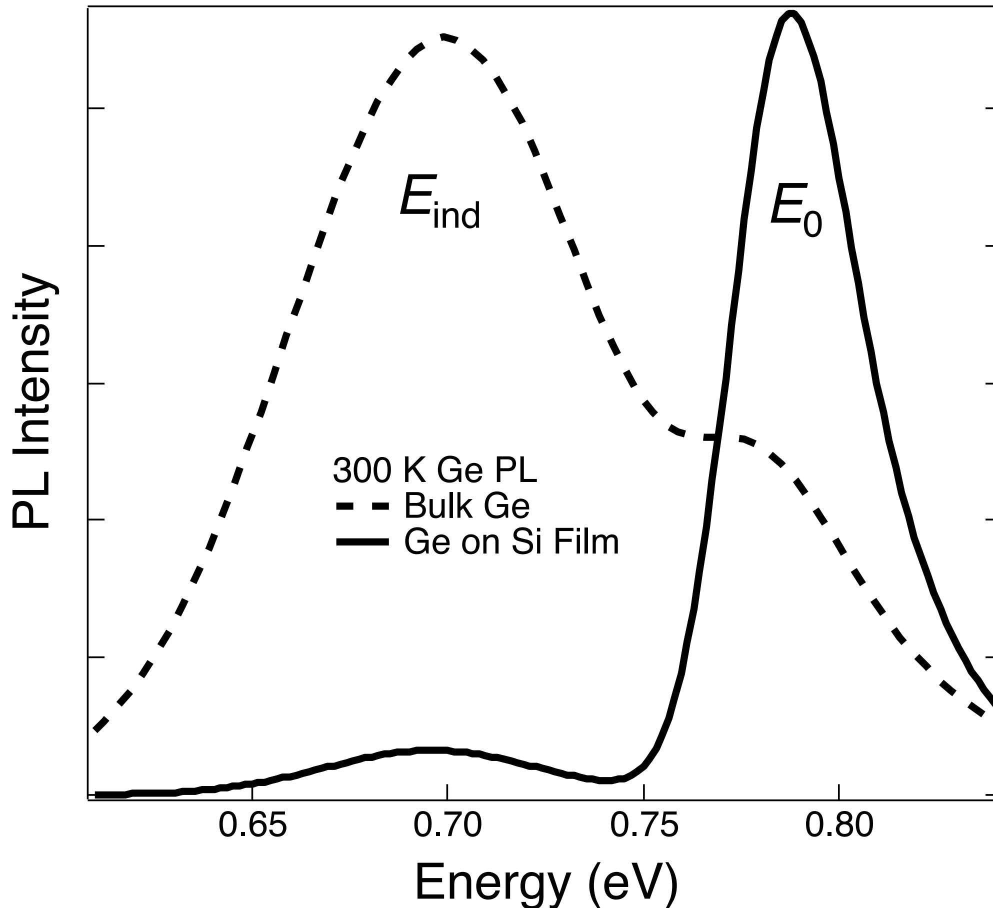

Figure 3: 300 K PL of bulk Ge (dashed line) and thin film Ge (solid line) showing the relative difference in emission between the direct and indirect gap signals.

expression proposed by Varshni in 1967.[37]

Figure 3 plots the normalized 300 K PL spectra of bulk and thin film Ge specimens excited with a 980 nm laser, which enables carriers to populate all 3 valleys of the conduction band. The dashed line spectrum, representing bulk Ge, shows a dominant peak at ~0.68 eV due to emission from the indirect gap with a shoulder signal that peaks around ~0.78 eV from the direct gap. This can be understood as radiative recombination across the E_{ind} and E_0 gaps, respectively. In a typical semiconductor, PL is observed from

the fundamental band gap, whether direct or indirect, because the relaxation time of electrons (holes) to the lowest (highest) energy conduction (valence) band states is much faster than the electron-hole recombination across the band gap. In the case of Ge, however, one observes a shoulder at higher energy that corresponds to recombination across the fundamental gap. Because the conduction band minima are so close, at room temperature some electrons will reside at the Γ-valley minimum, and they produce an observable signal because their recombination probability, not being phonon-assisted, is much higher. In fact, the direct gap signal would be much stronger were it not for the fact that photoexcited electron-hole pairs in Ge can travel for several microns without recombining, and when they do deep inside the sample, the direct-gap light can be reabsorbed by phonon-assisted processes associated with the lower indirect gap. This is clearly demonstrated by studying the emission properties of submicron-thick Ge films, in which reabsorption is negligible and the emission is dominated by the E_0 feature, as seen in the figure.[38]

Based on the above electrical and optical properties Ge has the potential to extend the current capabilities of modern semiconductor technology. The higher carrier mobilities in Ge relative to Si offer an attractive alternative to Si-based transistors because these devices can be operated at higher frequencies. Traditionally, the performance of microchip processors has been expanded through miniaturization of the feature sizes. Current transistor technology has reduced the nodes to lengths smaller than 15 nm, approaching the length scales where surface and quantum effects begin to dominate the performance.[39] In devices this small, high-k dielectric materials have replaced traditional SiO_2 insulation, negating the convenience of Si-based processing.

This opens the door to revisit Ge-based transistors. Combining Ge with novel high-*k* dielectrics offers the combined advantages of higher carrier mobilities and a lower band gap channel material at the reduced feature sizes. This would enable circuits to lower on/off voltage thresholds, decreasing power consumption while increasing operating frequencies.[40] However the high cost of Ge substrates and the cost of revamping entire microprocessor production lines hinders the resurrection of a Ge-based semiconductor microelectronics industry. Additionally, Ge NFETs to date have not demonstrated superior performance relative to analogous Si devices due to an inability of conventional doping technologies to attain the required ultra high *n*-type densities in Ge.[41]

Already commercially available Ge-based photovoltaic, or solar, cells have the highest conversion efficiency of light to electrical energy thanks to the small band gap and high absorption coefficient. The current state of the art architecture uses heterojunction stacks of Ge/$In_{0.01}Ga_{0.99}As$/$In_{0.50}Ga_{0.50}N$ materials capable of achieving 30% conversion efficiency.[42,43] Again however, the cost of Ge substrates, stemming from the low natural abundance of the element, represents more than half the manufacturing expense of these devices. This limits their applicability to niche markets, meaning bulk Ge does not represent a solution to a global mandate for universal renewable energy.

Ge also has the potential to be used as a detector, modulator, and light source material in optoelectronic communication systems since its operational wavelengths fall within the range of interest for telecommunications (1300-1700 nm).[44] However the indirect nature of the electronic bandstructure means that for wavelengths longer than E_0, ~1550 nm, Ge is not very optically efficient. At the moment direct gap III-V materials such as GaAs and InGaAs alloys are standard for this application, since these materials

are the most efficient known at these wavelengths.[45] However, the dream of telecommunications on a chip requires the epitaxy and fabrication of components on a Si wafer,[46] and there are several issues with growing polar III-V materials on non-polar group-IV substrates. These issues include a significant lattice and thermal mismatch with the Si substrate, and the formation of antiphase domains caused by the polar/non-polar interface.[47,48,49] All of these problems contribute to the production of a high density of threading dislocations in the device active layer, which inhibits light emission.[50] Advances have been made by growing thin film quantum well/quantum dot laser structures consisting of InAs, GaAs, AlGaAs, and III-V nanopillars directly on Si using AlSb buffer layers, which has been found to reduce the typical defects associated with III-V growth on Si.[51] However the growth, processing, and implementation of these structures is highly complex and may not be CMOS compatible.[52,53]

One option to revolutionize the telecommunications industry would be to produce group-IV light sources on Si substrates, such as lasers and LEDs, that are capable of operating effectively in the same wavelength regime as the current state of the art technology based on III-V materials.[54] However, as mentioned above, bulk Ge does not appear to be a practical candidate suited for this purpose. On the other hand, the epitaxy of Ge on Si offers some intriguing possibilities to not only reduce the cost of integrating Ge technologies with standard platforms, but also offers solutions to a few of the limitations of bulk Ge.

3. Epitaxy of Ge for Applications

As mentioned above, the high cost of Ge wafers limits the possible applications for Ge-based technologies to epitaxially grown thin films of the material on suitable

substrates. To integrate Ge technologies with standard platforms requires epitaxy on Si. However there is a 4.2% lattice mismatch between Ge and Si,[55] which means that any Ge films grown on Si will suffer from a high density of defects if grown beyond a certain critical thickness for layer-by-layer growth, which is only ~1.0 nm for Ge films on Si.[56,57,58]

Initial efforts to produce defect-free Ge on Si involved the use of compositionally graded $Ge_{1-x}Si_x$ buffer layers grown between the Si and Ge layers to gradually accommodate the lattice mismatch. In this scheme the composition of Si in the buffer layer decreases until pure Ge is obtained.[59] This approach to Ge has been shown to produce threading dislocations that terminate in the graded buffer layer and do not penetrate into the Ge layer of interest. Using this strategy, researchers have produced relaxed Ge films on Si with defect densities as low as 10^6 cm^{-2}.[60] The major drawback to this approach is that the compositionally graded buffer layer is costly, technologically complex to produce, and is not a viable option as an electrical medium between the Si and the Ge due to carrier scattering and losses caused by the defects that are produced to accommodate the lattice mismatch.

Advances in growth technology and processing have made it possible to grow device quality Ge films directly on Si. In recent years, ASU has developed strategies to routinely produce intrinsic and *n*-type Ge on Si templates via low temperature routes.[61] Critical to this achievement has been the development of the more reactive higher order germane precursor molecules trigermane (Ge_3H_8) and tetragermane (Ge_4H_{10}) for epitaxial growth.[62] Following the growth utilizing these precursors, a thermal treatment is applied to reduce the threading dislocation density. Employing these protocols, Ge layers with

defect densities as low at 10^7 cm^{-2} are routinely produced on Si substrates at growth rates as high as 20 nm/min.[63] The recent introduction of the specialty designed hydride precursors V-$(GeH_3)_3$ and V-$(SiH_3)_3$ (V = P, As) as *n*-type dopant sources has been shown to suppress the issue of incomplete donor ionization in highly doped Ge films as well.[64] These dopant sources, when combined with the higher order germane molecules at ultra-low temperatures, deliver device-quality *n*-Ge films with donor densities approaching the 10^{20} cm^{-3} range of interest for photonic and electronic applications, boding well for the development of Ge NFETs.[41,55,65]

One of the byproducts of thermally treating Ge films grown on Si in conjunction with the growth is the introduction of biaxial tensile strain in the Ge-layer. The thermal expansion coefficient of Ge is about twice that of Si, so if a thermal treatment is applied to Ge films grown on Si, such as annealing followed by quenching, the Ge layer will be left with a tensile strain. This fortuitously enhances the sought-after optical and electrical properties of Ge. Introducing lattice deformation to a material produces strain that perturbs the bandstructure. In Ge, strain lifts the degeneracy between the HH and LH bands and adjusts the relative separation between the L and Γ-valleys. The application of biaxial tensile strain has been found to decrease the separation between the L and Γ-valleys while lowering the overall band gap, allowing Ge take on the features of a more direct gap material that operates at longer wavelengths.[66,67] This increases the light emission efficiency and offers a means to materials with excellent optical performance in the wavelength range of interest for communications. Direct gap Ge films with tensile strains greater than 2% have been demonstrated by growing the material on InGaAs-buffered GaAs substrates.[68] However the theoretical maximum tensile strain that can be

attained in Ge films on Si is only 0.34%,[69] well below the 2% threshold to direct gap materials.[66] Biaxial compressive strain on the other hand increases the separation between the L and Γ-valleys, making the material more indirect in nature, which decreases the ability to emit light efficiency. For this reason, researchers have focused on developing tensile strained Ge films on Si for photonic applications.

There have been several successful demonstrations of tensile strained Ge films operating as quasi-direct materials due to the decrease in separation between the Γ and L-valleys that occurs. Most notably, the reduction in Γ-L separation has been documented by PL measurements of thin films and EL measurements of diode devices.[70,71] The optical output of Ge can be further enhanced by doping the material *n*-type in the 10^{19}-10^{20} cm^{-3} range.[72] Doping at these levels increases the quasi-Fermi level for carriers in the conduction band so that higher population of the Γ-valley is obtained. This increases the probability of radiative recombination occurring across the direct gap relative to the indirect gap, which can introduce non-radiative losses, once a hole is introduced into the valence band. PL measurements of such materials have been shown to increase the emission output by almost an order of magnitude.[70,73,74,75] In addition to promoting more efficient E_0 radiative recombination, heavy *n*-type doping of Ge materials also causes an overall renormalization of the bandgap to slightly lower energies as a function of dopant concentration.[76,77] This is due to the presence of the impurity atoms perturbing the electronic wavefunctions of the band-edge states.[78,79] The combined approach of biaxial tensile strain and heavy *n*-type doping led to the first report of an optically pumped Ge waveguide laser in 2010,[80] followed by an electrically pumped laser about two years later.[81]

C. Background and Motivation for $Ge_{1-y}Sn_y$ Materials

An alternative strategy to tensile strain for obtaining direct gap group-IV materials is to compositionally tune Ge by alloying it with the semi-metal Sn. This idea was originally proposed in 1982.[82] At temperatures below 13.2^{o}C, elemental Sn takes on the diamond cubic structure, α-Sn. Above this temperature it transitions to the tetragonal β-Sn phase. This suggests that a small amount of Sn placed on substitutional sites in a Ge parent lattice should form a metastable alloy with a diamond cubic structure under ambient conditions. The idea that direct gap group-IV material can be achieved via alloying Ge with Sn is based on inspecting the bandstructure of Ge and α-Sn, the latter of which was first calculated by Steven Groves and William Paul.[83] At the Γ-point of α-Sn the E_0 band gap is -0.40 eV while the gap between the conduction band L-valley to valence band Γ-maximum, E_{ind}, is 0.16 eV. Therefore a linear interpolation between the endpoint gap values of Ge and α-Sn means a direct gap $Ge_{1-y}Sn_y$ material occurs at some critical composition (y_c) in the composition space. Initial theoretical calculations utilizing tight-binding and pseudopotential methods predicted $y_c = 0.20$.[84,85] However, experimental work measuring the optical properties of these materials showed that this likely occurred at much lower compositions,[86] likely in the range of ~10% Sn.[87] Another motivating factor for the development of $Ge_{1-y}Sn_y$ alloys is as tailored substrates to tensile strain Ge films. Since the lattice constant of α-Sn is 6.4912 Å,[88] diamond cubic $Ge_{1-y}Sn_y$ alloys will take on a continuous range of lattice constants between Ge and the α-Sn value.[89] Such materials would be completely compatible substrates for the subsequent epitaxy of tensile strained direct gap Ge.

The first $Ge_{1-y}Sn_y$ materials were produced by sputtering and pulsed UV laser annealing, resulting in polycrystalline films.[90] It took several years for the first single-crystal materials to be grown due to the low solid solubility limit of Sn in Ge, which is under 1.1%.[91] Ultimately, success came by growing $Ge_{1-y}Sn_y$ on alternative substrates such as Ge, GaAs, and InSb.[92,93,94] Molecular bean epitaxy (MBE) growths in the late 1990's produced films with high enough quality on Si that allowed systematic measurement of the optical properties.[86,95] However the MBE growth mechanism tended to produce films where the Sn would precipitate to the surface.[94,96]

In 2001, ASU demonstrated the first epitaxial deposition of $Ge_{1-y}Sn_y$ in a high-vacuum environment by a commercially-compatible chemical vapor deposition (UHV-CVD) route on Si substrates.[97] These depositions were conducted at 350°C through reactions of phenyl-stabilized deuterated stannane ($(Ph)SnD_3$) and digermane (Ge_2H_6). The resultant films were shown to be random alloys with no deuterium or C impurities based on forward scattering RBS and C-resonance, with a diamond structure as demonstrated by TEM diffraction and Raman scattering. Following this initial breakthrough, a new method was developed utilizing the stabilized precursor deuterated stannane (SnD_4) which was reacted between 250°C and 350°C with Ge_2H_6 by a similar UHV-CVD route as in Ref. 97. These experiments produced single crystal diamond cubic $Ge_{1-y}Sn_y$ alloys on Si(100) which led to device-quality materials.[98,99] In subsequent studies, this method was used in conjunction with newly developed *p* and *n*-type doping protocols using the gas-source diborane (B_2H_6) and trigermyl-phosphene ($P(GeH_3)_3$) molecular precursors,[100] respectively, to systematically produce photodiodes devices on Si(100) that demonstrated extended IR performance relative to analogous Ge

devices.[101,102,103,104] These systems showed tunable direct gap PL and EL emission in $Ge_{1-y}Sn_y$ materials and devices with thicknesses up to 1 μm and $y < 0.05$.[105,106] Other CVD routes to high-quality $Ge_{1-y}Sn_y$ materials on Si have been developed by other groups and involve reactions of tin-tetrachloride ($SnCl_4$) as the Sn source with germane (GeH_4) or Ge_2H_6.[107,108]

The growth of $Ge_{1-y}Sn_y$ using the SnD_4/Ge_2H_6 strategy experiences shortcomings with attempts to grow relaxed films at higher Sn concentrations approaching direct gap alloys. This is due to the growth rate declining quickly as the temperature is lowered in order to substitute more Sn into the Ge parent lattice. This results in very thin films (thickness < 300nm) with a high degree of compressive strain. Thus a new strategy to $Ge_{1-y}Sn_y$ materials was introduced based on the higher-order molecule trigermane (Ge_3H_8), which is a more reactive species than Ge_2H_6. Reactions between Ge_3H_8 and SnD_4 were found to increase the growth rate on Si and enabled incorporation of up to 9% Sn in films that closely reflected the stoichiometry of the gas-source mixtures.[109] Use of this molecule as the Ge-source was also found to not change the doping protocols of $Ge_{1-y}Sn_y$ materials.[109] PL of these materials showed a continuation of the trend toward direct gap materials based on a systematic redshift of the direct gap emission peak as a function of composition. The PL intensities however remained too low to distinguish a significant E_{ind} signal that would enable accurate measurement of this gap for determination of the y_c composition. The inability to resolve the E_{ind} feature in these films is attributed to the high interface recombination velocity between the $Ge_{1-y}Sn_y$ layer and Si substrate due to the high defect density inherent to this interface.[38]

In order to reduce the non-radiative recombination at the epilayer/substrate interface, Chapter II of this dissertation begins by describing the development of $Ge_{1-y}Sn_y$ materials grown on Ge-buffered Si(100) substrates using higher-order Ge-hydride gas source precursors. The Ge buffers enable the epitaxy of $Ge_{1-y}Sn_y$ materials on a virtual platform with a lower lattice mismatch compared to the Si substrate. This is intended to reduce the number of threading dislocations penetrating into the $Ge_{1-y}Sn_y$ epilayer enabling the growth of highly crystalline materials with compositions between 0 and 12% Sn. Room temperature PL from such samples allowed simultaneous observation of the E_0 and E_{ind} transitions, producing a systematic study of the compositional dependence of these band gaps leading to the determination of y_c. Practical devices are demonstrated extending the previous studies of devices on Si(100) by growing on an *n*-Ge contact buffer layer. Other researchers have employed similar methods of $Ge_{1-y}Sn_y$ on Ge-buffered Si growth and these have resulted in successful detectors, LEDs, and even optically pumped lasers operating at low temperature.[110]

D. Background and Motivation for $Ge_{1-x-y}Si_xSn_y$ Materials

The use of ternary $Ge_{1-x-y}Si_xSn_y$ alloys was initially proposed in 1991 as a group-IV analog to III-V ternaries that allow tuning of the electronic structure at a fixed lattice constant to be used as a band offset material in Ge/$Ge_{1-y}Sn_y$ quantum well structures.[111,112] In addition, calculations have shown that the performance of the current state-of-the-art high-efficiency photovoltaic (PV) cells based on the Ge/$In_{0.01}Ga_{0.99}As$/$In_{0.50}Ga_{0.50}N$ architecture can be extended with the insertion of a 1.00 eV gap material.[113] However, such a material must also lattice match Ge. $Ge_{1-x-y}Si_xSn_y$ offers a solution to this ambition because at a Si:Sn ratio of ~4:1 this system possesses a

lattice constant equal to Ge with adjustable band gaps tunable in energy above Ge.[114] Thus in principle, at a special composition, such a material should possess the necessary E_{gap} = 1.00 eV of interest for Ge-based PV applications.

The $Ge_{1-x-y}Si_xSn_y$ ternary was first synthesized at ASU in 2003 by Bauer *et. al.* via reactions of SnD_4 and silyl-germane (SiH_3GeH_3) on $Ge_{1-y}Sn_y$-buffered Si(100) substrates in a UHV-CVD environment.[115] Later generations of the synthesis protocols replaced the SiH_3GeH_3 molecule with the commercially available compounds trisilane (Si_3H_8) and Ge_2H_6.[116] This led to epitaxy of intrinsic and doped alloys directly on Si(100) and Ge(100) using this method.[117,118,119] These materials were subsequently shown to possess the key property that initiated their exploration: a tunable band gap at a fixed lattice constant equal to that of Ge.[120] With the development of the higher order germane precursors Ge_3H_8 and Ge_4H_{10},[61] the current generation of ternary synthesis involves reactions of Ge_4H_{10} (Ge_3H_8), tetrasilane (Si_4H_{10}), and SnD_4.[114,121] These materials were fabricated into solar cell devices and photodiodes on Ge(100) and Si(100) substrates featuring materials with 1.0 eV band gaps.[114,122,123]

An important consequence of Si incorporation is that ternary $Ge_{1-x-y}Si_xSn_y$ is more thermally robust than binary $Ge_{1-y}Sn_y$ for the same Sn concentration due to increased mixing entropy.[117] This opened the opportunity to explore Sn-rich $Ge_{1-x-y}Si_xSn_y$ materials as alternatives to $Ge_{1-y}Sn_y$ for photonic applications as detector and emitter materials for integrated Si photonics. Initial PL measurements of Sn-rich films grown on Si showed a systematic redshift of E_0 as a function of Sn concentration, analogous to that observed for $Ge_{1-y}Sn_y$.[124] Photodiode devices fabricated from the Sn-rich class of ternary alloy

demonstrated an extension of the absorption edge in detectors on Ge(100) covering all telecommunication bands, strengthening the analogy with $Ge_{1-y}Sn_y$.[125]

Chapter III is devoted to the systematic investigation of this analogy. A parallel study of the fundamental E_{ind} and E_0 band gaps by PL is presented demonstrating a crossover to direct gap materials in the Sn-rich ternary family of materials when grown on Ge-buffered Si substrates, which reduces the lattice mismatch with the light-emitting epilayer. These materials are then fabricated into photodiode devices on *n*-Ge buffered Si(100) platforms to show EL for the first time. A global fit to the ternary band gaps shows that incorporating a small fraction of Si into $Ge_{1-y}Sn_y$ alloys with $y > y_c$ may widen the Γ-L separation in favor of enhanced direct gap materials. This is attributed to a very large SiSn bowing coefficient in the electronic band gaps.

II. OPTICAL AND ELECTRONIC PROPERTIES OF GE-SN MATERIALS AND DEVICES

Portions of text and figures in this chapter were previously published as J. D. Gallagher, C. L. Senaratne, J. Kouvetakis, and J. Menéndez, *Appl. Phys. Lett* **105**, 142102 (2014) and have been reproduced with permission. Portions of text and figures in this chapter were previously published as J. D. Gallagher, C. L. Senaratne, P. Sims, T. Aoki, J. Menéndez, and J. Kouvetakis *Appl. Phys. Lett* **106**, 091103 (2015) and have been reproduced with permission. Portions of text and figures this chapter were previously published as J. D. Gallagher, C. L. Senaratne, C. Xu, P. Sims, T. Aoki, D. J. Smith, J. Menéndez, and J. Kouvetakis *J. Appl. Phys.* **117**, 245704 (2015) and have been reproduced with permission.

A. Optical Properties of $Ge_{1-y}Sn_y$ Materials

1. Introduction

As discussed in Chapter I, the development of high-quality single crystal $Ge_{1-y}Sn_y$ materials grown on Si(100) by UHV-CVD led to the first demonstration of light emission from these alloys by PL.[105] Strain-relaxed films containing up to 5% Sn approaching 1 μm thicknesses were grown by the Ge_2H_6/SnD_4 method directly on Si.[99] Room temperature PL experiments of these materials confirmed the early theoretical predictions and experimental data by absorption-based measurements that $Ge_{1-y}Sn_y$ becomes a direct gap semiconductor at some composition y_c.[84,86] In this initial study, room temperature PL was demonstrated to be a uniquely advantageous technique for mapping the compositional dependence of the fundamental band gaps in $Ge_{1-y}Sn_y$. The spectra in this case contained features corresponding to Ge-like E_0 and E_{ind} emission. This enabled the

first compositional mapping of the separation between the Γ and L conduction band valleys, allowing an empirical extrapolation of $y_c \sim 0.11$.[105] Despite this success, direct measurement of y_c was initially unobtainable due to an incapacity to grow PL-quality materials containing $y > 0.05$ using the Ge_2H_6/SnD_4 method. Attempts to grow samples in this composition range must be done at systematically lower temperatures to ensure full Sn substitution. Due to the lower reactivity of Ge_2H_6 at lower temperatures the growth rates of the films were so low that the materials did not fully relax on the Si substrate and had a limited maximum thickness. The growth of high quality materials directly on Si is also complicated by the 4.2% lattice mismatch with Ge. This increases concurrently as a function of Sn and so a large number of dislocations are inveitably generated at the $Ge_{1-y}Sn_y$/Si interface. Since the alloy becomes more thermally unstable at higher Sn compositions, thermal annealing treatments quickly become very limited in their ability to adequately annihilate these defects and yield low defect density post-growth materials without decomposing the material by Sn segregation.[126,127]

Misfit dislocations are highly undesirable from the perspective of producing PL-quality samples because they act as carrier trap sites that quench radiative recombination, lowering the signal-to-noise ratio in PL spectra. This is due to the ~0.4 mm diffusion length of carriers in Ge,[128,129] such that having a highly defective $Ge_{1-y}Sn_y$/Si interface increases the non-radiative recombination rate significantly for typical film thicknesses. Overall this complicates an accurate determination of y_c, which requires precise line-shape modeling of the spectral features. In order to obtain high quality $Ge_{1-y}Sn_y$ materials with Sn contents near y_c, two adjustments to the growth were made. The first adjustment substituted Ge_2H_6 for the more reactive Ge_3H_8 precursor, which increased the growth rate

of $Ge_{1-y}Sn_y$ films on Si and produced PL quality materials with y up to 0.09.[109] The second adjustment was to grow $Ge_{1-y}Sn_y$ alloys on Ge-buffered Si(100) substrates that are produced by a gas-source molecular epitaxy route (GSME) using Ge_4H_{10}.[61] This yields a high-quality template with a reduced lattice mismatch between the target alloy film and substrate, thereby reducing the density of parasitic dislocations that hinder clear and distinct E_0 and E_{ind} PL features. Growth of the alloy on a Ge buffer is also predicted to have a Type-I band offset alignment.[130] This type of band offset is favorable for light emission because it confines the photoexcited carriers in the $Ge_{1-y}Sn_y$ layer, further increasing the probability of radiative recombination occurring there.

2. *Growth and Materials Properties of $Ge_{1-y}Sn_y$ on Ge/Si(100) Substrates*

Thick (~500 nm), luminescent $Ge_{1-y}Sn_y$ films containing up to 11% Sn were grown on Ge-buffered Si by UHV-CVD reactions of Ge_3H_8 and SnD_4. The specific growth details such as temperature, pressure, and mixture ratios are reported in Refs. 131

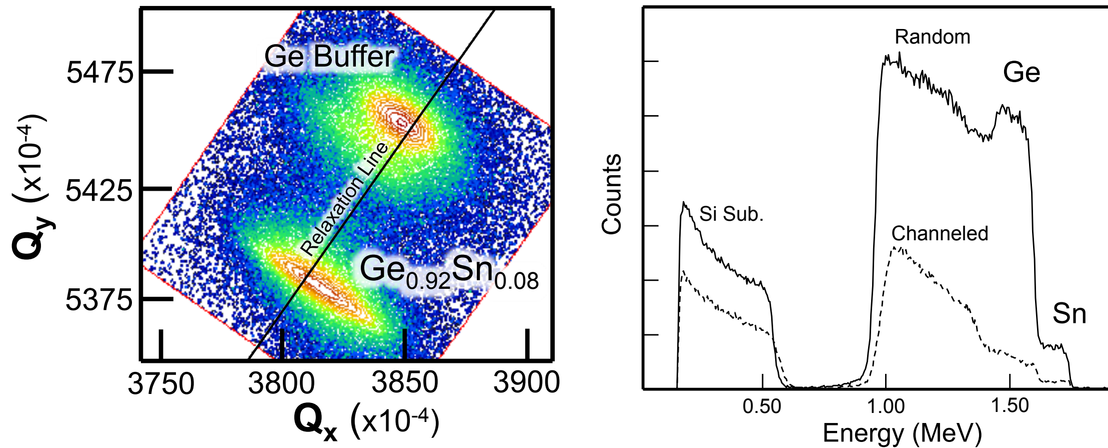

Figure 4: (Left) XRD 224 RSM of a 8% Sn layer grown on a Ge buffer. This layer is almost fully relaxed. (Right) 2 MeV RBS showing channeling and random spectra of both the Ge and Sn signals in the Ge and $Ge_{1-y}Sn_y$ epilayers. Samples and data produced and collected by Charutha Senaratne. See C. L. Senaratne, J. D. Gallagher, L. Jiang, T. Aoki, D. J. Smith, J. Menéndez, and J. Kouvetakis, *Journal of Applied Physics*, 116, 133509 (2014).

and 132. The Sn concentrations were determined from Rutherford Backscattering (RBS) and X-ray diffraction (XRD). The agreement between the two techniques is excellent when the compositional dependence of the cubic lattice parameter from Ref. 89 is applied. The left panel of Figure 4 plots a representative high-resolution XRD reciprocal space map taken along the off-axis (224) reflection for a 8% Sn alloy grown on a Ge buffered Si(100) substrate. The map shows a symmetric peak corresponding to the Ge buffer layer exhibiting a slight tensile strain as can be seen by the position of this peak above the cubic relaxation line. The peak corresponding to the $Ge_{0.92}Sn_{0.08}$ alloy demonstrates a single-phase material with a residual level of compressive strain. Despite the large critical thickness for pseudomorphic growth of $Ge_{1-y}Sn_y$ alloys on Ge,[133] the samples produced in this study routinely exhibit highly relaxed $Ge_{1-y}Sn_y$ films grown on the virtual Ge substrate. The right panel of Figure 4 plots the 2 MeV random and channeled RBS spectra from this sample. The layers of the Ge and $Ge_{0.92}Sn_{0.08}$ materials are modeled to be 620 nm and 500 nm, respectively. The high degree of channeling across the Ge and $Ge_{1-y}Sn_y$ layers is indicative of excellent crystallinity, good epitaxial alignment to the Si wafer, and full substitution of the alloy Sn atoms into the parent Ge diamond lattice. Additionally, the Sn profile across the alloy layer is flat, indicating no compositional gradients, phase segregation, or surface precipitation.

Further characterizations on the microstructural properties of these films were conducted on portions of the specimens prepared for systematic investigation by transmission electron microscopy (TEM).[131,134] Low magnification micrographs showed low defectivity in the GeSn epilayer, indicating that the Ge buffer serves as an excellent lattice mismatch negotiator. Images taken of plan view TEM samples revealed a

dislocation density of 5×10^7 cm^{-2}.[131] Finally, elemental mapping by electron energy loss spectroscopy (EELS) revealed substitution of Sn into a diamond lattice, supporting the interpretation of the channeling observed in RBS.[134] These microstructural results corroborated with the XRD and RBS data support the notion that the $Ge_{1-y}Sn_y$ alloys used in this PL investigation are highly crystalline random alloys.

3. *Optical Properties of $Ge_{1-y}Sn_y$ Materials on Ge/Si(100) Substrates*

Photoluminescence (PL) experiments were performed at room temperature on samples excited with 400 mW of continuous wave (cw) 980 nm radiation focused to ~ 20 μm spot. The laser is modulated by an optical chopper enabling lock-in detection of the light emitted by the sample, improving the signal-to-noise ratio. The emitted light is

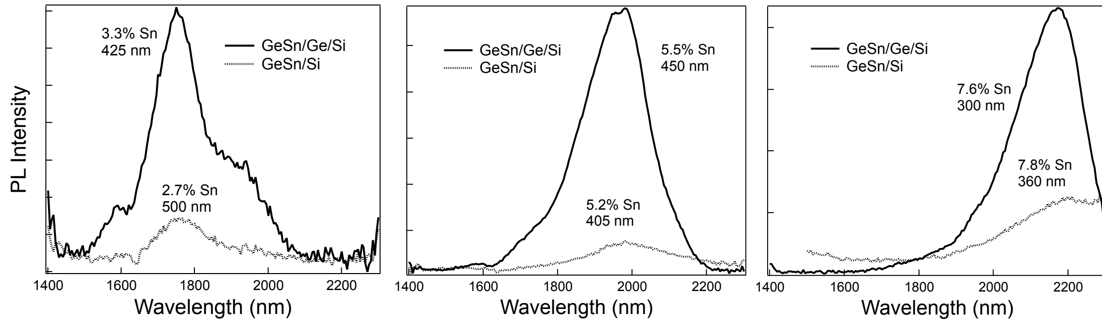

Figure 5: PL spectra for analogous GeSn/Ge/Si(100) and GeSn/Si(100) samples. Note the significantly stronger PL signal in the samples grown on Ge buffers. Samples produced by Charutha Senaratne. See C. L. Senaratne, J. D. Gallagher, L. Jiang, T. Aoki, D. J. Smith, J. Menéndez, and J. Kouvetakis, *Journal of Applied Physics*, 116, 133509 (2014).

passed through a grating spectrometer (f = 140 mm Horiba MicroHR) with a 600 grooves/mm grating blazed at 2 μm. Long pass filters were used to block visible radiation and possible emission from the Si substrate. In spite of the long pass filters, a residual laser signal was observed in second-order at 1860 nm. The light is detected by a photodiode placed at the exit slit. The laser line was subtracted from the spectra by fitting it with a Gaussian lineshape. From the width of this Gaussian we estimate the spectral

resolution to be 10 nm for the spectrometer's slit settings. The wide composition range of the samples used in this study requires the use of three detectors: a liquid-nitrogen (LN_2) cooled InGaAs diode (up to 2300 nm), a thermoelectrically-cooled (TE) InGaAs device (up to 2500 nm), and a TE cooled PbS detector (up to 2700 nm). The system response with the three detectors was calibrated with a tungsten-halogen lamp and the spectral energy accuracy was verified by measuring the emission lines from an argon-arc lamp. Spectral corrections were applied to the data to account for the spectrometer response and long pass filter transmission, as discussed in Appendix E.

Figure 5 plots a series of room temperature PL spectra comparing $Ge_{1-y}Sn_y$ materials grown on Ge-buffered Si(100) substrates with samples grown directly on Si(100) wafers that have comparable thicknesses and compositions. We note that over the entire range of compositions, the emission from $Ge_{1-y}Sn_y$ materials on the Ge buffers display systematically higher intensities than their counterparts on Si. The higher intensities produced by the alloys grown on the Ge buffers improves the signal-to-noise ratio to such an extent that the E_0 and E_{ind} features can clearly be resolved in these spectra, whereas the difference between these features is much more ambiguous for the samples grown on Si. This enables the $Ge_{1-y}Sn_y$/Ge/Si(100) spectra to be modeled very accurately, facilitating line-shape based fits of the data that yield band gap energies with meV precision.

Figure 6 plots representative PL spectra for $Ge_{1-y}Sn_y$/Ge/Si(100) samples across a composition range of 0-9% Sn with similar thicknesses acquired on the LN_2 cooled InGaAs detector. From this figure we are able to see qualitatively the evolution of the PL spectra from indirect to direct gap materials. Firstly, as more Sn is incorporated into the

alloy epilayer the resultant PL spectrum shows a reduction in the separation between the E_0 and E_{ind} peaks. For instance, the 0.3%, 3.1%, and 4.2% Sn layers show a lower energy shoulder that is assigned to emission from the E_{ind} transition while the main peak is assigned as the E_0 emission. In the 7.5% Sn sample however, these features have merged to produce a single broad peak, indicating that the separation between the Γ and L conduction band valleys has become very narrow. In fact, due to the systematic decrease

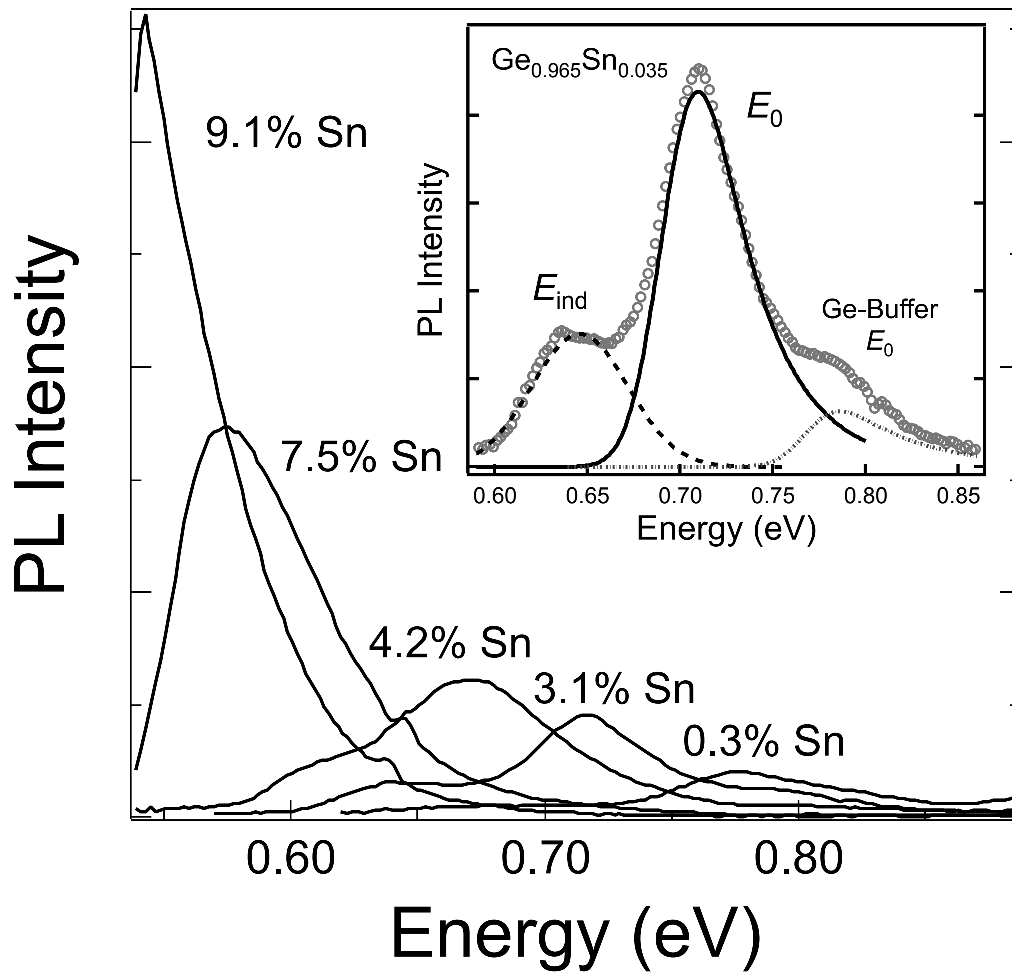

Figure 6: Room temperature PL for samples of similar thickness spanning a range of 0-9% Sn. Inset demonstrates the line-shape fitting performed on the spectra to assign the E_{ind} and E_0 contributions. Samples produced by Charutha Senaratne. See C. L. Senaratne, J. D. Gallagher, T. Aoki, J. Kouvetakis, and J. Menéndez, *Chemistry of Materials*, 26(20), pg. 6033 (2014).

between the Γ and L valley separation as a function of Sn content, the E_{ind} feature could not be discerned, or produce a converging fit if taken into consideration, in any samples with $y > 0.06$. Secondly, we see a redshift of both these signals confirming the notion that the addition of Sn continuously perturbs the electronic band structure from pure Ge, where the gaps are larger and the Γ valley sits higher than the L, to α-Sn, where the gap across the Γ-point is negative and the E_{ind} is just less than 0.2 eV. Lastly, as more Ge is substituted by Sn atoms the PL intensity increases. This is observed because as the separation narrows between the Γ and L conduction band valleys, the number of carriers that populate the Γ valley under quasi thermal equilibrium increases, which in turn increases the probability of radiative transitions taking place across the Γ-point, enhancing the PL signal strength.

The inset of Figure 6 demonstrates a typical lineshape fit to the PL spectra features in order to extract the E_0 and E_{ind} band gaps from the data from a 3.5% Sn film grown on a Ge buffer. Here we see a clear lower energy E_{ind} peak, a dominant E_0 feature, and a minor contribution from the buffer E_0 that does not obscure the $Ge_{1-y}Sn_y$ spectral features of interest in any significant way. It should be noted that the E_{ind} from the Ge buffer in this sample also does not alter the $Ge_{1-y}Sn_y$ spectrum to a measureable degree despite its expected presence near 0.68 eV. This is due to the low PL intensity of the E_{ind} in Ge films on Si relative to the E_0, as seen in Figure 3.

To fit these spectra, a two-step approach is adopted. In the first step the experimental PL profile is fit with empirical line shapes assigned to the direct and indirect emission. The E_{ind} emission is fit with a single Gaussian which accounts for 3 possible radiative recombination pathways that can occur across this gap: phonon

emission with photon emission, phonon absorption with photon emission, and a no phonon interaction with photon emission due to symmetry breaking by alloy disorder. The contributions from these 3 pathways overlap strongly around the E_{ind} gap, making precise deconvolution very tricky. For simplicity we absorb all three of these features into a single Gaussian function which is found to fit this part of the spectrum very well. The E_0 is fit by an exponential decay modified Gaussian (EMG) function. The EMG is formed by the convolution of a simple Gaussian with an exponential decay tail and this produces a lineshpe that agrees very well with the shape of the theoretically calculated spontaneous emission spectrum. Next, the empirical line shapes are fit by hand to theoretical expressions describing the spontaneous emission from $Ge_{1-y}Sn_y$ alloys.

The spontaneous emission rate of photons emitted per unit volume from a sample into an external angle is given by a generalized van Roosbroeck-Shockley expression.[135,136]

$$\frac{1}{V}\frac{d^2R}{d\Omega dE}=\frac{2}{h^3}\left(\frac{n_{\mathrm{op}}E}{c}\right)^2\left[\frac{\alpha(E)}{\exp\left(\frac{E-\Delta F}{k_BT}\right)-1}\right], \tag{2.1}$$

This equation describes the emission rate, R, per unit sample volume of photons with energy E into the solid angle $d\Omega$. By employing this model we are assuming the sample is under continuous photo-excitation and that the carriers in the conduction band reach quasi-equilibrium between the Γ and L valleys. Because in this model the emission is proportional to the absorption, an analytical model is used that includes excitonic effects.[137] However alloying with Sn perturbs the band structure of pure Ge and so the relevant band parameters needed to describe the absorption in $Ge_{1-y}Sn_y$ are extrapolated

from bulk Ge using ***k·p*** expressions. The effect of any residual strain on the band structure is accounted for using deformation potential theory. The hydrostatic

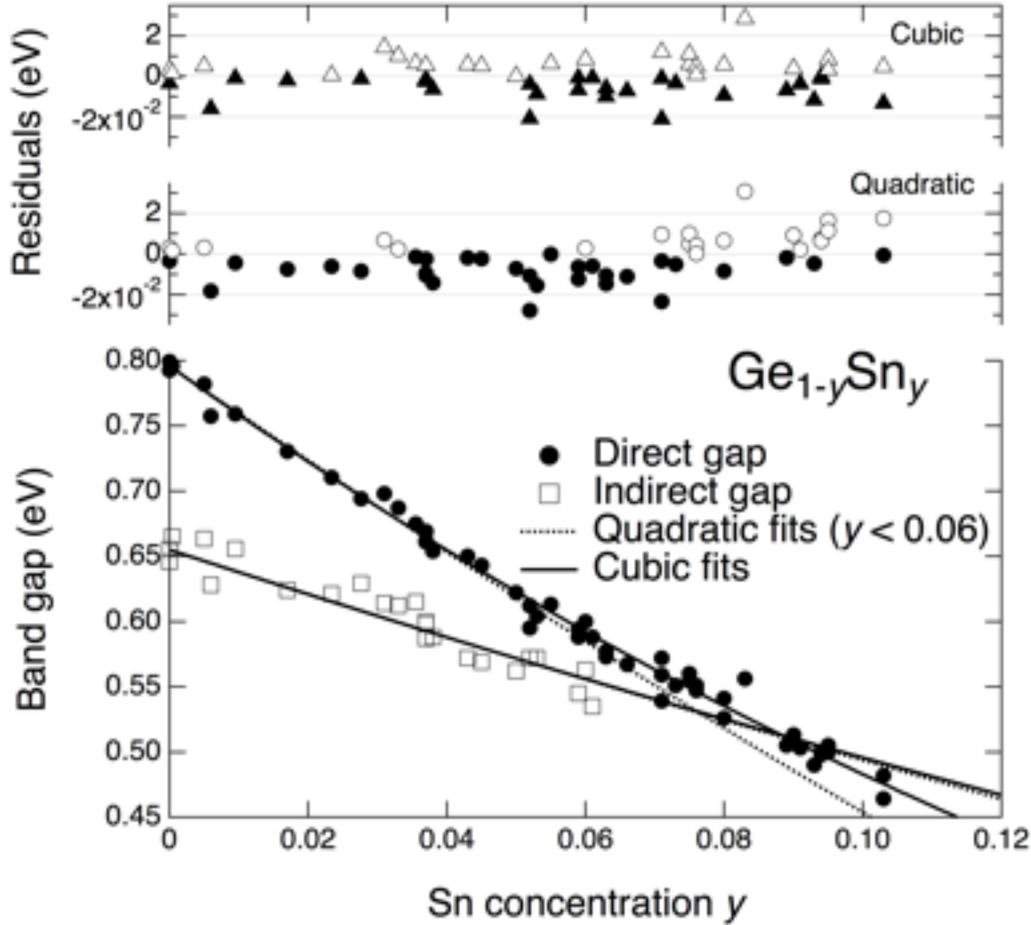

Figure 7: Direct (black circles) and indirect (open squares) band gap energies of GeSn materials extracted from PL measurements. The cubic fits to the data give the best result and show a crossover to direct gap materials at ~9% Sn.

deformation potential parameters used for the Ge direct gap were measured by Goñi *et. al.*[138] and the indirect gap values are given by Ahmad and Adams.[26] The deformation potentials used for the α-Sn direct and indirect gaps are derived by multiplying the calculated potentials by a the same correction factor that is necessary to adjust the theoretical values of Ge to the experimental values.[139,140] The total hydrostatic deformation potential for a given alloy is then determined by linearly interpolating

between the Ge and α-Sn endpoints. The emission due to the direct gap can be calculated by combining a standard absorption expression for parabolic bands given in Ref. 135 with the van Roosbroeck-Shockley equation from the same source. By adjusting the parameters of the calculated spontaneous emission it is possible to obtain an excellent agreement between the theoretical shape of the emission and the EMG profile. Once a converged fit is obtained the band gap is automatically computed by a user-defined program in IgorPro. This model used to describe absorption and emission by the direct gap is not valid for the indirect gap however.[141] Instead the correct expression for absorption by the indirect band gap contains a prefactor that is proportional to $(E_0 - E)^{-2}$ that arises in second-order perturbation theory for a phonon-assisted process. Due to the decreasing difference between the Γ and L valleys, this value diverges as the separation between E_0 and E_{ind} goes to 0. Thus a rigorous quantitative theory for the spontaneous emission from $Ge_{1-y}Sn_y$ alloys remains an unsolved problem for the moment. Instead it is assumed that the value of E_{ind} is the value of the Gaussian peak maximum position shifted by a constant of 0.031 eV to lower energy. This shift value of 0.031 eV was determined by measuring the PL spectrum of Ge films under identical conditions since the E_{ind} value of Ge is well known. This shift agrees with the zone edge LA, LO, and TO phonon energies in Ge which are 0.027 eV, 0.031 eV, and 0.035 eV, respectively. A shift due to the sample strain is also incorporated assuming that the predominant radiative recombination is with the heavy hole band. For specific details on how the fits are performed by hand to extract the E_0 band gap using the IgorPro program the reader is referred to Appendix E of this dissertation. Further details regarding the effect of specific parameters on the fits can be found in Ref. 134.

Figure 7 shows the direct and indirect gap energies determined from fits of room temperature PL data on over 50 $Ge_{1-y}Sn_y$ samples spanning $y = 0.000$-0.105, including data points from Ref. 134. The compositional dependence of optical transition energies is usually written as a quadratic expression which in the case of $Ge_{1-y}Sn$ alloys takes the form $E_{cv}\left(y\right)=E_{cv}^{\mathrm{Ge}}\left(1-y\right)+E_{cv}^{\mathrm{Ge}}\left(y\right)-b_{cv}y\left(1-y\right)$, where the subscript *cv* highlights the fact that E_{cv} is a transition energy from the conduction band to the valence band. At the simplest level of theory, when the shift is viewed as a perturbation to the VCA transition energies, the bowing parameter b_{cv} is given by (in eV):[142]

$$b_{cv}=-\left|M(y)\right|^{2}\left[F(E_{c},y)-F(E_{v},y)\right], \tag{2.2}$$

where $M(y)$ is a matrix element arising from the potential difference between the actual alloy and the VCA alloy and E_c/E_v are conduction and valence band energies, respectively. The function $F(E,y)$ is (in eV/cm^6):

$$F(E,y)=\frac{1}{\Omega^{2}(y)}\wp\int dE'\,\frac{\rho_{at}(E',y)}{E-E'}, \tag{2.3}$$

where $\Omega(y)$ is the volume of the unit cell of the virtual crystal and $\rho_{\mathrm{at}}(E',y)$ is the VCA electronic density of states (DOS) (in states per atom per unit of energy). The symbol $\wp$ denotes a principal part integration. Even under the crude assumption $\left|M\right|$ = constant (Ref. 142), $F(E,y)$ is in general a function of *y,* and therefore the bowing parameter b_{cv} becomes a function of composition. In previous work on $Ge_{1-y}Sn_y$ alloys, however, the number of data points and/or the compositional range explored was too small to detect any possible compositional dependence in the bowing parameters b_0 and b_{ind} for the direct

and indirect gaps. In Ref. 134, for example, excellent agreement with experiment was found using constant $b_0 = 2.46\pm0.06$ eV and $b_{\rm ind} = 0.99\pm0.11$ eV. (The end values were taken as $E_0^{\rm Ge} = 0.796$ eV, $E_0^{\rm Sn} = -0.413$ e , $E_{\rm ind}^{\rm Ge} = 0.655$ eV, and $E_{\rm ind}^{\rm Sn} = -0.035$ eV). Fits with constant bowing parameters for $y < 0.06$ are shown as dotted lines in Figure 7, and it is apparent that in the case of the direct gap such fit systematically underestimates the measured energies at Sn-concentrations beyond $y = 0.07$. Fitting the entire compositional range of Figure 7 with a constant bowing expression yields $b_0 = 2.24$ eV, well beyond the error of the bowing determined in Ref. 134. Thus it appears that a constant bowing model is not accurate enough to explain the compositional dependence of the direct gap.

The simplest phenomenological extension of the constant bowing model is to assume the bowings to be linear functions of composition:

$$b_0(y) = b_0^{(0)} + b_0^{(1)} y\,, \qquad (2.4a)$$

$$b_{ind}(y) = b_{ind}^{(0)} + b_{ind}^{(1)} y\,, \qquad (2.4b)$$

This assumption is more rigorously justified by the calculations described below. The use of Eq. (2.4a) implies that the overall compositional dependence of the band gap energy is given by a cubic polynomial, which has been shown to apply in the case of $Ga_{1-x}Al_xAs$[143] and $Ga_{1-x}Al_xSb$.[144] A cubic fit of the E_0 energies gives $b_0^{(0)} = 2.66\pm0.09$ eV and $b_0^{(1)} = -5.4\pm1.1$ eV, and is shown as a solid line in Figure 7. We see that it provides an excellent account of the experimental data. In addition, the expression implies $E_0(0.14) = 0.40$ eV, in very good agreement with the band gap $E_0 = 0.41$ eV reported in Ref. 145 for a sample grown following a similar CVD approach. By contrast, if we use a constant bowing

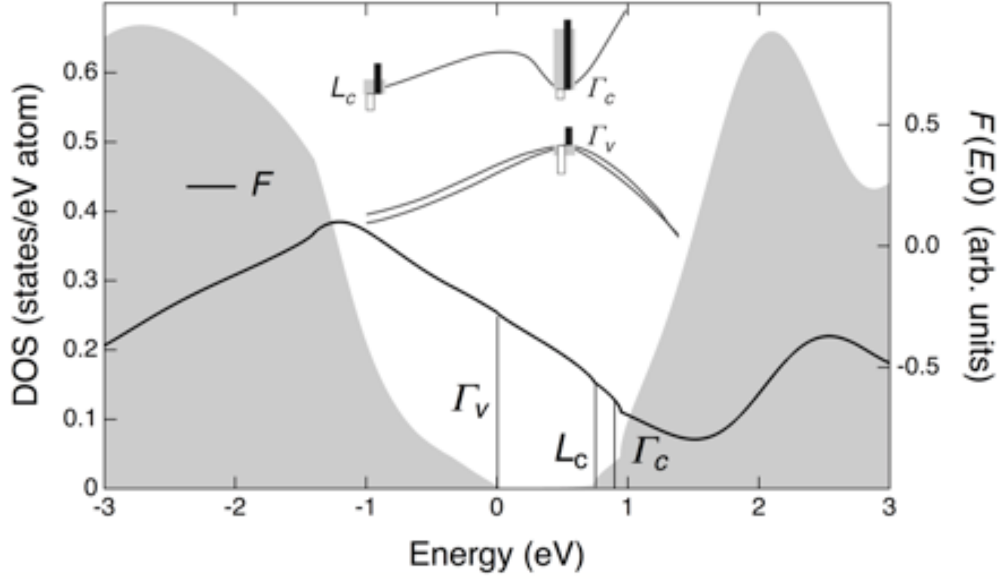

Figure 8: Calculated density of states based on the theory of CC. the inset diagram displays a model of the effect of level repulsion between the three conduction band valleys L, Γ, and Δ and the valence band Γ maximum.

parameter $b_0 = 2.46$ eV, as recommended in Ref. 134, the predicted value is $E_0(0.14) = 0.33$ eV, which clearly underestimates the experimental value.

The upper panels in Figure 7 show the residuals from quadratic and cubic fits of the E_0 energy over the entire compositional range, and it is apparent that the quadratic residuals are larger and more structured. In fact, an F-test comparison of the two models gives $F = 24.1$ for the 52 data points in the figure, which corresponds to a probability $p < 1.5\times10^{-5}$ that the improved cubic fit is accidental.

A critical consequence of the cubic fit is that the indirect to direct crossover composition is shifted to from $y_c = 0.073$ to $y_c = 0.087$. However, this assumes that $E_{ind}(y)$ is still given by a quadratic expression. Unfortunately, a fit of $E_{ind}(y)$ using Eq. (2.4b) with no additional constraints gives unphysical results. This is mainly because the

compositional range is too narrow, since $E_{\rm ind}$ cannot be clearly identified beyond y = 0.06. However, we can expect that the same physics that produces the compositional dependence of b_0 will also generate a similar effect for $b_{\rm ind}$. The idea is then to combine the elementary theory in Eq. (2.2) and (2.3) with experimental data to generate additional constraints that will make it possible to estimate $b_{\rm ind}^{(0)}$ and $b_{\rm ind}^{(1)}$.

An important consideration when applying the theory in Eqs. (2.2) and (2.3) to $Ge_{1-y}Sn_y$ alloys is the non-negligible increase in lattice parameter as a function of y. We note in this context that our definition of the function $F(E,y)$ contains an explicit factor $\Omega^{-2}\left(y\right)$ that does not appear in Ref. 142, where it is absorbed into the matrix element definition. In our case, however, we follow Hall and coworkers[146,147] to define a matrix element M from which all possible dependencies on the unit cell volume have been extracted, so that we can extend Stroud's $\left|M\right|$ = constant approximation to virtual crystals with different unit cell sizes. For the DOS, we use as a starting point the results from Chelikowsky and Cohen (CC) for Ge and α-Sn.[148] The DOS regions near the Γ_v, L_c, and Γ_c states, however, are modeled using accurate analytical expressions, which are joined smoothly with the CC DOS. The conduction band is described as the sum of three parabolic edges, corresponding to the L, Γ, and Δ minima, with $\boldsymbol{k}\cdot\boldsymbol{p}$ effective masses from El Kurdi *et al* (Ref. 149). To this we added five Gaussians whose amplitudes, energies and widths were adjusted to match the CC DOS. The alloy DOS in the conduction band was simulated by linearly interpolating the L, Γ, and X edges, scaling the effective masses using $\boldsymbol{k}\cdot\boldsymbol{p}$ theory, and interpolating the parameters of the five Gaussians. We use a similar approach for the valence band, starting from the analytical results of Rodríguez

Bolívar *et al*. (Ref. 150) for the region near the Γ_v state. An example of the DOS computed this way is shown in Figure 8 for the case of pure Ge (y = 0). The function $F(E,0)$ corresponding to this DOS is also shown in the figure. We note that, as expected from Ref. 142, $F(0,0) > F(E_{\text{ind}},0)$, so that $b_{\text{ind}}^{(0)} > 0$. We also find that $F(0,0) > F(E_0,0)$, which implies $b_0^{(0)} > 0$. Both results, which can be understood in terms of level repulsion between the two conduction band valleys as the separation between them decreases, are consistent with the experimental data. Proceeding in this fashion we also computed $F(E,y)$ and we find that for $y < 0.2$ it is a linear function of y when evaluated at the energy of the Γ_v, Γ_c and L_c states and concentration y. Therefore, we can write

$$F(E,y) = F(E,0) + \left.\frac{dF(E,y)}{dy}\right|_{y=0} y\,, \tag{2.5}$$

Thus the quantities $F(E_0,0)$, $F(E_{\text{ind}},0)$, and $F(0,0)$ when inserted in Eq. (2.2) give $b_0^{(0)}$ and $b_{\text{ind}}^{(0)}$, whereas if we insert $dF(E_0,y)/\partial y$, $dF(E_{\text{ind}},y)/\partial y$ and $dF(0,y)/dy$ we obtain $b_0^{(1)}$ and $b_{\text{ind}}^{(1)}$. The linearity in y of $F(E,y)$ provides a more rigorous justification for the use of Eqs. (2.3a) and (2.4b). It remains approximately valid beyond y = 0.2 and up to y = 0.66, where our DOS model ceases to be valid because E_0 becomes negative. If we adjust $|M|$ so that the calculated $b_0^{(0)}$ agrees with the experimental value $b_0^{(0)}$ = 2.66 eV, we calculate $b_{\text{ind}}^{(0)}$ = 2.14 eV, $b_0^{(1)}$ = -4.4 eV, and $b_{\text{ind}}^{(1)}$ = -1.5 eV.

Our theory predicts all signs in agreement with experiment, but the relative magnitude of the E_{ind} and E_0 bowing would imply a much stronger compositional dependence of E_{ind} than observed experimentally. This is most likely a result of the crude

constant matrix element approximation. Clearly, matrix elements involving the L_c state need not be the same as those involving the Γ_c state. On the other hand, the *same* matrix elements are involved in $b_0^{(0)}$ and $b_0^{(1)}$, so that we might expect the ratio $b_0^{(1)}/b_0^{(0)}$ to be less dependent on matrix elements, and indeed the theoretical value $b_0^{(1)}/b_0^{(0)} = -1.65$ is in good agreement with the experimental result $b_0^{(1)}/b_0^{(0)} = -2\pm1$. If we assume the same to be valid for E_{ind}, we can fit the compositional dependence of this transition using Eq. (2.4b) subject to the constraint $b_{\text{ind}}^{(1)}/b_{\text{ind}}^{(0)} = -0.7$, as obtained from our theoretical model. We then find $b_{\text{ind}}^{(0)} = 1.06\pm0.07$ eV and $b_{\text{ind}}^{(1)} = -0.74\pm0.07$ eV. The corresponding curve is shown as a solid line in Figure 7, and we see that it intercepts the E_0 line at $y_c = 0.087$. Thus the predicted cross-over composition from indirect to direct gap behavior in $Ge_{1-y}Sn_y$ alloys is increased by more than 1% relative to earlier work that ignored the compositional dependence of the bowing parameters.[134]

The theoretical value $b_{\text{ind}}^{(1)}/b_{\text{ind}}^{(0)} = -0.7$, as opposed to $b_0^{(1)}/b_0^{(0)} = -1.65$, implies that the difference between cubic and quadratic fits are more pronounced for E_0 as is apparent in Figure 7. It is important to understand the origin of this difference, since it is critical for the shift in y_c relative to purely quadratic fits. For this we write $b_0^{(1)} = \left[b_{\Gamma_c,c}^{(1)} + b_{\Gamma_c,v}^{(1)}\right] - \left[b_{\Gamma_v,v}^{(1)} + b_{\Gamma_v,c}^{(1)}\right]$ and $b_{\text{ind}}^{(1)} = \left[b_{L_c,c}^{(1)} + b_{L_c,cv}^{(1)}\right] - \left[b_{\Gamma_v,v}^{(1)} + b_{\Gamma_v,c}^{(1)}\right]$, where each of the square brackets corresponds to a state involved in the transition, and the contribution from each state is split into two terms (subscripts c and v) corresponding to writing the DOS in Eq. (2.3) as a sum of conduction and valence band contributions $\rho_{\text{at}}(E') = \rho_{\text{at},c}(E') + \rho_{\text{at},v}(E')$. The inset to Figure 8 shows the energy shifts associated with the

different contributions to $b_0^{(1)}$ and $b_{\text{ind}}^{(1)}$. The thick grey bars represent the shift of each state, and the thin black and white bars its decomposition into conduction and valence band contributions, respectively. We notice that both gaps are increasing. This illustrates the fact that $b_0^{(1)}$ and $b_{\text{ind}}^{(1)}$ are found to be negative. However, the effect is much larger for the direct gap, and this is mainly associated with the positive shift caused by the interaction of the Γ_c state with the conduction band (thin black bar), which is almost twice that of the L_c state. The origin of this different behavior can be traced back to the fact that in pure Ge the Γ_c state is only 55 meV below the Δ_c minimum in the conduction band, so that we can expect a strong repulsion between the two states. By contrast, the separation between Δ_c and L_c is 200 meV, so that the repulsion is weaker. The Δ_c state is found at similar energies in Si, Ge, and α-Sn, which implies that its compositional dependence is weak. On the other hand, when y increases the Γ_c state shifts rapidly down, *increasing* its separation from Δ_c and therefore reducing the level repulsion with this state. This is represented by a positive large bar in the Figure 8 inset, or, equivalently, by a large, negative $b_{\Gamma_c,c}^{(1)}$ coefficient. By contrast, in the case of the L_c state the level repulsion change is greatly diminished by the fact that the initial separation at $y = 0$ is already relatively large, and also by the fact that the L_c state moves down more slowly than Γ_c as a function of y. Thus the corresponding black bar is much smaller, which means $\left|b_{L_c,c}^{(1)}\right| < \left|b_{\Gamma_c,c}^{(1)}\right|$. Since these derivative-like subtleties in the Ge DOS have a strong impact on the value of $b_0^{(1)}$ and $b_{\text{ind}}^{(1)}$, it is not surprising that supercell calculations using different band structure methods make wildly different predictions, ranging from $b_0^{(1)}$ = -

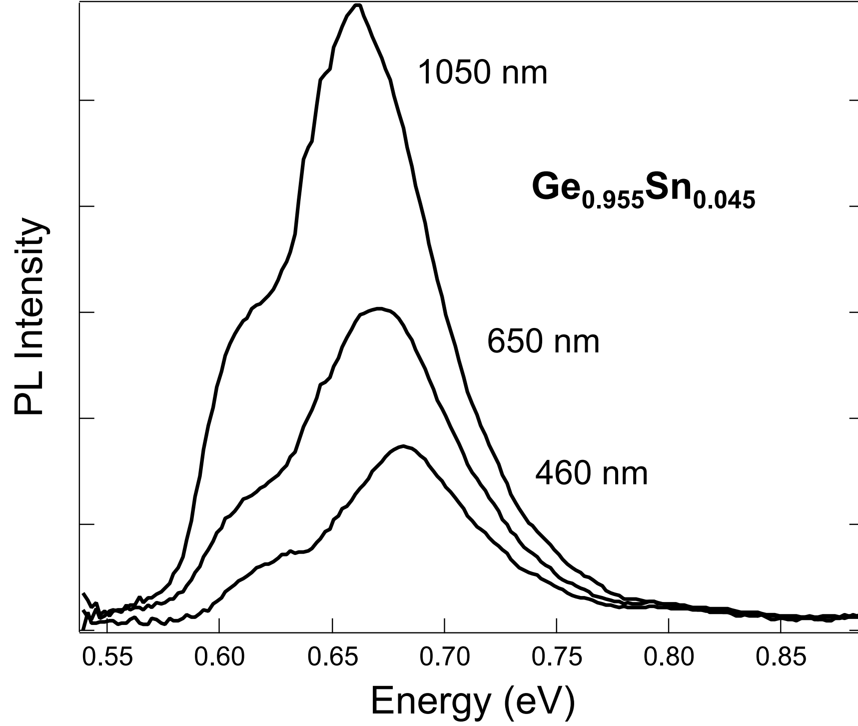

Figure 9: PL intensity of a series of ~4.5% Sn samples and varying layer thicknesses, demonstrating the emission enhancement attainable with thicker bulk-like layers.

5.6 eV (Ref. 151) to $b_0^{(1)}$ = -0.9 eV (Ref. 152). It is now possible to speculate on the reason why experimentally we find $\left|b_0^{(0)}\right| > 2\left|b_{\text{ind}}^{(0)}\right|$, whereas our theory predicts $\left|b_0^{(0)}\right| \sim \left|b_{\text{ind}}^{(0)}\right|$. It is apparent from Figure 8 that in the relevant energy scale of the DOS, the energy separation between L_c and Γ_c is too small to obtain a large difference in bowing parameters for E_0 and E_{ind} using constant matrix elements. However, if the coupling with Δ_c is stronger than with other states, it is conceivable that a large difference in bowing parameters might result even for these closely lying states.

With an accurate determination of y_c completed, the next aim of the PL investigation is to enhance the light emission from $Ge_{1-y}Sn_y$/Ge/Si(100) materials.

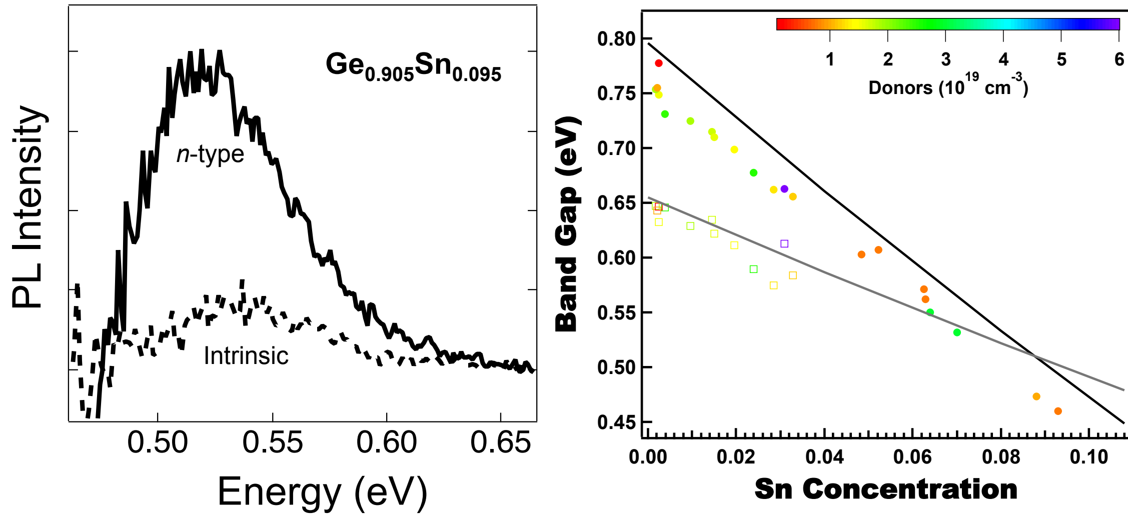

Figure 10: (Left) PL from *n*-type and intrinsic 9.5% Sn samples with comparable thickness acquired on the PbS detector. Note the significant emission enhancement and renormalization of the peak to lower energy for the *n*-type sample relative to the intrinsic. (Right) Plot of the band gaps for *n*-type samples compared with the empirical values for intrinsic samples.

4. *Enhancing $Ge_{1-y}Sn_y$ Light Emission*

Thus far it has been demonstrated that one method for improving light emission of $Ge_{1-y}Sn_y$ alloys is to grow them on Ge-buffered Si templates to reduce the density of threading dislocations that act as non-radiative recombination traps. In this section the PL enhancement results from five other methods, two growth-based and three processing techniques, will be discussed. These methods consist of growing thicker films, heavily doping the material *n*-type in the 10^{19}-10^{20} cm^{-3} range, rapid thermal treatments (RTA), classical furnace annealing treatments, and passivating the surface with hydrogen plasma.

Growing thicker films is advantageous for light emission because this increases the volume fraction of material removed from the defective interface between $Ge_{1-y}Sn_y$ and Ge, increasing the amount of high quality material available to emit light. Figure 9 displays the optical performance enhancements available through the growth of thicker

materials. Fixing the composition at ~4.5% Sn, the PL intensity increases by approximately a factor of 4 when the thickness is slightly more than doubled.

Doping nearly-direct gap group-IV materials *n*-type to carrier densities in the degenerate limit have been shown in to produce enhanced light emission by elevating the quasi Fermi level in the conduction band.[38,132,153] The left panel of Figure 10 illustrates the effect of an elevated Fermi level on the emission by comparing the PL spectra from *n*-type ($n \sim 10^{19}$ cm^{-3}) and intrinsic samples containing ~9.5% Sn and similar thicknesses. The *n*-type sample shows a peak that is ~7x more intense than the analogous intrinsic sample, which is in agreement with previous intensity enhancements reported in Ref. 38 on doped and undoped Ge films that purported *n*-type doping nearly direct gap group-IV materials enhances the emission by an order of magnitude. Additionally, the *n*-layer peak is redshifted slightly to a lower energy. This is also expected due to band gap renormalization that takes place at the high doping levels employed here.[132] The PL spectra from *n*-type samples are modeled using the same procedures described in the previous section, yielding E_0 and E_{ind} energies as a function of composition and doping in these materials. The right panel of Figure 10 plots the E_0 and E_{ind} energies measured from a set of *n*-$Ge_{1-y}Sn_y$/Ge/Si(100) samples as colored points. The color scale corresponds to the doping density of the alloy in the range of 1-6×10^{19} cm^{-3}. The solid lines in the figure are the cubic fits to the E_0 and E_{ind} data for the *i*-$Ge_{1-y}Sn_y$ samples discussed in the previous section that intersect at $y_c = 0.087$. Each *n*-type sample shows a E_0 that is systematically lower than the expected E_0 energy for an intrinsic $Ge_{1-y}Sn_y$ sample by ~32 meV. This is in agreement with previous measurements of the band gap renormalization in group-IV materials due to *n*-type doping at these levels.[38,132,153]

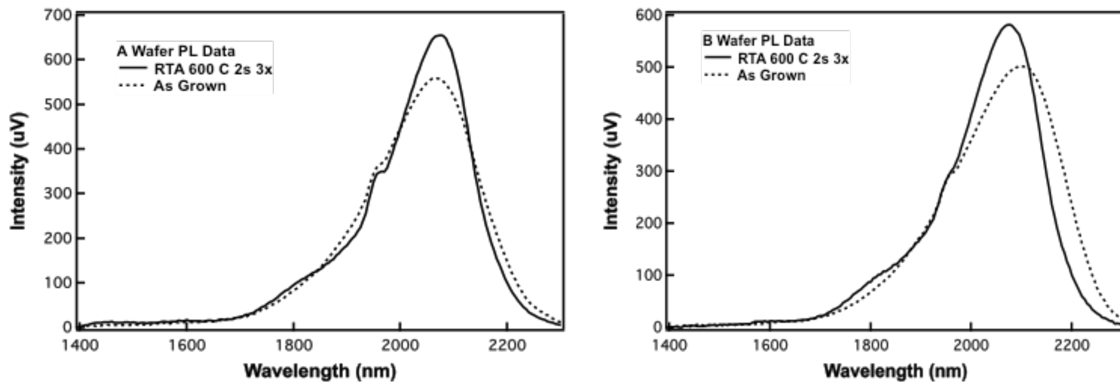

Figure 11: Raw PL data from sample A (left) and sample B (right) comparing the as-grown and post RTA processing at 600°C spectra. This produces an intensity enhancement of ~1.2x in each sample.

Processing-based techniques such as thermal annealing and surface passivation treatments can also produce PL emission enhancement. RTA treatments induce stronger light emission by annihilating deleterious threading dislocations. This process is carried out by performing a series of quick heating and quenching cycles. A typical process begins by ramping the temperature from ambient to a high target value (400-900°C) in 30-50 seconds, followed by a hold step at the target for 3-10 seconds, and ended with a rapid cooling to lower temperatures within 60 seconds. The cycle is then repeated 2-3 times. The motivation for performing furnace anneals is the same as in the case of the RTA treatments: applying heat to a crystal eliminates dislocations. Furnace annealing however offers a thermal profile that is less aggressive with longer annealing times at lower temperatures, allowing a means to handle the increasing metastability of $Ge_{1-y}Sn_y$ materials with higher Sn concentrations. Finally, surface passivation by hydrogen plasmas have been demonstrated to assist with light emission from $Ge_{1-y}Sn_y$ and $Ge_{1-x}Si_x$ semiconductors and this method is discussed here.[132,154]

As a control for the processing based experiments, two $Ge_{0.94}Sn_{0.06}$ samples are run in parallel to test reproducibility of the results. In the following text, tables, figures,

and captions these will be referred to as sample “A” and sample “B.” Table I summarizes the as-grown properties of samples A and B:

TABLE I: Material science properties of samples A and B prior to any processing treatment.

	Sample A	Sample B
Thickness (nm)	735	675
a_0 (Å)	5.7052	5.7076
Strain (%)	-0.1279	-0.0880
(004) FWHM (arcsec)	650.16	719.28
Sn by RBS (%)	6.0	6.1
Sn by XRD (%)	6.2	6.5

Following characterization of the as-grown films the various PL enhancing treatments (RTA, furnace anneal, and hydrogen plasma passivation) are performed on the samples and they are subsequently characterized by XRD along the Bragg (004) and (224) reflections to measure any changes in strain, composition, crystal structure, and film quality. Following this characterization, the PL is measured with the LN_2 cooled InGaAs detector.

The RTA process used on these samples is a series of 3 cycles at 600°C for 2 seconds. Previous experience working with $Ge_{1-y}Sn_y$ samples showed that for 6% Sn alloys this is the highest temperature the sample can be exposed to before phase segregation begins through Sn precipitation, based on XRD (004) reflections. Table II summarizes the properties of the samples post-RTA treatment. Figure 11 shows the PL response from the 600°C RTA treated samples overlaid with the as grown samples PL.

TABLE II: Post-RTA treatment properties of samples A and B.

	Sample A	Sample B
a_0 (Å)	5.7048	5.7059
Strain (%)	-0.0761	-0.1021
(004) FWHM (arcsec)	650.52	684.00

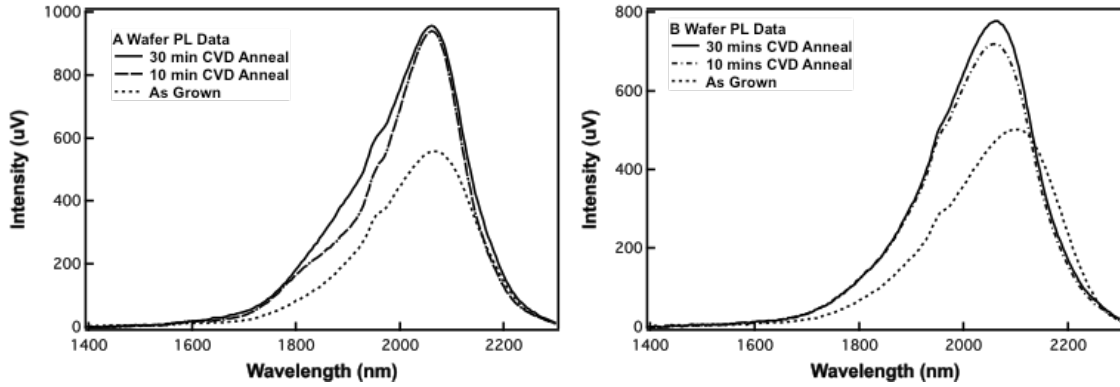

Figure 12: Raw PL data from sample A (left) and sample B (right) annealed via CVD compared with the as grown A and B counterparts. The CVD process ceases to improve emission performance beyond a 30 minute anneal. This produces ~1.5x intensity enhancement.

From Figre 11 we see an enhancement in the PL intensity of ~100 μV for each sample out of an intensity of 600 μV, corresponding to an intensity enhancement of ~1.2x.

The second annealing technique is performed in a 3-zone CVD tube furnace reactor for a longer period of time at a lower temperature than those used in the RTA process.

TABLE III: Materials properties of samples A and B after the 30-minute furnace annealing treatment.

	Sample A	Sample B
a_0 (Å)	5.7044	5.7060
Strain (%)	-0.1702	-0.1802
(004) FWHM (arcsec)	613.80	699.84

The sample is loaded into the CVD chamber after the chamber has been passivated by a flow of Si_3H_8 for at least 30 minutes to prevent memory effects from any previous growth conducted in the reactor that may affect the samples. The temperatures applied to the zones are: 425°C, 450°C, and 450°C for zones 1,2, and 3 respectively. The sample sits in zone 2 for 10-30 minutes during the process while H_2 is dynamically pumped through the chamber from zone 1 to 3 by a process turbo pump, maintaining a pressure of 100 mTorr.

Table III summarizes the properties of the samples post-CVD annealing after a 30-minute process. Figure 12 shows the PL response of CVD annealed samples overlaid against the as grown sample PL. From Figure 12 we see an improvement in the PL emission over the RTA processed samples. The intensity enhancement seen here is ~300 uV for each sample after both the 10 and 30-minute processes, corresponding to ~1.5x intensity enhancement of the PL signal. Note that the 10 and 30-minute processes produce comparable intensities. Therefore 30 minutes can be viewed as the ceiling time for this process beyond which significant improvements in the crystal quality that enhance the PL emission will not be produced.

The third technique exposes the sample to a hydrogen plasma in an inductively coupled plasma (ICP) etch tool. Typically this tool is intended to process semiconductor devices by selectively etching features in conjunction with lithography processes.

TABLE IV: Material science properties of samples A and B after a 10 minute hydrogen plasma treatment.

	Sample A	Sample B
a_0 (Å)	5.7049	5.7069
Strain (%)	-0.1452	-0.0831
(004) FWHM (arcsec)	692.64	745.20

This is accomplished by cooling the backside of the sample through a flow of He gas while forming a plasma of a highly reactive gas over the sample that is accelerated by a potential difference toward the sample surface. This enables etching to be done through a combination of chemical and bombardment mechanisms. To use this tool for surface passivation, the backside He cooling is turned off along with all other reactive gas flows, admitting only H_2 into the chamber during the process. Before loading the sample, an O_2 clean is performed on the chamber and ceramic chuck the sample sits on during the

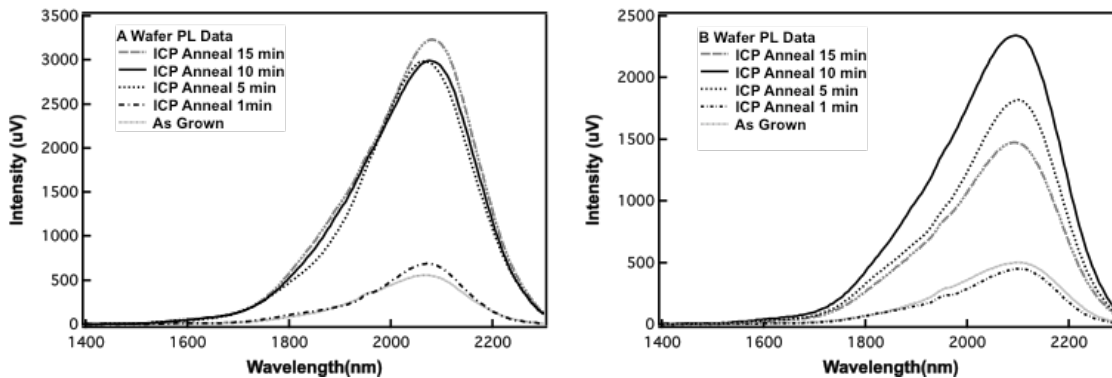

Figure 13: Raw PL data from sample A (left) and sample B (right) ICP annealed. Short processes of 1 minute don't have much of an effect on emission, while longer processes of 5-15 minutes show significant emission enhancement.

process to get rid of any potential contaminant materials on the chamber walls and chuck from previous processes run by other users. This is analogous to the Si_3H_8 passivation of the CVD furnace. After performing the O_2 clean, the sample is loaded into the chamber and the process forms a hydrogen plasma at a pressure of 90 mTorr by applying a RF frequency power of 300W in the coil region above the sample and 50W in the platen region level with the sample. Spectroscopic ellipsometry measurements of the film thickness after this process found that the hydrogen plasma etches the surface at a rate of ~5 nm/min under these conditions. Table IV summarizes the properties of the samples after a 10-minute exposure to hydrogen plasma.

Figure 13 displays the PL response of ICP-treated samples for 1-15 minute processes. From Figure 13 we see PL intensity enhancements ranging 3-6x the as grown intensity by applying this ICP procedure. For the short 1-minute processes there is no significant difference between the as grown and ICP processed samples. For sample A, there is no significant difference between the 5 and 10-minute exposures, with a slight improvement seen in the 15-minute process. All three of these processes for sample A

yielded intensity enhancements ~6x that of the as grown sample. In the case of sample B the PL intensity improved by factors of ~4x to ~5x between the 5 and 10-minute processes, respectively. However, the 15-minute process exhibits an enhancement factor of only ~3x over the as grown spectrum. It is likely that this process produces

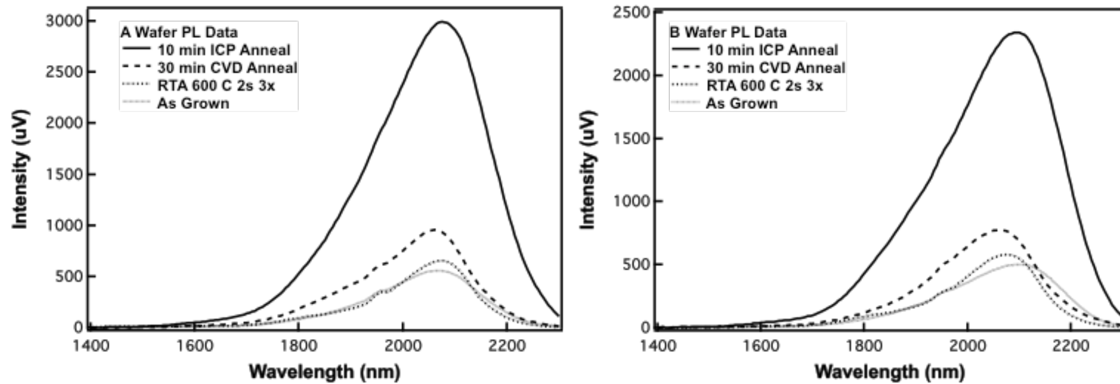

Figure 14: Raw PL data from sample A (left) and sample B (right), comparing the emission of the most optimized spectra from all annealing techniques discussed here.

diminishing returns beyond a 10-minute plasma exposure because a significant fraction of the film will have been etched away beyond this point. This is likely the case for sample B's 15 minute exposure. The intensity increases observed here are attributed to passivation of the surface dangling bonds by hydrogen, which lowers the surface recombination velocity, promoting increased radiative recombination in the sample bulk.

Enhancement of the PL intensity in samples treated by hydrogen plasma has also been documented in the case of α-Si/α-$Si_{1-x}N_x$ quantum well superlattices grown by plasma enhanced CVD.[155] In these systems the main source of non-radiative recombination is the dangling bonds that appear at the interfaces between successive α-Si and α-$Si_{1-x}N_x$ layers.[156,157] The authors demonstrated that treating the surface with a hydrogen plasma between the supperlatice layer growths improved the PL intensity. Electron spin resonance (ESR) measurements demonstrated a decrease in the number of

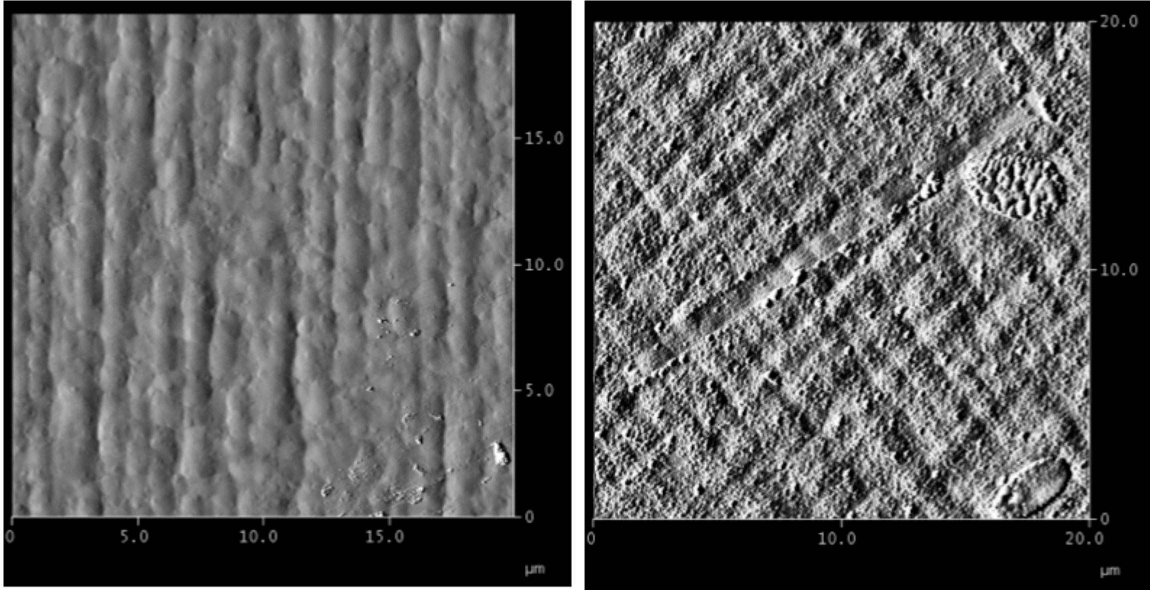

Figure 15: AFM of a sample as grown (Left) before a 10-minute ICP treatment (Right).

non-radiative defect centers as well in samples treated with hydrogen plasma between layer growths.

Figure 14 compares the optimal processing conditions across the three processing-based light enhancement techniques presented. The ICP annealing process produces the most enhancement out of the three types of treatments. To understand why this surface treatment has such a profound effect on the emission, atomic force microcopy (AFM) was performed to assess the surface morphology. Figure 15 compares the surface morphology of the sample before and after a 10-minute ICP etch. It is clear that the surface has roughened substantially after the ICP treatment. The as-grown film has a RMS roughness of only 6.2 nm over the 20 μm × 20 μm window while the roughness of the sample after the plasma exposure is 11.5 nm. The surface of the ICP treated film appears to show troughs and peaks that form very rough 90° intersections reminiscent of cross-hatch patterns commonly seen on the surface of films grown on a substrate with a

small lattice mismatch. This suggests that the etching of the film may preferentially propagate farther down the cross-hatch valleys than over the peaks. Since the ICP process is a surface treatment, and the material science in Table IV is not very different than the as grown data, it unlikely that the enhancement observed is due to defect relief as in the case of annealing, or strain relaxation of the residual compressive stress that would produce a more direct gap material. What is more likely the case for the increased emission is that a fresh hydrogen-terminated surface is continually formed during the ICP process once the initial native oxide surface is removed by the etching. In the case of samples that have been exposed for 5-10 minutes, this only removes the top 25-50 nm of material.

Overall, *n*-type doping $Ge_{1-y}Sn_y$ alloys by *in-situ* methods produced the highest performing PL emission. As discussed above, the intensity enhancement from *n*-doped materials routinely approaches an order of magnitude. Unfortunately however, it was found that a combination of the processing techniques with *n*-doped materials did not yield any further enhancements. *N*-type materials are not compatible with annealing treatments because P and As dopants in Ge-like materials have very high diffusion coefficients. So as defects are removed, so are the dopants. Also, there was virtually no change in PL intensity when *n*-type samples were exposed to the optimal ICP treatment. This is likely due to the surface charge inversion that occurs for Ge-like narrow band gap materials. In the case of *n*-type Ge, it has been shown that to maintain charge neutrality the region near the surface becomes *p*-type.[158] This effectively produces a *pn* junction that forms an energy barrier at the surface, keeping free carriers in the bulk material and away from the nonradiative dangling bonds at the surface. This likely explains why

shallow donors in Ge appear to be insensitive to hydrogen treatments because the dangling bond centers exist near the mid-gap, so the *pn* junction also prevents the hydrogen ions from penetrating into the material as well. To date, all known attempts to passivate shallow donors in Ge using hydrogen have been unsuccessful.[159] A combination of processing techniques, such as RTA/CVD annealing of intrinsic samples followed by ICP, was also found to not produce noteworthy PL intensity enhancements relative to the samples that were just ICP treated.

5. Conclusion

In summary of Chapter II (A), the indirect to direct gap crossover for $Ge_{1-y}Sn_y$ alloys was determined to be $y_c = 0.087$. This result was made possible by advances in the growth of high quality samples on Ge-buffered Si(100) platforms that produced clear PL signals allowing precise line shape modeling of the spectra E_0 and E_{ind} features. Routes to optimized PL emission were explored by growing thicker films, heavily doping the materials *n*-type, annealing by RTA and in a tube furnace, and treating the surface with a hydrogen plasma. Overall *n*-type materials show the strongest emission.

B. Optical and Electronic Properties of $Ge_{1-y}Sn_y$ *pin* Diodes

1. Introduction

The PL study in part (A) of this chapter determined an indirect-to-direct-gap transition at $y_c = 0.087$ for $Ge_{1-y}Sn_y$ alloys, confirming this system to be an intriguing alternative to Ge for purely group-IV interband lasers that can be easily integrated onto Si-platforms.[134,160] The required Sn concentration to achieve direct gap conditions is much less than originally predicted by theory,[84,85] which should facilitate the fabrication of appropriate *pn* junction devices as the first step towards electrically injected $Ge_{1-y}Sn_y$

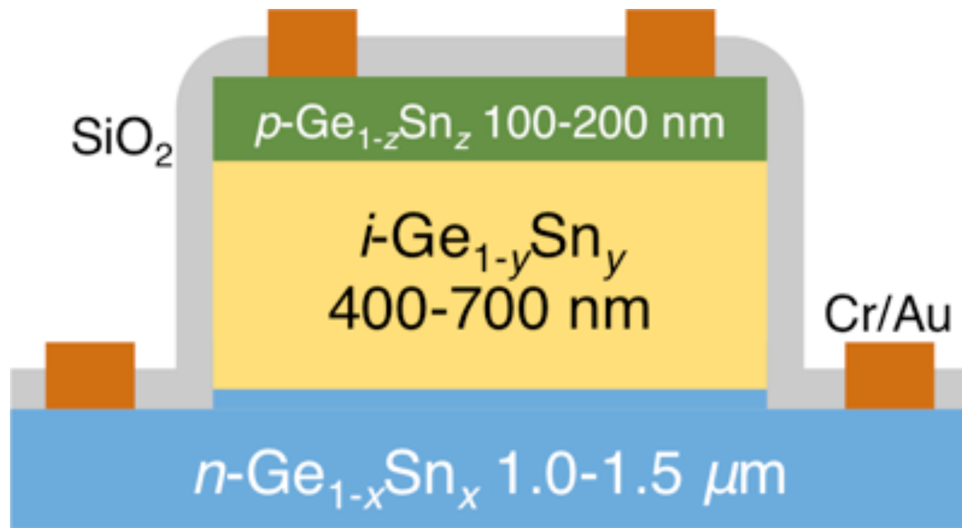

Figure 16: Schematic illustration of the basic heterostructure (n-$Ge_{1-x}Sn_x$/i-$Ge_{1-y}Sn_y$/p-$Ge_{1-z}Sn_z$) diode grown on Si. The composition of the bottom layer is varied so that devices are produced that contain either a single defected interface or no defective interfaces.

lasers, following the recent demonstration of optically-pumped devices.[110] However, systematic studies of light-emitting diodes at and beyond the indirect-to-direct threshold are still lacking. After the initial report of electroluminescence (EL) from $Ge_{0.98}Sn_{0.02}$ diodes by Roucka *et al*.(Ref. 106), several groups have observed EL from $Ge_{1-y}Sn_y$ devices,[161,162,163,164,165,166] but the highest reported Sn concentration in those devices is y = 0.08, still below y_c. A significant issue to be reckoned with in reaching high concentrations is the strong compositional dependence of the lattice parameter. Even at the modest $y_c = 0.09$ value, the lattice mismatch with pure Ge is 1.2%, a very substantial amount. Fully strained $Ge_{1-y}Sn_y$ films on relaxed Ge buffer layers cannot exceed the critical thickness for strain relaxation. For $y_c = 0.09$ this critical thickness is less than 10 nm, and even the metastable critical thickness at typical $Ge_{1-y}Sn_y$ growth temperatures is estimated to be less than 100 nm.[131] In addition, the compressive nature of the mismatch strain makes the material more indirect, which is undesirable for light emission. Strain-

relaxed films can be grown much thicker and have a band line-up more favorable to light emission, but at the price of generating misfit dislocations that increase the non-radiative recombination rate.

This section of the chapter is devoted to discussing the optical and electronic properties of $Ge_{1-y}Sn_y$ *pin* diodes as a function of *i*-layer composition and microstructure. Devices containing 0-14% Sn in the active layer are fabricated. Based on the microstructural properties, two types of devices are presented. In the first type of *pin* device, a mostly relaxed *i*-layer is produced directly on a *n*-Ge buffer akin to the samples produced in the previous PL study. In this type of structure the samples are produced so that only one layer has a strain-relaxed interface where misfit dislocations are present. The second set of samples investigates the effect on performance when misfit dislocations are removed by creating samples with no strain-relaxed interfaces.

2. Growth and Materials Properties of $Ge_{1-y}Sn_y$ pin Devices

Figure 16 shows a schematic diagram of the light emitting diode (LED) design. All structures are grown on Ge-buffered Si substrates. They include a thick $Ge_{1-x}Sn_x$ bottom contact layer doped *n*-type, a thin intrinsic Ge spacer, a nominally intrinsic $Ge_{1-y}Sn_y$ region, and a *p*-type $Ge_{1-z}Sn_z$ top electrode. The choices $y > x$ and $y > z$ promote carrier confinement in the *i*-layer, and the latter also improves light extraction. However, as discussed in the introduction, they can lead to defects associated with the strain relaxation. In all cases, y and z are chosen in such a way that the *i-p* interfaces are pseudomorphically lattice-matched, with no strain relaxation. This allows us to concentrate on a single interface, namely that between the *i*-$Ge_{1-y}Sn_y$ and the *n*-$Ge_{1-x}Sn_x$

layers, for which the Sn concentrations are chosen in such a way that fully pseudomorphic as well as strain-relaxed structures can be compared.

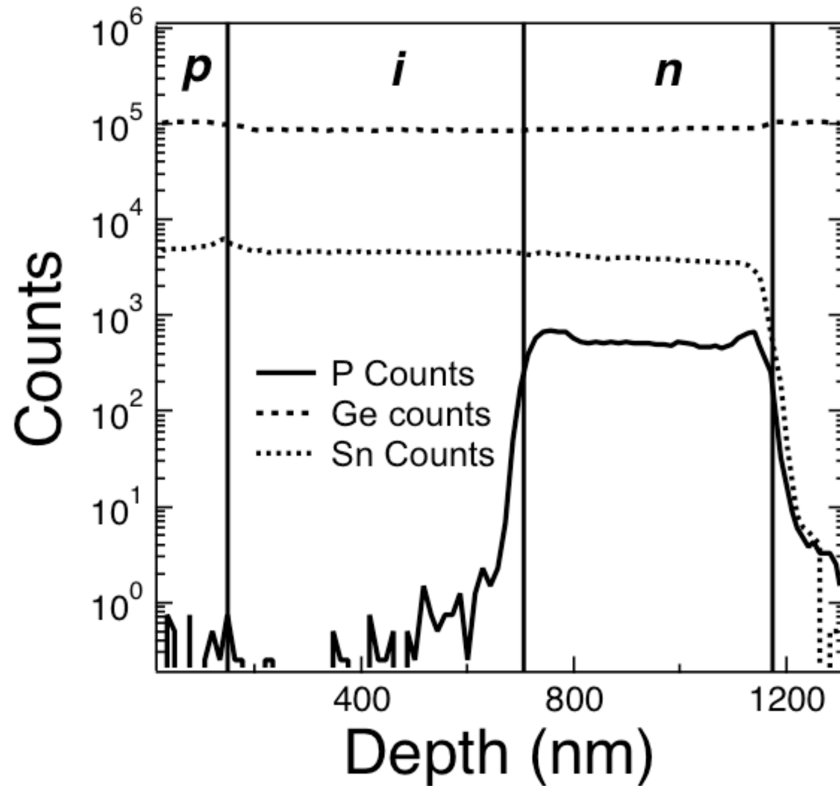

Figure 17: SIMS elemental profile of a typical $Ge_{0.93}Sn_{0.07}$ sample showing a uniform distribution of Ge and Sn atoms across the entire sequence of device layers as expected. The P atom content is constant through the *n* region and drops sharply down to noise levels through the intrinsic layer precluding the possibility of inter-diffusion or cross contamination from the reactor ambient. Sample and data produced by Charutha Senaratne. See J. D. Gallagher, C. L. Senaratne, C. Xu, P. Sims, T. Aoki, D. J. Smith, J. Menéndez, and J. Kouvetakis, *Journal of Applied Physics*, 117, 245704 (2015).

All samples in this study were produced using a CVD approach based on high reactivity Ge_3H_8 and Ge_4H_{10} precursors. This method yields active $Ge_{1-y}Sn_y$ layers with thicknesses of 400-700 nm that are mostly relaxed of misfit strains. The very low temperature growth process in this case generates relatively benign edge-type dislocations and short stacking faults penetrating down into the buffer layer rather than propagating upward into the active region. This is in contrast to most MBE samples, where the active components are either compressively strained as grown on Ge-buffered

Si or highly defected. Devices grown using conventional CVD precursors contain relatively thin active layers (200 nm),[166] which are also susceptible to significant strain effects. On the basis of the above benefits we have been able to produce diodes in the previously unexplored 9-12% Sn direct-gap regime. These diodes exhibit strong, tunable electroluminescence and superior electrical response irrespective of composition.

In the case of devices where the Sn content of the bottom contact was 0% (x = 0.00 in Figure 16), the fabrication begins with the growth of a Ge layer thick enough that contacts could be made far from the Si/Ge interface. Layers with carrier densities of ~ 2×10^{19} cm^{-3} and thicknesses of 1-1.5 μm were grown on 4” Si (100) wafers using a single wafer gas-source molecular epitaxy (GSME) reactor and Ge_4H_{10} as the source of Ge.[61] The doping was achieved by adding $P(GeH_3)_3$ to the reaction mixture.[132] The resultant Ge layers were annealed *in situ* at 650°C for 3 minutes to reduce the density of threading defects and then characterized to ensure their suitability for subsequent epitaxy of device components. The wafers were then cleaved into quarter segments, dipped in 5% HF to remove Ge surface oxides, and loaded into a UHV-CVD reactor for depositions of $Ge_{1-y}Sn_y$ intrinsic layers with $0 \leq y \leq 0.14$. For samples with $0.02 \leq y \leq 0.08$, a further cleaning step was performed by flowing 5% Ge_2H_6 at 30 mTorr for 5 min. For samples with $y > 0.08$ this procedure was insufficient to prevent formation of deleterious surface defects, which become more prevalent with increasing thickness above 350 nm and interfere adversely with subsequent device fabrication. To mitigate this problem an additional Ge spacer layer was grown *in situ* on top of the Ge buffer using Ge_3H_8 to generate a fresh surface devoid of structural imperfections. The growth of this layer was started at 340°C, allowed to proceed for 15 minutes, and then continued while the reactor

was cooled to the required growth temperature of the target $Ge_{1-y}Sn_y$ intrinsic layers. The latter were grown between 300°C and 285°C, depending on composition in the range of 8-11% Sn using appropriate mixtures of Ge_3H_8, and SnD_4. The ratio of these precursors

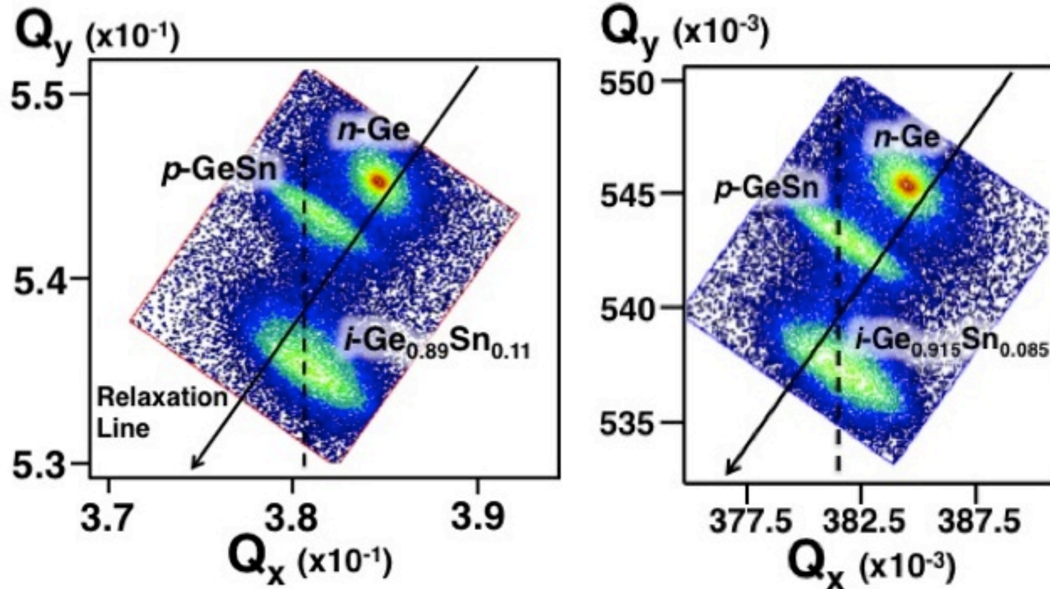

Figure 18: (224) reciprocal space maps of devices with intrinsic layer compositions $Ge_{0.89}Sn_{0.11}$ (left) and $Ge_{0.915}Sn_{0.085}$ (right). The *p*- and *i*-layers are nearly lattice matched in the plane of growth as shown by the vertical alignment of the peak maxima along the dotted lines in both panels. Sample and data produced by Charutha Senaratne. See J. D. Gallagher, C. L. Senaratne, C. Xu, P. Sims, T. Aoki, D. J. Smith, J. Menéndez, and J. Kouvetakis, *Journal of Applied Physics*, 117, 245704 (2015).

and other growth parameters such as temperature were adjusted in order to achieve the target composition under optimal conditions, as described in detail in Refs. 131 and 132. By following this strategy it was possible to obtain intrinsic $Ge_{1-y}Sn_y$ active layers with thicknesses of 400-700 nm and strain relaxation states up to 75-80% grown on the *n*-type virtual Ge substrates.

The final stage of the device production was the growth of the *p*-type top layer. Prior to this step, the *n*-*i* layers were characterized by high resolution XRD and spectroscopic ellipsometry to ensure that the crystallinity, thickness and composition

were suitable for the fabrication of the intended devices. Subsequently, the samples were chemically cleaned and loaded into a dedicated CVD system for growth of the *p*-type electrode using diborane (B_2H_6). The Ge_2H_6 clean was again used in this case to prepare an epi-ready free surface. Appropriate concentrations of Ge_2H_6 and SnD_4 were combined with H_2 diluent to produce reaction mixtures. B_2H_6 was introduced separately using a calibrated mass flow device to ensure systematic control of the dopant concentrations in the layers. For devices with Sn concentrations ranging from 2% to 5%, the intrinsic layer and the top electrode possess the same composition ($y = z$). For devices with higher Sn contents $0.07 \leq y \leq 0.14$, the *p*-layer Sn content was kept in the range of $z \sim 0.05$. These were grown at temperatures of 330-320°C, which are higher than the 290-285°C range for the corresponding *i*-layers, so that this step also acts as a thermal treatment to further reduce any residual compressive strain in the high Sn content samples. In all cases the *p*-layers were fully strained to the intrinsic regions, creating pseudomorphic *i-p* junctions devoid of interfacial defects. After completing the entire device stack, the samples were once again characterized by XRD and ellipsometry to measure strain, thickness and doping concentrations. Further analysis by RBS was used to corroborate the thickness and composition.

In order to produce bottom contact layers with $x > 0.00$, a *n*-type layer with thickness of ~ 400 nm and a composition approaching 6-7% Sn was grown by UHV-CVD on a Ge-buffered silicon substrate. In this case, $P(SiH_3)_3$ was used as the source of P atoms. Next, a 550 nm-thick $Ge_{0.93}Sn_{0.07}$ intrinsic layer was grown *in situ* and followed by a *p*-type top-contact layer incorporating a similar amount of Sn and a thickness of 120 nm. The latter was doped using diborane (B_2H_6). The donor (P) and acceptor (B) levels in

the resultant films were measured using spectroscopic ellipsometry to be in the range of 3×10^{19} cm^{-3}. The P and Sn atomic distribution in the *pin* region was analyzed by Secondary Ion Mass Spectroscopy (SIMS). Figure 17 shows that the P profile is flat across the *n*-contact layer and drops below the detection limit at the *n*-GeSn/*i*-GeSn interface. The sharp transition in the amount of P indicates that no diffusion or segregation of the dopant atoms has occurred. The flat and continuous Sn profile in the figure reveals that the distribution of Sn is uniform and the mass counts are very similar across the entire *pin* region, providing strong evidence that the constituent layers exhibit closely matched Sn compositions. This observation is corroborated by RBS and XRD measurements which show that the alloy layers in the stack exhibit very similar lattice parameters and Sn concentrations approaching 7% in all cases.

Figure 18 shows HR-XRD reciprocal space maps (RSM) of the (224) reflection for representative devices with intrinsic layer compositions $Ge_{0.915}Sn_{0.0.85}$ and $Ge_{0.89}Sn_{0.11}$ in the vicinity of the indirect-to-direct gap transition. These devices are grown on 1.2 μm thick Ge buffers and are capped with ~150-200 nm thick *p*-type top-layers containing 4-5% Sn and 1-2 $\times10^{19}$ cm^{-3} activated B atoms. The figure shows diffraction maps of the entire device stack comprising *n*-Ge, *i*-Ge, *i*-GeSn and *p*-GeSn layer sequence. The maps are well defined, narrow, and highly symmetrical. This indicates that the samples are single-phase materials exhibiting comparable crystal quality and similar strain properties irrespective of Sn content. For each layer, the in-plane and out-of-plane lattice parameters *a* and *c* are obtained from the (224) peaks. The latter can also be extracted from the (004) reflections, and the two values are found to be in excellent agreement. Using *a* and *c*, a simple elasticity calculation—as described in Ref. 89—gives the relaxed

cubic lattice parameter a_0, from which the strain $\varepsilon = (a-a_0)/a_0$ is computed. The Sn-concentration can also be extracted from a_0 (Ref. 89), and the value so obtained agrees with the RBS simulations. The combined *n*- and *i*-Ge buffers in both samples in Figure 18 exhibit residual tensile strains of ~ 0.15%, as shown by their common (224) peak maxima located slightly above the relaxation line. The top *i*- and *p*-$Ge_{1-y}Sn_y$ layers of each device exhibit widely separated (224) peaks along the Q_y direction, as expected due to their dissimilar Sn contents. The (224) peak maxima are vertically aligned along the pseudomorphic direction (marked by dotted lines) indicating that *i*-$Ge_{1-y}Sn_y$ and *p*-$Ge_{1-z}Sn_z$ components are lattice-matched and fully strained to one another. The *i*-$Ge_{1-y}Sn_y$ layers exhibit residual compressive strains of ~ 0.30%. This corresponds to a strain relaxation of 75-77%. The top *p*-type electrodes are tensile strained by ~ 0.5% to the underlying *i*-$Ge_{1-y}Sn_y$.

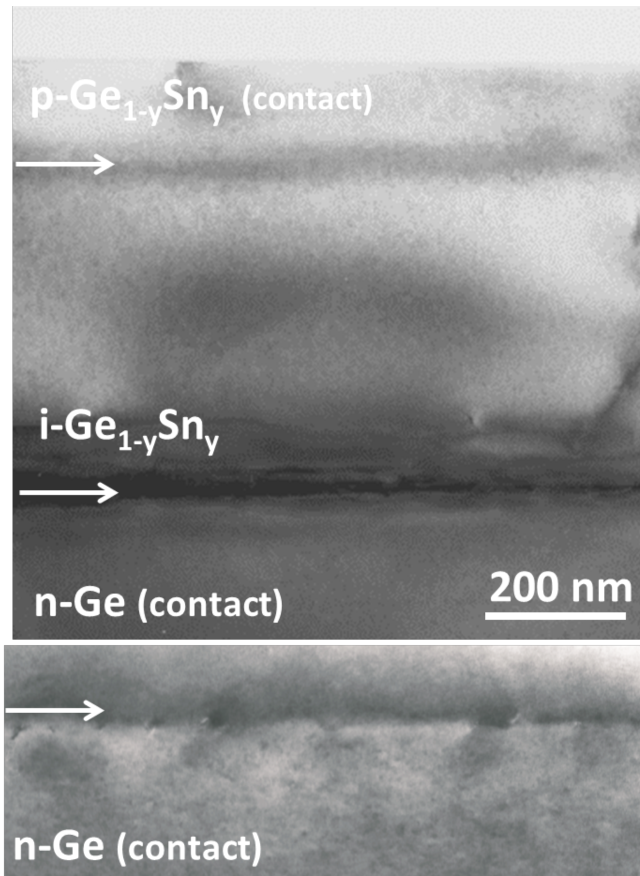

Figure 19: XTEM images of a *n*-Ge/*i*-$Ge_{0.895}Sn_{0.105}$/*p*-$Ge_{0.95}Sn_{0.05}$ device grown upon Si(100). The top image shows the entire three-layer stack illustrating a smooth surface and a defected bottom interface. A magnified view of the latter is presented in the image below showing random distribution of edge-type dislocations and short stacking faults confined within the interface region. Sample produced by Charutha Senaratne. See J. D. Gallagher, C. L. Senaratne, C. Xu, P. Sims, T. Aoki, D. J. Smith, J. Menéndez, and J. Kouvetakis, *Journal of Applied Physics*, 117, 245704 (2015).

Additional structural characterizations were performed by cross-sectional transmission electron microscopy (XTEM) using a JEOL−4000 EX microscope. Insights into the local microstructure provide correlations between crystal quality and device properties, leading to improvements in design and performance. The micrograph in Figure 19 shows a low magnification image of the entire sequence of the *n*-Ge, *i*-Ge, *i*–$Ge_{0.895}Sn_{0.105}$, and *p*-$Ge_{0.95}Sn_{0.05}$ device layers. The free surface of the stack is flat and the top interface is defect free, since the *p*-type top layer grows fully strained to the intrinsic counterpart, despite their compositional difference. The bottom interface between Ge and $Ge_{0.895}Sn_{0.105}$ is highly defected due to extensive relaxation of the highly concentrated alloy. The layer thickness is ~ 450 nm, far exceeding the critical value, making strain relaxation unavoidable even under the metastable growth conditions applied in this case.[131] The defects in the samples are primarily edge dislocations and short stacking faults which do not thread upward into the active region, but penetrate downward a short distance into the buffer.

Aberration-corrected imaging was also employed using a JEOL ARM 200F microscope to further study the local microstructure and identify the types and distribution of dislocations generated at the mismatched interface of these devices. The bright field image in the top panel of Figure 20 corroborates the previous observation in Figure 19 that the top *p*-type layers are grown defect-free fully strained to the underlying intrinsic counterparts. The white band across the middle region of the image marked by the arrow is due to strain contrast associated with the pseudomorphic growth. The middle panel image shows that the bottom interface contains several defected spots appearing as dark contrast features that correspond to 60° dislocations and short stacking faults. These

latter defects are randomly distributed along the interface plane and penetrate down a short distance into the Ge layer. The bottom panel of Figure 20 shows two {111}-type stacking faults originating at the interface and intersecting inside the buffer layer. These defects and the 60° dislocations represent the commonly found defects that compensate the misfit strain in these device structures. The microstructure illustrated in Figure 20 is common to all 8-11% Sn samples grown on relatively higher mismatched Ge platforms.

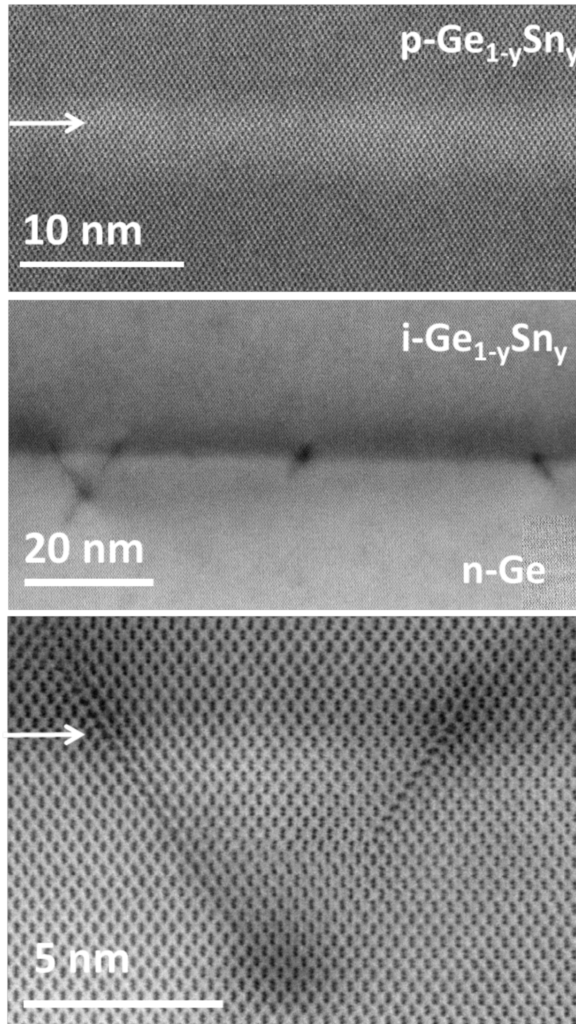

Figure 20: XSTEM images of the interface microstructure of a $Ge_{0.93}Sn_{0.07}$ device. (a) Top defect free interface between fully strained intrinsic and *p*-type $Ge_{1-y}Sn_y$ layers. (b) Micrograph of bottom intrinsic-(*n*) interface showing edge dislocations and short stacking faults appearing as dark contrast areas along the heterojunction. (c) Enlarged view of two stacking faults crossing down into the Ge buffer along distinct {111} planes. Sample produced by Charutha Senaratne. See J. D. Gallagher, C. L. Senaratne, C. Xu, P. Sims, T. Aoki, D. J. Smith, J. Menéndez, and J. Kouvetakis, *Journal of Applied Physics*, 117, 245704 (2015).

Devices were fabricated using protocols similar to those employed for $Ge_{1-y}Sn_y$/Si prototypes in prior work.[106] The samples in this study were first coated with a protective SiO_2 layer to allow patterning of the device architectures. For samples with $y < 0.08$ the SiO_2 depositions were conducted at 350°C, while for $y > 0.08$ the temperature was lowered to 250°C to prevent possible Sn precipitation that may occur due to the thermal environment. All

samples were processed into circular mesas with sizes varying from 50-500 μm in diameter. The patterns were first outlined by photolithography and then etched down 250-600 nm into the n-$Ge_{1-x}Sn_x$ contact layer by reactive ion methods using a BCl_3 plasma source. The protective oxide coating was removed and a second passivating oxide layer was deposited. The thickness of the latter was chosen to minimize the reflectance of SiO_2 to photons with energy equal to the alloy band gap. Accordingly, the thickness of this layer was monotonically increased from 290-470 nm for samples with Sn compositions varying from 2-11%. The devices were then exposed to photolithography to pattern metal contacts for the top and bottom electrodes. The contacts consist of 20/200 nm Cr/Au layer stacks deposited by electro-thermal evaporation. The metal pads were lastly defined as circular rings using an acetone liftoff process. All samples were subjected to a final cleaning step using oxygen plasma to remove residual photoresist contaminants prior to EL measurements.

3. Theoretical Model of $Ge_{1-y}Sn_y$ pin Diode Electroluminescence Spectra for Carrier Lifetime Analysis

From a theoretical perspective, an attractive feature of these devices is that the EL signal is almost exclusively due to the i-$Ge_{1-y}Sn_y$ layers, whereas PL experiments from the same structures reveal contributions from all layers reached by the incident light, including the bottom n-type layer and sometimes even the Ge buffer in contact with the Si substrate. Since the n-buffer/i-layer interface can be carefully engineered, EL provides an ideal optical probe for such interfaces.

If the thickness of the intrinsic layer is d_i, the power per unit device area emitted into an external solid angle $d\Omega$ is given by:

$$I_i = \frac{d^2 P_i}{dA d\Omega} = \frac{2d_i}{c^2 h^3} \int_0^\infty dE \left[\frac{E^3 \alpha_i(E) S_i(E) T_p(E)}{\exp\left(\frac{E-\Delta F}{k_B T}\right) - 1} \right], \tag{2.6}$$

where we use the standard notation for fundamental physical constants, $\alpha_i(E)$ is the absorption coefficient of the intrinsic layer at energy E, $S_i(E)$ a reabsorption correction for the same layer, T_p the transmittance of the top p-layer, T the absolute temperature, and $\Delta F = E_{Fc} - E_{Fv}$ is the difference between quasi-Fermi levels in the conduction and valence bands of the intrinsic layer. Eq. (2.6) follows from a generalized van Roosbroeck-Shockley expression that is calculated as in Ref. 134. For the LED applications we take into account the fact that the depth of focus of our collection optics far exceeds the thickness of the i-layer, and we make the additional assumption that the injected carrier density is uniformly distributed over the i-layer, which should be a very good approximation because the carrier diffusion lengths are longer than d_i. Within this framework, the reabsorption correction is given by $S(E) = \left\{1 - \exp\left[-\alpha_i(E) d_i\right]\right\} / \alpha_i(E) d_i$. Furthermore, $T_p(E) = \exp\left[-\alpha_p(E) d_p\right]$, where α_p is the absorption coefficient of the top p-layer and d_p its thickness.

The steady-state carrier concentration in the i-layer under forward bias is given by:[135]

$$n = p = \frac{J\tau}{ed_i}, \tag{2.7}$$

where J is the current density, e the electron charge, and τ the total recombination lifetime. These carrier concentrations determine the quasi-Fermi levels E_{Fc} and E_{Fv} that are needed for the computation of Eq. (2.6). For the conduction band, we include the

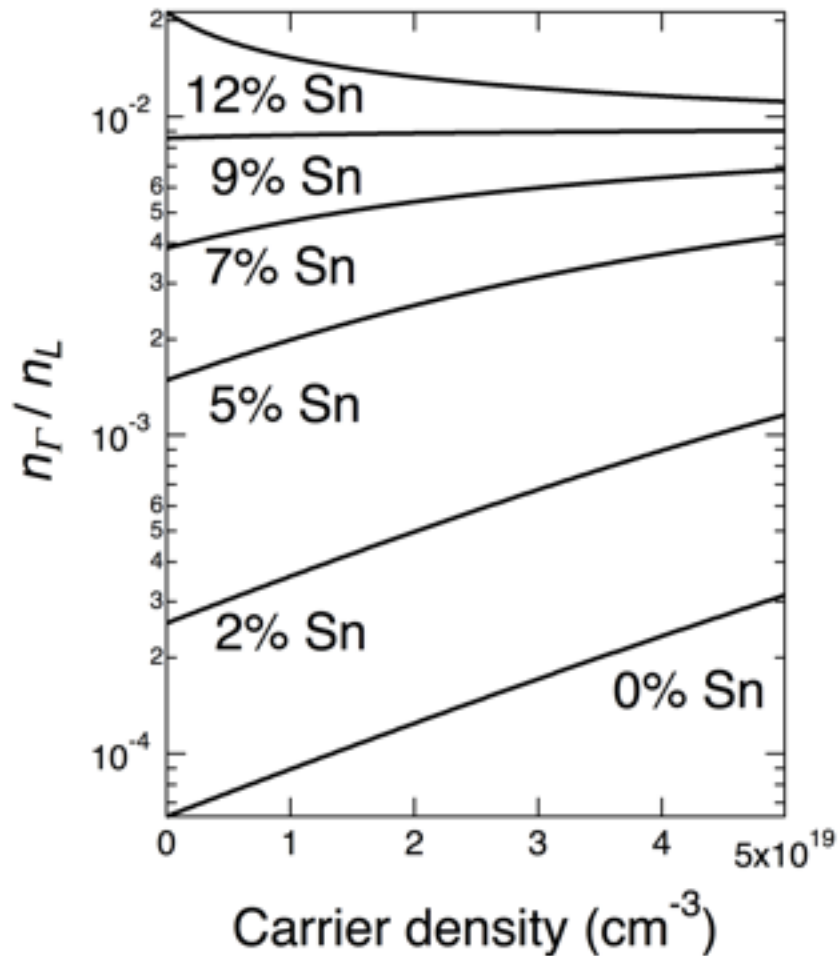

Figure 21: Computed ratio n_Γ/n_L between the Γ- and L-valley populations at 300 K shown as a function of the total carrier concentration $n = n_\Gamma + n_L$ for several $Ge_{1-y}Sn_y$ alloys. The model assumes parabolic bands with effective masses extrapolated from pure Ge values using $k{\cdot}p$ theory. Notice the change of slope at $y = 0.09$, where the alloy becomes a direct gap semiconductor.

contribution from the two nearby minima located at the L and Γ points of the Brillouin zone. In Figure 21 we show the calculated population ratio n_Γ/n_L as a function of the total carrier concentration $n = n_\Gamma + n_L$ for different $Ge_{1-y}Sn_y$ alloys. The compositional dependence of the valley energies is taken from Ref. 160. It implies an indirect-to-direct (L absolute minimum equal to Γ absolute minimum in the conduction band) crossover at $y_c = 0.087$. We see that at room temperature only a very small fraction of the carriers

occupy the Γ-valley, even for nominally direct gap alloys. There is, however, a switchover from positive to negative slope at $y = y_c$. The total recombination lifetime is given by contributions from non-radiative (defects and Auger), and radiative contributions:

$$\frac{1}{\tau} = \frac{1}{\tau_{\text{rad}}} + \frac{1}{\tau_{\text{non-rad}}} = \frac{1}{\tau_{\text{rad}}} + \left(A + \gamma_3 n^2\right), \tag{2.8}$$

The Auger coefficient in intrinsic Ge is $\gamma_3 = 1.1\times10^{-31}$ cm^6/s.[167] For typical values of n in our experiments ($n \sim 2\times10^{18}$ cm^{-3}, see below), the Auger-limited lifetime is about 2 μs. This is about an order of magnitude longer than the actually measured lifetime (see below), so that Auger contributions play a minor role in our experiments. The radiative contribution can be neglected in an indirect gap material. However, in our case there is a partial occupation of the Γ-valley. The radiative decay is then given by the weighted average

$$\frac{1}{\tau_{\text{rad}}} = \frac{1}{\tau_{\text{rad},\Gamma}}\left(\frac{n_\Gamma}{n_\Gamma + n_L}\right) + \frac{1}{\tau_{\text{rad},L}}\left(\frac{n_L}{n_\Gamma + n_L}\right), \tag{2.9}$$

where the valley weights in parenthesis can be trivially written in terms of the n_Γ/n_L ratio in Figure 21. For $y = 0.12$ and $n = 2\times10^{18}$ cm^{-3}, $n_\Gamma/n_L = 0.019$. For such concentration we estimate $\tau_{\text{rad},\Gamma} \sim 20$ ns. (Ref. 135) Neglecting the indirect contribution, this gives $\tau_{\text{rad}} \sim 1.1$ μs. Again, this is much longer that the lifetimes determined experimentally below, so that radiative recombination can be ignored. The important conclusion then is that the recombination lifetime is dominated by the defect term A in Eq. (2.8), which is a constant

independent of the carrier concentration. Thus we can assume, from Eq. (2.7), that the injected carrier density is directly proportional to the diode current. This assumption will be used below to fit the experimental results to Eq. (2.6).

It has been argued in Ref. 38 that for Ge-on-Si materials quasi-equilibrium in the conduction band may not be reached for sufficiently high non-radiative recombination lifetimes. In such cases the ratio n_Γ/n_L would be *higher* than the quasi-equilibrium values in Figure 21. The results from Ref. 38, however, were derived for the optical excitation case in which carriers are pumped into the Γ-valley. In electrical devices, on the other hand, carriers are pumped mainly into the L valleys, and under those conditions the same model predicts a negligible deviation from quasi-equilibrium. Thus a comparison between photoluminescence (PL) and electroluminescence (EL) spectra can provide important clues on carrier distributions in $Ge_{1-y}Sn_y$ alloys.

4. Optical and Electronic Properties of $Ge_{1-y}Sn_y$ pin Devices

Figure 22 (a) compares *I-V* curves for a series of representative samples containing 0-14% Sn in the active layer of the device. The diode ideality factors range from 1.10 to 1.55 and show good rectifying diode behavior in all cases. The reverse-bias dark currents measured for the 5.5-8.5% Sn devices are similar to those reported for similar samples within this composition range.[166] However, in forward bias our currents are 10 times higher, indicating that our fabrication approach leads to better ideality factors and/or lower parasitic series resistances. The reverse bias current for the 2% Sn device is lower than that of the pure Ge sample in spite of the significantly larger active layer thickness in the latter sample (530 nm vs. 800 nm, respectively). This result indicates that the electrical properties are independent of the presence of the Ge-Sn bonds or lattice

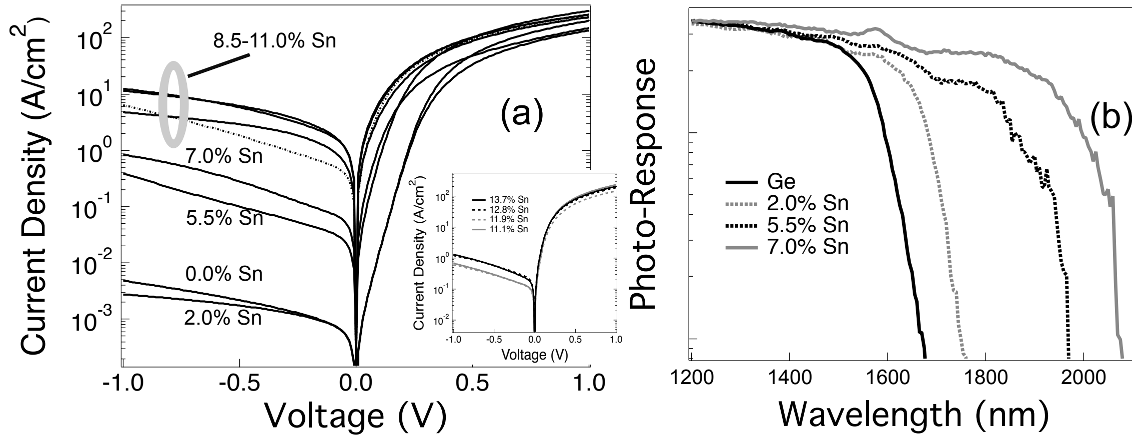

Figure 22: (a) Room temperature *I-V* data for devices containing 0-14% Sn showing an increase in dark current density as a function of alloy content. The inset shows that with improved processing a saturation limit is approached in the -1V dark current level for higher Sn content devices. (b) Photoresponse of devices containing up to 7% Sn showing an absorption edge beyond 2000 nm.

distortions arising from local bonding configurations in the alloy. In contrast to the $Ge_{0.98}Sn_{0.02}$ device, the dark current densities of the more concentrated samples increase by three orders of magnitude from 3 mA/cm^2 to 6 A/cm^2 for the $Ge_{0.89}Sn_{0.11}$ device. In the 5-7% Sn devices a surge in dark current density is observed. This is less pronounced in the 8-11% Sn samples where the currents appear to converge within a narrow range spanning 5-10 A/cm^2 indicating that this window may represent a saturation for the generation rate of leakage carriers by the defects at the *n*-Ge/*i*-$Ge_{1-y}Sn_y$ interface. The inset to panel (a) plots the dark current characteristics for a set of $y > 0.11$ samples that were processed under improved conditions conducive to attain good side-wall passivation that reduces the reverse bias dark current levels. This is demonstrated by the reverse bias dark currents straddling 1.0 A/cm^2 at -1V bias, despite a compositional variation over a 3% Sn range. This further supports the notion that carriers generated by the defected *n*/*i* interface reach a saturation limit. Figure 22 (b) plots the normalized optical responsivity absorption edges for hetero-structure *pin* $Ge_{1-y}Sn_y$ devices ranging from 0-7% Sn. These

experiments are performed at room temperature under 0V bias. The plots show a systematic redshift of the absorption edge to longer wavelengths beyond 2 μm, coinciding with successively higher Sn concentrations incorporated into the active region. These results support the notion that alloying Ge with Sn reduces the fundamental band gaps in the $Ge_{1-y}Sn_y$ alloy system relative to Ge, and demonstrates the applicability of these materials for integrated long wavelength detection systems.

To better understand the reverse bias electrical behavior, we investigated the temperature dependence of the reverse bias dark currents. Panel (a) of Figure 23 shows the activation energies determined from such measurements. We see that that for low Sn concentrations the activation energies clearly exceed $E_g/2$, where E_g is the fundamental band gap value, which were adjusted to include the shifts due to strain. This indicates a significant diffusion contribution to the dark current, which can only be observed in devices with low defect concentrations. For higher Sn concentrations, on the other hand, the activation energies approach $E_g/2$, as expected from a Shockley-Read-Hall (SRH) generation mechanism via defects.

Another method by which we may gain a further qualitative understanding of contribution to the dark current caused by the presence of defects at the *n*-Ge/*i*-$Ge_{1-y}Sn_y$ interface is to plot the -1V current values as points vs Sn content. This is shown in panel (b) of Figure 23. The data are compared with a theoretical model (solid line) which plots the expected compositional dependence of the dark current density at -1V bias assuming only SRH recombination and ignoring other defect-based current generation mechanisms. According to SRH theory, the reverse bias current goes as the inverse exponential of the band gap such that lower band gap materials produce larger reverse bias currents, as

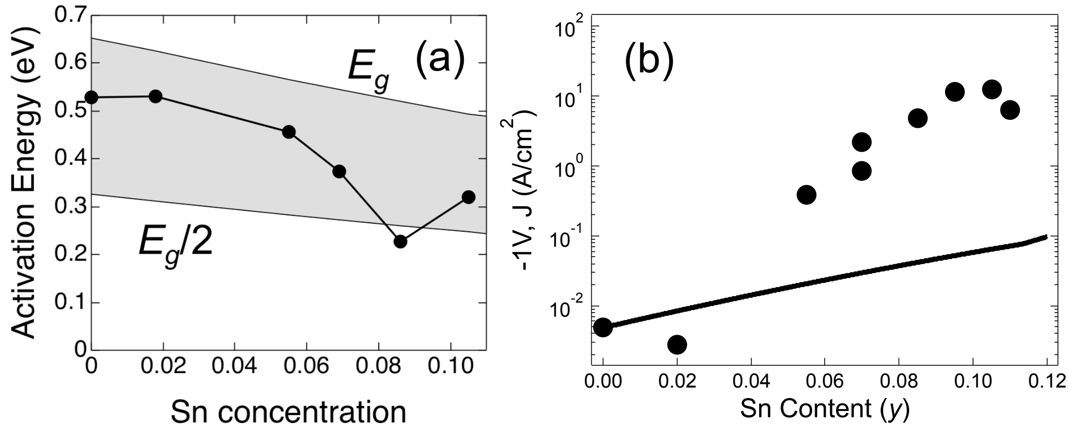

Figure 23: (a) Comparison of the activation energies of the dark currents at -0.2 V with the fundamental band gap and half its value. While the low Sn-concentration diodes shows evidence for a diffusion component of the current, at high Sn-concentrations Shockley-Read-Hall recombination at defects seems to be the dominant contribution. (b) -1V current levels (points) relative to a SRH theoretical model (solid line) that assumes recombination occurs between mid-gap defects in the devices.

shown by the line which increases by almost 2 orders of magnitude over a y = 0.00-0.12 range. This line is determined by calculating the product of the intrinsic carrier concentration (n_i) and the depletion layer thickness (W_d) for *pin* devices with ~400 nm active layers spanning the range of compositions in our samples. The quantity $n_i W_d$ is proportional to the drift component of the reverse bias dark current (I_{drift}) which is at least 3 orders of magnitude greater than the diffusion component (I_{diff}) at biases as large as -1V for kT near room temperature. Values of $I_{drift} \sim n_i W_d$ were calculated over the range y = 0-0.12 at -1V bias and normalized to the Ge reference device at y = 0. The compositional-dependence of the $Ge_{1-y}Sn_y$ band gaps and carrier effective masses used to perform the calculation are taken from Refs. 160 and 168, respectively. Comparing the SRH line with the points, we note that samples with *i*-layer concentrations $y > 0.05$ are at least an order of magnitude greater than expected based on SRH theory alone. Thus the difference between the points and the line represents the component that defects, likely formed by

TABLE V: Sample parameters of all devices used to conduct the EL study.

Name	Ge buffer thick (nm)	*n*-layer		Ge spacer thickness (nm)	*i*-layer		*i*-layer strain (%)	*p*-layer	
		d_n (nm)	x		d_i (nm)	y		d_p (nm)	z
Ge	N/A	1300	0	0	800	0	-0.15	125	0.003
GeSn2	N/A	1065	0	0	530	0.020	0.04	150	0.020
GeSn5	N/A	1400	0	0	440	0.055	0.16	150	0.041
GeSn7	N/A	1350	0	0	400	0.070	0.22	200	0.040
GeSn7-t	N/A	1638	0	125	700	0.068	0.21	120	0.065
GeSn7-h	1218	412	0.060	0	550	0.070	0.13	118	0.060
GeSn8	N/A	1025	0	160	375	0.085	0.30	145	0.042
GeSn10	N/A	1400	0	190	430	0.105	0.32	135	0.044

strain-relaxation at the *n*-Ge/*i*-$Ge_{1-y}Sn_y$ interface, contribute to the electrical properties in these devices.

EL measurements were performed at room temperature by forward-biasing the diodes using a Keithley 2602A source. The emitted light was collected using a focusing lens and then passed through a grating spectrometer (f=320 mm) and detected with an extended liquid nitrogen cooled InGaAs detector operating in the 1300-2300 nm wavelength range. For samples with Sn contents above 9% the spectra were acquired using a thermoelectrically (TE) cooled PbS detector with an extended collection range spanning 1500-2700 nm. The current source in all cases was pulsed at 50 Hz to provide modulation for lock-in detection. The EL response was recorded as a function of injection currents ranging from 0.1-0.5 A for all devices. To maximize the current density in the sample, the smallest device that contact probes could practically be placed on without obscuring the window were used in all measurements. In all cases the devices used have mesa optical windows of 300 μm in diameter. Table V summarizes the sample parameters used in the EL study.

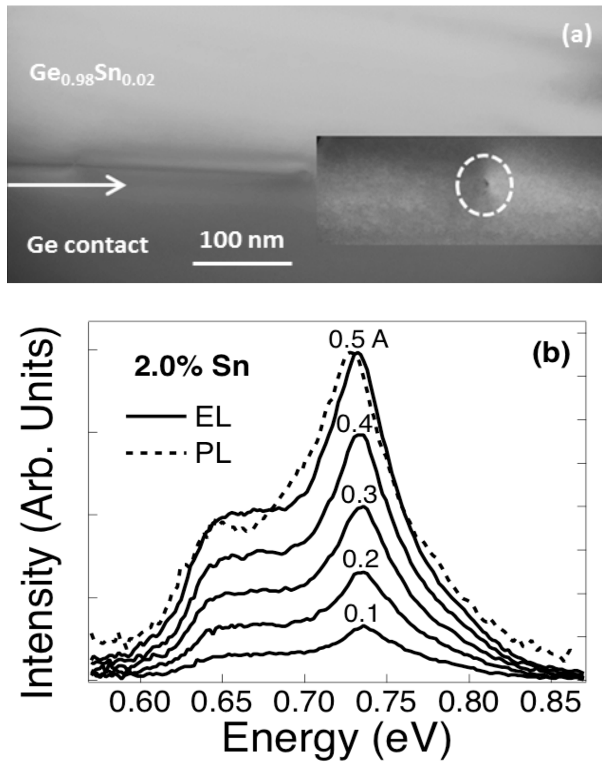

Figure 24: (a) XTEM image of $Ge/Ge_{0.98}Sn_{0.02}$ interface. Inset contains a rare edge dislocation marked by a white circle. (b) EL spectrum of the device at 0.1-0.5 A. The dashed is a PL spectrum from a single layer reference sample. Good agreement between the two experiments is noted between the higher energy direct gap and lower energy indirect gap peaks. Sample produced by Charutha Senaratne. See J. D. Gallagher, C. L. Senaratne, C. Xu, P. Sims, T. Aoki, D. J. Smith, J. Menéndez, and J. Kouvetakis, *Journal of Applied Physics*, 117, 245704 (2015).

Results for sample GeSn2 (y = 0.02) are presented in Figure 24. Panel (a) of this figure shows a XTEM micrograph illustrating that the film is devoid of threading defects within the field of view. The inset shows an isolated dislocation at the interface, the only such defect found over the 300 nm length scale of the figure. This is in principle unexpected because the film exceeds the critical thickness for growth on a Ge substrate.[131] However, the Ge buffer is under tensile strain due to the thermal expansion mismatch with the Si substrate, and therefore the two layers are fortuitously lattice matched (as corroborated by XRD measurements), leading to a defect-free *n*-*i* interface.

Figure 24 (b) shows a series of EL spectra as a function of current taken from this sample between 0.1-0.5 A. The spectrum at 0.5 A is compared with the PL counterpart measured from an equivalent single layer reference grown on Ge buffered Si using the same method. The main peak is attributed to direct gap emission and the low-energy shoulder is assigned to indirect gap transitions. It is apparent that the relative intensity and position of the direct/indirect signals are very similar for both the PL and EL. It was

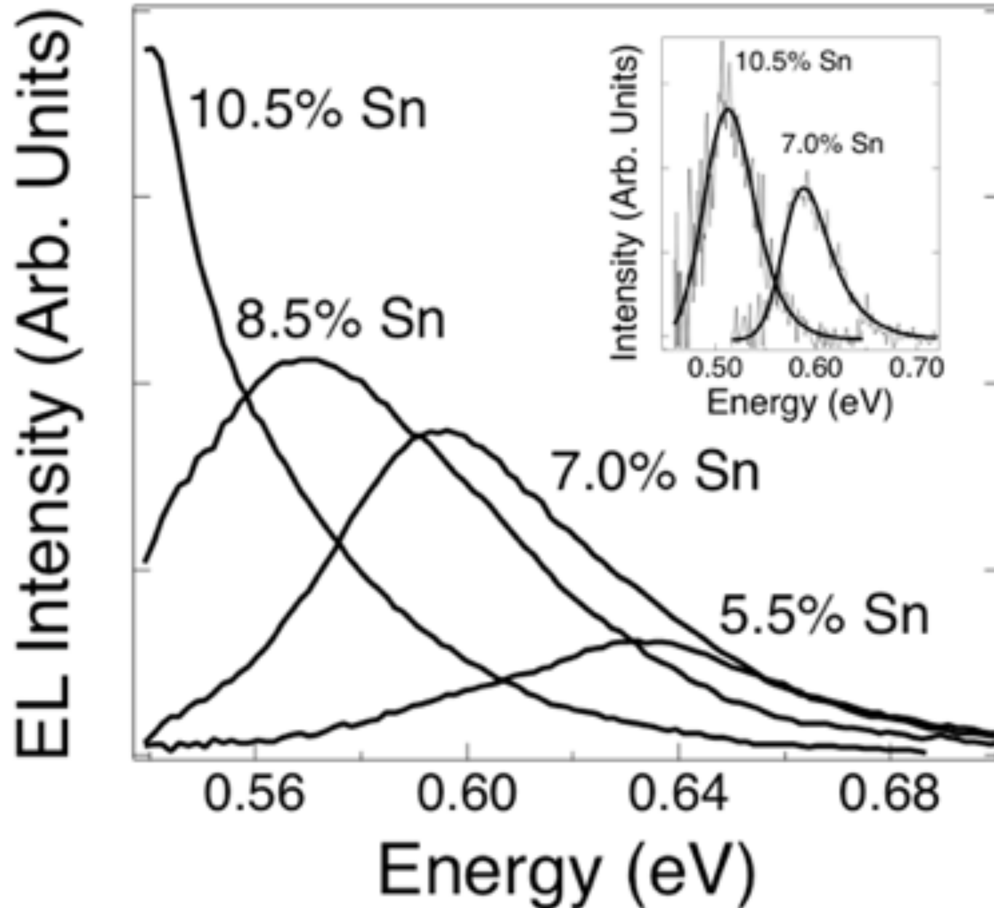

Figure 25: EL spectra of diodes with intrinsic layer compositions y = 0.055, 0.070, 0.085, and 0.105 taken at 0.5 A (GeSn5, GeSn7, GeSn8, GeSn10) using the InGaAs detector. The active layer thicknesses range from 400-440 nm. The peak maxima shift to lower energies and the signal intensities increase as Sn content approaches the direct gap transition. (Inset) EL spectra from GeSn10 and GeSn7 taken at 1.0 A using PbS detector. The solid black lines represent EMG fits to the data.

suggested above that a comparison between PL and EL could give insight into the achievement of quasi-equilibrium under optical excitation. Under quasi-equilibrium conditions, the ratio of indirect to direct gap emission would be obviously identical in PL and EL experiments if the total carrier density $n = n_\Gamma + n_L$ in the conduction band is the same in both experiments. Even if the values of n were different, the emission ratio would be similar if the n_Γ/n_L ratio were weakly dependent on n. From the fits to be described below, we estimate that for the GeSn2 diode 1.3×10^{18} cm^{-3} $\leq n \leq$ 6.4×10^{18} cm^{-3}, for which, according to Figure 21, the n_Γ/n_L ratio only changes by 20%. Thus the

similarity between the EL and PL is consistent with quasi-equilibrium conditions in photoexcited $Ge_{0.98}Sn_{0.02}$. Interestingly, significant differences were observed between PL and EL in previous generations of devices that used doped Si substrates as the *p*-type component of the diode.[106] In those experiments, the ratio of indirect to direct gap emission was larger in EL than in PL experiments. The discrepancy with the present results can be easily understood in the context of the non-equilibrium model of Ref. 38. The model predicts that an excess relative population of the Γ valley (deviating from quasi-equilibrium) is obtained if carriers are pumped into the Γ valley (PL experiments) in samples with sufficiently high non-radiative recombination rates. This was the case in previous generations of $Ge_{1-y}Sn_y$/Si layers, but the samples discussed here have longer non-radiative recombination lifetimes due to the buffer layer separation with the Si interface, and therefore they don't deviate substantially from quasi-equilibrium, as was previously the case. A quantitative corroboration of this analysis is provided below.

The EL spectra of samples GeSn5, GeSn7, GeSn8, and GeSn10, all with a relaxed *n*-Ge/*i*-$Ge_{1-y}Sn_y$ interface and similar values of d_i are plotted separately in Figure 25. The spectra are collected at 0.5 A and show strong peaks corresponding to direct gap emission. The peak maxima shift to lower energies and the emission intensities increase with Sn content, as expected. In addition to the main peak the spectrum of the 5.5% Sn device also shows a weak lower energy shoulder assigned to the E_{ind} transition. This feature coalesces with the main peak for $y \geq 0.07$ due to the reduction in separation between the direct and indirect edges with increasing Sn content. The 10.5% Sn spectrum cannot be fully measured with an InGaAs detector. To obtain the full peak profile for this material we used a PbS detector with an extended range down to 2700 nm. The

results are shown in Figure 25 inset, which compares the 10.5% Sn emission peak with that of a 7% Sn analog, illustrating the expected shift in direct-gap energy vs composition. The signal-to-noise ratio is inferior in the PbS detector, but the peaks are

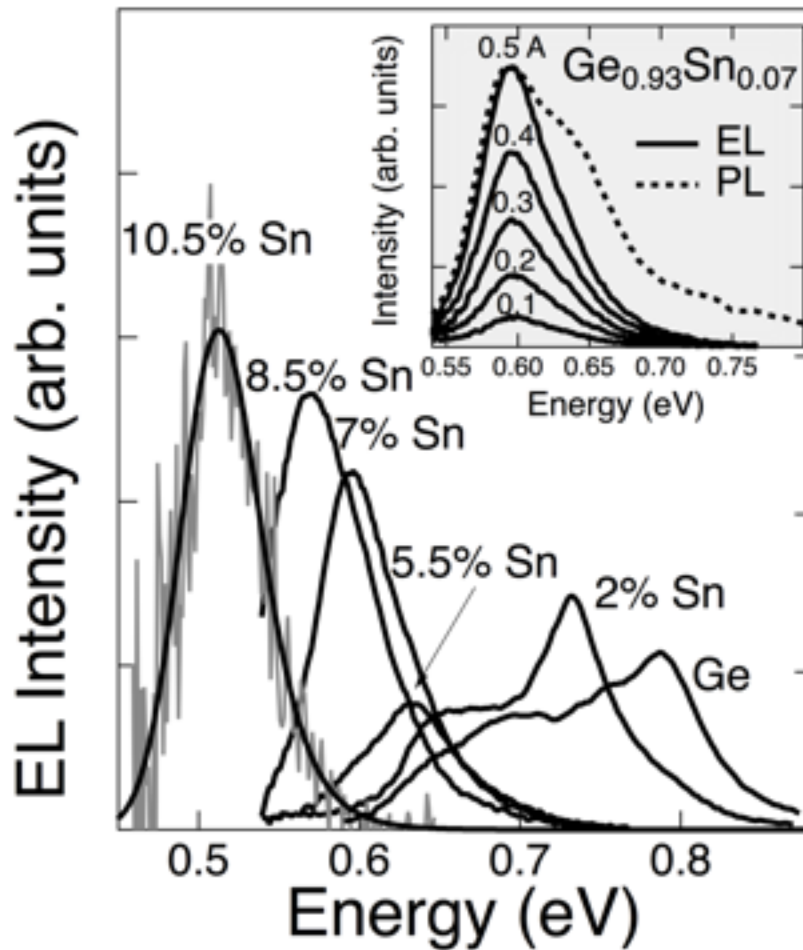

Figure 26: Room temperature EL spectra of GeSn heterostructure diodes at a current density of 490 A/cm^2 (I = 0.5 A), normalized to the intrinsic layer thickness. The noisier data for the 10.5% Sn is due to the use of a PbS detector, as opposed to the InGaAs detector used for the other diodes. For this sample, the solid black line is the EMG fit of the emission profile. The inset shows the current dependence of the EL for the 7% Sn diode and the PL spectrum for the same sample, normalized to the intensity of the EL emission for the highest current.

very well resolved.

Figure 26 shows the thickness normalized EL spectra for all of the n-Ge/i-$Ge_{1-y}Sn_y$ heterojunction diodes used in this study. Again, for low Sn concentrations, we see

clear evidence of direct and indirect gap emission, whereas at high values of y, a single peak is observed. A strong signal is seen from the diode with a $Ge_{0.915}Sn_{0.085}$ intrinsic layer, very close to y_c, and from the diode with a $Ge_{0.895}Sn_{0.105}$ intrinsic layer, which is a direct gap material according to the known compositional dependence of the band gaps.[160] The inset shows the experimental EL spectra as a function of the injection current for a diode with a $Ge_{0.93}Sn_{0.07}$ *i*-layer, together with a photoluminescence (PL) spectrum for the same sample. The main peak in the EL spectra is assigned to direct gap emission from the intrinsic layers in the device. The PL signal also shows contributions from the top *p*-layer (which has a lower Sn concentration for the sample in the inset) and even from the *n*-Ge buffer layer. The spectral lineshapes as well as the peak energies are in excellent agreement with previous detailed studies of the compositional dependence of the PL signal from $Ge_{1-y}Sn_y$.[134,160] As in the PL case, the data are well described using an Exponentially Modified Gaussian (EMG) for the direct gap emission and a simple Gaussian for the indirect gap emission. An example of a fit EMG extrapolated to describe the lower energy spectrum of the sample is shown in Figure 26 for the case of a diode with a $y = 0.105$ intrinsic layer.

The compositional dependence of the EL signal strength is quite remarkable. At room temperature, we expect a monotonic increase as the direct gap approaches the indirect gap, without any observable discontinuity at y_c. Instead, the EL intensity decreases between $y = 0.02$ and $y = 0.055$, and reverts to the expected trend for $y > 0.055$. To understand these results, we take advantage of our ability to model the direct gap emission in these systems very accurately, as discussed in Ref. 106 and more recently in Ref. 134. The emission spectrum can be expressed as a generalized van Roosbroeck-

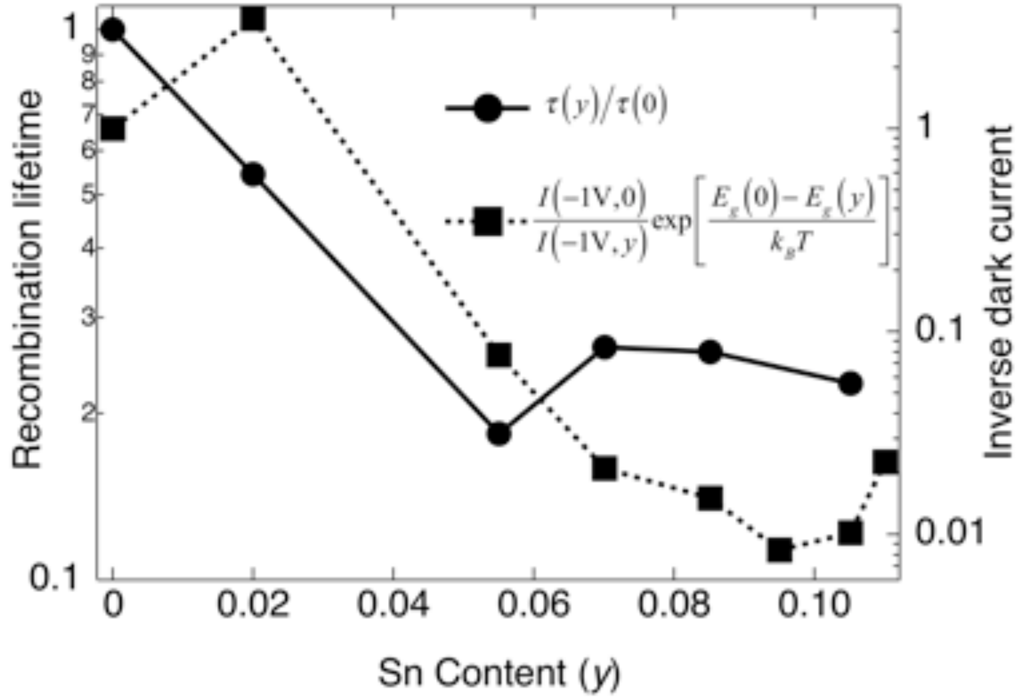

Figure 27: Recombination lifetimes obtained from the relative intensity of the EL spectra compared with the inverse dark currents from the *I-V* characteristic of the diodes. The recombination lifetime is normalized to the value τ(0) for a pure Ge diode (y = 0). The inverse dark currents are also normalized to the pure Ge value and further multiplied by a factor that corrects for the band gap reduction as a function of composition.

Shockley expression that depends on the non-equilibrium carrier concentration n and the energies of the direct and indirect gap, as explained in detail in previous work.[134] Since the non-equilibrium carrier concentration is related to the diode current by[135] $n = J\tau/(ed)$ (where J is the current density, e the elemental charge, d the i-layer thickness, and τ the total recombination time), we can adjust the relative values of τ to

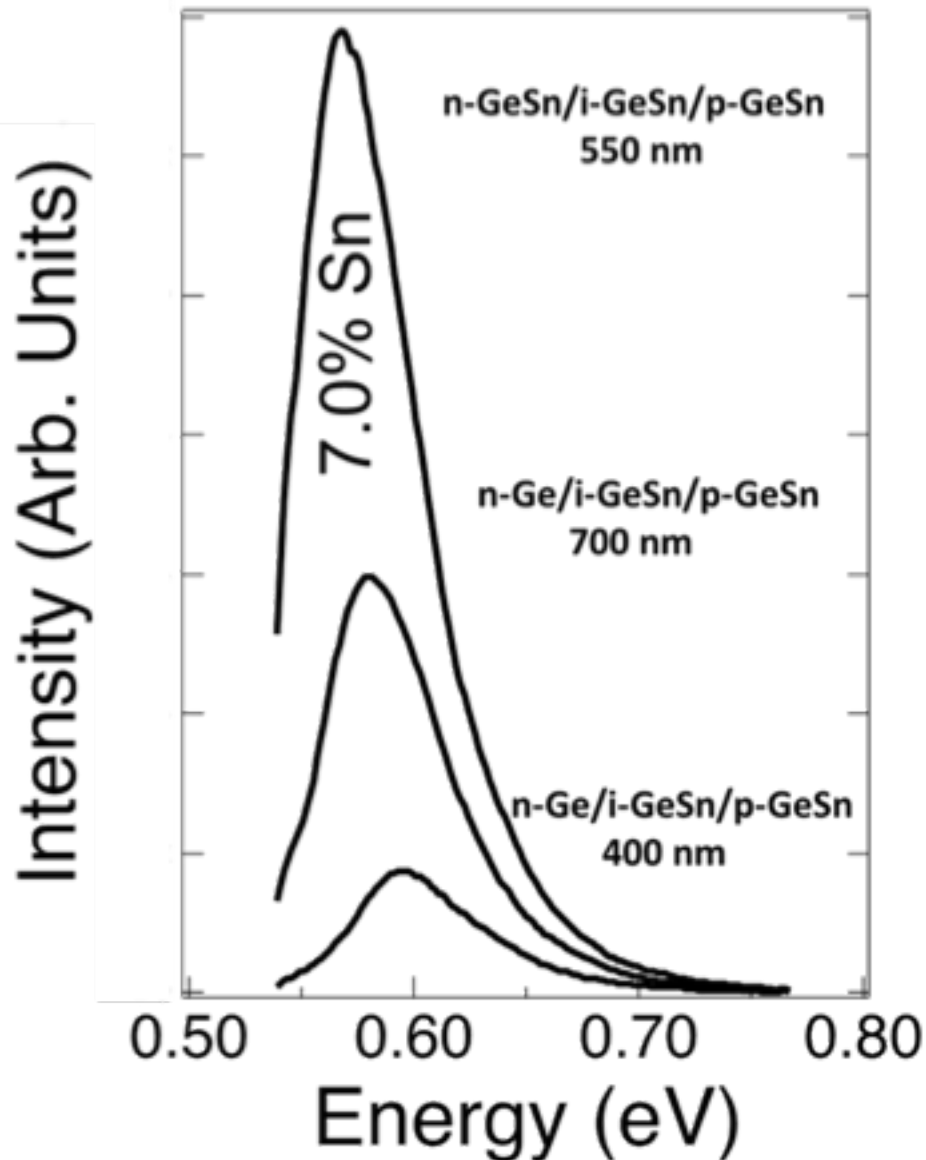

Figure 28: EL spectra of three diodes with the same nominal Sn concentration $y = 0.07$ in the intrinsic layer. The two low-intensity plots correspond to diodes with a pure Ge *n*-layer and *i*-layer thicknesses of 400 nm and 700 nm (GeSn7 and GeSn7-t). The highest intensity plot corresponds to sample GeSn7-h whose *n*-layer has a Sn concentration $x = 0.06$ and the i-layer thickness is 550 nm.

match the spectra in Figure 26. The results are shown in Figure 27, and we see that the recombination time decreases sharply until it reaches at minimum near $y = 0.05$. Beyond this concentration, the recombination time is roughly constant. We also show in Figure 27 the inverse of the dark currents at -1V, which are also proportional to the carrier

lifetime, and we see a similar trend. We attribute this behavior to the onset of strain relaxation in the intrinsic layer. Whereas the 2% Sn device is fully strained, the 5.5% Sn device, with an intrinsic layer thickness of 440 nm that exceeds the metastable critical thickness,[131] is found to be 70% relaxed. The associated misfit dislocations shorten the non-radiative recombination time, overwhelming the increase in EL intensity predicted from the reduction of the direct-indirect separation relative to pure Ge. For the $y > 0.055$ samples, on the other hand, the level of strain relaxation is comparable,[131] and therefore we expect the non-radiative recombination time to saturate, so that the compositional dependence of the EL intensity follows the theoretical prediction again, increasing as the separation between direct and indirect gaps decreases and eventually reverses.

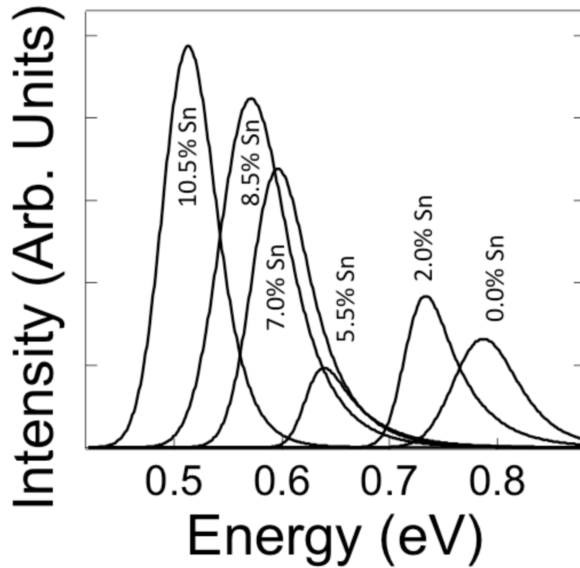

Figure 29: EMG fits of the direct-gap component of the EL spectrum of selected diodes, normalized to the intrinsic layer thickness. Actual spectra and their current density dependence are shown in Figs. 24-26, and 28. The intensity drop between the 2% Sn and 5.5% Sn is discussed in the text.

The samples in Figure 25 and Figure 26 have a defected *n*-*i* interface, since the intrinsic layer mismatch strain with the *n*-layer is largely relaxed. Experimental evidence for the deleterious effect of such defected interfaces is provided in Figure 28, which compares the EL spectrum from sample GeSn7, also shown in Figure 25, with those from samples GeSn7-t and GeSn7-h. Sample GeSn7-t has a 70% thicker intrinsic layer, but its

integrated emission intensity is over three times higher. Even stronger emission is obtained from sample GeSn7-h, whose *n*-layer has a Sn concentration $x = 0.060$, so that the *n*/*i* interface is defect free. This sample shows a seven times integration intensity enhancement over sample GeSn7.

To better quantify our observations, we compared our results with theoretical predictions developed in part 3 of this section. Our first step is to separate the contributions from the direct and indirect gaps in the experimental spectra. We follow the analysis in previous work and fit all the spectra with an EMG function, which represents the direct gap E_0, and a Gaussian function representing the indirect gap E_{ind}. Results of the EMG fits from such fits for selected samples are shown in Figure 29.

We then obtain experimental integrated intensities $I_{\exp}$ for the direct gap emission by integrating the EMG functions over the energy for each value of current, and compare with the predictions from Eq. (2.6). For this we first compute the integrated power I_{theory} as a function of the total carrier concentration $p = n = n_\Gamma + n_L$ for each sample using the parameters in Table V. The temperature is taken as 310 K, slightly above room values, to account for device heating. The results are shown as lines in Figure 30. Next we add the experimental data points to the same figure using Eq. (2.7) to convert the current to carrier density. The value of the recombination lifetime for each sample is taken as an adjustable parameter, chosen to minimize the expression

$$S = \sum_{j\,(\text{diodes})} \sum_{k_j\,(\text{currents})} \left(\frac{I_j^{\text{theory}}\left(J_{j,k_j} \tau_j \big/ e d_j\right) - \alpha I_{j,k_j}^{\exp}}{\alpha I_{j,k_j}^{\exp}} \right)^2 , \tag{2.10}$$

where the sum over j runs over all diodes and the sum over k_j over each of the values of current used (about 5) for sample j. The independence of the adjustable parameter τ_j on the index k reflects the assumption that the recombination lifetime is independent of the carrier density. An additional adjustable parameter α provides the needed overall scaling between theory and experiment, since we are not preforming absolute intensity measurements. The result of this global adjustment is shown in Figure 30, and we see that the agreement obtained is excellent. The recombination lifetimes obtained from the minimization are shown separately in Figure 31.

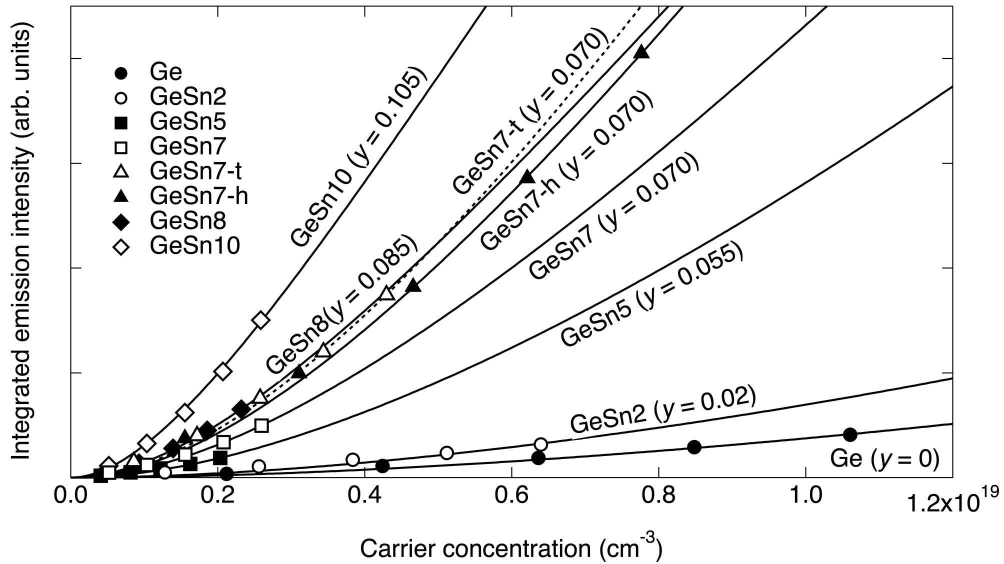

Figure 30: Integrated EL intensity as a function of the injected carrier density for all diodes. The solid lines represent calculations based on the theory of Eq. (2.6) using the sample parameters from Table V. The markers correspond to experimental data for each diode, collected as a function of the diode current. The diode currents were converted to carrier concentrations and the overall normalization parameter that matches theory to experiment were determined as discussed in the text, by minimizing Eq. (2.10).

This approach to measuring the carrier lifetimes represents an improvement over the previous method. The lifetimes shown in Figure 27 are derived by simultaneous fits of the emission lineshape and its intensity for all injection currents. However this procedure is flawed by an inconsistency because the carrier densities that optimized the

lineshape fits were up to one order of magnitude different from the ones that gave the best agreement with the intensities. A thorough discussion of the effect of the carrier concentration on the emission lineshape is given in Ref. 134. For typical values of broadening and spectral resolution, the sensitivity to n is only significant for high concentrations $n \sim 10^{19}$ cm^{-3}. This is also the range for which systematic errors due to temperature fluctuations and band non-parabolicity/warping, are largest. Not surprisingly, then, simultaneous global fits of the spectral lineshape and relative intensities between spectra do not converge well. Since the dependence of the intensities on n is much stronger, we chose in our second method of lifetime measurement to compare integrated intensities with the theoretical predictions, thereby bypassing the need to adjust the emission profiles. This also has the significant advantage of drastically simplifying the numerical analysis of the data, since performing simultaneous fits of spectra using the van Roosbroeck-Shockley expressions with full inclusion of non-parabolicity and excitonic effects is a daunting task.

It is important to point out that our ability to extract absolute values of n—and therefore, of the recombination lifetimes via Eq. (2.7)—depends on the intensities $I^{j}_{\text{theory}}\left(n\right)$ having different functional dependencies on n, since we are not performing absolute measurements of the emitted intensities. This is indeed the case over broad carrier density ranges, as can be expected from the very different carrier dependencies of the n_Γ/n_L ratios in Figure 21. Over the carrier density range in Figure 30 however, the differences are smaller. Fitting the computed $I^{j}_{\text{theory}}\left(n\right)$ functions with expressions of the form $I^{j}_{\text{theory}}\left(n\right) \propto n^{\beta}$ over that range, we obtain values of β ranging from 1.3 to 1.8

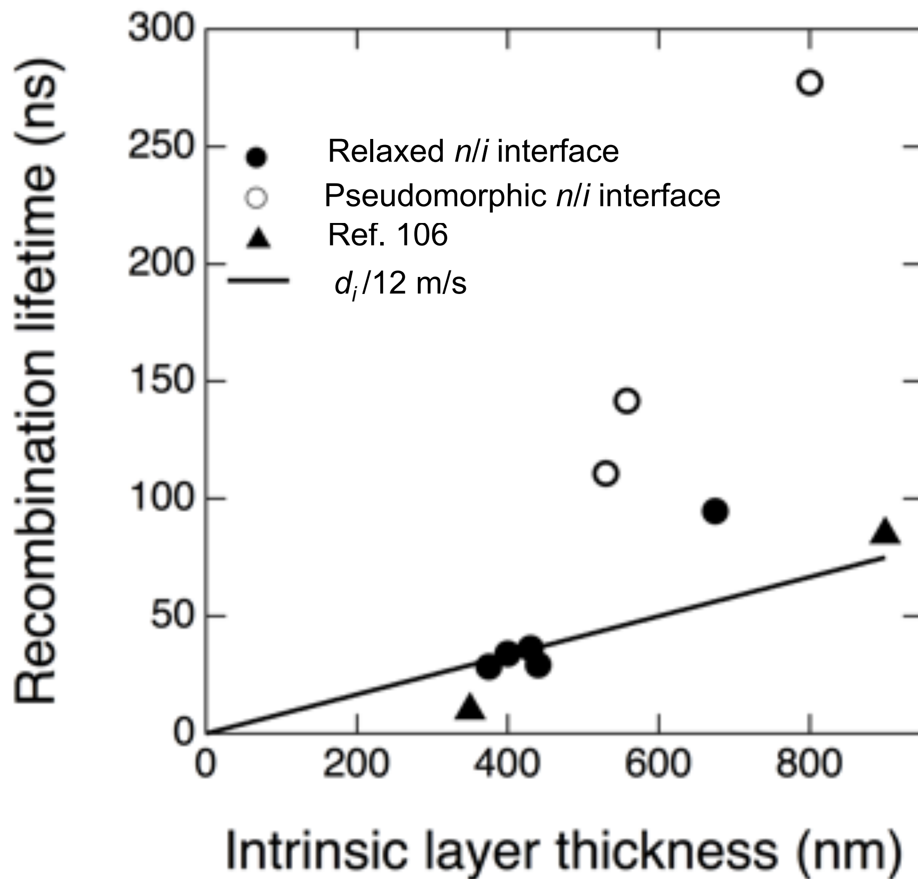

Figure 31: Recombination lifetimes extracted from the adjustment in Figure 30. Notice the much longer times obtained for samples with no defected interfaces.

depending on *y*. This is enough to ensure numerical convergence with our data set, but we cannot rule out the possibility that measurements with a different set of samples might converge to somewhat different absolute values of the recombination lifetimes. An additional practical complication is that the pure Ge diode is a nearly perfect homostructure, and some of the other diodes have little confinement between the *i*- and *p*-layers, so that the assumption that the emission arises solely from the intrinsic layer may break down in those samples. We recomputed the minimization in Eq. (2.10) using different values of thickness and we obtain similar recombination lifetimes, but we suggest conservatively that the absolute values in Figure 31 should be taken as accurate

within a factor of two. The relative values of the recombination parameters, on the other hand, are very robust and show unmistakable trends. First, samples with relaxed *n/i* interfaces and similar thicknesses also have similar recombination lifetimes. Second, the three samples with unrelaxed *n*/*i* interfaces show the longest recombination lifetimes. These observations confirm that defects at the intrinsic layer interfaces have a strong influence on the LED performance. The solid line in Figure 31 shows the function d/v for v = 12 m/s. This would be the interface recombination velocity in the samples with d_i ~ 400 nm if the recombination lifetime were entirely dominated by the interface contribution. In fact, the actual recombination velocity is most likely significantly less than 12 m/s, since the lifetime τ_i = 95 ns of sample GeSn7_t, a thicker sample with d_i = 700 nm (but otherwise with composition and strain relaxation values very similar to GeSn7), is longer than predicted from the line in Figure 31. This suggests that in addition to reducing the interface recombination velocity, maintaining a pseudomorphic, non-relaxed *n*/*i* interface reduces the bulk recombination contribution. The triangles in Figure 31 correspond to the two *nip* samples reported in Ref. 106, which we computed using Eq. (2.7) and the carrier concentrations given in that reference. Those samples contain defected *p*/*i* interfaces with the Si substrate. While the diode geometries are not the same, it is interesting to compare the recombination lifetime of 10 ns for a $Ge_{0.98}Sn_{0.02}$ diode in Ref. 106 with the value of 110 ns for our sample GeSn2, with a similar intrinsic layer concentration but no interfacial defects. The order-of-magnitude improvement is a clear confirmation of the superior sample quality using our latest device architectures.

5. *Conclusion*

The optical and electronic properties of $Ge_{1-y}Sn_y$ *pin* diodes have been presented. Samples grown on *n*-Ge-buffered Si platforms showed increased reverse bias dark current densities as a function of composition. The reverse biases current levels appear to saturate in devices with greater than ~8% Sn. This has been attributed to a shift from a diffusion dominated recombination mechanism, to one better described by SRH and defect traps. The EL spectra of these devices showed the same trends to direct gap materials as was seen in the previous PL study and devices with Sn compositions beyond the indirect to direct gap crossover were fabricated. We also demonstrate that by removing strain relaxation at both interfaces, a much enhanced EL signal is obtained.

Two models for measuring the recombination lifetime based on the EL spectra are presented. The first one simultaneously fits the line shape and intensity profile across the composition span of all devices for spectra taken at the same current injection. This model found that at the lifetimes fall very quickly as a function of composition and then appear to plateau at onset of strain relaxation at the *n*-Ge/*i*-$Ge_{1-y}Sn_y$ interface. The second model improves upon the first one by considering how the integral intensity of the spectra change as a function of current injection. A global fit is then performed with the lifetime as an adjustable parameter. The results reveal that devices with no strain relaxed interfaces have a significantly longer lifetime than devices with strain relaxed interfaces.

III. OPTICAL AND ELECTRONIC PROPERTIES OF GE-SI-SN MATERIALS AND DEVICES

Portions of text and figures in this chapter were previously published as J. D. Gallagher, C. Xu, L. Jiang, J. Kouvetakis, and J. Menéndez, *Appl. Phys. Lett* **103**, 202104 (2013) and have been reproduced with permission. Portions of text and figures in this chapter were previously published as J. D. Gallagher, C. Xu, C. L. Senaratne, T. Aoki, P. M. Wallace, J. Kouvetakis, and J. Menéndez, *J. Appl. Phys.* **118**, 135701 (2015) and have been reproduced with permission.

A. Optical Properties of Sn-Rich $Ge_{1-x-y}Si_xSn_y$ Materials

1. Introduction

As outlined in Chapter I, initial investigations into ternary $Ge_{1-x-y}Si_xSn_y$ alloys were confined to the compositional case of materials with a Si:Sn ratio of 3.7:1, which perfectly lattice matches that of Ge. Despite the successful integration of device quality materials on Si and Ge substrates and the demonstration that these materials have tunable direct band gaps near 1.0 eV,[114,122] attempts to measure room temperature PL from these materials did not yield any results, unlike the PL experiments of Ge and $Ge_{1-y}Sn_y$ materials grown on Si. Thus the inability to measure luminescence from the ternary alloy in this composition range was not attributed to crystal defects or structural imperfections, but to the fact that the material possessed an electronic structure more closely resembling Si than Ge.[125] However the inability to measure the fundamental indirect band gap, which is the paramount property in order to design materials for photovoltaics, lasers and quantum well/strain structures, was an unresolved problem.

In order to obtain the first observation of light emission from $Ge_{1-x-y}Si_xSn_y$ alloys a new class of materials was explored in the composition space. With the aim of recovering light emission analogous to that documented in $Ge_{1-y}Sn_y$ alloys, Sn-rich ($y > x$) $Ge_{1-x-y}Si_xSn_y$ materials were grown directly on Si.[124] These showed a tunable E_0 PL emission peak at longer wavelengths than Ge indicating that the ternary could replicate the electronic properties of $Ge_{1-y}Sn_y$. Unfortunately, the spectral features of the PL from these films was not of sufficient quality to accurately measure the fundamental E_{ind} band gaps and thus obtain valuable insights into the compositional dependence of the ternary electronic structure. In order to improve the light emission from the Sn-rich class of $Ge_{1-x-y}Si_xSn_y$ materials so that E_{ind} energies could be well resolved by PL experiments, the materials were grown on Ge-buffered Si(100) substrates, analogous to the $Ge_{1-y}Sn_y$ samples used to determine y_c value in Chapter II (A).

2. *Growth and Materials Properties of Sn-rich $Ge_{1-x-y}Si_xSn_y$ on Ge/Si(100) Substrates*

Sn-rich ($y > x$) $Ge_{1-x-y}Si_xSn_y$ films were deposited on Ge/Si(100) platforms in a UHV-CVD reactor. The gas mixtures were freshly prepared prior to each experiment using electronic grade Si_4H_{10} (Voltaix Corp.) and custom-developed SnD_4 and Ge_3H_8 reagents produced and purified in house. The desired molar amounts of the compounds were combined in a 3 liter container and diluted with H_2 to a total volume at 30 Torr following previously described recipes using near stoichiometric ratios of the molecular components.[124] In most cases we find that the Sn, Ge and Si fractions in the fabricated samples closely track the corresponding gas-phase atomic concentrations in a given mixture, indicating a high degree of reaction control and deposition efficiency afforded

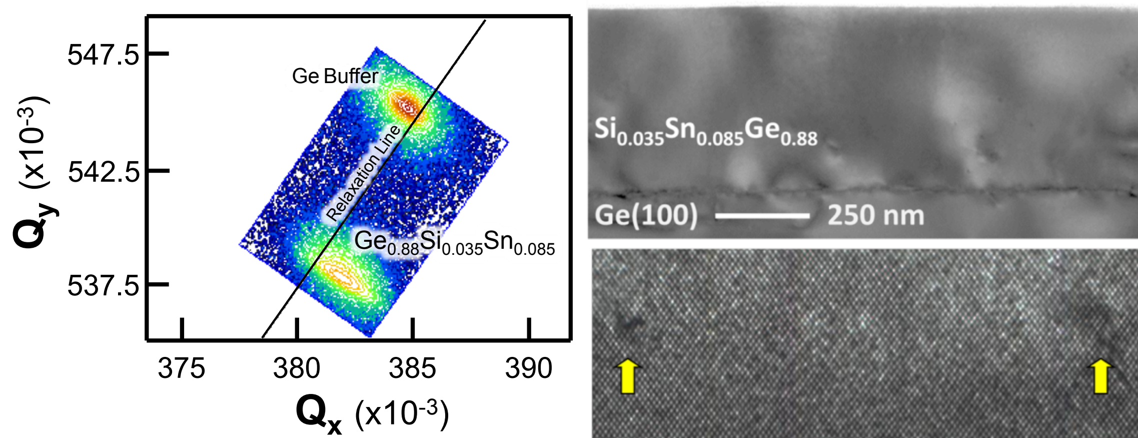

Figure 32: (Left) 224 RSM of a 3.5% Si, 8.5% Sn material grown on a Ge-buffered Si platform showing a high degree of relaxation. (Right) XTEM micrographs of the same material (Right Top) Phase contrast image shows a relatively defective interface region while the upper portion of the layer is mostly devoid of threading defects. (Right Bottom) High resolution image shows sparsely spaced edge dislocations marked by arrows. These are confined to the growth plane and serve to relax the misfit strain between the Ge and GeSiSn layers.

by the compatible reactivity of the Si and Ge precursors. The duration of each experiment was typically 90 minutes, yielding films with thicknesses of 450-550 nm at an average growth rate of ~5- 6 nm/min. The film thicknesses were measured by spectroscopic ellipsometry and corroborated by RBS. The RBS spectra also showed a high degree of channeling indicating good substitutionality of the alloy atoms into the Ge-like lattice. High-resolution XRD measurements of the on-axis (004) peaks and (224) reciprocal space maps were obtained and used to determine the in-plane (a) and vertical (c) lattice dimensions of the films. Using the elasticity model described in section 3 of Chapter II (A), the a and c lattice constants from these measurements were used to determine the relaxed cubic lattice constant of the alloy material (a_0) and the strain. The samples that show strong PL signals have $a_0(Ge_{1-x-y}Si_xSn_y) > a_0(Ge)$, by virtue of incorporating more Sn than Si. For pseudomorphic growth on the Ge buffers, a significant level of compressive epitaxial strain near 1% should be present in these films.

However, we only find compressive strains in the 0.15%-0.55% range, indicating significant relaxation. Samples with $0.05 < y < 0.06$ were annealed at 700-600°C for 10 seconds twice, resulting in a further strain reduction down to 0.025-0.068%, compressive. The annealing temperature was progressively reduced for higher Sn concentrations to maintain the single-phase integrity of the material. At the highest Sn concentrations ($y \sim 0.10$), the annealing was carried out at 500ºC and did not cause any additional strain relaxation.

Alloy compositions were determined by combining the RBS and XRD data. The Sn concentration was obtained from the RBS fits. These fits also yield the Si concentration, but the associated error at the 2 MeV energies the experiments were conducted at is large due to the presence of the Ge-buffer layer background. We then used the X-ray data to obtain the a_0 lattice constants using standard elasticity theory. From these values we derived the Si concentration by assuming the validity of Vegard's law and using the Sn-concentrations from RBS. As expected, the RBS and X-ray methods are in excellent agreement at the highest Si concentrations near $x = 0.07$ for which the RBS method has the smallest error.

The left panel of Figure 32 shows the map of the (224) reflections near the Ge buffer and $Ge_{0.88}Si_{0.035}Sn_{0.085}$ material. Similar to the properties of $Ge_{1-y}Sn_y$ materials grown on these Ge-buffered Si platforms, the alloy film has a residual compressive strain based on its position below the relaxation line. The Ge buffer displays its characteristic slight tensile strain based on its peak position above the relaxation line. High resolution cross-sectional XTEM characterizations revealed highly uniform layers exhibiting flat surface profiles, as well as distinct interfaces with the underlying buffer, as shown in the

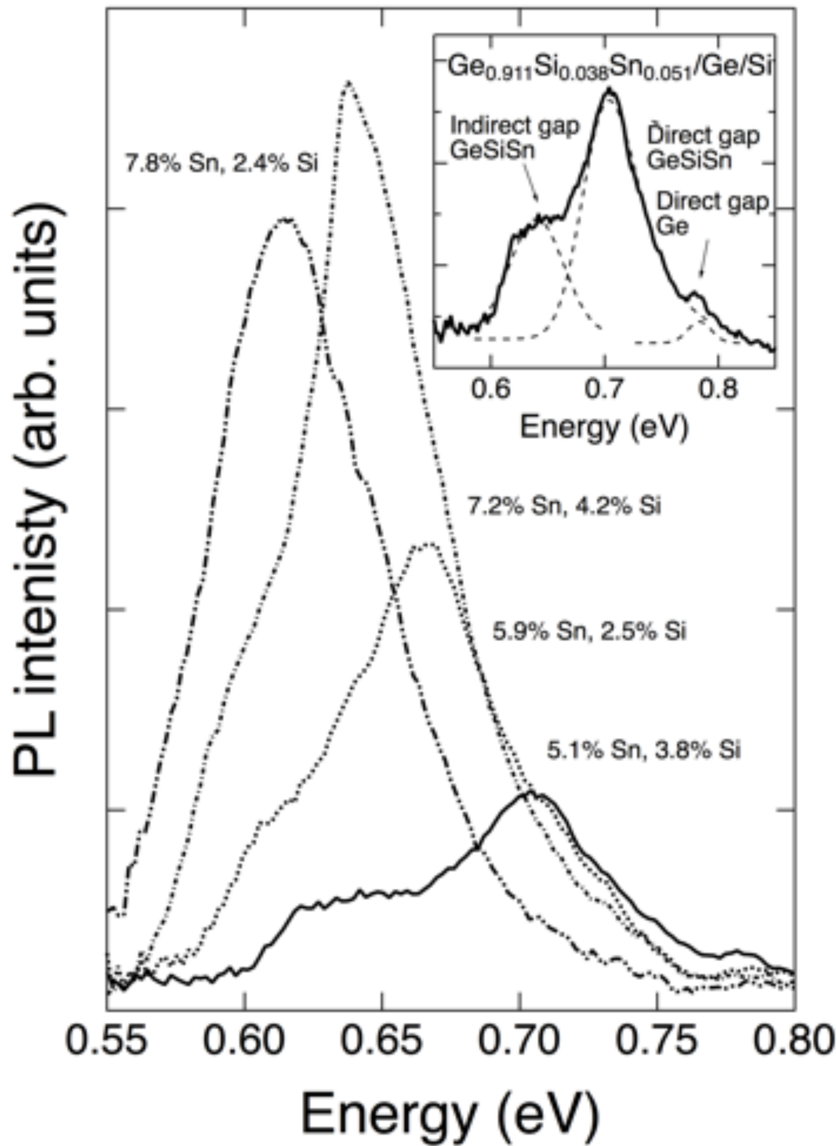

Figure 33: PL spectra from selected $Ge_{1-x-y}Si_xSn_y$/Ge/Si samples, excited with 980 nm radiation. The main peak corresponds to direct-gap transitions, and the low-energy shoulder is assigned to the Ge-like indirect gap. The inset illustrates the fit procedure to extract the band gap values. The direct gap transitions are fitted with an EMG function, whereas the indirect gap contribution is fit with a simple Gaussian. A weak high-energy peak corresponding to direct-gap emission from the Ge buffer layer is also fit with a Gaussian.

right panel of Figure 32 for the same 500 nm $Ge_{0.88}Si_{0.035}Sn_{0.085}$ film in the left panel. The bulk film above the interface possesses a low defect density microstructure, as indicated by the homogeneous phase contrast in the micrograph. The high-resolution

images show 60° dislocations at the interface rather than the Lomer defects found in films grown directly on Si surfaces. The images also show occasional stacking faults originating near the alloy/buffer heterojunction and terminating slightly above the growth plane of the film. The observed interface microstructure in these samples is consistent with AFM images of the film surface which reveal cross hatched patterns aligned along the (110) crystallographic direction, as typically observed for similarly mismatched $Ge_{1-x}Si_x$ films grown on Si wafers.

3. Optical Properties of Sn-rich $Ge_{1-x-y}Si_xSn_y$ Materials on Ge/Si(100) Substrates

Photoluminescence (PL) experiments were carried out with the samples held at room temperature as described in section 3 of Chapter II (A).

Figure 33 shows selected spectra from a few samples, illustrating the main qualitative features of the $Ge_{1-x-y}Si_xSn_y$/Ge photoluminescence. We observe a main peak and a clear weaker feature on the low-energy side. Based on the similarity between these spectra and those obtained from Ge-on-Si and $Ge_{1-y}Sn_y$ films on Si, we assign the main peak to direct-gap transitions and the weaker peak to indirect gap transitions from the L minimum of the conduction band. The spectra show that as the Sn- and Si-concentrations are changed in such a way that the direct gap decreases in energy, the separation between the direct and indirect gaps decreases and the photoluminescence intensity increases. This is consistent with the electronic structure of Ge-like materials, where a reduced separation between the direct and indirect edges (either due to the application of tensile strain or as a result of alloying with Sn) increases the thermal population of the Γ-valley associated with the direct gap, leading to an enhanced PL signal.[68,74,153,169]

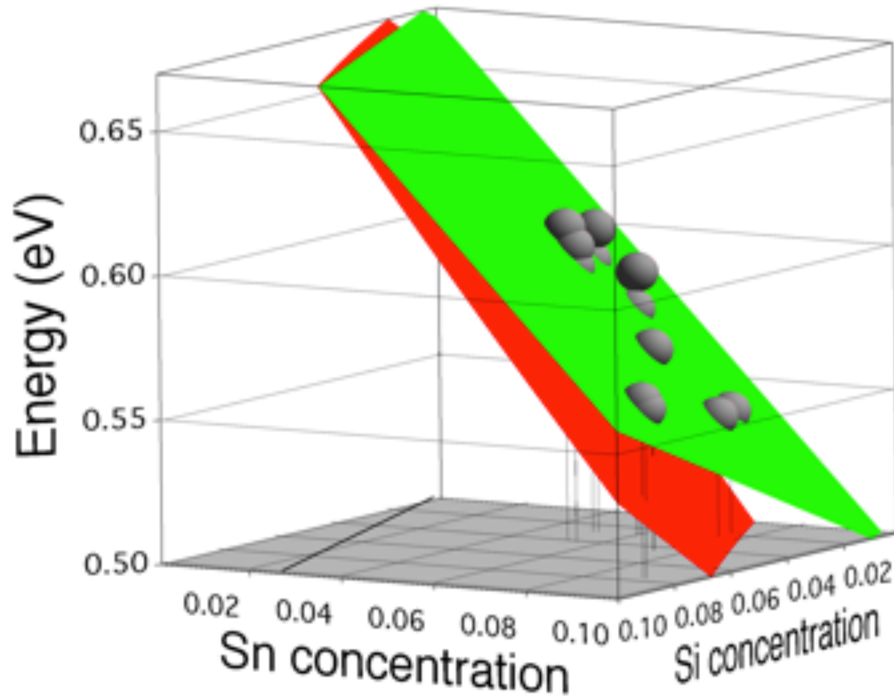

Figure 34: Compositional dependence of the measured E_{ind} energies in $Ge_{1-x-y}Si_xSn_y$ alloys, obtained from fits of the photoluminescence experiments. The grey spheres represent the experimental data points, the green plane is the linear fit in Eq. (3.1) and the red plane was calculated with theoretical bowing parameters from Ref. 172. The line in the coordinate plane corresponds to lattice-matching with Ge.

The inset in Figure 33 shows details of the spectral analysis for the case of a $Ge_{0.911}Si_{0.038}Sn_{0.051}$ film. The direct-gap emission is modeled with a four-parameter exponentially modified Gauss (EMG) function,[170] which reproduces the expected asymmetry of this line. The indirect emission in Ge-like materials is the result of at least three contributions associated with absorption-emission of LA phonons plus a zero-phonon line,[171] but the spectral resolution, alloy broadening, and temperature broadening make the resulting lineshape undistinguishable from a three-parameter Gauss function. Finally, we note that there is a weak additional peak just below 0.8 eV. This peak is assigned to direct-gap emission from the underlying Ge buffer layer, and it is modeled as a Gaussian.

In the case of the direct gap, we obtain its energy E_0 by fitting the EMG function with a theoretical expression based on the van Roosbroeck-Shockley theory for spontaneous emission, as described in Ref. 124. For the indirect gap energy E_{ind}, we performed PL measurements on a thick (> 1 μm) Ge-on-Si layer. Here the indirect gap emission peaks at 0.687 eV after a strain correction. The corresponding band gap, however, is expected to be E_{ind} = 0.655 eV (including the effect of laser heating, estimated to be about 20ºC). The resulting shift Δ_{Ge} = (0.687-0.655) eV = 0.032 eV is assumed to be independent of composition and subtracted from the peak energies of the Gaussian fits to obtain the indirect gap energies for the alloys. In all cases, a strain correction is computed using the measured strain from XRD and published deformation potentials.[119]

Figure 34 shows the resulting indirect band gaps as a function of the Si and Ge concentrations in the samples. It is important to point out that for some samples the peaks associated with the indirect and direct transitions are too close for the fit to be reliable. In these samples, we were only able to obtain the direct gap energies E_0. The results for the samples that allowed a reliable determination of E_{ind} were fit with a bilinear expression, yielding (in eV):

$$E_{\mathrm{ind}} = \left(0.665 \pm 0.042\right) + \left(0.65 \pm 0.12\right)x - \left(1.75 \pm 0.12\right)y\,, \tag{3.1}$$

The fit expression appears as a green-colored plane in Figure 34 while the red plane plots the values of E_{ind} based on theoretical bowing parameters for this transition in $Ge_{1-x-y}Si_xSn_y$ alloys from Ref 172. We see fairly good agreement between the bowing

parameter model (red plane) and the bilinear fit to the experimental data (green plane). The resulting expression of a bilinear fit to the E_0 data gives (in eV):

$$E_0 = (0.790 \pm 0.011) + (2.27 \pm 0.10)x - (3.83 \pm 0.14)y, \quad (3.2)$$

which overlaps, within experimental error, with the expression proposed in Ref. 124. If one plots these bilinear E_0 and E_{ind} fit planes it is clear there is a closing of the separation between the Γ and L valleys in the conduction band of the ternary alloy, qualitatively similar to that observed in binary $Ge_{1-y}Sn_y$ alloys. The direct-indirect gap boundary is along the line $y = (0.066 \pm 0.026) + (0.78 \pm 0.14)\, x$ according to these fits, which is just within agreement of the $y_c = 0.087$ value found in the previous chapter for $Ge_{1-y}Sn_y$ if extrapolated to $x = 0$.

If the direct and indirect edges were truly linear functions of composition, the linear coefficients should be given by the difference of the corresponding energy eigenvalues in Si, Ge, and α-Sn. From an inspection of the band structures, the predicted dependencies at room temperature for the fundamental gaps are (in eV):

$$E_{ind} = 0.664 + 1.27x - 0.52y, \quad (3.3a)$$

$$E_0 = 0.806 + 3.29x - 1.21y, \quad (3.3b)$$

Comparison with Eqs. (3.1) and (3.2) reveals a systematic deviation between this theoretical prediction and the experimental results. Here we find that the linear coefficients related to the Si-dependence are smaller than predicted while the ones corresponding to the Sn-dependence are larger in magnitude in Eqs. (3.3a) and (3.3b). This provides evidence for a large negative bowing in the compositional dependence of band gap energies in alloy semiconductors containing Sn. Earlier ellipsometric studies

demonstrated the existence of such bowing for the direct gap E_0, (Ref. 173) the findings here confirm that the same phenomenon is observable for the indirect gap as well.

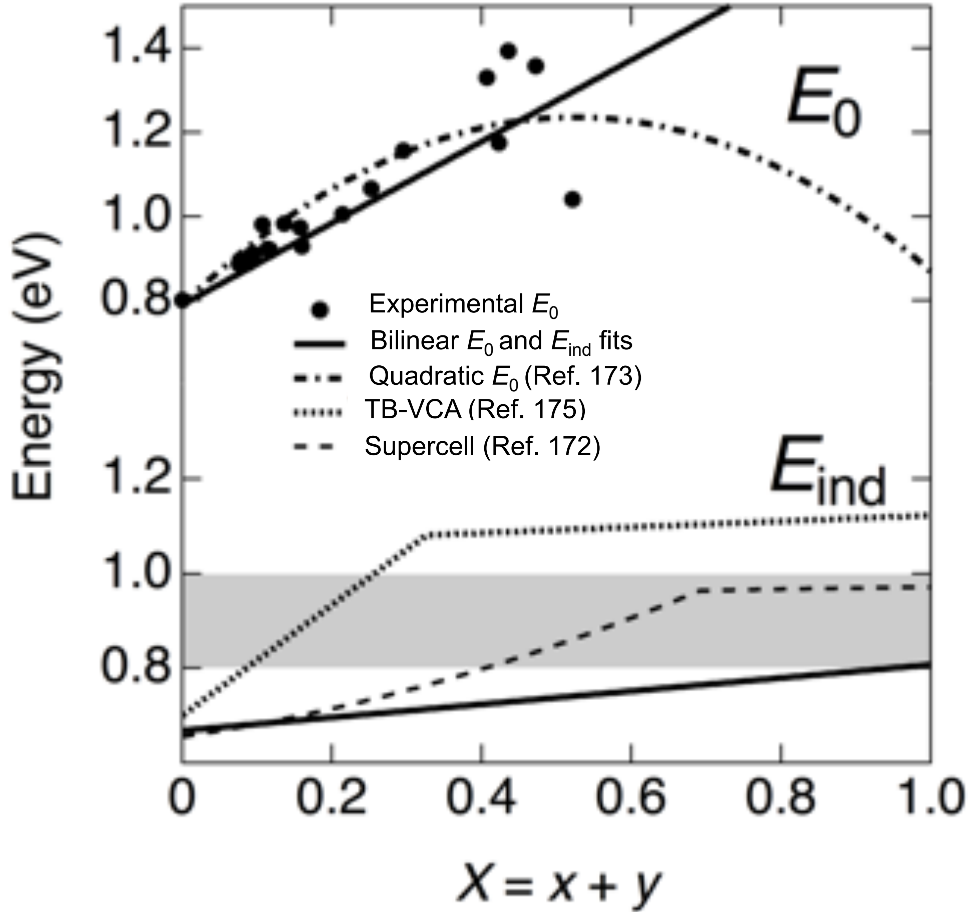

Figure 35: Compositional dependencies of the direct E_0 and indirect gaps in $Ge_{1-X}(Si_{0.79}Sn_{0.21})_X$ alloys lattice-matched to Ge. Circles represent experimental points from Refs. 153 and 174. The solid lines are the fits from Eqs. (3.1) and (3.2) computed for the lattice-matching case. The curved dashed-dotted line is the quadratic fit of E_0 from Ref. 173. The dotted line is the TB-VCA calculation of Ventura *et al*. (Ref. 175), and the dashed line is the empirical pseudopotential supercell result from Ref. 172. The discontinuous slope change in both calculations corresponds to the change from Ge-like to Si-like in the nature of the fundamental band gap. The grey area highlights the band gaps region of interest for photovoltaic applications.

The above considerations suggests that particular care should be exercised in extrapolating our measured indirect gap to an extended compositional range—especially at the $x = 3.7y$ Ge-lattice matching line of interest for photovoltaics—since we know that a bilinear expression cannot be valid over the entire compositional space. To investigate

this in more detail, we show in Figure 35 experimental and theoretical band gap data for lattice-matched $Ge_{1-X}(Si_{0.79}Sn_{21})_X$ alloys. The solid lines in Figure 35 are extrapolations of Equations (3.1) and (3.2). Of interest for our analysis is the fact that Eq. (3.2) does provide a reasonably good account of the E_0 gap data from Refs. 153 and 174, comparable to the more sophisticated quadratic fit from Ref. 173, which takes into account bowing effects. As indicated above, the linear fit cannot be valid over the entire compositional range, and we see large deviations for $X > 0.5$, but this is beyond the range of available experimental data.

If we assume that the linear fit of the indirect gap is also valid for $X < 0.5$, as in the case of the direct gap, the solid line in Figure 35 suggest that E_{ind} in this range does not exceed 0.75 eV, which may not be high enough for photovoltaic applications. On the other hand, it is instructive to compare the indirect gap data with theoretical predictions. The dotted line in Figure 35 corresponds to the calculations by Ventura and co-workers within the virtual crystal approximation (VCA).[175] The predicted indirect gap is close to a simple linear interpolation as in Eq. (3.3a), as expected for the VCA. The dashed line is computed using a quadratic expression that uses experimental band gaps for Ge, Si, and α-Sn combined with theoretical bowing parameters from Ref. 172. These bowing parameters were extracted from supercell calculations based on the empirical pseudopotential method. The same expression corresponds to the red surface in Figure 34, and we see that it underestimates somewhat the experimental indirect gaps. When applied to alloys lattice matched to Ge, on the other hand, the expression gives a higher value of E_{ind} than the linear extrapolation from Eq. (3.1) reaching values in desired photovoltaic range for $X > 0.4$. Direct measurements of the indirect gap for samples

lattice-matched to Ge will be needed to determine whether the linear extrapolation from Eq. (3.1) or the theoretical prediction from Ref. 172 is closer to the experimental band gap.

4. Conclusion

In conclusion, the optical properties of Sn-rich $Ge_{1-x-y}Si_xSn_y$ alloys have been investigated by room temperature PL. Spectra of samples grown on Ge-buffered Si substrates revealed clear electronic transitions between Ge-like direct and indirect band gaps. This enabled measurement the fundamental band gap E_{ind} of these materials from the PL data. The compositional dependence of the E_{ind} transition reveals that a significant negative bowing parameter affects the band gap, similar to that found earlier for the direct gap in the Ge lattice-matched composition region. This bowing must be taken into account for the design of future photonic $Ge_{1-x-y}Si_xSn_y$ devices, including solar cells.

B. Optical and Electronic Properties of Sn-Rich $Ge_{1-x-y}Si_xSn_y$ *pin* Diodes

1. Introduction

Lasing was reported very recently from optically pumped $Ge_{1-y}Sn_y$ waveguide devices, making the material a propitious light source candidate for integration of Si-based electronics with optical components.[110] The ultimate goal of this research is the fabrication of electrically pumped lasers, for which an essential prelude is the demonstration of highly efficient light emitting diodes (LEDs). As discussed in Chapter II, several examples of $Ge_{1-y}Sn_y$ LEDs have been demonstrated by various research groups.[164,165,166] These devices adopt a conventional heterostructure diode design in which the active regions are grown on Ge buffer layers and capped with pure Ge. A major issue with these designs is non-radiative recombination caused by the defected

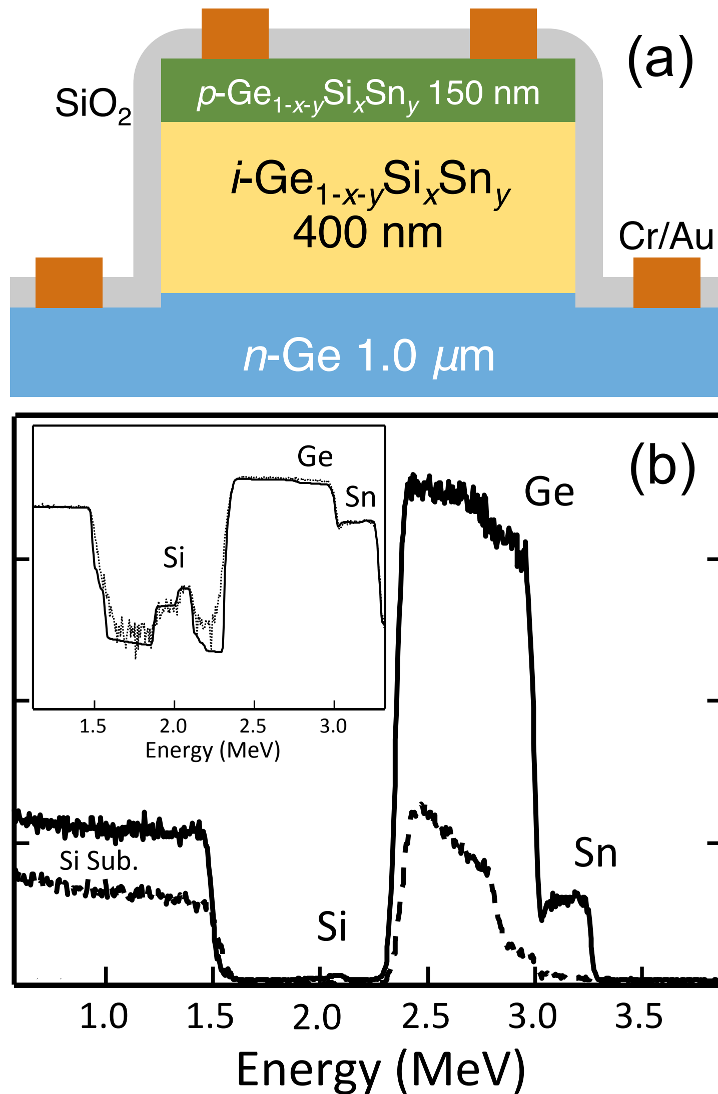

Figure 36: (a) Schematic representation of devices with *p*-$Ge_{1-x-y}Si_xSn_y$ capping layers. (b) 3.8 MeV RBS spectra of a 7% Sn, 3% Si device. The random spectrum is plotted by a solid line and shows Sn, Ge and Si signals from the various layers in the stack. Inset is a logarithmic view of the Si peaks from the top *i,p*-layers. The aligned spectrum is plotted by a dotted line and demonstrates a high level of channeling across the stack. Sample produced by Charutha Senaratne and Chi Xu. See J. D. Gallagher, C. Xu, C. L. Senaratne, T. Aoki, P. M. Wallace, J. Kouvetakis, and J. Menéndez, *Journal of Applied Physics*, 118, 135701 (2015).

interfaces between $Ge_{1-y}Sn_y$ and Ge, which for direct gap conditions ($y > 0.09$) have equilibrium critical thicknesses below 10 nm, and therefore are strain-relaxed in most practical devices.[131] Strain-management strategies were introduced in the last chapter,

consisting of replacing the pure-Ge contact layers with $Ge_{1-x}Sn_x$ alloys whose Sn concentrations satisfy $x < y$ to ensure carrier confinement and promote light extraction, while keeping the difference $y - x$ small enough to prevent the generation of misfit dislocations.[176,177] These devices exhibit strong tunable emission peaks and offer promise that judicious lattice engineering of the layer assembly could lead to the creation of enhanced performance devices for applications in near-IR photonic technologies.

Even though the strain relaxation issues appear to be manageable in the $Ge_{1-y}Sn_y$ system, a potential additional problem in the direct gap regime ($y > 0.09$) is the low thermal stability associated with high Sn contents. These alloys are metastable and at high temperatures they tend to decompose via Sn segregation and phase precipitation, compromising device functionality and structural integrity.[127,178] A thermally robust alternative to $Ge_{1-y}Sn_y$ is the $Ge_{1-x-y}Si_xSn_y$ ternary analog, with enhanced stability due to the increased mixing entropy associated with Si incorporation in the lattice for the same concentration of Sn.[179] In the previous section of this chapter the PL study found that ternary $Ge_{1-x-y}Si_xSn_y$ alloys also undergo an indirect to direct gap transition in the $y > x$ region of the compositional space.[180] This data was obtained from samples that contained a fixed amount of Si at ~ 4% and a progressively increasing amount of Sn in the 3-9% range. Growing the materials on a Ge-buffered Si platform enabled these materials to exhibit strong PL that allowed the determination of their direct and indirect band gaps. The separation of the gaps was found to systematically decrease as a function of y relative to Ge, replicating the basic features of the $Ge_{1-y}Sn_y$ electronic structure, including the indirect to direct gap crossover as required for potential laser materials.

The above considerations suggest that Sn-rich $Ge_{1-x-y}Si_xSn_y$ alloys could be suitable candidate materials for the creation of thermally robust alternatives to $Ge_{1-y}Sn_y$ light sources for operations requiring high temperature conditions. This section discusses the electrical and electroluminescent (EL) properties of $Ge_{1-x-y}Si_xSn_y$ photodiodes with x = 0.02-0.09 and y = 0.03-0.11.

2. *Growth and Materials Properties of Sn-rich $Ge_{1-x-y}Si_xSn_y$ pin Devices on n-Ge/Si(100) Substrates*

The $Ge_{1-x-y}Si_xSn_y$ devices were fabricated in a heterostructure *pin* geometry [*n*-Ge/*i*-$Ge_{1-x-y}Si_xSn_y$/*p*-Ge(Sn/Si)] in which the intrinsic layer is surrounded by a Ge bottom contact doped *n*-type and a *p*-type capping layer containing small amounts of Sn and Si (in some cases). The Si/Sn amounts were selected to (a) maintain a larger band gap in the top layer relative to the underlying *i*-$Ge_{1-x-y}Si_xSn_y$ to maximize the external quantum efficiency, and to (b) mitigate the lattice mismatch so that the top interface grows fully strained and defect-free. These devices possess only one defected interface between the *n*-Ge buffer and the relaxed *i*-$Ge_{1-x-y}Si_xSn_y$ epilayer, thereby reducing the deleterious effects of mismatch induced dislocations on the optical and electrical properties. The Si content of the *i*-$Ge_{1-x-y}Si_xSn_y$ layer is maintained between 2 and 3%, which is considered sufficient to impart the desired thermal stability in the alloy,[63] while the Sn content was varied from ~ 3.3% to 11.1%.

The devices were produced in two stages using separate reactors. The *n*-type Ge buffers are grown on 4” Si(100) wafers with ~ 1 μm thicknesses via deposition of Ge_4H_{10} at 350°C using a gas source molecular epitaxy chamber.[61] The single-source $P(GeH_3)_3$ was used to dope the material with P atoms at levels of 2×10^{19} cm^{-3}. The resultant layers

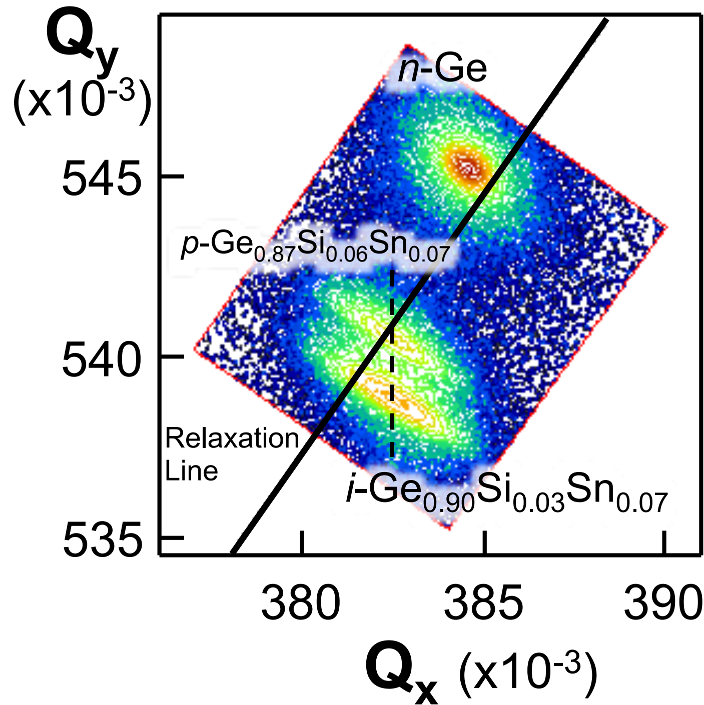

Figure 37: (224) reciprocal space map of a *n*-Ge/*i*-$Ge_{0.90}Si_{0.03}Sn_{0.07}$/*p*-$Ge_{0.87}Si_{0.06}Sn_{0.07}$ device showing that the intrinsic and *p*-layers are fully lattice matched within the plane of growth. Sample produced by Charutha Senaratne and Chi Xu. See J. D. Gallagher, C. Xu, C. L. Senaratne, T. Aoki, P. M. Wallace, J. Kouvetakis, and J. Menéndez, *Journal of Applied Physics*, 118, 135701 (2015).

were subjected to post-growth annealing at 650°C for 3 minutes *in situ* on the wafer stage to reduce the threading dislocations. Thereafter intrinsic epilayers with compositions x = 0.02-0.03 and y = 0.035-0.08 were grown *in situ* on the Ge buffer layers at pressures of 1×10^{-4} Torr. The 3.3-5.2% Sn samples were produced at 260°C, while the 7-8% Sn counterparts were produced at a lower temperature of 240°C to ensure full Sn substitution. The depositions utilized nearly stoichiometric mixtures of Ge_4H_{10}, Si_4H_{10}, and SnD_4 yielding materials with atomic content closely reflecting those of the gas mixtures.[181] For samples containing higher Sn contents an alternative set of reactants (Si_4H_{10}, Ge_3H_8, and SnD_4) and a separate UHV-CVD reactor was employed. This

arrangement produced highly concentrated materials (y = 0.09-0.11) at enhanced growth rates due to the higher temperatures (300°C) and pressures (0.200 Torr) allowed by the reactor geometry.[124]

All samples were characterized for quality control using RBS, XRD and spectroscopic ellipsometry. The 2.0 MeV RBS spectra showed strong Sn and Ge peaks, which were fitted to give 3.3-11.1% Sn content. The fits yielded 300-800 nm thicknesses depending on the Sn content. Analysis for silicon was conducted at 3.8 MeV in order to resolve the Si signal from the dominant Ge background. All samples revealed distinct Si peaks which were fitted to yield concentrations between 2 and 3%. The RBS Si content was corroborated by XRD using the measured lattice constants (a_0) in conjunction with Vegard's law, indicating excellent agreement between the two techniques. The RBS channeled spectra were also collected showing good substitution of the alloys on tetrahedral sites epitaxially aligned to the Si wafer. The XRD data revealed that in all cases the epilayers are mono-crystalline single phase crystals. Ellipsometry corroborated the RBS thicknesses and provided estimates of the *n*-Ge layer doping density.

The samples were subsequently loaded into a separate low pressure CVD reactor that was configured for *p*-type doping using diborane (B_2H_6) to grow the top electrodes. The wafers were initially dipped in aqueous HF to remove the surface oxide and then cleaned again inside the reactor by flowing Ge_2H_6 for 5 minutes to produce an epi-ready surface. Reaction mixtures combining appropriate concentrations of Ge_2H_6 and SnD_4 were used in most experiments, while the B_2H_6 dopant was delivered separately to avoid side reactions with SnD_4 before reaching the reaction zone. For devices with Sn contents 3.3-5.2%, the top electrode was chosen to be a dilute $Ge_{1-y}Sn_y$ alloy containing up to ~

1% Sn. This material was grown pseudomorphically to the intrinsic layers at 340°C and exhibited an average thickness of 150-200 nm and a *p*-carrier density of 2-5×10^{19} cm^{-3}. We emphasize that the amounts of Sn in the capping layers are lower than in the active layers in order to maximize quantum efficiencies. As a consequence the structures are tensile strained and exhibit defect free interfaces. For the 7-11% Sn devices the top layer was selected to be a $Ge_{1-x-y}Si_xSn_y$ alloy (rather than $Ge_{1-y}Sn_y$) with more closely matched stoichiometry to the intrinsic layer such as ~ 6-9% Sn and ~ 4-6 % Si. The higher/lower Si/Sn content in a given sample was intended to induce a larger gap in the *p*-layer. The latter was grown at 320°C using Ge_2H_6, Si_4H_{10}, SnD_4 and B_2H_6, and exhibited thicknesses of ~ 150 nm and carrier densities of 1-9×10^{19} cm^{-3}. Contrary to the above *i*-$Ge_{1-x-y}Si_xSn_y$/*p*-$Ge_{1-y}Sn_y$ devices, this design depicted in Figure 36 (a) comprises exclusively $Ge_{1-x-y}Si_xSn_y$ *i-p* stacks that can be engineered to achieve the lowest mismatch strain in the upper interface while ensuring carrier confinement in the active layer.

The completed as-grown devices were subjected to further RBS, XRD and ellipsometry characterizations to determine composition, doping and crystallinity. The results revealed that the elemental content and carrier densities of *n*-Ge and *i*-$Ge_{1-x-y}Si_xSn_y$ are essentially identical to their original values prior to growth of the top electrode, indicating that the final growth step does not affect the initial materials properties. RBS spectra acquired at 3.8 MeV proved particularly useful for measuring the Si compositions of the top layers. Figure 36 (b) shows representative 3.8 MeV RBS plots for a *n*-Ge/*i*-$Ge_{0.90}Si_{0.03}Sn_{0.07}$/*p*-$Ge_{0.87}Si_{0.06}Sn_{0.07}$ device. A weak Si signal appears slightly above the baseline on the left side of the main Ge peak. This feature is attributed to combined contributions of the Si content from the intrinsic and top *p*-layers. A

logarithmic view (inset) of the spectra shows two clearly resolved Si peaks indicating 3% and 6% Si contents, respectively, in excellent agreement with XRD measurements. The RBS channeled spectrum was also recorded demonstrating that the layers combine seamlessly to form a contiguous *n*-*i*-*p* stack highly aligned in the direction of the substrate. High resolution XRD provided strain states and lattice constants allowing correlation of the optoelectronic properties as a function of the active layer composition. Figure 37 illustrates a (224) reciprocal space maps of the *n*-Ge/*i*-$Ge_{0.90}Si_{0.03}Sn_{0.07}$/*p*-$Ge_{0.87}Si_{0.06}Sn_{0.07}$ device stack. The *n*-Ge peak lies slightly above the relaxation line, indicating that the material is tensile strained. The corresponding strain value is 0.143%. The *i*-$Ge_{0.90}Si_{0.03}Sn_{0.07}$ layer exhibits a residual compressive strain of -0.22% on the Ge buffer. The top *p*-$Ge_{0.87}Si_{0.06}Sn_{0.07}$ layer is fully lattice-matched to the *i*-$Ge_{0.90}Si_{0.03}Sn_{0.07}$ material in the horizontal direction as shown by the close alignment of the (224) peaks along the pseudomorphic direction. This layer is found to be fortuitously

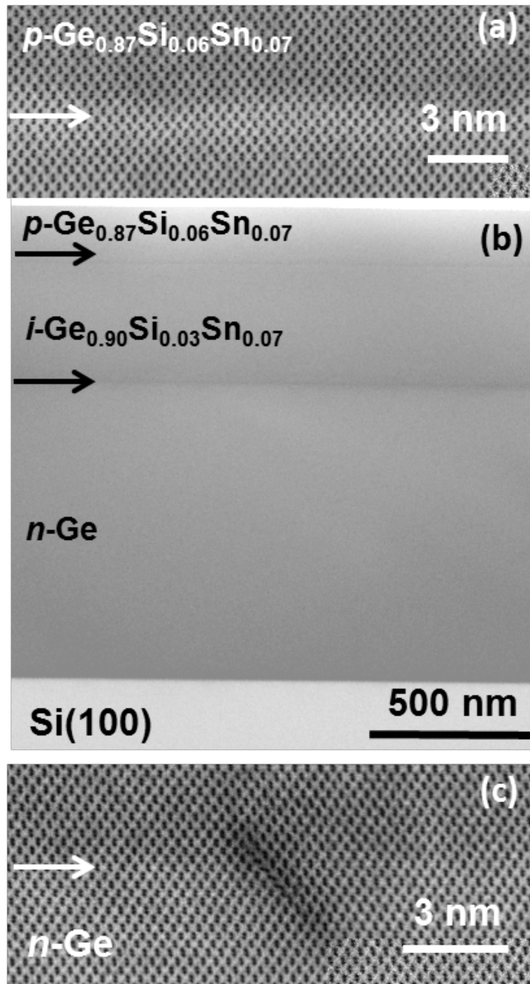

Figure 38: XSTEM images of the *n*-Ge/*i*-$Ge_{0.90}Si_{0.03}Sn_{0.07}$/*p*-$Ge_{0.87}Si_{0.06}Sn_{0.07}$ device structure. Panels (a) and (c) show atomic resolution images of the *i-p* and *n-i* interfaces, respectively. Panel (b) shows a low-magnification view of the entire device, including the Si substrate. Arrows mark the location of the various interfaces. Sample produced by Charutha Senaratne and Chi Xu. See J. D. Gallagher, C. Xu, C. L. Senaratne, T. Aoki, P. M. Wallace, J. Kouvetakis, and J. Menéndez, *Journal of Applied Physics*, 118, 135701 (2015).

relaxed with respect to bulk Si since the in-plane lattice parameter of the residually strained *i*-layer is 5.6961 Å, which is ~ 0.04% less than the relaxed cubic value of 5.6986 Å for the *p*-layer.

Cross-sectional scanning transmission electron microscopy (XSTEM) was next employed to corroborate the full commensuration of the top layers and investigate the bulk microstructure. The XSTEM data were collected on a STEM-corrected JEOL-ARM200F and representative images of a complete *p*-$Ge_{0.87}Si_{0.06}Sn_{0.07}$/*i*-$Ge_{0.90}Si_{0.03}Sn_{0.07}$/*n*-Ge/Si(100) LED structure are shown in Figure 38. The atomic-resolution images in panels (a) and (c) show details of the top *i-p* and bottom *n-i* interfaces, respectively. The top interface is defect-free, as expected due to the close lattice matching between the adjoining layers. The bottom interface with the Ge buffer is highly defected due to significant relaxation of the misfit strain. The typical microstructure encompasses short stacking faults which appear as dark contrast areas extending down into the Ge layer along the (111) planes. Edge dislocations and dislocations loops are also present (not shown) within the plane of growth, but no dislocation cores seem to propagate upward into the active region. Panel (b) in Figure 38 shows a low-magnification view of the entire device stack illustrating the location of the various layers and their interfaces marked by arrows. The free surface is flat and the bulk device structure above the Ge interface is largely devoid of threading defects within the field of view of the image. The typical microstructure seen in Figure 38 was further corroborated using a JEOL-4000 EX microscope operated at 400 kV, which also showed highly defective bottom interfaces and sparsely defective active regions. The absence of threading defects in the bulk devices represents a significant design advantage; however,

the high density of misfit induced dislocations at the bottom interface is unavoidable and likely to lead to non-radiative recombination and thereby degrade the device efficiency. The samples were then processed into circular mesa devices as described in section 2 of Chapter II (B).

3. *Optical and Electronic Properties of Sn-Rich $Ge_{1-x-y}Si_xSn_y$ pin Devices on n-Ge/Si(100) Substrates*

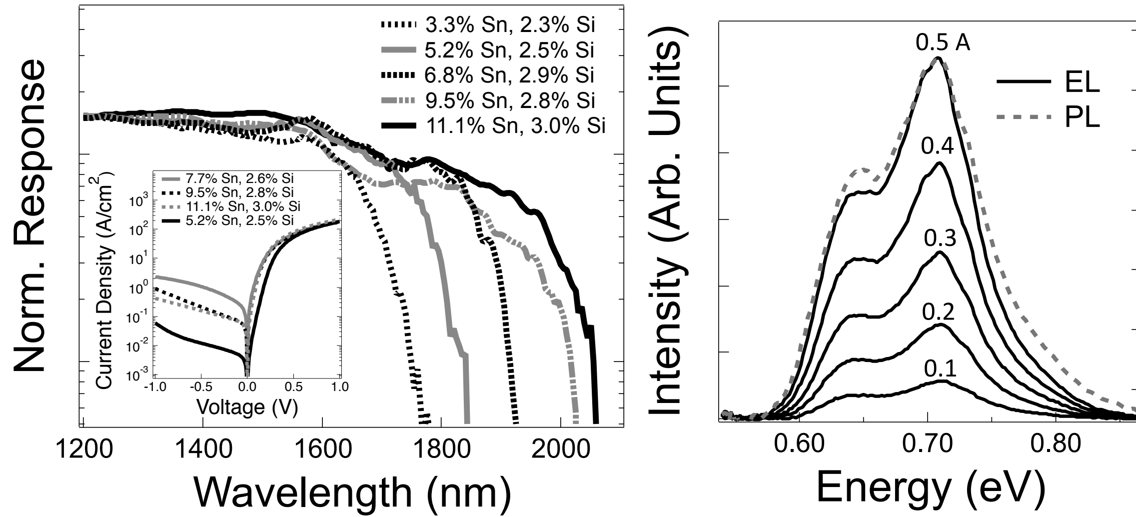

Figure 39: (Left) Normalized absorption spectra of devices with Sn content spanning 3.3-11.1%, demonstrating tunability in the absorption edge from 1775 to 2060 nm. Inset shows typical *IV* characteristics over the full composition range of devices used in this study. (Right) EL vs excitation current for a $Ge_{0.94}Si_{0.02}Sn_{0.04}$ device showing a super-linear increase in peak intensity. Overlay of PL and EL shows excellent agreement between the two techniques.

Spectral responsivity experiments were carried out in unbiased diodes under illumination from monochromatized light generated by a tungsten-halogen lamp. The light was transferred along a fiber optic cable with an optical bridge and chopper assembly to provide modulation for lock-in detection of the photogenerated current. The left panel of Figure 39 compares spectral responsivity plots for representative samples containing a common Si fraction $x \sim 0.03$ and varying amounts of Sn ranging from $y = 0.033$ to 0.111. The plots are normalized to account for thickness variations among the

active layers. A systematic red shift of the absorption edge is observed from 1775 nm for $y = 0.033$ to 2060 nm at $y = 0.111$ as the Sn fraction is increased. The results demonstrate the capability of Sn-rich ternaries to extend the optoelectronic properties of Ge into the mid IR through compositional tuning of their absorption edge to cover all telecom bands, as previously observed for binary $Ge_{1-y}Sn_y$ analogs.[101] The inset of Figure 39 left panel shows *I-V* curves from various devices. The curves show typical rectifying diode behavior in this family of samples. The large current at forward bias points to low series resistances with diode ideality factors between 1.20-1.40. The reverse bias dark current density values span a range of 60 mA/cm^2 to 2.5 A/cm^2 at -1V for the 5.2% and 7.7% Sn devices, respectively. Increasing reverse-bias currents as a function of Sn concentration have been observed in $Ge_{1-y}Sn_y$ devices.[176] In the current $Ge_{1-x-y}Si_xSn_y$ devices there is a large variability in dark currents, as evidenced by the lower current density of the 11.1% Sn sample relative to the 7.7% and 9.5% Sn devices. This is probably due to the difficult-to-control defects at the *n*-Ge/*i*-$Ge_{1-x-y}Si_xSn_y$ interface, which could be eliminated in future optimizations by introducing an additional $Ge_{1-x-y}Si_xSn_y$ layer as the *n*-component of the diode stack.

The EL measurements were carried out as described in section 4 of Chapter II (B). The right panel of Figure 39 displays representative EL results for a $Ge_{0.94}Si_{0.02}Sn_{0.04}$ device. The current dependence of the EL peaks is depicted by solid black lines. The peak intensities increase super-linearly with injection current from 0.1-0.5 A while their emission energies remain essentially unchanged. This panel also shows an overlay between the normalized PL spectrum of the device structure (dashed line) with the EL counterpart indicating close correspondence of direct and indirect gap energies between

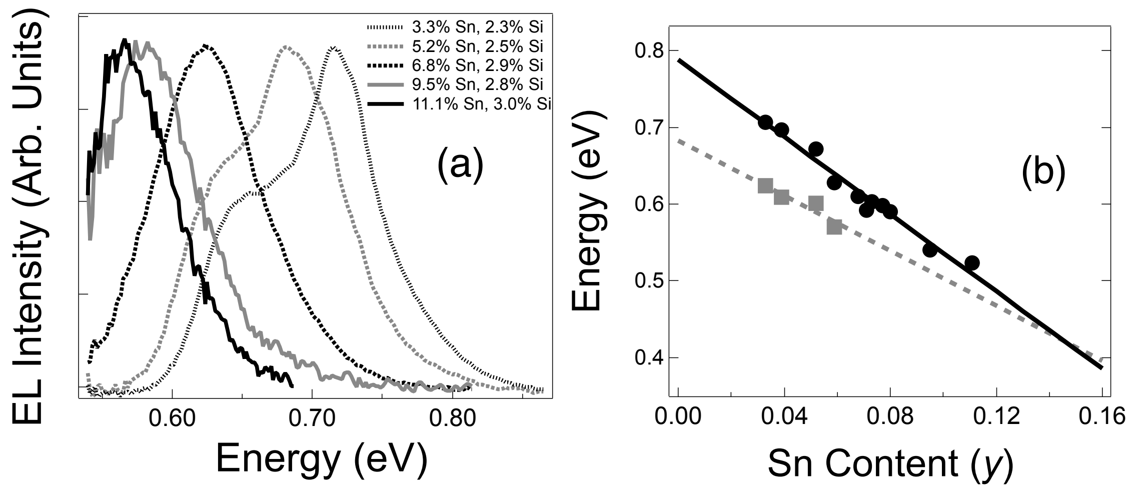

Figure 40: (a) Normalized EL spectra of devices with 3.3-11.1% Sn contents showing a redshift of E_0 and E_{ind} peaks with increasing Sn content. Overlap of the peaks is observed for $y \geq 0.07$ devices. (b) E_0 (dots) and E_{ind} (squares) extracted from the EL spectra in (a). The intersection of the solid and dashed lines suggests the crossover to direct gap alloys.

the two techniques. Finally we note that the excess intensity in the PL spectrum near 0.80 eV can be assigned to a contribution from the adjoining *n*-Ge and *p*-$Ge_{0.99}Sn_{0.01}$ layers. This effect is not present in the EL spectra, confirming that the signal in this case is predominately generated from the *i*-$Ge_{1-x-y}Si_xSn_y$ region. Similar EL/PL relationships were observed for all samples fabricated in this study including the super-linear dependence of the emission vs current.

Figure 40 (a) plots representative EL spectra from samples covering the composition range. For the 3.3% and 5.2% Sn samples the plots show strong peaks due to direct gap (E_0) emission and lower intensity shoulders at lower energies due to indirect gap (E_{ind}) transitions. Both features shift to longer wavelengths and their separation becomes smaller with increasing Sn content. This can be interpreted as the Γ-point of the Ge-like band structure falling faster than the L-point at a given Sn content in analogy with $Ge_{1-y}Sn_y$ binaries containing similar amounts of Sn. For samples with Sn contents 7% and above the plots show that these features (E_0, E_{ind}) merge into a single broad peak

suggesting that the Sn concentration approaches toward the range where the materials become direct gap semiconductors. The band gap energies are extracted from the EL spectra by fitting with EMG functions for E_0 and simple Gaussians for E_{ind} as discussed in previous chapters and sections. The energies are plotted as a function Sn of composition in Figure 40 (b). The E_0 values in the plots are shown as black circles and the E_{ind} as grey squares. The black and grey lines are empirical linear fits to the E_0 and E_{ind} data sets, respectively. The lines intersect at $y = 0.145$, which represents the transition point where the $Ge_{0.97-y}Si_{0.03}Sn_y$ materials used in this study are expected to become direct gap semiconductors. If we apply the bilinear fits from the PL data in the last section of this chapter, we predict that the cross over point for our EL devices should be at 10.5% Sn, which is significantly lower than the aforementioned 14.5% value. The significant disagreement between these two crossover compositions is a further indication that bowing effects need to be considered to give an accurate description of the compositional dependence of the fundamental E_0 and E_{ind} in $Ge_{1-x-y}Si_xSn_y$ materials. Lastly, the 14.5% Sn crossover is much higher than the 9% Sn transition point determined for $Ge_{1-y}Sn_y$ alloys in Chapter II, indicating that the effect of Si on the band gap energies is significant.

4. Optical and Electronic Properties of Si and Sn-Rich $Ge_{1-x-y}Si_xSn_y$ pin Devices on n-Ge/Si(100) Substrates

To further explore the optoelectronic properties of ternary alloys across the composition space, another set of $Ge_{1-x-y}Si_xSn_y$ heterostructure *pin* devices were produced with a fixed composition of Sn and a variable Si content. The aim here is to investigate regions of the composition space with Sn contents close to where $Ge_{1-y}Sn_y$ becomes a

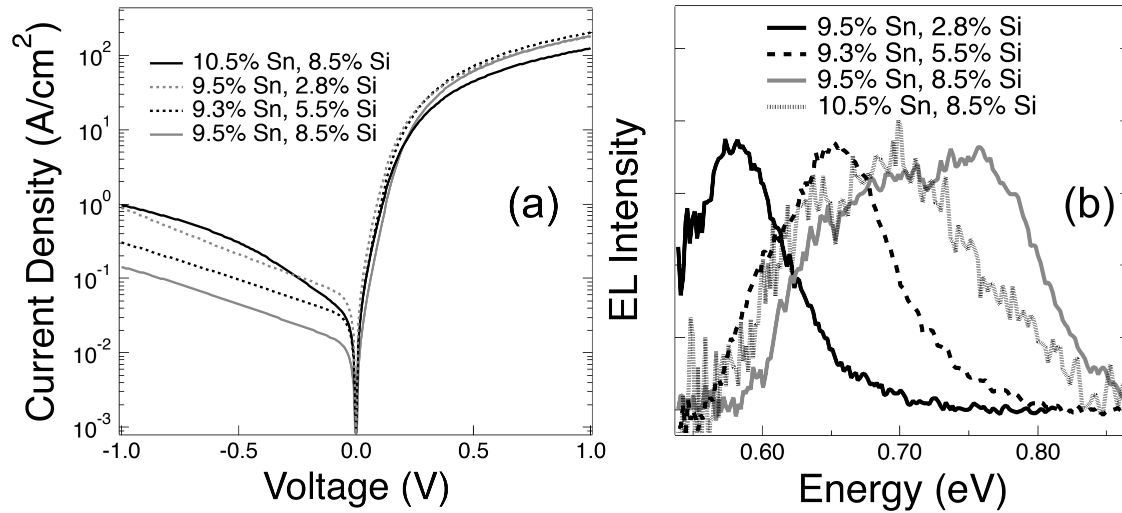

Figure 41: (a) Room temperature *I-V* plots of the fixed Sn, variable Si ternary alloy devices. These devices show strong rectifying characteristics. (b) EL from $Ge_{1-x-y}Si_xSn_y$ diodes in this composition region demonstrate a separation of the E_0 and E_{ind} signals as a function of Si content.

direct-gap semiconductor (9% Sn and above), while adjusting the Si composition to find optimized materials with greater separation between the L and Γ points in the conduction band. Band gap measurements of such materials may give target ternary alloys an electronic structure that is more direct than analogous $Ge_{1-y}Sn_y$ materials and could provide insight into the compositional dependence of the bowing parameters that are expected to be significant in describing the full electronic structure of $Ge_{1-x-y}Si_xSn_y$ alloys.

Figure 41 (a) overlays plots of the *IV* measurements for a variety of devices representing the composition range of materials investigated (~9% Sn and 3-9% Si). Good rectifying properties are demonstrated in the plots over the ±1V bias range shown with ideality factors between 1.10 and 1.20. These devices show dark current levels comparable to or less than that of the $Ge_{1-y}Sn_y$ devices discussed in Chapter II at the same Sn concentrations. The variation in -1V bias dark current densities spans an order-of-magnitude range from ~0.1-1.0 A/cm^2. This suggests that with improved processing

conditions, lower dark currents should be achievable in ternary devices relative to analogous $Ge_{1-y}Sn_y$ diodes. This may be attributable to the incorporation of Si providing closer lattice matching with the underlying *n*-Ge contact, mitigating some of the mismatch-induced defects. Evidence for this is comes from that fact that the 9.5% Sn, 8.5% Si device has the lowest reverse-bias dark currents. Figure 41 (b) plots the normalized room temperature EL from the devices shown in panel (a). The plots show that the incorporation of successively higher Si contents shifts the fundamental band gaps to higher energies and increases the separation between the E_0 and E_{ind} peaks. The band gaps of these materials were determined using the same modeling procedures discussed in previous sections. Using this modeling procedure, it was found that the difference $E_0 - E_{ind}$ between the 9.5% Sn, 8.5% Si sample is 110 meV and this value in 10.5% Sn, 8.5% Si device is 70 meV. This indicates that direct-gap ternary alloys should be attainable despite high Si concentrations by incorporating Sn contents that further reduce the separation $E_0 - E_{ind}$.

5. Conclusion

In summary this section has demonstrated the first-generation of $Ge_{1-x-y}Si_xSn_y$ light emitting diodes integrated onto a Si platform. This development is made possible by the low temperature reactions and *in situ* doping strategies afforded by the rationally designed hydride precursors employed in the growth stages of sample preparation. This approach enabled the formation of finely tuned device architectures with one defective interface, providing the opportunity to systematically assess the optoelectronic capabilities of these materials. Spectral responsivity and EL measurements suggest the existence of a transition to direct gap semiconductors, in analogy with $Ge_{1-y}Sn_y$

optoelectronic devices. Thus the ternary materials that contain more Sn than Si may be viewed as thermally robust alternatives to $Ge_{1-y}Sn_y$ materials for Si-integrated optoelectronics. By fixing the Sn content near 10% and varying the Si incorporation, it has been confirmed that the addition of Si reverts the material back towards a more Ge-like indirect gap material.

C. Compositional Dependence of the $Ge_{1-x-y}Si_xSn_y$ Fundamental Band Gaps

1. Introduction

Ternary $Ge_{1-x-y}Si_xSn_y$ alloys can be considered as a superposition of its constituent binary alloys: $Ge_{1-x}Si_x$, $Ge_{1-y}Sn_y$, and $Si_{1-z}Sn_z$. In Chapter II, room temperature PL measurements were used to accurately determine the compositional dependence of the E_0 and E_{ind} energies in $Ge_{1-y}Sn_y$. Both of these electronic transitions were shown to have a bowing parameter that turned out to have a linear dependence as a function of Sn content in the Ge-rich limit, leading to empirical cubic expressions which best described the band gaps. Previous work based on ellipsometry has revealed that the bowing parameter associated with the $Si_{1-z}Sn_z$ alloy is very large and very likely compositionally dependent as well.[173,182] Due to a lack of adequate materials and virtually no studies concerned with a systematic study of the lowest gaps in $Si_{1-z}Sn_z$ alloys, any bowing associated with this binary component must be left as an adjustable parameter in a global fit to the ternary band gaps.

2. Motivation to Investigate Ge-rich $Ge_{1-x}Si_x$ Alloys

Surprisingly, there is very little data on the compositional dependence of $Ge_{1-x}Si_x$ alloys in the Ge-rich limit. The only known investigation that provides any description of the band gaps near this composition regime was conducted by Kline, Pollak, and Cardona

(KPC). This study measured the E_0 in $Ge_{1-x}Si_x$ alloys (with $0.06 < x < 0.5$) from electroreflectance measurements.[183] The compositional dependence was found to be very linear. This linearity is quantified by a recent fit of the KPC data using an expression of the form $E_0(x) = E_0^{Ge}(1-x) + E_0^{Si}x - b_0^{GeSi}x(1-x)$, which gives a small bowing parameter b_0^{GeSi} = 0.21 eV. Electroreflectance measurements in fully strained, single-crystalline $Ge_{1-x}Si_x$/Si films with $x > 0.7$ are also consistent with a small bowing parameter.[184] However, more recent results on partially relaxed $Ge_{1-x}Si_x$/Si films with $x < 0.06$ show significant deviations from the E_0 energies predicted from the KPC dependence combined with standard deformation potential theory.[185] The uncertainty regarding the value of E_0 in Ge-rich $Ge_{1-x}Si_x$ not only makes it very difficult to design optical devices based on these alloys, but also creates serious obstacles to the study of new materials such as the ternary $Ge_{1-x-y}Si_xSn_y$ alloy. Given the two-dimensional compositional space of the ternaries, which makes it much more difficult to map, it is essential to validate interpolation expressions for all relevant transitions, including E_0. A quadratic interpolation formula for the ternary involves the three binary alloy bowing parameters b_0^{GeSi}, b_0^{GeSn}, and b_0^{SiSn}. Since the bowing parameter b_0^{SiSn} for the binary $Si_{1-z}Sn_z$ alloy has not been determined experimentally, attempts have been made to determine b_0^{SiSn} from fits to the ternary alloy using the known bowing parameters b_0^{GeSi} and b_0^{GeSn} for $Ge_{1-x}Si_x$ and $Ge_{1-y}Sn_y$ alloys, respectively. However, since all available $Ge_{1-x-y}Si_xSn_y$ samples are near the Ge-rich end, the leading bowing contributions to the E_0 energy are of the form $b_0^{GeSi}x$, $b_0^{GeSn}y$, and $b_0^{SiSn}xy$, respectively. This means that that any uncertainty Δb_0^{GeSi} translates into a much larger $\Delta b_0^{GeSi}/y$ uncertainty in b_0^{SiSn}. In other words, meaningful fits of b_0^{SiSn} in the

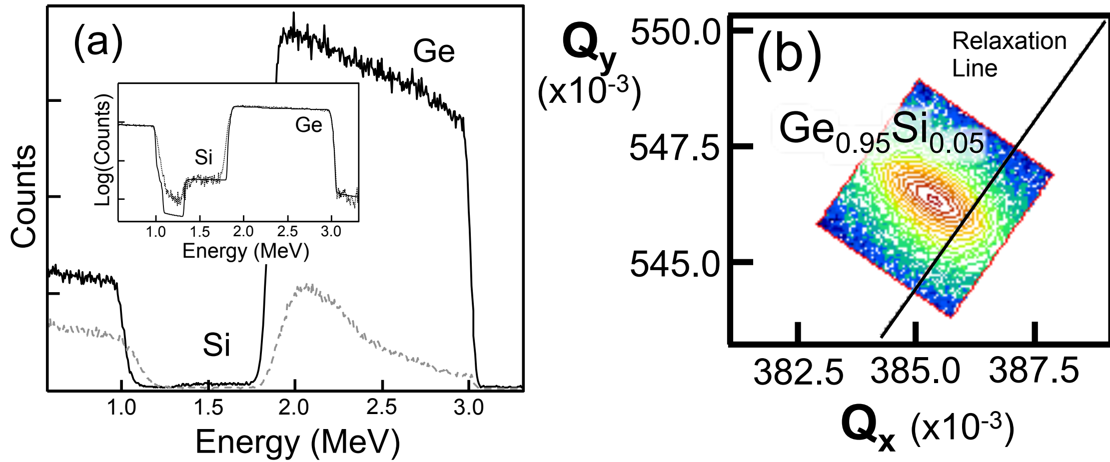

Figure 42: (a) 3.7 MeV RBS from a 6.0% Si sample showing clear Ge and Si signals in the top $Ge_{0.94}Si_{0.06}$ layer. The Ge and $Ge_{0.94}Si_{0.06}$ thicknesses are measured to be 650 and 1600 nm respectively. (b) 224 reciprocal space map of a $Ge_{0.95}Si_{0.05}$ alloy grown on Si(100).

ternary alloy require a very accurate knowledge of the bowing parameters in binary $Ge_{1-x}Si_x$ and $Ge_{1-y}Sn_y$ alloys. Ironically, Chapter II presents accurate data for the more exotic $Ge_{1-y}Sn_y$ system and it is the uncertainty in the case of $Ge_{1-x}Si_x$ alloys that represents the main bottleneck for further progress in this field. Thus, before a reliable global fit of the ternary band gaps can be performed, it is necessary to have an accurate description of the $Ge_{1-x}Si_x$ band gaps. To resolve this issue, this section of Chapter III digresses into a study of the fundamental band gaps in Ge-rich $Ge_{1-x}Si_x$ alloys.

3. *Growth and Materials Properties of Ge-Rich $Ge_{1-x}Si_x$ Alloys*

$Ge_{1-x}Si_x$ samples with $0 < x < 0.13$ were produced for this study on 4-inch Si(100) wafers in a Gas Source Molecular Epitaxy (GSME) chamber through reactions of Ge_4H_{10} and Si_4H_{10} at 380°C using mixtures with a Ge:Si molar ratio roughly half of that which was measured in the resultant films. Upon completion of the growth, the wafers were subjected to an *in situ* anneal at 700°C for 3 minutes to improve the crystal quality of the epilayer. Once removed from the growth chamber the samples were characterized by

high resolution XRD, RBS, and spectroscopic ellipsometry to determine crystallinity, composition, and thickness. For samples with Si contents less than 5%, high-crystal quality materials could be grown directly onto the Si substrate following this procedure. XRD scans along the (004) reflection measured single-phase alloy peaks with full width at half maxima (FWHM) as low as 0.05^o. In the case of samples containing more than 5% Si, it was found that the FWHM of materials grown directly on the Si wafer were greater than 0.10^o. To improve the crystallinity of these materials, another set of layers containing more than 5% Si were grown on Ge-buffered Si platforms. In this case, it was found that the post-growth annealing treatment yielded $Ge_{1-x}Si_x$ materials with FWHM values approaching 0.05^o. Off-axis XRD (224) maps revealed that residual biaxial tensile strains ranging up to 0.2% were produced in all samples during the annealing step due to the mismatch in thermal expansion coefficient between the GeSi alloys and the Si substrate. The Si content of the films was obtained directly from RBS and indirectly from the known compositional dependence of the relaxed lattice constant a_0, including non-linear deviations from Vegard's law.[186] This relaxed lattice constant was computed from standard elasticity theory expressions using the in-plane (a) and out-of-plane (c) lattice parameters obtained from (224) reciprocal space maps. The Si film compositions measured between these two techniques were found to agree within experimental error. RBS channeling experiments demonstrated a high degree of epitaxial alignment of the films to the Si substrate. The X-ray measurements also made it possible to determine the level of strain, defined as $(a-a_0)/a_0$. This strain is tensile in most samples and quite modest in magnitude, never exceeding 0.2%. Nevertheless, strain corrections were applied in all cases to extract relaxed values of the optical transition energies. The

thicknesses obtained by RBS and ellipsometry were in agreement for all samples in the study. They ranged either between 700-800 nm or 1400-1600 nm depending on the amount of gas precursors consumed for the growth.

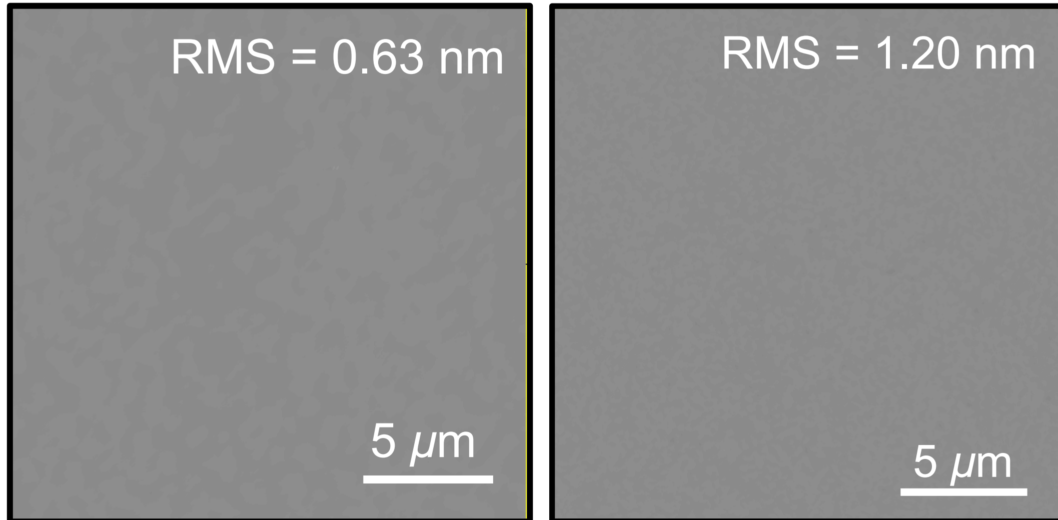

Figure 43: (Left) AFM of a 1.3% Si sample grown using lower-order germane and silane precursors. (Right) AFM image of a 13% Si sample grown using the standard method described above. Both samples show featureless morphologies and low roughness values.

Figure 42 (a) plots the random and channeled 3.7 MeV RBS spectra from a representative 6.0% Si layer grown on a Ge buffer as the solid black and dashed gray lines respectively. A high degree of channeling is observed across the entire sample stack indicating good epitaxial alignment of both epilayers (Ge buffer and $Ge_{1-x}Si_x$ alloy) to the Si substrate. The channeling is also evidence for full substitution of Si into the average diamond lattice. The inset plots the random spectrum on a logarithmic scale the accentuate the Si signal from $Ge_{1-x}Si_x$ layer. The solid line over these data represents the model fit to the spectrum, which demonstrates that the Si profile is flat across the layer indicating that compositional gradients are not produced during the growth. Panel (b) of Figure 42 shows the off-axis 224 XRD reflection from a layer containing 5% Si that is

grown directly on a Si wafer. A biaxial tensile strain of 0.139% is measured from the peak position slightly above the cubic relaxation line. These data demonstrate that the materials grown by this process are single-phase random $Ge_{1-x}Si_x$ alloys with high crystal quality.

As a test of the robustness of the growth mechanism employed in this study, another set of growths were done using the lower-order germane and silane precursors Ge_3H_8 and Si_3H_8. The growth of a 750 nm thick, 1.3% Si sample on a 4-inch Si wafer was conducted at 360-380^oC at 1×10^{-4} Torr, conditions which are virtually identical to those employed on all the other samples. This was produced at an average growth rate of 16.1 nm/min, competitive with the growth rates observed in the other samples grown with the higher-order Ge_4H_{10} and Si_4H_{10} precursors. The (004) reflection showed a single-phase alloy peak with a FWHM of 0.0706^o. Due to the *in-situ* annealing treatment, the (224) reflection showed a residual tensile strain of 0.1363%. Furthermore, it is stressed here that the optical properties of this sample were identical to those of samples produced with the higher order precursors at the same composition, demonstrating the high level of flexibility in the growths of these materials.

The surface morphology was investigated using atomic force microscopy (AFM). The left panel of Figure 43 shows a 20 μm x 20 μm AFM image of the 1.3% Si sample described in the previous paragraph, while the right panel is an AFM image with the same dimensions of a 13% Si sample grown using the Ge_4H_{10} and Si_4H_{10} precursors. Analysis of the surface roughness measures an RMS value of 0.63 and 1.20 nm for the 1.3% Si and 13% Si samples, respectively. In addition the surface appears flat and devoid of the pit defects reported in Ref. 185. Due to the close similarity in roughness between

these two samples with over a 10% Si content difference, it is unlikely that the lower roughness of the left panel sample is due to the choice of precursors. The surface morphology seen here is characteristic of all samples used in this study.

4. Optical Properties and the Compositional Dependence of Ge-Rich $Ge_{1-x}Si_x$ Fundamental Band Gaps

The band gaps of the $Ge_{1-x}Si_x$ samples were measured by two methods: spectroscopic ellispsometry and room temperature PL, with the aim to study the compositional dependence of the E_0 energy in detail. Two fitting methods were employed to measure E_0 by ellipsometery. The first uses a point-by-point fit to the data and the other takes a numerical second-derivative which is then smoothed. The PL measurements were conducted under the same conditions described earlier in Chapter II (A).

The complex dielectric function $\varepsilon_1 + i\varepsilon_2$ of the $Ge_{1-x}Si_x$ films was determined from the ellipsometric data following a standard two-step procedure. In the first step, the known dielectric functions for the substrate and buffer layers were combined with a parametric model dielectric function for the $Ge_{1-x}Si_x$ layers.[187] The dielectric function parameters plus the thickness of all layers were then adjusted to obtain the best possible fit. In a second step, the layer thicknesses were kept unchanged, and the ellipsometric data were fit again at each energy point using the values of ε_1 and ε_2 for the $Ge_{1-x}Si_x$ layer as adjustable parameters, and the previous point's values as initial guess. This procedure largely eliminates any possible bias introduced by specific parametric models with a pre-defined set of critical points. In addition, it does not impose Kramers-Kronig consistency between the real and imaginary parts, so that the verification of such consistency can be used as an additional control criterion for the quality of the fit. In general, the "point-by-

point" dielectric functions obtained in the second iteration are found to be very close to the model dielectric functions of the first iteration, which are Kramers-Kronig consistent by construction. Critical point energies are traditionally extracted from the experimental dielectric function by computing second or third numerical derivatives with respect to energies. These derivatives are particularly noisy when the imaginary part approaches zero, and therefore they must be combined with robust smoothing methods. We investigated different Savitzky-Golay smoothing-differentiation algorithms and found that an 11-point filter reduces noise sufficiently to allow for critical point fits while introducing a negligible distortion of the lineshapes.

An elementary calculation of the E_0-contribution to the dielectric function, assuming parabolic bands, no broadening, and free electron-hole pairs, shows that the imaginary part is the sum of two terms of the form

$$\varepsilon_2(E) = \left(\frac{4\sqrt{2}e^2 P^2}{3m^2 \hbar E^2} \right) \mu_{eh}^{3/2} (E - E_0)^{1/2}, \quad (3.4)$$

where e and m are the free-electron charge and mass, μ_{eh} is the reduced effective mass of the electron-hole pair, and P the momentum matrix element. The two terms to be added correspond to the two degenerate light- and heavy-hole bands at the top of the valence band, which give different values of the reduced effective mass. In the case of germanium-like materials, the square-root energy dependence in Eq. (3.4) is in poor agreement with the experimental data, as demonstrated previously.[31] The disagreement can be partially concealed by introducing a multiplicative amplitude pre-factor in Eq. (3.4), but this is physically unsatisfactory because all prefactors in the equation are well

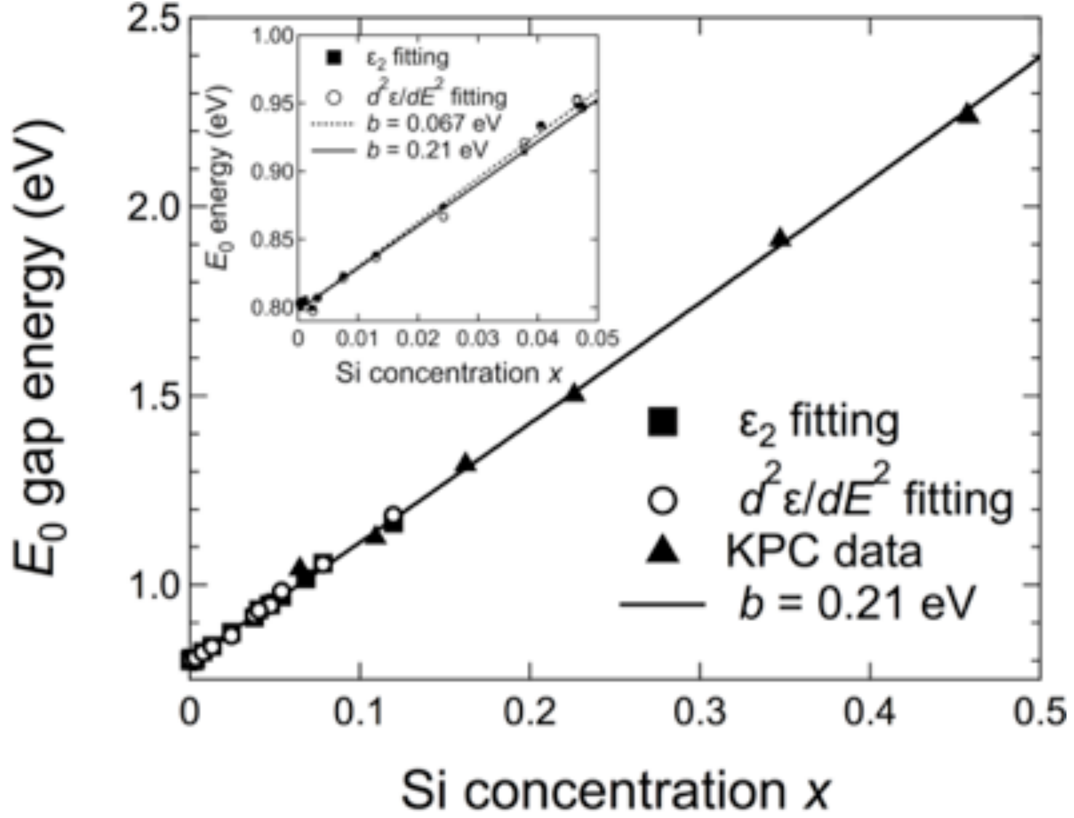

Figure 44: Compositional dependence of the E_0 transition energy in $Ge_{1-x}Si_x$ alloys (circles and squares) combined with previous measurements of this transition by KPC (Ref. 183). The solid line is a fit of the data which yields b_0^{GeSi} = 0.21 eV and E_0^{Si} = 4.093 eV. The inset shows a detail of the $x \leq 0.05$ range. A fit restricted to this range gives b_0^{GeSi} = 0.067 eV and is shown as a dashed line.

known experimentally. Much better agreement with experiment can be obtained by introducing excitonic effects. For a single pair of parabolic valence-conduction bands, the imaginary part of the excitonic dielectric function is given by

$$\varepsilon_2(E) = \varepsilon_{2x}(E) + \varepsilon_{2f}(E)S(E), \tag{3.5}$$

where ε_{2x} is the below-band gap contribution from bound excitons, ε_{2f} is the dielectric function for free-electron hole pairs, given by Eq. (3.4), and $S(E)$ is the so-called Sommerfeld enhancement factor for states in the continuum. Analytical expressions for ε_{2x} and $S(E)$ are given in Ref. 35, where it was shown that Eq. (3.5) is in very good

agreement with experiment, both in terms of lineshape and absolute value. We have used this expression, convoluted with a broadening function, to fit the rising edge of the imaginary part of the dielectric function. We find that Gaussian broadening is in better agreement with the data, even for pure Ge. The adjustable parameters of the fit are the width of the broadening function and the band gap E_0. The momentum matrix elements and effective masses were calculated as in Ref. 35, and the effect of the residual strain was fully included using deformation potential theory with hydrostatic and shear deformation potentials a = -9.47 eV from Goñi *et al*. (Ref. 138) and b = 1.88 eV from Liu *et al*. (Ref. 188). No sharp excitonic peak is observed in ε_2 at room temperature, but excitonic effects introduce a strong deviation from the square-root dependence of the edge, and the excitonic enhancement is critical to match the absolute value of ε_2 to the experimental data. The high-energy deviations between the calculated and observed dielectric function are expected, since the assumed parabolic dispersion ceases to be a good approximation about 50 meV above the E_0 gap. The values of E_0 obtained by this method are shown as black squares in Figure 44.

The most common approach for extracting band gap energies from ellipsometric data, as indicated above, is to enhance the critical point singularities by computing derivatives of the dielectric function. To use this method, we fit the numerical second derivatives of the real and imaginary parts of the dielectric function with an expression of the form:

$$\frac{d^2\varepsilon}{dE^2} = \frac{Ae^{i\Phi}}{\left(E - E_0 + i\Gamma\right)^{3/2}}, \qquad (3.6)$$

with A, Φ, Γ, and E_0 as adjustable parameters. Eq. (3.6) corresponds to free electron-hole pairs, except that the phase angle Φ is taken as an adjustable parameter to mimic excitonic effects. An additional, more subtle reason for the need of an adjustable phase factor is the fact that the addition of $-i\Gamma$ to the energy gap is not a fully consistent way to treat broadening, as pointed out by Kim *et al*. (Ref. 189). The convolution of the calculated dielectric function with a broadening function is not fully consistent either. However, while the precise form in which broadening is introduced is relatively unimportant in fits of ε_2, it becomes critical for its second derivative $d^2\varepsilon/dE^2$, and therefore the parameter Φ corrects, in a phenomenological way, for some of the lineshape deviations caused by an approximate treatment of broadening. Theoretical expressions that treat broadening rigorously have been given in Ref. 189, but the results do not lead to analytical forms that can be easily used to fit experimental data.

Since the samples possess some residual amounts of strain, fits with the oscillator in Eq. (3.6) do not give the value of E_0 corresponding to relaxed alloys. To correct for this deficiency, the data should in principle be fit with two such oscillators, one for the light-hole transition and one for the heavy-hole transition, shifted from E_0 following deformation potential theory. An alternative approach, which we have utilized to minimize the number of initial fit parameters, is to fit the data with the single oscillator represented by Eq. (3.6) and then adjust the resulting fit lineshape with two oscillators, separated by a fixed energy given by deformation potential theory. In this second fit, only E_0 and the value of Γ are allowed to be further adjusted. Values of E_0 extracted from these fits are shown in Figure 44 as white circles.

The agreement between the E_0 values determined following the two methods described above is excellent, so that they will be combined for the analysis of the compositional dependence of E_0. It was noted however, that the second-derivative analysis is less robust, and for some samples the noise is simply too large to obtain meaningful fits.

The compositional dependence of the E_0 values in Figure 44 is clearly very linear over the Si-concentration in the figure. A straight-line fit yields $E_0 = 0.800 + 3.162x$ (in eV). The extrapolation of this expression to $x = 1$ gives $E_0 = 3.96$ eV. Unfortunately, this cannot be directly compared with measurements in pure Si because the only experimental value available was obtained at 4.2 K by Aspnes *et al*., who found $E_0 = 4.185$ eV. (Ref. 190). Lautenschlager *et al*. have calculated the temperature dependence of all important transitions in Si and found very good agreement with all available experimental data.[191] If we combine the value of E_0 at 4.2 K (Ref. 190) with the theoretical temperature dependence, we estimate a value $E_0 = 4.093$ eV for Si at room temperature. This would imply a modest non-linearity in the compositional dependence of E_0. As indicated in the introduction, deviations from linearity in the compositional dependence of transition energies are accounted to lowest order by introducing a bowing parameter b_0^{GeSi}. When the KPC data was fit $E_0^{\mathrm{Si}} = 4.093$ eV, a value $b_0^{\mathrm{GeSi}} = 0.21$ eV was obtained.[87] A new fit that combines the KPC data with our results, show as a solid line in Figure 44, gives $E_0^{\mathrm{Ge}} =$ 0.803 eV and the same bowing parameter $b_0^{\mathrm{GeSi}} = 0.21$ eV. Thus our data are consistent with the KPC measurements. For very low concentrations $x \leq 0.05$, which are of particular interest in modern applications, the fit gives $E_0^{\mathrm{Ge}} =$ 0.7979 eV, $b_0^{\mathrm{GeSi}} = 0.067$

eV, essentially a linear dependence. This is shown as a dashed line in the inset of Figure 44. The difference in bowing parameters between the $x \leq 0.5$ and $x \leq 0.05$ fits suggests that b_0^{GeSi} is not a constant but a function of composition. A bowing parameter of the form $b_0 = b_0^{(0)} + b_0^{(1)} y$ has already been found necessary to describe the compositional dependence of E_0 in $Ge_{1-y}Sn_y$ as outlined in Chapter II (A). Similar similar expressions have been used for III-V alloy systems.[143,144] However, in the case of $Ge_{1-x}Si_x$ the bowing parameters are very small, making it very difficult to carry out a fit using $b_0^{\mathrm{GeSi}} = b_0^{(0),\mathrm{GeSi}} + b_0^{(1),\mathrm{GeSi}} x$. The values of $b_0^{(0),\mathrm{GeSi}}$ and $b_0^{(1),\mathrm{GeSi}}$ obtained from such fits are not well converged and vary dramatically if single points are removed from the fit. This is understandable in view of the small difference between the

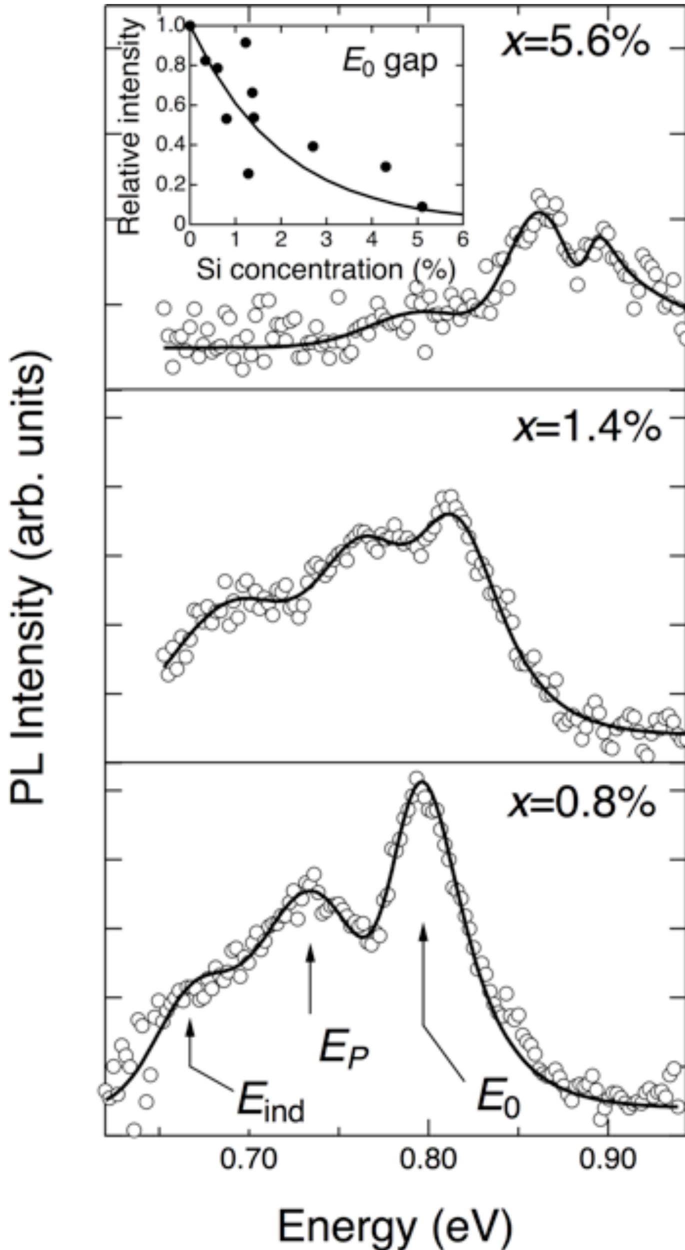

Figure 45: Representative room temperature PL spectra for selected $Ge_{1-x}Si_x$ samples. The inset in the top panel shows a comparison between measured and calculated integrated intensities (normalized to unity for pure Ge).

b_0^{GeSi} = 0.21 eV and b_0^{GeSi} = 0.067 eV curves in the inset in Figure 44.

Typical PL spectra of $Ge_{1-x}Si_x$ alloys are shown in Figure 45. PL studies of these alloys are usually carried out at low temperatures, for which sharp features associated with band edge excitons and phonon replicas are clearly observed.[25] For the spectroscopy of the E_0 transition, however, room temperature conditions are needed to populate the Γ-valley in the conduction band. In Ge- and $Ge_{1-y}Sn_y$ thin films, these conditions lead to the observation of a dominant peak, assigned to the E_0 transition, and a weaker, low-energy peak assigned to the indirect transition E_{ind} between the L-valley in the conduction band and the top of the valence band at the Γ-point. In $Ge_{1-x}Si_x$ alloys, on the other hand, we observe a three-peak structure. By comparison with pure-Ge films, we assign the high-energy peak to E_0 and the low-energy peak to E_{ind}. The E_0 peak is fit as it was before with an EMG profile and the E_{ind} peak with a Gaussian. The extra peak, labeled E_P in Figure 45, is also modeled as a Gaussian. The corresponding gap energies are extracted as discussed previously. Briefly, the EMG component is fit with a theoretical expression for the spontaneous emission from the E_0 gap based on a generalized van Roosbroeck–Shockley formula for which we compute the absorption coefficient using the same model as in Eq. (3.5). The quasi-Fermi levels required for the calculation are evaluated as a function of the photoexcited charge density by including the L-, Γ, and Δ-valleys in the conduction band, and the light-heavy hole manifold in the valence band. The effect of strain is built into the absorption coefficient expressions using deformation potential theory. The values of E_{ind} are obtained from the low-energy Gaussian component using a correction adjusted to pure Ge.

The E_0 values obtained from the PL data are plotted in Figure 46 and compared with the best fit to the ellipsometry data (dotted curve in the Figure 44 inset). The agreement is quite good, but we notice that the energies obtained from the PL experiments are somewhat downshifted with respect to the ellipsometry values,

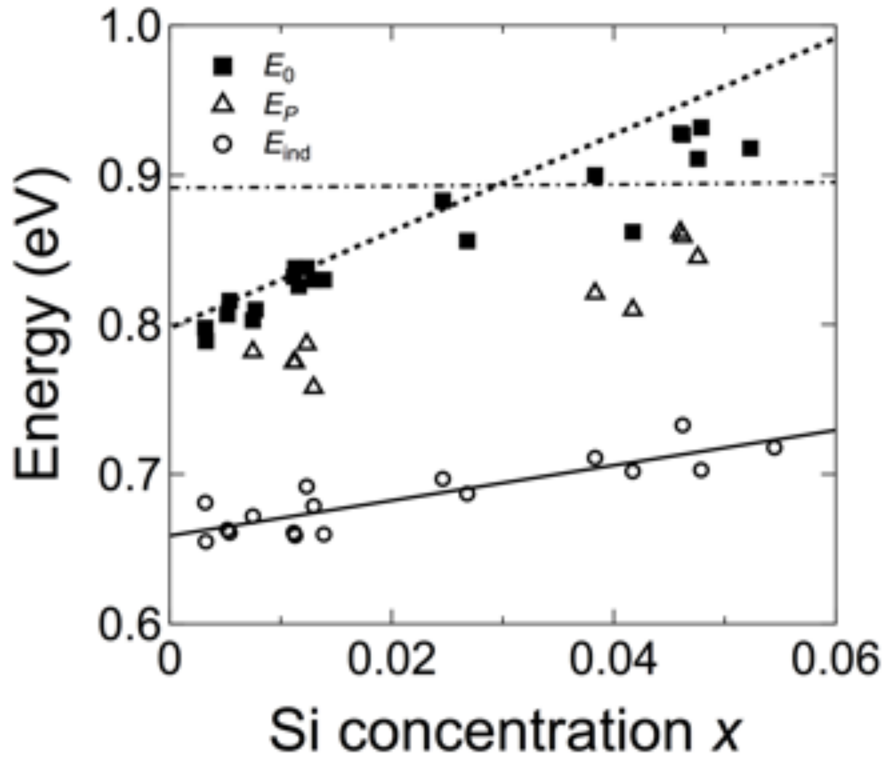

Figure 46: The E_0 and E_{ind} values extracted from the PL data are shown as black squares and empty circles, respectively. The peak energies for the E_P features shown in Figure 45 are summarized as empty triangles. The solid line is a linear fit to the compositional dependence of $E_{ind.}$ The dashed line is our best fit to the E_0 values obtained from ellipsometry. The dash-dotted line is the calculated peak energy for emission from the Δ-valley.

particularly for the highest Si concentrations. A downshift of the PL signal with respect to the absorption edge (Stokes shift) is quite common in semiconductors. However, we cannot confirm this Stokes shift in our samples due to the presence of the E_P feature, which partially overlaps with the E_0 signal and could systematically shift the EMG fit.

This is further complicated by the dramatic reduction in E_0 signal intensity as a function of the Si concentration. The reason behind this reduction is the increased separation between the Γ- and L minima in the conduction band, which exponentially reduce the population of the Γ-minimum. We have used our Roosbroeck–Shockley calculation to estimate the effect of the Si-concentration on the PL integrated intensity, and the calculation is compared with experimental data in the Figure 45 inset. Good agreement is obtained, which indirectly supports our assignment of the leading peak to the E_0 transition. The order-of-magnitude reduction in PL intensity at the highest Si concentrations introduces larger errors in the determination of E_0, which could further contribute to the apparent discrepancy with the ellipsometry data.

The values of E_{ind} obtained from our PL lineshape analysis are also shown in Figure 46. A linear fit gives $E_{\text{ind}} = 0.659+1.18x$ (in eV). This is in good agreement with the low-temperature PL measurements of Weber and Alonso, (Ref. 25) who find a linear coefficient of 1.27 eV.

A first candidate for the additional peak E_P observed in Figure 45 is emission from the Δ-valley along the (100) direction of the BZ, which becomes the fundamental band gap for $x > 0.15$. By extrapolating low temperature PL measurements in samples with $x > 0.15$, the Δ-valley in pure Ge is predicted to be $\Delta E_{L\text{-}\Delta} = 0.19$ eV above the absolute minimum of the conduction band at the L point of the BZ.[25] This should be compared with a value $\Delta E_{L\text{-}\Delta} = 0.21$ eV obtained by Ahmad and Adams from electrical transport measurements,[26] and $\Delta E_{L\text{-}\Delta} = 0.22$ eV from an analysis of the broadening of the direct gap excitonic absorption under pressure.[27] Thus the Δ-minimum lies about 70 meV above the Γ-minimum in pure Ge, and this difference becomes smaller and eventually

reverses sign in $Ge_{1-x}Si_x$ alloys. But even in the case of pure Ge, the population of Δ-valley under photoexcitation is calculated to be one order of magnitude higher than that of the Γ-valley, due to its much higher density of states. To compute the peak energy for possible emission from the Δ-valley we use the expression:

$$I \propto \left[m_v^{3/2} m_\perp \left(2m_\parallel\right)^{1/2} \right] \times \\ \left\{ \left(n_\Omega + 1\right) \exp\left[\tfrac{-\left(E + \hbar\Omega - \Delta F\right)}{k_B T}\right] E\left(E + \hbar\Omega - E_\Delta\right)^2 + n_\Omega \exp\left[\tfrac{-\left(E - \hbar\Omega - \Delta F\right)}{k_B T}\right] E\left(E - \hbar\Omega - E_\Delta\right)^2 \right\}, \quad (3.7)$$

where E is the emitted photon energy, m_v is the effective hole mass, $m_\parallel$ and $m_\perp$ are the longitudinal and transverse effective masses at the Δ-valley, Ω a phonon frequency, E_Δ the Δ-valley minimum energy with respect to the top of the valence band, and ΔF the separation between quasi-Fermi levels in the conduction band. Combining the above result $\Delta E_{L\text{-}\Delta} = 0.21$ eV with the compositional dependence of the E_Δ energy measured by Weber and Alonso, we obtain at room temperature $E_\Delta = 0.874 + 0.046x + 0.206x^2$ (in eV). The maxima of the emission profiles computed by inserting this expression in Eq. (3.7) with a phonon energy $\hbar\Omega = 34.5$ meV (corresponding to a Ge-Ge like optical vibration) are shown as a dashed-dotted line in Figure 46, and we see the calculated values not only exceed the observed E_P energies by a considerable amount by fail to account for the compositional dependence of E_P. Our calculation assumes fully relaxed layers, but if we incorporate strain effects (including the splitting of the six Δ-valleys), the predicted peak energies remain almost unchanged for the low levels of strain in our samples. Alternatively, one might assume that the dominant contribution arises from a Si-Ge like vibration with $\hbar\Omega \sim 50$ meV. This would slightly lower the dotted line in Figure 46, but

would not change its compositional dependence. Thus it seems unlikely that the E_P emission arises from the Δ-valley contribution.

Since the E_P energy seems to be tracking the E_0 energy, an alternative explanation for the E_P emission might be a phonon replica of the E_0 emission. The average energy separation between E_0 and E_P is 60 meV. This corresponds to Si-Si-like phonon energies in the $Ge_{1-x}Si_x$. However, it is hard to see why Si-Si vibrations would make such aprominent contribution at Si-concentrations where there are very few Si-Si bonds in our samples, and it is not clear why a phonon replica of E_0 would have an intensity comparable to no-phonon direct gap E_0 emission. Yet another explanation might involve the existence of Si-depleted regions in the samples, for example at the interface with the buffer/substrate or near the surface. These regions might occupy a negligible volume, so that they do not become apparent in the ellipsometry measurements, but their contribution might be enhanced in emission because E_0 in those regions would have a lower value. However, this explanation would imply that all E_P peak energies should be higher than that of pure Ge, and this is not the case experimentally, as clearly seen in Figure 45 and Figure 46. Further work will be needed to find a plausible explanation for E_P.

With a detailed understanding of the compositional dependence of the $Ge_{1-x}Si_x$ E_0 gap, we can now approach the subject of a global $Ge_{1-x-y}Si_xSn_y$ fit.

5. *A Global Description of $Ge_{1-x-y}Si_xSn_y$ Band Gaps*

When examining the global band gaps for the ternary alloy we will be interested a given composition's degree of directness. Here we define the degree of directness as the parameter δ, given by $\delta = E_0 - E_{\text{ind}}$. This is the difference between the direct and indirect

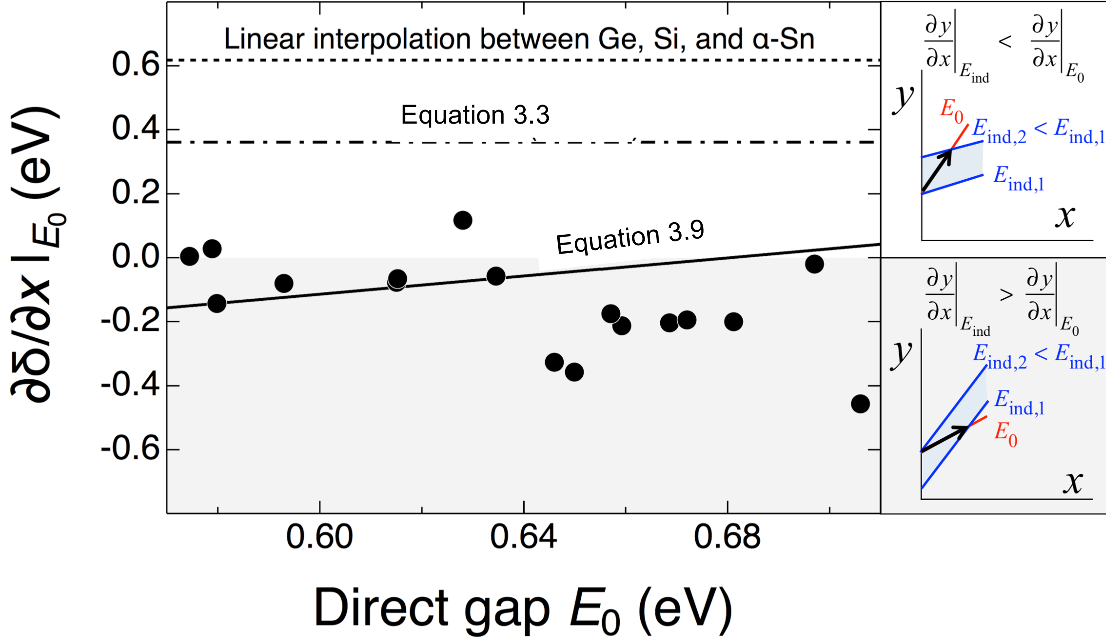

Figure 47: Si-composition derivative (at constant direct gap) of the degree of indirectness in several $Ge_{1-x-y}Si_xSn_y$ alloys. The experimental values correspond to EL results from diodes as well as PL data from section A of this chapter. The solid line is from Eq. 3.9. The dotted line is the prediction assuming a linear interpolation of band gaps between the three elemental semiconductors. The dash-dotted line is the prediction from the bilinear model presented previously. The schematic constant band gap contour lines on the right panels illustrate the positive and negative derivative situation. The arrow shows the compositional "path" at constant direct gap E_0.

band gap energies. To compare the degree of indirectness in $Ge_{1-y}Sn_y$ and $Ge_{1-x-y}Si_xSn_y$ alloys with the same E_0, we examine the derivative $\left.\partial\delta/\partial x\right|_{E_0} = -\left.\partial E_{ind}/\partial x\right|_{E_0}$. From the measured E_0 and E_{ind} data, we obtain an estimate of this derivative as $\left.\partial\delta/\partial x\right|_{E_0} = \left[E_{ind}(0,y') - E_{ind}(x,y)\right]/x$, where $E_{ind}(x,y)$ is the measured indirect gap in the $Ge_{1-x-y}Si_xSn_y$ sample and $E_{ind}(0, y')$ is the indirect gap in a $Ge_{1-y'}Sn_{y'}$ alloy where y' is such that its direct gap E_0 is the same as the measured E_0 in the ternary $Ge_{1-x-y}Si_xSn_y$ sample. The values y' and $E_{ind}(0,y')$ are obtained using the known compositional dependence of E_0 and E_{ind} in $Ge_{1-y}Sn_y$ that were presented in Chapter II. The results are shown in Figure 47. Since the derivative is computed as a difference between two large

numbers, the noise is large, but it is apparent that most data points indicate a negative derivative, which implies that adding Si makes the band structure less indirect. It is easy to show, as schematically illustrated on the right panels in Figure 47, that negative values correspond to the constant band gap contour derivative $\partial y/\partial x|_{E_{\mathrm{ind}}}$ being greater than $\partial y/\partial x|_{E_0}$. A simple linear interpolation between Si, Ge and α-Sn would lead to the opposite conclusion. Using the room temperature values E_0^{Ge} = 0.80 eV, E_0^{Si} = 4.1 eV, E_0^{Sn} = -0.42 eV, $E_{\mathrm{ind}}^{\mathrm{Ge}}$ = 0.66 eV, $E_{\mathrm{ind}}^{\mathrm{Si}}$ = 1.93 eV, and $E_{\mathrm{ind}}^{\mathrm{Sn}}$ = -0.035 eV, we find $\partial y/\partial x|_{E_{\mathrm{ind}}} = \left(E_{\mathrm{ind}}^{\mathrm{Si}} - E_{\mathrm{ind}}^{\mathrm{Ge}}\right)/\left(E_{\mathrm{ind}}^{\mathrm{Ge}} - E_{\mathrm{ind}}^{\mathrm{Sn}}\right)$ = 1.8 but $\partial y/\partial x|_{E_0} = \left(E_0^{\mathrm{Si}} - E_0^{\mathrm{Ge}}\right)/\left(E_0^{\mathrm{Ge}} - E_0^{\mathrm{Sn}}\right)$ = 2.7. This leads to a positive $\partial \delta/\partial x|_{E_0}$, as shown in Figure 47. In section (A) of this chapter we proposed bilinear fit expressions for the ternary $Ge_{1-x-y}Si_xSn_y$ E_0 and E_{ind} energies. Using those linear coefficients, we predict the dash-dotted line in Figure 47, which is closer to the experimental data but still much larger. A major shortcoming of such bilinear fits is that they do not agree well with the known compositional dependencies in $Ge_{1-x}Si_x$ and $Ge_{1-y}Sn_y$. To enforce such agreement, we perform new fits using the quadratic expressions

$$E_0 = E_0^{\mathrm{Ge}}(1-x-y) + E_0^{\mathrm{Si}}x + E_0^{\mathrm{Sn}}y - b_0^{\mathrm{GeSi}}x(1-x-y) - b_0^{\mathrm{GeSn}}y(1-x-y) - b_0^{\mathrm{SiSn}}xy, \quad (3.8a)$$

$$E_{\mathrm{ind}} = E_{\mathrm{ind}}^{\mathrm{Ge}}(1-x-y) + E_{\mathrm{ind}}^{\mathrm{Si}}x + E_{\mathrm{ind}}^{\mathrm{Sn}}y - b_{\mathrm{ind}}^{\mathrm{GeSi}}x(1-x-y) - b_{\mathrm{ind}}^{\mathrm{GeSn}}y(1-x-y) - b_{\mathrm{ind}}^{\mathrm{SiSn}}xy, \quad (3.8b)$$

Here the first three terms represent the linear interpolation between the end points Ge, Si and α-Sn, and the remaining terms give a quadratic correction whose coefficients are the

bowing parameters for the three possible binary alloys in the Si-Ge-Sn system. As seen previously, the $Ge_{1-x}Si_x$ bowing parameters are very small. We use $b_0^{\mathrm{GeSi}} = 0.21$ eV and $b_{\mathrm{ind}}^{\mathrm{GeSi}} \sim 0$. The most accurate bowing parameters for $Ge_{1-y}Sn_y$ were discussed in Chapter II (A). For the $y < 0.1$ range, the values are (in eV) $b_0^{\mathrm{GeSn}} = 2.66 - 5.4y$ and $b_{\mathrm{ind}}^{\mathrm{GeSn}} = 1.1 - 0.78y$. Inserting all known parameters into Eqs. (3.8a) and (3.8b), fits with this equation only require the adjustment of the "SiSn" bowing coefficients.

Band gap data are shown in a three-dimensional plot in Figure 48 (a). To improve the robustness of the fit parameters, we have included not only EL/PL data but also responsivity measurements of E_0 from Ref. 114. The fit results are shown as colored surfaces in Figure 48 (a). We obtain $b_0^{\mathrm{SiSn}} = 28.3 \pm 4$ eV and $b_{\mathrm{ind}}^{\mathrm{SiSn}} = 7.8 \pm 2$ eV. These are extremely large, reminiscent of "giant" bowing parameters[192] in systems such as GaAsN, where values as high as $b_0^{\mathrm{AsN}} = 40$ eV have been reported for the dilute N limit.[193,194] Using Eqs. (3.8a) and (3.8b) parameters, an approximate expression for $\partial\delta/\partial x|_{E_0}$ in the $x \to 0$ limit of interest is:

$$\left.\frac{\partial\delta}{\partial x}\right|_{E_0} = 0.19 + 0.27\left(E_0^{\mathrm{Ge}} - E_0\right)\left[0.47C_0 - C_{\mathrm{ind}}\right], \tag{3.9}$$

where $C_0 = b_0^{\mathrm{GeSi}} + b_0^{\mathrm{GeSn}} - b_0^{\mathrm{SiSn}} \sim -26 \pm 4$ eV and $C_{\mathrm{ind}} = b_{\mathrm{ind}}^{\mathrm{GeSi}} + b_{\mathrm{ind}}^{\mathrm{GeSn}} - b_{\mathrm{ind}}^{\mathrm{SiSn}} = -6.8 \pm 2$ eV are the xy coefficients in Eqs. (3.8a) and (3.8b). Here we used constant values $b_0^{\mathrm{GeSn}} = 2.46$ eV and $b_{\mathrm{ind}}^{\mathrm{GeSn}} = 1.03$ eV, since the compositional dependence of these parameters is not essential for our directness argument. Eq. (3.9) is plotted in Figure 47, and we see that

it is in much better agreement with the experimental results. We note that a necessary condition to obtain negative values of $\partial\delta/\partial x|_{E_0}$ is $|C_0| > 2|C_{\text{ind}}|$, which is fulfilled by the fit parameters. The reason why adding Si to $Ge_{1-y}Sn_y$ turns out to be qualitatively different from adding Si to Ge is that the contour derivatives in Figure 47 are modified by additional $C_0 y/\left(E_0^{\text{Ge}} - E_0^{\text{Sn}}\right)$ and $C_{\text{ind}} y/\left(E_{\text{ind}}^{\text{Ge}} - E_{\text{ind}}^{\text{Sn}}\right)$ terms, which are comparable to unity for $y \geq 0.1$.

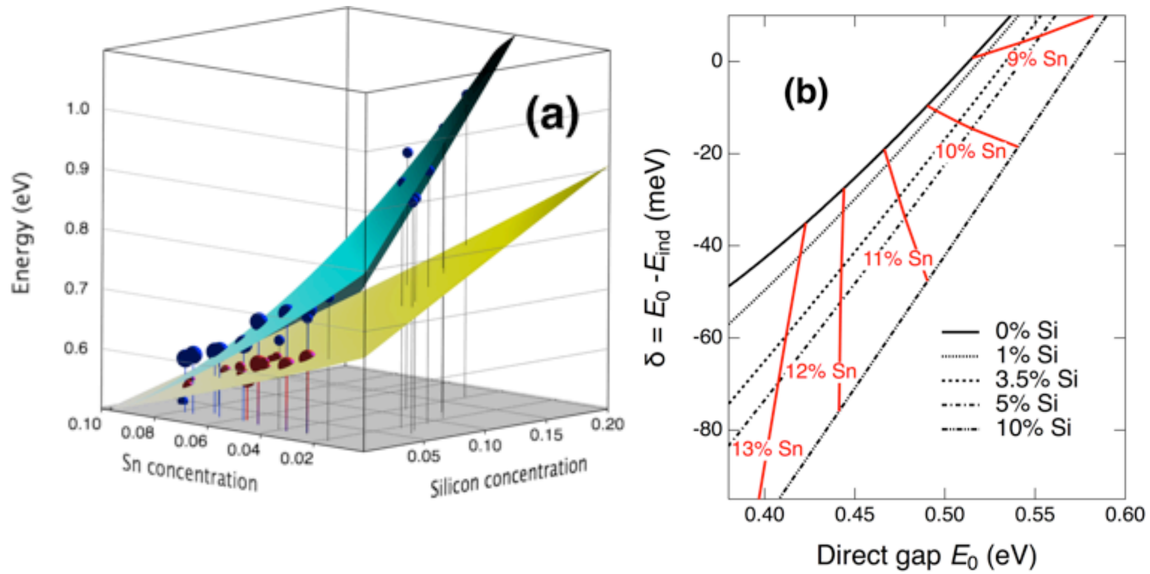

Figure 48: The blue (red) spheres are experimental data for the direct (indirect) gaps from PL and EL presented in this dissertation along with data from Ref. 114. The blue (yellow) surface is a two-dimensional fit of the compositional dependence of the direct (indirect) band gap in $Ge_{1-x-y}Si_xSn_y$ alloys. (b) Calculated degree of indirectness δ of the fundamental band gap in $Ge_{1-x-y}Si_xSn_y$ alloys using the parameters from the two-dimensional fit in panel (a).

The dramatic implications of these results are seen in Figure 48 (b). For samples with $y > y_c$, $Ge_{1-x-y}Si_xSn_y$ becomes a better direct gap material than $Ge_{1-y}Sn_y$. The compositional dependence of the bowing parameters may add some uncertainty to this prediction, particularly because giant bowing parameters comparable in size to b_0^{SiSn} and $b_{\text{ind}}^{\text{SiSn}}$ are in fact found to be strong functions of composition.[192,193,194] In fact, in the only

prior attempt to determine b_0^{SiSn} by fitting Eq. (3.8a) to experimental data, a value b_0^{SiSn} = 13.2 eV was found in alloys lattice-matched to Ge up to compositions approaching 40% Si and 10%Sn.[173] This is less than half the value fitted here to samples with $y > x$ that exhibit direct gap emission. It should be emphasized, however, that the condition in Eq. (3.9) can be satisfied for much smaller values of b_0^{SiSn} as long as $b_{\mathrm{ind}}^{\mathrm{SiSn}}$ decreases as well, so the expected compositional dependence of b_0^{SiSn} does not necessarily invalidate the predictions in Figure 48 (b). Moreover, while it is true that the measured E_{ind} correspond to samples with $y \leq 0.05$, E_0 has been fit to samples with $y \leq 0.095$, so that extrapolation to the $y \sim 0.10$-0.13 range is likely to be far more reliable.

Giant bowing in the $Ge_{1-x-y}Si_xSn_y$ system has not been predicted theoretically.[172,175,195] The largest calculated bowing parameter is b_0^{SiSn} = 3.9 eV. (Ref. 172). There is however substantial experimental evidence of much larger bowing parameters, not only for the direct and indirect gaps discussed here but also for a number of other direct electronic transitions, such as E_1, $E_1+\Delta_1$, and E'_0, as reported in Ref. 196.

6. Conclusion

In summary, the fundamental band gaps of the ternary alloy $Ge_{1-x-y}Si_xSn_y$ have been measured by PL and EL. The ability to resolve the indirect gap signal is owed to the growth of low-defect density materials on Ge-buffered Si platforms. Performing a global fit to the experimental E_0 and E_{ind} $Ge_{1-x-y}Si_xSn_y$ band gaps reported to date reveals that this system possesses an unexpected potential as a direct gap group-IV semiconductor, with extended band gap tunability and increased directness relative to $Ge_{1-y}Sn_y$. These results, combined with the demonstration of $Ge_{1-x-y}Si_xSn_y$ LEDs, should stimulate further

experimental and theoretical studies on the compositional dependence of the band gaps in the ternary alloy. Of particular interest is the range near $x \sim 0.5$, $y \sim 0.1$, where giant bowing parameters might lead to direct band gap materials with emission near the 1550 nm range of fundamental interest for telecommunications.

IV. STEPS TO A DIRECT GAP GROUP-IV LASER ON SI: DEGENERATE GE-SN JUNCTIONS AND WAVEGUIDES

Portions of text and figures in this chapter were previously published as J. D. Gallagher, C. L. Senaratne, P. M. Wallace, J. Menéndez, and J. Kouvetakis, and J. Menendez, *Appl. Phys. Lett.* **107**, 123507 (2015) and have been reproduced with permission.

A. Degenerate *pn* Junction Devices

1. Introduction

To date Si has been shown to be a suitable waveguide and signal transport medium over the 1300-1700 nm wavelength range of interest for dual photonic communication and computation. Several materials, including the $Ge_{1-y}Sn_y$ and $Ge_{1-x-y}Si_xSn_y$ systems discussed thus far in this dissertation, have demonstrated the capacity to serve as integrated signal detectors and modulators within such a scheme. The elusive challenge in this field has been the successful integration of a suitable light source, preferably a laser, within these wavelengths of operation on a Si wafer.

Electrically-pumped Ge-laser devices have been demonstrated using diode structures consisting of polycrystalline *p*-type Si deposited on *n*-type Ge.[81] The optimization of such structures based on carrier and light confinement is not trivial due to the requirement to maintain the quasi-direct character of the emitting layer, which depends very sensitively on the separation between the Γ-point conduction band state and the quasi-Fermi level. Alloying with Sn and Si represents the main tool available to achieve better confinement.[173,197,198] However, $Ge_{1-y}Sn_y$ and $Ge_{1-x-y}Si_xSn_y$ *pn* light emitting diodes (LEDs), the basic starting block for such optimization work, have received very little attention so far. In fact, virtually all reports of light emission from

$Ge_{1-y}Sn_y$ and $Ge_{1-x-y}Si_xSn_y$ diodes are based on *pin* designs in which a relatively thick nominally intrinsic layer is inserted between the *p*- and *n*-electrodes.[106,164,165,166,176,177] Here the fabrication and optical properties of $Ge_{1-y}Sn_y$ *pn* LEDs are presented. It is shown that the emission properties depend very sensitively on the doping levels and Sn-concentrations on both sides of the junctions, making this system not only a serious candidate for a laser device but also an ideal model system to study the properties of quasi-direct light emitting devices.

2. *Growth and Materials Properties of $Ge_{1-y}Sn_y$ Degenerate pn Junctions on Ge/Si(100) Substrates*

TABLE VI: Sample parameters for the devices discussed in this study.

	n-Layer Properties					*p*-Layer Properties				
Sample	Sn (*y*%)	d (nm)	Strain (%)	*n* (cm^{-3})	EL peak (eV)	Sn (*z*%)	d (nm)	Strain (%)	*p* (cm^{-3})	EL peak (eV)
A	6.5	450	-0.15	1.30×10^{19}	0.576	3.5	100	0.26	11.70×10^{19}	
B	12.3	535	-0.29	0.53×10^{19}		8.5	100	0.20	3.00×10^{19}	
C	10.5	360	-0.35	1.80×10^{19}	0.504	8.5	125	-0.08	1.00×10^{19}	0.557
D	9.3	525	-0.35	0.48×10^{19}	0.512	8.6	300	-0.25	2.40×10^{19}	

The devices investigated in this study were grown on Ge-buffered Si wafers as discussed in previous chapters of this dissertation. Figure 49 (a) shows a schematic representation and Table VI summarizes the important parameters of the samples discussed in detail. The Ge buffers (not shown in Figure 49 (a)) were produced on 4" Si(100) with 1 μm thickness using depositions of Ge_4H_{10} at 360°C. The substrates were cleaved into four quadrants and cleaned by dipping in 10% aqueous HF prior to growth. The deposition experiments were performed using two separate reactors. The *n*-$Ge_{1-y}Sn_y$ layers were grown in an ultra-high vacuum chemical vapor deposition (UHV-CVD) system between 305°C and 280°C using gas mixtures of Ge_3H_8 and SnD_4 diluted by

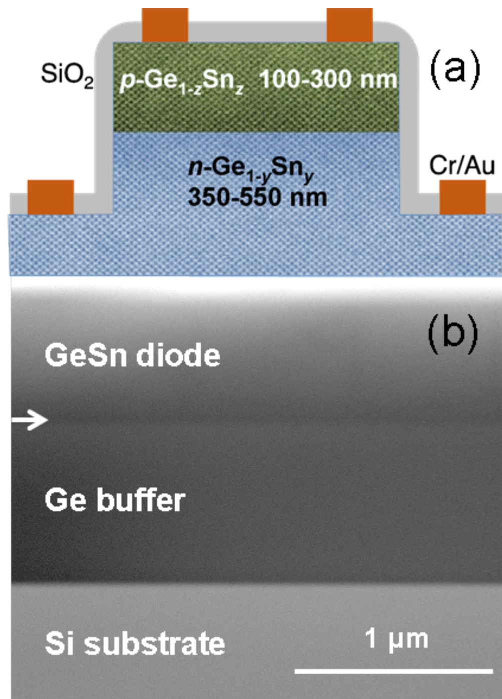

Figure 49: (a) Cross sectional schematic of LED *pn* device. Background is a high resolution XSTEM image of sample D, where the approximate location of the *p-n* interface is marked by the change in color. The image is taken in (110) projection and the lines represent (111) lattice fringes. (b) XSTEM bright field image of entire structure for sample D showing the Si substrate, Ge buffer and *pn* GeSn diode. The arrow marks the buffer-diode interface. Sample produced by Charutha Senaratne. See J. D. Gallagher, C. L. Senaratne, P. M. Wallace, J. Menéndez, and J. Kouvetakis, *Applied Physics Letters*, 107, 123507 (2015).

research-grade H_2. The film thicknesses ranged from 350-550 nm and their compositions varied from 6.5 to 12.3% Sn depending on temperature and precursor flux. *N*-type doping was performed by adding $P(SiH_3)_3$ to the $Ge_3H_8/SnD_4/H_2$ precursor mixture. $P(SiH_3)_3$ concentrations of 0.14 – 0.40 L-Torr in the reaction mixture yielded film donor densities in the 5×10^{18} cm^{-3} – 2.5×10^{19} cm^{-3} range. The latter values were determined by IR ellipsometry and corroborated by SIMS, indicating that the P atoms in the samples are fully activated, despite the low growth temperatures.[64] The doping levels are thus of the same magnitude as those used in prior studies to enhance pure-Ge emission.[74,80,199] The SIMS data also revealed residual Si levels typically lower than P and significantly below that expected from the 1:3 P/Si ratio in the precursor. This is presumably due to side reactions that remove SiH_3 groups from the precursor. The Si impurities are substitutional and do not affect the emission properties of the alloys described here in any measurable way.

The *p*-layers were produced in a separate UHV-CVD chamber using diborane (B_2H_6). The tool in this case comprised a horizontal quartz reactor resistively heated by a

three-zone furnace. The setting of each zone can be independently adjusted to allow tuning the temperature profile to pre-activate the compound by heating the gas stream before reaching the reaction zone. This procedure promoted the incorporation of B contents up to 1.2×10^{20} cm^{-3} and ensured near full activation of the acceptor atoms at ultra-low temperatures between 285^oC and 305^oC. Prior to growth a cleaning step was applied by flowing Ge_2H_6 over the *n*-layer for 5 minutes to create a deposition-ready surface for subsequent epitaxy of the *p*-layer. Under these conditions *p*-$Ge_{1-z}Sn_z$ (z = 3.5 – 12% Sn) layers with thicknesses up to 300 nm were grown on top of the *n*-$Ge_{1-y}Sn_y$ counterparts yielding complete *pn* junctions, as illustrated by the XSTEM image in Figure 49 (b) which shows a typical device stack with ~ 9% Sn. SIMS measurements revealed uniform distributions of the B and P atoms in the *p* and *n* regions of the devices followed by sharp transitions of the atomic counts at the interfaces.

For each sample produced in this study the Sn content of the *p*-layer was chosen to be sufficiently close to the *n*-layer so that the two materials grow fully coherent and lattice matched. The fringes in Figure 49 (a) are from a high resolution image at the interface for sample D and demonstrates no defects in the field of view due to the pseudomorphic growth conditions of the *p*-layer to the *n*-material. XRD measurements of the Bragg (004) reflections and (224) reciprocal space maps of the same sample reveal that the diode is lattice matched within the plane of growth and exhibits minimal interface strains due to the close similarity of Sn content in the constituent layers.

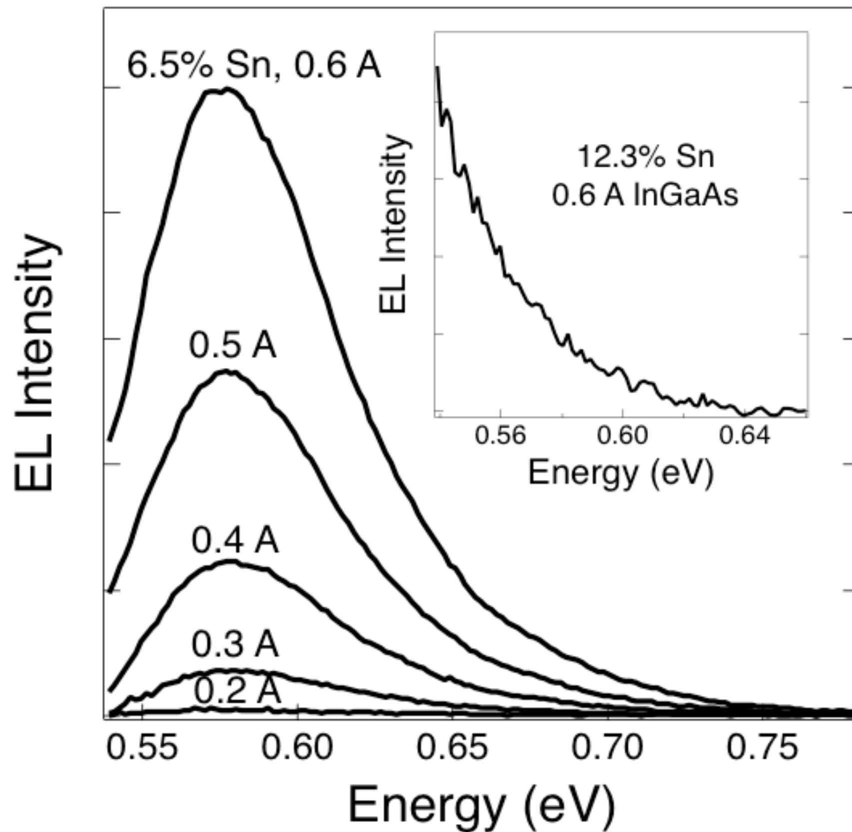

Figure 50: Room temperature EL from sample A as a function of injection current. Inset shows the EL signal from the *n*-layer of sample B obtained using an InGaAs detector.

The LEDs were fabricated using the methods described in section 2 of Chapter II (B) this dissertation. In this case the mesa patterns are defined by photolithography followed by etching the film approximately halfway down (200-300 nm) into the *n*-$Ge_{1-y}Sn_y$ layer using a BCl_3 reactive-ion source. The design of the final device is shown in the schematic of Figure 49 (a).

3. *Optical and Electronic Properties of $Ge_{1-y}Sn_y$ Degenerate pn Junctions on Ge/Si(100) Substrates*

The EL measurements were performed at room temperature under forward bias as discussed in section 4 of Chapter II (B). For samples with Sn content above 7% Sn, the

EL spectra were acquired using a thermoelectrically cooled PbS device as well with a detection range extending down to 2700 nm.

The initial *pn* devices fabricated using the above procedures were designed so that the *p*-doping of the top layer was significantly higher than that of the underlying *n*-layer. Under these conditions the depletion region should be largely displaced into the *n*-region where carrier recombination predominately occurs. In this case we should expect the EL spectra to exhibit emission peaks emanating primarily from the *n*-layer. This is corroborated by the EL spectrum from sample A in Figure 50, which shows a single peak at 0.576 eV, consistent with direct gap emission from the *n*-$Ge_{0.935}Sn_{0.065}$ material for this layer's strain and doping. Because the *p*-layer Sn concentration is significantly less, emission from this layer should be easily distinguishable from that of the *n*-layer if present. The spectra in the figure also show that the peak intensity increases super-linearly as a function of injection current in the 0.2-0.6 A range. This behavior was shown in previous sections from *pin* type $Ge_{1-y}Sn_y$ devices.

Next we produced an analogous *pn* sample with much higher Sn concentrations (sample B). Similarly to the sample A case, we do not see evidence of emission from the *p*-layer with 8.5% Sn, but a tail that we assign to emission from the *n*-layer with 12.3% Sn. In fact, this layer is expected to have a peak emission wavelength of ~2860 nm based on the sample composition and strain, well beyond the detection threshold of the PbS detector. Since the $Ge_{0.877}Sn_{0.123}$ material is expected to be a direct-gap semiconductor, this result suggests a viable path toward electrically injected laser devices based on such structures.

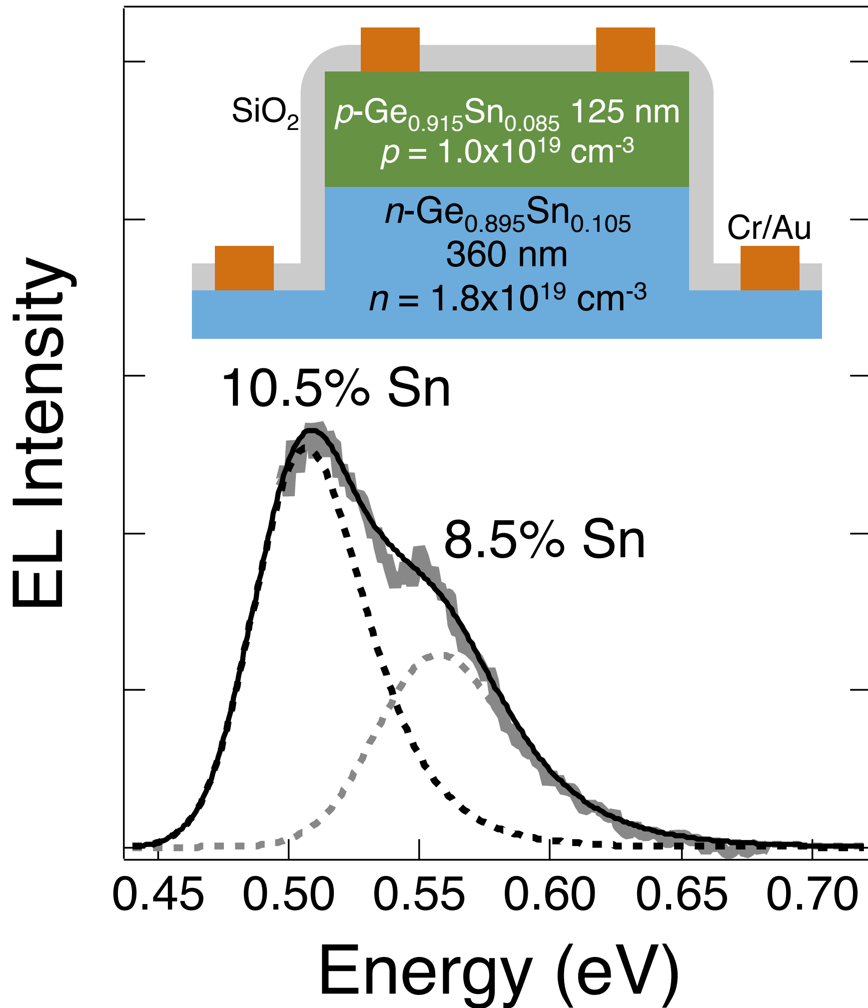

Figure 51: EL spectrum from sample C, a device with similar doping levels but dissimilar Sn contents, as shown in the schematic. The lines show a two-peak fit of the emission. The peaks are assigned to the *n*- and *p*-layer emission.

Next we changed the doping distribution profile of the depletion region in the device design by using nearly equal amounts of *p* and *n* doping. An example is Sample C, whose emission in Figure 51 shows two peaks at 0.504 eV and 0.557 eV corresponding to direct gap emission from the *n*- and *p*-layers, respectively. This is assigned to the more symmetric depletion layer in the $n \sim p$ case. The lines in Figure 51 are fits with EMGs, the motivation for using this lineshape has been discussed thoroughly in prior sections. The inset of Figure 51 displays the detailed device design used to obtain this result.

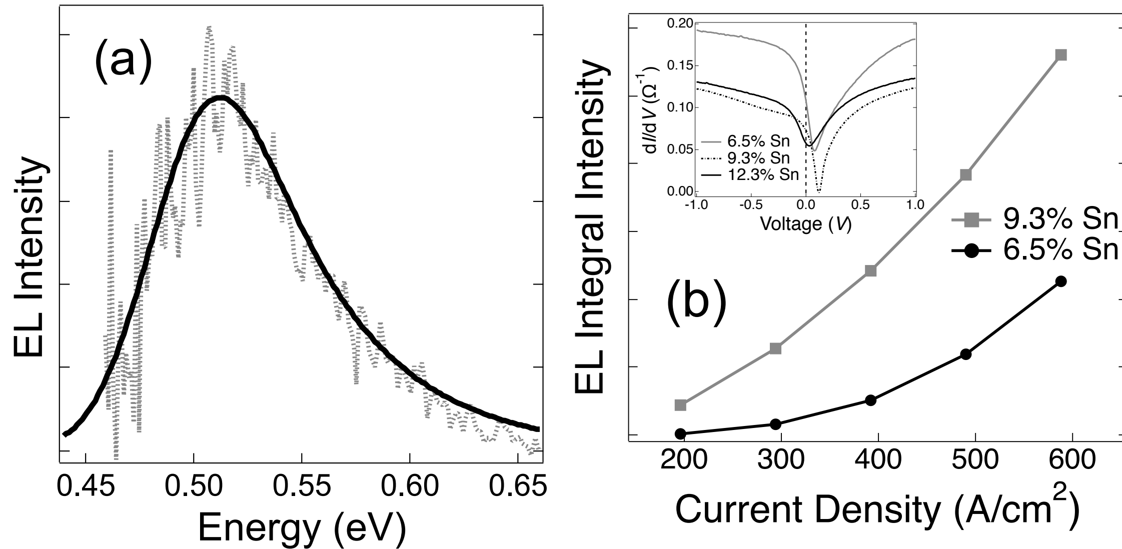

Figure 52: (a) Room-temperature (EL) spectra from sample D at a current density of 980 A/cm^2. The higher noise level is due to the use of a thermoelectrically cooled PbS detector to cover the entire spectral range. The solid line is a model fit with an EMG profile. (b) EL integral intensity plots from samples A and D. The inset shows differential conductance vs. voltage for samples A, B, and D.

The differences in Sn concentration in the layers of the above devices, while significant to produce a clear spectral signature, are small enough to keep the layers fully strained with defect-free interfaces. However, due to the potential for generating strain relaxation defects under demanding processing conditions, we proceeded to produce samples with similar amounts of Sn on both layers, so that the relative strain is minimized. Sample D is an example whose EL spectrum is shown for the diode in Figure 52 (a). The single peak at 0.512 eV, is attributed to direct gap emission from the *n*-type layer based on the $p >> n$ argument discussed above.

Figure 52 (b) shows the current dependence of the EL intensity for samples A and D. The data points are obtained by integrating the fit EMG profiles over their energy range. Both devices demonstrate a super-linear dependence of this integral intensity on injection level. The greater intensity output from sample D relative to the sample A is attributed to the former being more direct, since its composition lies at the threshold of

transition to direct gap semiconductors. Sample A shows a stronger intensity dependence on the injection current. This is because the ratio of the population in the Γ and L valleys of the conduction band (n_Γ/n_L) increases as a function of total injected carrier concentration for indirect gap materials such as 6.5% Sn, whereas in the case of 9.3% Sn this ratio is expected to remain constant as more carriers are added.

The inset in Figure 52 (b) shows plots of differential conductance (d*I*/d*V*) vs. applied bias for samples A, B, and D. The *p*-doping concentrations for each of these samples are nearly one order of magnitude greater than the corresponding *n*-doping counterparts. The plots from each device show a conductance minimum at forward bias levels less than 0.2 V, which is reminiscent of Esaki-type electrical behavior.[200] We note that sample D, for which the relative interfacial strain is lowest, is the only sample that reaches truly negative differential conductance conditions. This outcome is consistent with a reduction of excess currents originating from of interfacial defects.[201]

4. Conclusion

The demonstration of working *pn* junctions in this section should stimulate further studies to produce entire families of devices with varying film parameters whose optical and electrical properties are refined and optimized. The observation of significant light emission described here represents a step forward for the development of electrically pumped quasi-direct $Ge_{1-y}Sn_y$ lasers.

B. Optically Pumped Waveguides

1. Introduction

As discussed previously in this dissertation, reports of lasing devices based on group-IV materials have emerged within the last 5 years. Initially Liu *et. al.* reported the

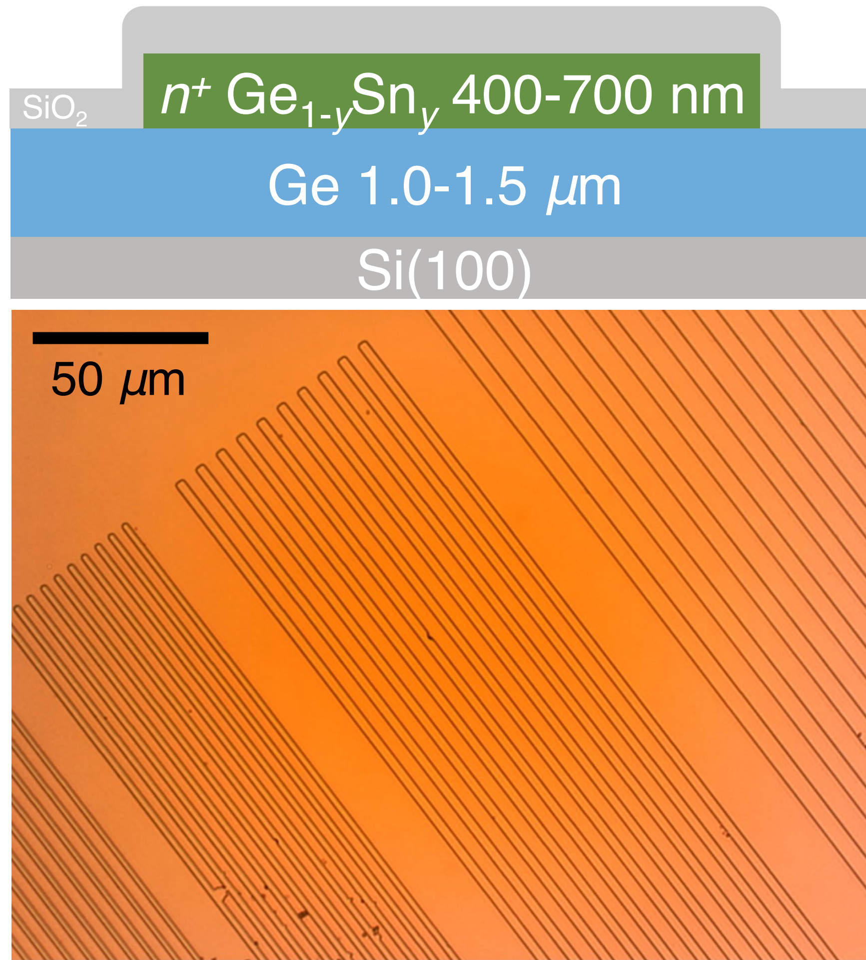

Figure 53: (Top) Schematic stack of a n-$Ge_{1-y}Sn_y$ laser waveguide sample. (Bottom) Top-down optical image of waveguides after passivation layer deposition.

first optically pumped Ge device.[80] In this case, lasing at room temperature was obtained from tensile strained materials that were heavily doped *n*-type in the range of 10^{19} cm^{-3}. A few years later, this same group produced an electrically pumped device on Si as well.[81] The same strategies were employed to obtain quasi-direct band gap characteristics so that lasing could be achieved at room temperature. Namely, the Ge layer was tensile strained and doped *n*-type into the degenerate limit. A disadvantage to these devices is the heavy *n*-type doping of the active region which exhibits a high degree of free carrier absorption and the fundamentally indirect character of the band structure, limiting the practical

functionality of these lasers. This is highlighted by the high current densities that were necessary to obtain lasing from the electrically injected device (over 300 kA/cm^2). Lasing has also been reported in optically pumped $Ge_{1-y}Sn_y$ waveguides.[110] In this case, intrinsic materials at compositions $y > y_c$ were grown on Ge-buffered Si platforms, similar to the protocols discussed in previous chapters to obtain high-quality $Ge_{1-y}Sn_y$ layers. However lasing was only obtained at low temperature in an optically stimulated device, likely due to the relatively low population of the Γ valley relative to the L, even in the case of technically direct gap materials (see Figure 21).

In this section, we discuss the development of a hybrid approach between these two methods to attempt to obtain lasing in $Ge_{1-y}Sn_y$ materials. The strategy is to produce high quality materials on Ge-buffered Si platforms that contain a significant Sn fraction to decrease the Γ-L separation and are doped *n*-type into the degenerate limit to enhance the optical capabilities. These samples are then processed into waveguide structures and are being measured at the University of Dayton. To date these devices have been reported as showing signs of stimulated emission from optical pumping under ambient conditions.[202]

2. Growth and Materials Properties of n-$Ge_{1-y}Sn_y$ Waveguides

Figure 53 top panel demonstrates the design and fabrication of heavily-doped (n = 0.5-8.0×10^{19} cm^{-3}) $Ge_{1-y}Sn_y$ waveguide structures integrated on Si(100). These samples consist of thick (400-700 nm), bulk-like *n*-$Ge_{1-y}Sn_y$ materials with Sn compositions above and below the threshold to direct gap semiconductors grown upon Ge-buffered Si. The advantage of heavy *n*-type doping $Ge_{1-y}Sn_y$ layers is that it provides the opportunity to observe lasing in samples at room temperature, possibly at compositions below the

indirect-to-direct gap crossover, due to the enhanced population of carriers in the conduction band combined with a reduced Γ-L valley separation. The doping is achieved by use of the rationally designed tetrahedral $P(SiH_3)_3$ unit. The integration of this molecule with the growth process was described in part A of this chapter. RBS, XRD, spectroscopic ellipsometry, and SIMS measurements revealed that the layers produced by this growth method are thick, single phase crystals aligned to the Si substrate with fully substitutional Sn atoms and activated P dopants.

Waveguide mesas 4 mm long and widths ranging from 1.6-100 μm are defined by standard photolithography and reactive ion etch techniques as shown in the bottom panel of Figure 53. These patterns were formed by the same processing techniques described in prior sections. The mesas are passivated with a thin SiO_2 film with thickness optimized to minimize the reflectance of this layer to the pump photons incident on the sample. After this, sections of the waveguides are cut from the wafer using a diamond saw and both ends perpendicular to the waveguides are polished to a mirror finish using diamond lapping paper. The finest grit of lapping paper applied in this case was 0.1 μm. Once polishing is completed metals are deposited onto one end of the polished facets to optimize confinement of the light in the cavity and to minimize losses.

3. Optical Properties of n-$Ge_{1-y}Sn_y$ Waveguides

The optical properties of the waveguides were initially characterized at Arizona State University in collaboration with Prof. Cun-Zheng Ning's lab. Briefly, excitation was achieved using two light pump sources: a Ti:Sapphire laser with an 810 nm wavelength operating at 80 MHz and a UV laser with a 349 nm wavelength pulsed at 2 kHZ. The pulse widths of these lasers are 150 fs and 4 ns, respectively. The maximum

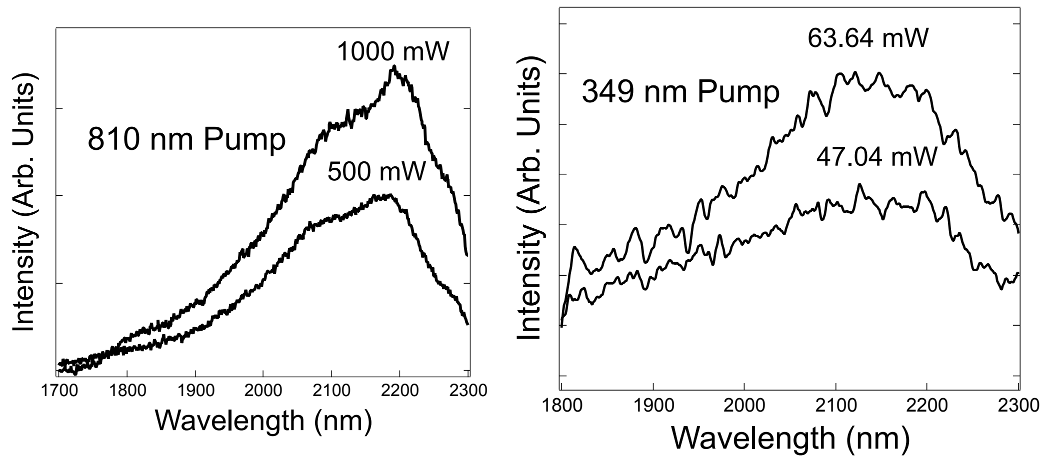

Figure 54: Optical properties of 10 μm waveguides containing ~6.5% Sn from 2 separate excitation sources. No waveguide modes are observed as the optical output appears to be reproducing the PL spectra of the unprocessed material.

average power of the Ti:Sapphire laser is 1.1 W while the UV laser can deliver up to 36 μJ/pulse. The beam profile of the lasers were formed into a ~ 1 cm x 20 μm stripe using cylindrical and spherical lenses such that a single waveguide could be excited at a time, as confirmed by using a Si-based IR camera. The laser light was incident from the top of the waveguide while the light was collected out of the facet without a metallic film. The light was sent through a Triax320 spectrometer with a 150 grooves/mm grating and a slit size of 2 mm. The signal was detected by a LN_2 cooled InGaAs photodiode. An optical chopper was placed in the beam path prior to the light reaching the sample so that lockin detection could be employed for the measurement.

Figure 54 shows the results from a 6.5% Sn sample from two different laser pump sources on a set of 10 μm wide waveguides as a function of the average light power incident on the sample. We observe an intensity increase as a function of pumping power, however there is no narrowing of any spectral features that would indicate waveguide modes are present as these features are very broad. The spectra are reminiscent of the

room temperature PL of the sample material prior to processing into the waveguide device. We note that although waveguide modes were not obtained by these measurements, this is likely due to an improperly aligned and/or not-optimized optical apparatus rather than poor quality materials and processing protocols. The main issue is likely to be a suitable pumping source. The Ti:Sapphire laser pulse is very short compared to the carrier lifetimes, it could be that the carriers completely recombine before another pulse reaches the sample, eliminating any chance to achieve the necessary population inversion for lasing. The issue with the UV-laser is likely due to the fact this light pumps carriers into states high above the Γ-valley in the conduction band. The carriers may then bypass the Γ-valley in a relaxation cascade. However the collection optics may not be well suited for these wavelengths as well. Recent work demonstrated in Ref. 202 on the same samples at the University of Dayton in Prof. Jay Mathews's lab have produced more promising results that show lasing is likely occurring at room temperature from these devices.

4. Conclusion

In summary, the waveguides discussed in this chapter did not show optical modes with the resources at ASU. Prof. Jay Mathews's lab at the University of Dayton however is making progress demonstrating that these materials are on their way to realizing their potential as group-IV lasers integrated onto Si.

V. CONCLUSIONS AND PROPOSAL FOR FUTURE WORK

This dissertation has presented a series of systematic investigations into the optical and electronic properties of the group-IV alloys $Ge_{1-y}Sn_y$ and $Ge_{1-x-y}Si_xSn_y$. In Chapter II we demonstrated from room temperature PL of optimized samples that the indirect to direct gap crossover composition in $Ge_{1-y}Sn_y$ alloys occurs at $y_c = 0.087$. The bowing parameters for E_0 and E_{ind} in this system were found to be compositionally dependent and this had a significant impact on the y_c value compared with previous reports. We further went on to show that the emission from these materials was most optimized by doping the material *n*-type which leads to an order of magnitude intensity enhancement of the PL signal over intrinsic samples. Passivating the surface with hydrogen through plasma techniques was found to best optimize the emission of intrinsic samples, but this was still not quite as strong as the *n*-doped samples. *Pin* devices using these materials as the active *i*-layer were then fabricated and showed the same transition to direct gap materials due to the improved light emission that was obtained as more Sn was incorporated into the *i*-layer. Two models of lifetime measurements based on the EL spectra intensities showed that defects at the layer interfaces cause a significant efficiency droop due to strain relaxation occurring between lattice mismatched materials. Much longer carrier recombination lifetimes are obtained in devices with no strain relaxed fully pseudomorphic interfaces.

In Chapter III, PL measurements of Sn-rich $Ge_{1-x-y}Si_xSn_y$ materials demonstrated a crossover to direct gap materials exists in the group-IV ternary alloy. This discovery was enabled by the first documentation of the E_{ind} energies over the composition space in this system. LEDs based on these materials were then fabricated in analogy to the previous

$Ge_{1-y}Sn_y$ *pin* devices of Chapter II and showed good rectifying characteristics, tunable absorption edges beyond the detection limit of Ge, and functional LEDs integrated onto Si with quasi-direct E_0 emission peaks. To enable a complete description of the ternary band gaps over the composition space, the E_0 energies of $Ge_{1-x}Si_x$ alloys were meticulously measured in the Ge-rich limit, providing the bowing parameters necessary to carry out an accurate global fit leaving the SiSn bowing coefficients adjustable. The PL from these materials displayed a third peak not attributable to defects or compositional inhomogeneities, the origin of which is still unknown. Global fits to all available ternary E_0 and E_{ind} data showed that there is a very large, compositionally dependent bowing coefficient associated with the binary SiSn constituent. The analysis revealed that a slight addition of Si into direct gap $Ge_{1-y}Sn_y$ alloys could produce improved direct gap materials, contrary to common understanding.

In Chapter IV the lasing potential of group-IV materials was explored through the development of electrically injected $Ge_{1-y}Sn_y$ degenerate *pn* junctions and optically pumped waveguides. The heavily doped *pn* diodes show potential to be the building block for future designs of high-efficiency $Ge_{1-y}Sn_y$ light sources while the waveguides have been reported elsewhere to show signs of lasing at room temperature.

In order to expand on the work presented here, several device based research projects can be pursued to determine the best design for a group-IV laser on Si. The first set of devices to explore would be ternary degenerate *pn* junctions. Essentially the study would aim to produce analogs to the $Ge_{1-y}Sn_y$ devices presented in Chapter IV to measure the effect of Si incorporation on the electronic and optical performance. This development could be extended by producing homostructure *pin* $Ge_{1-x-y}Si_xSn_y$ diodes to

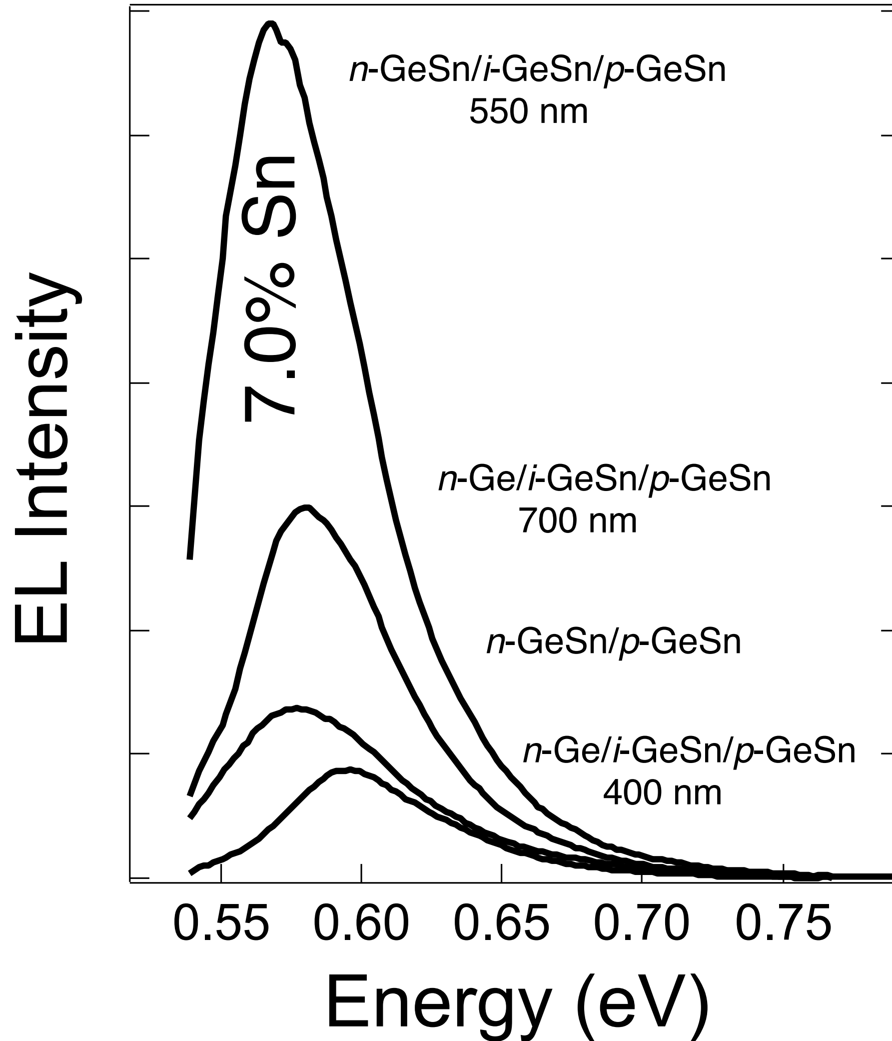

Figure 55: Room temperature EL from the various $y = 0.07$ $Ge_{1-y}Sn_y$ LEDs presented in this dissertation. The figure illustrates the importance of lattice matched interfaces and optimal *i*-layer thickness for the design of electrically pumped group-IV lasers.

eliminate all defective interfaces. In this case the lifetime model developed in Chapter II can be applied to measure the effect of Si content on the carrier lifetimes.

The recent development of homostructure $Ge_{1-y}Sn_y$ devices can be expanded on by producing devices with varying *i*-layer thicknesses while holding the Sn content fixed. The aim here would be to produce *pin* devices where all layers are at a fixed Sn composition with emission peaks that can be easily resolved with the InGaAs detector. The *i*-layer thickness could be systematically varied over a range of 0-600 nm. The

recommended composition for such a study would be ~7.0% Sn since in Chapters IV and II, respectively, we essentially already have data for the starting and end-point devices at this composition (See samples GeSn7_h in Chapter II and sample D in Chapter IV).

To achieve optimal confinement of carriers in the active region, devices with a Type-I band offset should be sought out. A systematic approach to this would be to begin with a relaxed *n*-$Ge_{1-x-y}Si_xSn_y$ contact layer with equal Si and Sn contents (for example 5% Si and 5% Sn). For comparison across all samples to be studied and to enable easier measurement of the degree of confinement, the *p*-layer should be made to match the *n*-layer composition. The first strategy to obtain confinement in the *i*-layer would be to hold the Si content fixed while increasing the Sn in this layer. Typical compositions could be 5% Si and 5-15% Sn. The one constraint with this type of device will be that the thickness of the *i*-layer will likely need to be kept below ~300-400 nm in order to ensure pseudomorphic growth to the *n*-contact. Another strategy would be to use the same *n* and *p*-$Ge_{1-x-y}Si_xSn_y$ contacts as in the previous example while fixing the Sn content near 10% and decreasing the Si content from 5% to 0% in the *i*-layer. In both cases we would expect the emission to redshift to longer wavelengths for higher Sn devices. However the constraint for pseudomorphic growth will mean that these devices will be fighting against increasing compressive strain in the higher Sn samples. Overall the aim will be to investigate if the emission intensity improves due to increased carrier confinement to the *i*-layer in devices with no strain relaxation defects at both component interfaces.

Lastly, the results from this dissertation indicate that the growth technology of these materials has matured to the stage that the pursuit of an electrically pumped group-IV alloy laser on Si is a viable research project. In Figure 55 we compare the 0.5 A room

temperature EL spectra from all $Ge_{0.93}Sn_{0.07}$ LEDs devices discussed previously in this dissertation. As expected, the plots show that the strongest light emission comes from the lattice matched *pin* device architecture with no defective interfaces. The two other *pin* diodes in the figures contain a defected *n*-Ge/*i*-$Ge_{1-y}Sn_y$ interface and show quenched emission relative to the lattice-matched structure. On the other hand, these devices also show an increased intensity emission is achieved when the intrinsic layer thickness is varied from 400 nm to 700 nm. The importance of intrinsic layer thickness engineering to optimize the emission is further illustrated by comparing the intensities of the degenerate *pn* junction LED with the lattice matched *pin* device containing a 550 nm *i*-layer. In this particular case the *pn* junction LED is acting as a lattice matched *pin* diode with a 0 nm *i*-layer thickness. For the strain-relaxed 400 nm and 700 nm *i*-layer devices, the integral intensity increases ~3x for a 175% increase in *i*-layer thickness, however, for the lattice matched devices we see the integral intensity increase by ~4.5x between 0 nm and 550 nm *i*-layers. This suggests that the long minority carrier diffusion lengths cause a significant portion of radiative recombination to occur in the *n*-$Ge_{1-y}Sn_y$ layers of lattice matched $Ge_{1-y}Sn_y$ LEDs. As previously shown in PL studies comparing *n*-type and *i*-$Ge_{1-y}Sn_y$ materials, the *n*-$Ge_{1-y}Sn_y$ PL emission is nearly an order of magnitude greater than *i*-$Ge_{1-y}Sn_y$ emission. From a device design perspective then, *i*-layers aid to increase the emission intensity by providing a greater volume of material that can emit light, however the emission from *n*-type materials is stronger per unit volume. Thus to design an optimal electrically pumped $Ge_{1-y}Sn_y$ laser diode, these considerations must be taken into account. It is also significant to note that the *pn* LED peak is redshifted relative to the *pin* diodes since the emission from this device primarily originates in the *n*-type region where the

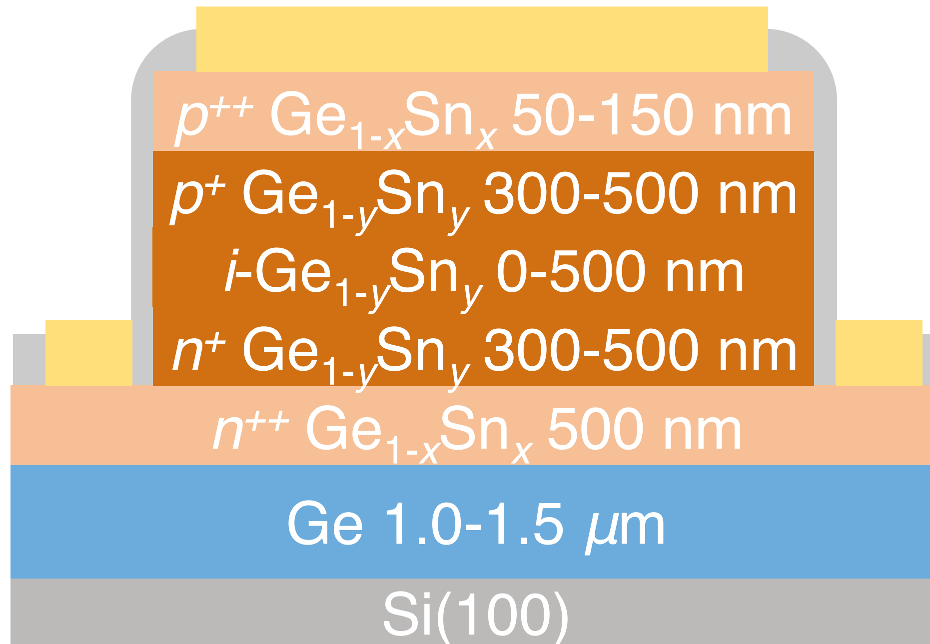

Figure 56: Schematic architecture design for a proposed electrically injected $Ge_{1-y}Sn_y$ laser diode integrated onto Si.

band gap has been renormalized to a lower energy due to the heavy-doping levels. Finally we note that at this level of current injection the *pn* LED has a higher EL intensity than the 400 nm *pin* device despite the significantly smaller active region volume where radiative recombination takes place in the former relative to the latter, a testament to the deleterious effects of interface defects on overall device performance.

Based on these outcomes, the schematic in Figure 56 would likely be the optimal structure to achieve electrically pumped lasing in $Ge_{1-y}Sn_y$ materials at room temperature. This structure would begin by growing thick (1.0-1.5 μm) low-defect density Ge on Si(100) platforms to accommodate the large lattice mismatch between the Si and direct-gap $Ge_{1-y}Sn_y$ materials ($y \geq 0.09$). Next, a heavily doped ($n \sim 0.5\text{-}1.0\times10^{20}$ cm^{-3}) $Ge_{1-x}Sn_x$ bottom contact layer is grown by the UHV-CVD methods discussed throughout this work. This layer is made thick (~500 nm) on the Ge buffer so that the material relaxes during growth and so that Ohmic contacts can be formed well away from the dislocations

generated at the Ge/$Ge_{1-x}Sn_x$ interface. A judicious choice $x < y$ is made such that the target direct gap $Ge_{1-y}Sn_y$ active materials grow lattice matched to the contact layer. This choice also has the effect of creating a wider the band gap in the contact layer that confines the carriers to the emitting layers by a Type-I band offset. In order to create the necessary population inversion across the diode junction when it is forward-biased, heavily doped ($n, p \sim 0.5\text{-}2.0\times10^{19}$ cm^{-3}) direct gap $Ge_{1-y}Sn_y$ materials are grown next by the same methods as the bottom contact layer. The quantum efficiency of the device may be optimized by inserting an intrinsic layer of the $Ge_{1-y}Sn_y$ alloy between the doped regions. The thickness of this layer is left as a parameter that may be tuned to optimize the efficiency. Finally a thin capping p-$Ge_{1-x}Sn_x$ ($p \sim 0.5\text{-}1.0\times10^{20}$ cm^{-3}) confinement layer that mirrors the effect of the n-$Ge_{1-x}Sn_x$ layer is grown to complete the stack. Upon completion of the blanket layer growths the wafer should be processed into equilateral triangle resonator waveguide mesa structures[203,204] using the previously described photolithography, reactive ion etching, and metal evaporation/liftoff techniques.

REFERENCES

[1] "On the relationship of the properties of the elements to their atomic weights", D. I. Mendeleev.

[2] C. Winkler and J. Prak, *Chemie* **34**, 177 (1886).

[3] F. Bloch, *Z. Phys.* **52**, 555-600 (1928).

[4] A. H. Wilson, *Proc. Roy. Soc.*, **A133**, 458-491 (1931).

[5] L. Hoddeson, E. Braun, J. Teichmann, and S. Weart, *Out of the Crystal Maze* (Oxford, New York, 1992), pp. 455-460.

[6] K. Lark-Horovitz, "Preparation of Semiconductors," National Defense Research Council report 14-585, 1945 (unpublished).

[7] J. Bardeen and W. H. Brattain, *Phys. Rev.* **74**, 230 (1948).

[8] F. Herman and J. Callaway, *Phys. Rev.* **89**, 518 (1953).

[9] C. Kittel, *Physica* **20**, 829 (1954).

[10] W. Shockley and J. Bardeen, *Phys. Rev.* **77**, 407 (1950).

[11] D. Navon, R. Bray, and H. Y. Fan, *Proc. IRE* **40**(11), 1342-1347 (1952).

[12] H. Gummel and M. Lax, *Phys. Rev.* **97**, 146 (1955).

[13] S. G. Kalashnikov, *J. Phys. Chem. Solids* **8**, 52 (1959).

[14] G. K. Teal and J. B. Little, *Phys. Rev.* **78**, 647 (1950).

[15] F. S. Goucher, G. L. Pearson, M. Sparks, G. K. Teal, and W. Shockley, *Phys. Rev.* **81**, 637 (1951).

[16] W. Shockley, M. Sparks, and G. K. Teal, *Phys. Rev.* **83**, 151 (1951).

[17] J. Kilby, *IEEE T. Electron. Dev.* **ED-23**, 648 (1978).

[18] S. Benzer, *Phys. Rev.* **72**, 1267 (1947).

[19] M. Becker and H. Y. Fan, *Phys. Rev.* **78**, 301 (1950).

[20] W. Shockley, *Phys. Rev.* **78**, 294 (1950).

[21] F. S. Goucher, *Phys. Rev.* **78**, 816 (1950).

[22] J. A. Hoerni, *IRE T. Electron. Dev.* **ED-8**, 178 (1961).

[23] C. S. Wang and B. M. Klein, *Phys. Rev. B* **24**(6), 3393-3416 (1981).

[24] O. Madelung, *Semiconductors: Group IV Elements and III-V Compounds* (Springer, New Jersey, 1991), pp. 31.

[25] J. Weber, and M. I. Alonso, *Phys. Rev. B* **40**(8), 5683 (1989).

[26] C. N. Ahmad, and A. R. Adams, *Phys. Rev. B* **34**(4), 2319 (1986).

[27] G. Li, A. Goñi, K. Syassen, and M. Cardona, *Phys. Rev. B* **49**(12), 8017 (1994).

[28] M. Fox, *Optical Properties of Solids* (Oxford, New York, 2001), pp. 64.

[29] J. R. Chelikowsky and M. L. Cohen, *Phys. Rev. B* **30**, 556 (1976).

[30] J. C. Hensel and K. Suzuki, *Phys. Rev. B* **9**, 4219 (1974).

[31] G. G. MacFarlane, T. P. McLean, J. E. Quarrington, and V. Roberts, *Phys. Rev.* **108**, 1377 (1957).

[32] S. Zwerdling, B. Lax, L. M. Roth, K. J. Button, *Phys. Rev.* **114**, 80 (1959).

[33] G. Mak, and H. M. van Driel, *Phys. Rev. B* **49**, 16817(R) (1994).

[34] W. C. Dash and R. Newman, *Phys. Rev.* **99**(4), 1151-1155 (1955).

[35] V. R. D'Costa, Y. Fang, J. Mathews, R. Roucka, J. Tolle, J. Menéndez, and J. Kouvetakis, *Semicond. Sci. Technol.* **24**, 115006 (2009).

[36] K. P. O'Donnell and X. Chen, *Appl. Phys. Lett.* **58**, 2924 (1991).

[37] Y. P. Varshni, *Physica* **34**(1), 149-154 (1967).

[38] G. Grzybowski, R. Roucka, J. Mathews, L. Jiang, R. T. Beeler, J. Kouvetakis, and J. Menéndez, *Phys. Rev. B* **84**, 205307 (2011).

[39] L. Kelion, *Intel Launches First 14-nanometre Processor for Thin Fanless PCs* (BBC News: Technology) Sept. 5, 2014.

[40] E. Kasper and D. J. Paul, *Silicon Integrated Circuits* (Springer, Berlin, 2005) pp. 344.

[41] C. Xu, J. D. Gallagher, P. Sims, D. J. Smith, J. Menéndez, and J. Kouvetakis, *Semicond. Sci. Technol.* **30**, 045007 (2015).

[42] K. Nishioka, T. Takamoto, T. Agui, M. Kaneiwa, Y. Uraoka, *Sol. Energ. Mat. Sol. C.* **90**, 1308 (2006).

[43] R. R. King, C. M. Fetzer, P. C. Colter, K. M. Edmondson, D. C. Law, A. P. Stavrides, H. Yoon, G. S. Kinsey, H. L. Cotal, J. H. Ermer, R. A. Sherif, K. Emery, W. Metzger, R. K. Ahrenkiel, and N. H. Karam, *Proceedings of the Third World Conference on Photovoltaic Energy Conversion* (Arisumi, Japan, 2003), pp. 622.

[44] R. Ramaswami, *IEEE Communications Magazine* (May, 2002), pp. 138-147.

[45] A. Lee, H. Liu, and A. Seeds, *Semicond. Sci. Technol.* **28**, 015027 (2013).

[46] R. Soref, *IEEE J. Sel. Top. Quant.* **12**, 1678-1687 (2006).

[47] R. Fischer, W. Kopp, H. Morkoc, M. Pion, and A. Specht, *Appl. Phys. Lett.* **48**, 1360-1361 (1986).

[48] R. D. Dupuis, J. P. van der Ziel, R. A. Logan, J. M. Brown, and C. J. Pinzone, *Appl. Phys. Lett.* **50**, 407 (1987).

[49] K. Morizane, *J. Cryst. Growth* **38**, 249-254 (1977).

[50] C. Choi, R. Ai, and S. Barnett, *Phys. Rev. Lett.* **67**, 2826-2829 (1991).

[51] W. I. Wang, *Appl. Phys. Lett.* **44**, 1149 (1984).

[52] T. Wang, H. Liu, A. Lee, F. Pozzi, and A. Seeds, *Opt. Express* **19**, 11381-11386 (2011).

[53] F. Lu, T. Tran, W. Ko, K. Ng, and R. Chen, *Opt. Express* **20**, 12171 (2012).

[54] G. T. Reed, W. R. Headley, and C. E. J. Png, *Proceedings SPIE* **5730**, (United States, 2005), pp. 1.

[55] C. Claeys and E. Simoen, *Germanium-Based Technologies: From Materials to Devices* (Oxford, Elsevier, 2007), pp. 387-449.

[56] L. N. Aleksandrov, R. N. Lovyagin, O. P. Pchelyakov, and S. I. Stenin, *J. Cryst. Growth* **24**(25), 298 (1974).

[57] A. G. Cullis and G. R. Booker, *J. Cryst. Growth* **9**, 132 (1971).

[58] D. J. Eaglesham and M. Cerullo, *Phys. Rev. Lett.* **64**(16), 1943 (1990).

[59] F. Scarinci, M. Fiordelisi, R. Calarco, S.j Lagomarsino, L. Colace, G. Masini, G. Barucca, S. Coffa, and S. Spinella, *J. Vac. Sci. Tech.* **B** 16, 1754 (1998).

[60] M. T. Currie, S. B. Samavedam, T. A. Langdo, C. W. Leitz, and E. A. Fitzgerald, *Appl. Phys. Lett.* **98**, 1718 (1998).

[61] C. Xu, R. T. Beeler, L. Jiang, G. Grzybowski, A. V. G. Chizmeshya, J. Menéndez, and J. Kouvetakis, *Semicond. Sci. Technol.* **28**, 105001 (2013).

[62] G. Grzybowski, L. Jiang, R. T. Beeler, T. Watkins, A. V. G. Chizmeshya, J. Menéndez, and J. Kouvetakis, *Chem. Mater.* **24**(9), 1619-1628 (2012).

[63] L. Jiang, C. Xu, J. D. Gallagher, R. Favaro, T. Aoki, J. Menéndez, and J. Kouvetakis, *Chem. Mater.* **26**(8), 2522-2531 (2014).

[64] C. Xu, C. L. Senaratne, J. Kouvetakis, and J. Menéndez, *Appl. Phys. Lett.* **105**, 232103 (2014).

[65] C. Xu, J. D. Gallagher, P. M. Wallace, C. L. Senaratne, P. Sims, J. Menéndez, and J. Kouvetakis, *Semicond. Sci. Technol.* **30**, 105028 (2015).

[66] T. –H. Cheng, K. –L. Peng, C. –Y. Ko, C. –Y. Chen, H. –S. Lan, Y. –R. Wu, C. W. Liu, and H. –H. Teng, *Appl. Phys. Lett.* **96**, 211108 (2010).

[67] J. Michel, J. Liu, and L. C. Kimerling, *Nature Photonics* **4**, 527-534 (2010).

[68] Y. Huo, H. Lin, R. Chen, M. Makarova, Y. Rong, M. Li, T. I. Kamins, J. Vuckovic, and J. S. Harris, *Appl. Phys. Lett.* **98**, 011111 (2011).

[69] Y. Ishikawa, K. Wada, J. Liu, D. D. Cannon, H. –C. Luan, J. Michel, and L. C. Kimerling, *J. Appl. Phys.* **98**, 013501 (2005).

[70] X. Sun, J. Liu, J. Michel, and L. C. Kimerling, *Opt. Lett.* **34**(8), 1198-1200 (2009).

[71] W. Hu, B. Cheng, C. Xue, S. Su, A. Bai, L. Luo, Y. Yu, and Q. Wang, *Appl. Phys. Lett.* **95**, 092102 (2009).

[72] M. El Kurdi, T. Kociniewski, T. –P. Ngo, J. Boulmer, D. Débarre, P. Boucaud, J. F. Damlencourt, O. Kermarrec, and D. Bensahel, *Appl. Phys. Lett.* **94**, 191107 (2009).

[73] R. T. Beeler, G. Grzybowski, R. Roucka, L. Jiang, J. Mathews, D. J. Smith, J. Menéndez, A. V. G. Chizmeshya, and J. Kouvetakis, *Chem. Mater.* **23**(20), 4480-4486 (2011).

[74] X. Sun, J. Liu, L. C. Kimerling, and J. Michel, *Appl. Phys. Lett.* **95**, 011911 (2009).

[75] J. Liu, X. Sun, L. C. Kimerling, and J. Michel, *Opt. Lett.* **34**(11), 1738-1740 (2009).

[76] C. Haas, *Phys. Rev.* **125**, 1965 (1962).

[77] S. –L. Cheng, G. Shambat, J. Liu, H. –Y. Yu, K. Saraswat, T. I. Kamins, J. Vuckovic, and Y. Nishi, *Appl. Phys. Lett.* **98**, 211101 (2011).

[78] P. B. Allen, *Phys. Rev. B* **18**, 5217 (1978).

[79] B. Chakraborty and P. B. Allen, *Phys. Rev. B* **18**, 5225 (1978).

[80] J. Liu, X. Sun, R. Camacho-Aguilera, L. C. Kimerling, and J. Michel, *Opt. Lett.* **35**(5), 679-681 (2010).

[81] R. Camacho-Aguilera, Y. Cai, N. Patel, J. T. Bessette, M. Romagnoli, L. C. Kimerling, and J. Michel, *Opt. Exp.* **20**(10), 11316-11320 (2012).

[82] C. H. L. Goodman, *Solid State and Electronic Devices,* IEE Proceedings I **129**(5), 189 (1982).

[83] S. Groves and W. Paul, *Phys. Rev. Lett.* **11**, 194 (1963).

[84] D. W. Jenkins and J. D. Dow, *Phys. Rev. B* **36**, 7994 (1987).

[85] K. A. Mäder, A. Baldereschi, and H. von Känel, *Solid State Commum.* **69**, 1123 (1989).

[86] G. He and H. A. Atwater, *Phys. Rev. Lett.* **79**(10), 1937-1940 (1997).

[87] V. R. D'Costa, C. S. Cook, A. G. Birdwell, C. L. Littler, M. Canonico, S. Zollner, J. Kouvetakis, and J. Menéndez, *Phys. Rev. B* **73**, 125207 (2006).

[88] *CRC Handbook of Chemistry and Physics*, 90th ed. (CRC Press, Boca Raton, 2009), pp. 12-80.

[89] R. T. Beeler, R. Roucka, A. V. G. Chizmeshya, J. Kouvetakis, and J. Menéndez, *Phys. Rev. B* **84**, 035204 (2011).

[90] S. Oguz, W. Paul, T. F. Deutsch, B. –Y. Tsaur, and D. V. Murphy, *Appl. Phys. Lett.* **46**, 848 (1983).

[91] F. A. Trumbore, *J. Electrochem Soc.* **103**(11), 597 (1956).

[92] S. I. Shah, J. E. Greene, L. L. Abels, Q. Yao, and P. M. Raccah, *J. Cryst. Growth* **83**, 3 (1987).

[93] E. A. Fitzgerald, P. E. Freeland, M. T. Asom, W. P. Lowe, R. A. Macharrie Jr., B. E. Weir, A. R. Kortan, F. A. Thiel, Y. –H. Xie, A. M. Sergent, S. L. Cooper, G. A. Thomas, and L. C. Kimerling, *J. Electron. Mater.* **20**, 489 (1991).

[94] W. Wegscheider, J. Olajos, U. Menczigar, W. Dondl, and G. Abstreiter, *J. Cryst. Growth* **123**, 75 (1992).

[95] M. Rojas-López, H. Navarro-Contreras, P. Desjardins, O. Gurdal, N. Taylor, J. R. A. Carlsson, and J. E. Greene, *J. Appl. Phys.* **84**(4), 2219-2223 (1998).

[96] O. Gurdal, R. Desjardins, J. R. A. Carlsson, N. Taylor, H. H. Radamson, J. –E. Sundgren, and J. E. Greene, *J. Appl. Phys.* **83**, 162 (1998).

[97] J. Taraci, J. Tolle, M. R. McCartney, D. J. Smith, J. Menéndez, M. A. Santana, and J. Kouvetakis, *Appl. Phys. Lett.* **78**(23), 3607-3609 (2001).

[98] M. Bauer, J. Taraci, J. Tolle, A. V. G. Chizmeshya, S. Zollner, D. J. Smith, J. Menéndez, C. Hu, and J. Kouvetakis, *Appl. Phys. Lett.* **81**(16), 2992-2994 (2002).

[99] M. Bauer, C. S. Cook, P. Aella, J. Tolle, J. Kouvetakis, P. A. Crozier, A. V. G. Chizmeshya, D. J. Smith, and S. Zollner, *Appl. Phys. Lett.* **83**, 3489 (2003).

[100] J. Xie, J. Tolle, V. R. D'Costa, C. Weng, A. V. G. Chizmeshya, J. Menéndez, and J. Kouvetakis, *Solid State Electron.* **53**, 216 (2009).

[101] J. Mathews, R. Roucka, J. Q. Xie, S. –Q. Yu, J. Menéndez, and J. Kouvetakis, *Appl. Phys. Lett.* **95**(13), 133506 (2009).

[102] R. Roucka, J. Mathews, C. Weng, R. T. Beeler, J. Tolle, J. Menéndez, and J. Kouvetakis, *IEEE J. Quantum Electron.* **47**(2), 213 (2011).

[103] R. Roucka, R. T. Beeler, J. Mathews, M. –Y. Ryu, Y. Kee Yeo, J. Menéndez, and J. Kouvetakis, *J. Appl. Phys.* **109**(10), 103115 (2011).

[104] R. T. Beeler, J. D. Gallagher, C. Xu, L. Jiang, C. L. Senaratne, D. J. Smith, J. Menéndez, A. V. G. Chizmeshya, and J. Kouvetakis, *ECS J. Solid State Sci. Technol.* **2**(9), Q172-Q177 (2013).

[105] J. Mathews, R. T. Beeler, J. Tolle, C. Xu. R. Roucka, J. Kouvetakis, and J. Menéndez, *Appl. Phys. Lett.* **97**(22), 221912 (2010).

[106] R. Roucka, J. Mathews, R. T. Beeler, J. Tolle, J. Kouvetakis, and J. Menéndez, *Appl. Phys. Lett.* **98**(6), 061109 (2011).

[107] J. Margetis, S. A. Ghetmiri, W. Du, B. R. Conley, A. Mosleh, R. A. Soref, G. Sun, L. Domulevicz, H. A. Naseem, S. –Q. Yu, and J. Tolle, *ECS Trans.* **64**(6), 711-720 (2014).

[108] S. Wirths, D. Buca, A. T. Tiedemann, B. Holländer, P. Bernardy, T. Stoica, D. Grützmacher, and S. Mantl, *ECS Trans.* **50**(9), 885-893 (2013).

[109] G. Grzybowski, R. T. Beeler, L. Jiang, D. J. Smith, J. Kouvetakis, and J. Menéndez, *Appl. Phys. Lett.* **101**, 072105 (2012).

[110] S. Wirths, R. Geiger, N. von den Driesch, G. Mussler, T. Stoica, S. Manti, Z. Ikonic, M. Luysberg, S. Chiussi, J. M. Hartmann, H. Sigg, J. Faist, D. Buca, and D. Grützmacher, Nature Photonics **9**, 88 (2015).

[111] R. A. Soref and C. H. Perry, *J. Appl. Phys.* **69**, 539 (1991).

[112] R. A. Soref and L. Friedman, *Superlattices Microstruct.* **14**, 189 (1993).

[113] D. Friedman, S. R. Kurtz, and J. Geisz, *Photovoltaic Specialists Conference* (29th IEEE, 2002), pp. 856-859.

[114] R. T. Beeler, C. Xu, D. J. Smith, G. Grzybowski, J. Menéndez, and J. Kouvetakis, *Appl. Phys. Lett.* **101**, 221111 (2012).

[115] M. Bauer, C. Ritter, P. A. Crozier, J. Ren, J. Menéndez, G. Wolf, and J. Kouvetakis, *Appl. Phys. Lett.* **83**(11), 2163-2165 (2003).

[116] Y. Y. Fang, J. Xie, J. Tolle, R. Roucka, V. R. D'Costa, A. V. G. Chizmeshya, J. Menéndez, and J. Kouvetakis, *J. Am. Chem. Soc.* **130**, 16095-16102 (2008).

[117] J. Xie, A. V. G. Chizmeshya, J. Tolle, V. R. D'Costa, J. Menéndez, and J. Kouvetakis, *J. Chem. Mater.* **22**(12), 3779-3789 (2010).

[118] J. Xie, J. Tolle, V. R. D'Costa, A. V. G. Chizmeshya, J. Menéndez, and J. Kouvetakis, *Appl. Phys. Lett.* **95**, 181909 (2009).

[119] V. R. D'Costa, Y. Y. Fang, J. Tolle, J. Kouvetakis, and J. Menéndez, *Thin Solid Films* **518**, 2531-2537 (2010).

[120] V. R. D'Coasta, Y. Y. Fang, J. Tolle, J. Kouvetakis, and J. Menéndez, *Phys. Rev. Lett.* **102**(10), 107403 (2009).

[121] C. Xu, R. T. Beeler, G. Grzybowski, A. V. G. Chizmeshya, J. Menéndez, and J. Kouvetakis, *J. Am. Chem Soc.* **134**(51), 20756-20767 (2012).

[122] R. T. Beeler, D. J. Smith, J. Menéndez, and J. Kouvetakis, *IEEE J. Photovoltaics* **3**(4), 434-440 (2012).

[123] R. T. Beeler, J. Menéndez, D. J. Smith, and J. Kouvetakis, *ECS Transactions* **50**(9), 591-599 (2012).

[124] C. Xu, L. Jiang, J. Kouvetakis, and J. Menéndez, *Appl. Phys. Lett.* **103**, 072111 (2013).

[125] C. Xu, R. T. Beeler, L. Jiang, J. D. Gallagher, R. Favaro, J. Menéndez, and J. Kouvetakis, *Thin Solid Films* **557**, 177-182 (2014).

[126] B. Vincent, F. Gencarelli, H. Bender, C. Merckling, B. Douhard, D. H. Petersen, O. Hansen, H. H. Henrichsen, J. Meersschaut, W. Vandervorst, M. Heyns, R. Loo, and M. Caymax, *Appl. Phys. Lett.* **99**(15), 152103 (2011).

[127] H. Li, Y. X. Cui, K. Y. Wu, W. K. Tseng, H. H. Cheng, and H. Chen, *Appl. Phys. Lett.* **102**(25), 251907 (2013).

[128] A. L. Smirl, S. C. Moss, and J. R. Lindle, *Phys. Rev. B* **25**(4), 2645 (1982).

[129] E. Gaubas and J. Vanhellemont, *Appl. Phys. Lett.* **89**(14), 142106 (2006).

[130] J. Menéndez and J. Kouvetakis, *Appl. Phys. Lett.* **85**(7), 1175 (2004).

[131] C. L. Senaratne, J. D. Gallagher, L. Jiang, T. Aoki, D. J. Smith, J. Menéndez and J. Kouvetakis, *J. Appl. Phys.* **116**, 133509 (2014).

[132] C. L. Senaratne, J. D. Gallagher, T. Aoki, J. Kouvetakis, and J. Menéndez, *Chem. Mater.* **26**(20), 6033-6041 (2014).

[133] F. Gencarelli, B. Vincent, J. Demeulemeester, A. Vantomme, A. Moussa, A. Franquet, A. Kumar, H. Bender, J. Meersschaut, W. Vandervorst, R. Loo, M. Caymax, K. Temst, and M. Heyns, *ECS J. Solid State Sci. Technol.* **2**(4), P134 (2013).

[134] L. Jiang, J. D. Gallagher, C. L. Senaratne, T. Aoki, J. Mathews, J. Kouvetakis, and J. Menéndez, *Semi. Sci. Technol.* **29**, 115028 (2014).

[135] E. Rosencher and B. Vitner, *Optoelectronics* (Cambridge University Press, Cambridge), 2002.

[136] S. L. Chuang, *Physics of Optoelectronic Devices* (Wiley, New York) pp. 718, 1995.

[137] V. R. D'Costa, Y. Y. Fang, J. Mathews, R. Roucka, J. Tolle, J. Menéndez, and J. Kouvetakis, *Semicond. Sci. Technol.* **24**, 115006 (2009).

[138] A. R. Goñi, K. Syassen, and M. Cardona, *Phys. Rev. B* **39**, 12921 (1989).

[139] Y. –H. Li, X. G. Gong, and S. –H. Wei, *Phys. Rev. B* **73**, 245206 (2006).

[140] T. Brudevoll, D. S. Citrin, M. Cardona, and N. E. Christensen, *Phys. Rev. B* **48**, 8629 (1993).

[141] R. H. Bube, *Electronic Properties of Crystalline Solids* (Academic, Boston) pp. 530, 1974.

[142] D. Stroud, *Phys. Rev. B* **5**(8), 3366 (1972).

[143] D. E. Aspnes, S. M Kelso, R. A. Logan, and R. Bhat, *J. Appl. Phys.* **60**(2), 754 (1986).

[144] V. Bellani, M. Geddo, G. Guizzetti, S. Franchi, and R. Magnanini, *Phys. Rev. B* **59**(19), 12272 (1999).

[145] M. Bauer, J. Tolle, C. Bungay, A. V. G. Chizmeshya, D. J. Smith, J. Menéndez, and J. Kouvetakis, *Solid State Commun.* **127**(5), 355 (2003).

[146] G. Hall, *Phys. Rev.* **116**(3), 604 (1959).

[147] A. Asch and G. Hall, *Phys. Rev.* **132**(3), 1047 (1963).

[148] J. R. Chelikowsky and M. L. Cohen, *Phys. Rev. B* **14**(2), 556 (1976).

[149] M. El Kurdi, G. Fishman, S. b. Sauvage, and P. Boucaud, *J. Appl. Phys.* **107**(1), 013710 (2010).

[150] S. Rodriguez-Bolivar, F. M. Gómez-Campos, and J. E. Carceller, *Semicond. Sci. Technol.* **20**(1), 16 (2005).

[151] Y. Chibane, and M. Ferhat, *J. Appl. Phys.* **107**, 053512 (2010).

[152] W. –J. Yin, X. –G. Gong, and S. –H. Wei, *Phys. Rev. B* **78**(16), 161203 (2008).

[153] G. Grzybowski, L. Jiang, J. Mathews, R. Roucka, C. Xu, R. T. Beeler, J. Kouvetakis, and J. Menéndez, *Appl. Phys. Lett.* **99**, 171910 (2011).

[154] A. I. Yakimov, V. V. Kirienko, V. A. Armbrister, and A. V. Dvurechenskii, *Semicond. Sci. Technol.* **29**, 085011 (2014).

[155] M. Yamaguchi, K. Yatabe, H. Ohta, and K. Morigaki, *Phil. Mag. Lett.*, **58**(4), pp. 213-218 (1988).

[156] R. A. Street, *Phys. Rev. B*, **23**, 861 (1981).

[157] M. Yamaguchi, H. Ohta, C. Ogihara, H. Yokomichi, K. Morigaki, S. Nonomura, and S. Nitta, *J. Non-cryst. Solids*, **97/98**, 931 (1987).

[158] P. Tsipas and A. Dimoulas, *Appl. Phys. Lett.*, **94**(1), 012114 (2009).

[159] S. K. Estreicher and Dj. M. Maric, *Phys. Rev. Lett.*, **70**(25), pp. 3963-3966 (1993).

[160] J. D. Gallagher, C. L. Senaratne, J. Kouvetakis, and J. Menéndez, *Appl. Phys. Lett.* **105**(14), 142102 (2014).

[161] M. Oehme, J. Werner, M. Gollhofer, M. Schmid, M. Kaschel, E. Kasper, and J. Schulze, *IEEE Photonics Technol. Lett.* **23**(23), 1751 (2011).

[162] M. Oehme, E. Kasper, and J. Schulze, *ECS J. Solid State Sci. Technol.* **2**(4), R76 (2013).

[163] J. P. Gupta, N. Bhargava, S. Kim, T. Adam, and J. Kolodzey, *Appl. Phys. Lett.* **102**(25), 251117 (2013).

[164] H. H. Tseng, K. Y. Wu, H. Li, V. Mashanov, H. H. Cheng, G. Sun, and R. A. Soref, *Appl. Phys. Lett.* **102**(18), 182106 (2013).

[165] M. Oehme, K. Kostecki, T. Arguirov, G. Mussler, Y. Kaiheng, M. Gollhofer, M. Schmid, M. Kaschel, R. A. Korner, M. Kittler, D. Buca, E. Kasper, and J. Schulze, *IEEE Photonics Technol. Lett.* **26**(2), 187 (2014).

[166] W. Du, Y. Zhou, S. A. Ghetmiri, A. Mosleh, B. R. Conley, A. Nazzal, R. A. Soref, G. Sun, J. Tolle, J. Margetis, H. A. Naseem, and S.-Q. Yu, *Appl. Phys. Lett.* **104**(24), 241110 (2014).

[167] D. Auston, C. Shank, and P. LeFur, *Phys. Rev. Lett.* **35**(15), 1022 (1975).

[168] K. L. Low, Y. Yang, G. Han, W. Fan, and Y. C. Yeo, *J. Appl. Phys.* **112**, 103715 (2012).

[169] R. Jakomin, M. de Kersauson, M. El Kurdi, L. Largeau, O. Mauguin, G. Beaudoin, S. Sauvage, R. Ossikovski, G. Ndong, M. Chaigneau, I. Sagnes, and P. Boucaud, *Appl. Phys. Lett.* **98**(9), 091901 (2011).

[170] J. P. Foley and J. G. Dorsey, *J. Chromatographic Sci.* **22**(1), 40 (1984).

[171] T. Arguirov, M. Kittler, and N. V. Abrosimov, *J. Phys.: Conference Series* **281**, 012021 (2011).

[172] P. Moontragoon, R. A. Soref, and Z. Ikonic, *J. Appl. Phys.* **112**(7), 073106 (2012).

[173] V. R. D'Costa, Y. Y. Fang, J. Tolle, J. Kouvetakis, and J. Menendez, *Phys. Rev. Lett.* **102**(10), 107403 (2009).

[174] R. T. Beeler, J. Menéndez, and J. Kouvetakis, *ECS Honolulu Prime 2012* (ECS, Honululu, Hawaii, 2012), Vol. MA2012-02.

[175] C. I. Ventura, J. D. Querales Flores, J. D. Fuhr, and R. A. Barrio, *Progress in Photovoltaics: Research and Applications*, n/a (2013).

[176] J. D. Gallagher, C. L. Senaratne, P. Sims, T. Aoki, J. Menéndez, and J. Kouvetakis, *Appl. Phys. Lett.* **106**(9), 091103 (2015).

[177] J. D. Gallagher, C. L. Senaratne, C. Xu, P. Sims, T. Aoki, D. J. Smith, J. Menéndez, and J. Kouvetakis, *J. Appl. Phys.* **117**, 245704 (2015).

[178] S. Takeuchi, A. Sakai, O. Nakatsuka, M. Ogawa, and S. Zaima, *Thin Solid Films* **517**, 159 (2008).

[179] J. Xie, R. T. Beeler, G. Grzybowski, A. V. G. Chizmeshya, J. Menéndez, and J. Kouvetakis, *Appl. Phys. Lett.* **95**(18), 181909 (2009).

[180] J. D. Gallagher, C. L. Senaratne, J. Kouvetakis, and J. Menéndez, Applied Physics Letters **105**, 142102 (2014).

[181] C. Xu, R. T. Beeler, L. Jiang, J. D. Gallagher, R. Favaro, J. Menéndez, and J. Kovuetakis, *Thin Solid Films* **55**, 177-182 (2014).

[182] V. R. D'Costa, C. S. Cook, J. Menéndez, J. Tolle, J. Kouvetakis, and S. Zollner, *Solid State Commun.* **138**(6), 309-313 (2006).

[183] J. S. Kline, F. H. Pollak, and M. Cardona, *Helvetica Physica Acta* **41**, 968 (1968).

[184] T. Ebner, K. Thonke, R. Sauer, F. Schaeffler, and H. J. Herzog, *Phys. Rev. B* **57**(24), 15448 (1998).

[185] D. D. Cannon, J. Liu, D. T. Danielson, S. Jongthammanurak, U. U. Enuha, K. Wada, J. Michel, and L. C. Kimerling, *Appl. Phys. Lett.* **91**(25), 252111 (2007).

[186] J. P. Dismukes, L. Ekstrom, and R. J. Paff, *J. Phys. Chem.* **68**(10), 3021 (1964).

[187] B. Johs, C. M. Herzinger, J. H. Dinan, A. Cornfeld, and J. D. Benson, *Thin Solid Films* **313-314**, 137 (1998).

[188] J. Liu, D. D. Cannon, K. Wada, Y. Ishikawa, D. T. Danielson, S. Jongthammanurak, J. Michel, and L. Kimerling, *Phys. Rev. B* **70**(15), 155309 (2004).

[189] C. C. Kim, J. W. Garland, H. Abad, and P. M. Raccah, *Phys. Rev. B* **45**(20), 11749 (1992).

[190] D. E. Aspnes and A. A. Studna, *Solid State Commun.* **11**, 1375 (1972).

[191] P. Lautenschlager, P. Allen, and M. Cardona, *Phys. Rev. B* **31**(4), 2163 (1985).

[192] S. H. Wei and A. Zunger, *Phys. Rev. Lett.* **76**, 664 (1996).

[193] T. Makimoto, H. Saito, T. Nishida, and N. Kobayashi, *Appl. Phys. Lett.* **70**, 2984 (1997).

[194] U. Tisch, E. Finkman, and J. Salzman, *Appl. Phys. Lett.* **81**, 463 (2002).

[195] A. Attiaoui and O. Moutanabbir, *J. Appl. Phys.* **116**(15), 063712 (2014).

[196] C. Xu, C. L. Senaratne, J. Kouvetakis, and J. Menéndez, *Solid-State Electronics* **110**, 76 (2015).

[197] G. Sun, R. A. Soref, and H. H. Cheng, *J. Appl. Phys.* **108**, 033107 (2010).

[198] R. A. Soref, J. Kouvetakis, J. Tolle, V. R. D'Costa, and J. Menéndez, *J. Mat. Research* **22**, pp 3281-3291 (2007).

[199] R. Camacho-Aguilera, Y. Cai, J. T. Bessette, L. C. Kimerling, and J. Michel, *Opt. Mat. Express* **2**(11), 1462 (2012).

[200] S. M. Sze, *Physics of Semiconductor Devices*, (Wiley-Interscience, New York, 1969), pp. 156-157.

[201] A. G. Chynoweth, W. L. Feldmann, and R. A. Logan, *Phys. Rev.* **121**(3), 684 (1961).

[202] Y. Zhao, J. D. Gallagher, Z. Li, I. Agha, J. Menéndez, J. Kouvetakis, and J. Mathews, *ECS Meeting Abstracts* **MA**2015-02, 1227 (2015).

[203] Y. Z. Huang, W. H. Guo, L. J. Yu, H. B. Lei, *IEEE J. of Quant. Electron.* **37**(10), (2010).

[204] Q. Chen, Y. H. Hu, Y. Z. Huang, Y. Du, Z. C. Fan, *IEEE J. Quant. Electron.* **43**(6), (2007).

APPENDIX A

MICROELECTRONIC DEVICE PROCESSING PROCEDURE

The following appendix is dedicated to disclosing the full details of processing the group-IV alloy materials discussed in this dissertation into microelectronic devices such as photodiode LEDs and waveguides using the resources available in the Ira A. Fulton Center for Solid State Electronics Research (CSSER) cleanroom at Arizona State University. The process presented here is very similar to that outlined in previous dissertations from the Kouvetakis/Menéndez research group by Dr. Richard Beeler and Dr. Jay Mathews, however there are a few subtle details that have amended the initial processing set out by these two which makes the fabrication of these materials into functional devices more robust. I will first outline in detail the photodiode LED processing procedure and then briefly discuss the fabrication of waveguide devices.

Photodiode LED Processing Procedure

It is critical to know the following details about the sample before taking it into the cleanroom for processing: sample wafer substrate (e.g. Si or Ge), sample layer thicknesses, sample layer compositions, intended epilayer etch depth, minimum initial oxide thickness, and target passivating/antireflective oxide thickness. The details of how to determine the latter of these will come later in this Appendix. If a device originating on a Si wafer is to be processed the first step is to sonicate the wafer in methanol for 5-10 minutes. However if the device to be processed originates with a Ge wafer, the way to initially clean one of these wafers is to rinse it with solvents in the following order: acetone, methanol, and isopropyl alcohol (IPA). Henceforth the process of cleaning a sample with solvents following this process will simply be referred to as a “rinse with solvents”. Dry both types of wafers with N_2 from one of the gas guns available. A few things to immediately note on handling Ge wafers throughout the entire processing

procedure: do not sonicate them and only dry them with the low-PSI N_2 guns (8-10 PSI) or there is a severe risk of breaking the wafer.

The next step in the process is to deposit the protective oxide layer. This is done in the Oxford PECVD or the PlasmaQuest RPCVD tools. Since this is just a protective oxide and will be removed later it is recommended to use the Oxford PECVD over the PlasmaQuest RPCVD as the former tool is has a much higher growth rate recipe and its operation is almost entirely automated. The recipe to use on the Oxford tool for this step is either "SiO_2 Dep at 350C 20W" or "SiO_2 Dep at 250C 20W". Both of these recipes deposit SiO_2 on Si and Ge at approximately 70 nm/min. Knowing that this SiO_2 has an etch rate in the Cloey tool, which will be discussed later, of 3-5 nm/min it is recommended that at least an extra 20-50 nm of clearance be accounted for in the thickness of this initial layer. For example, if it was determined prior to taking the sample into the cleanroom that the epilayer etch step in Cloey would require 20 minutes then the thickness of the protective oxide layer should be at least (20 mins x 5 nm/min) + 20 nm = 120 nm. However exceeding 150 nm in this case may make subsequent processing steps more tedious. If the Oxford tool is down, the PlasmaQuest tool may be used instead. The recipe which is used on this tool is called "SR_Rouck" and deposits SiO_2 on Si and Ge at 5.1-5.6 nm/min. This variance in growth rate is due to how well the plasma is tuned on this tool. PlasmaQuest is older than the Oxford tool and its operation requires manually tuning of the waveguide cavity to generate the plasma necessary for the growth.

The next step in the processing is the first photolithography step to pattern the device mesa structures. This procedure is designed to resolve feature sizes down to ~1 μm while also promoting good adhesion to the SiO_2 layer so that the photoresist does not

delaminate during subsequent oxide etches in HF-based solutions. To perform the UV exposure, the OAI 808 or EVG 620 aligners may be used. If the OAI is used the exposure time is set by the user so it is good to measure the power of the lamp and calculate the appropriate exposure time before processing. Additionally, it is good to use the OAI in a "contact vacuum" mode for this process as it gives higher feature resolution leading to better mesa definition. The EVG does not have this capability so only a "hard contact" can be used on this tool. If the EVG is to be used there is a recipe called "Jimmy_1st_Photodiode" that is programmed to expose the wafer to 38 mJ/cm^2 of UV light so no pre-exposure lamp check or exposure time calculation is necessary. The steps proceed as follows:

Rinse with solvents and dry with N_2

Dehydrate bake on a hot plate at 150C for 2 mins 30 sec.

Tape the sample face-up to a quarter piece of blue processing tape

Spin HMDS at 500 rpm, 2 sec ramp, 5 sec spin; 3000 rpm, 5 sec ramp, 30 sec spin

Bake at 150C for 2 mins

Spin AZ-3312 resist under the same conditions as the HMDS

Soft bake at 115C for 60 sec

Expose to 35-40 mJ/cm^2 UV light on the OAI or EVG

Post-exposure bake 110C for 50 sec

Develop in AZ-300 MIF developer for 55 sec

Rinse thoroughly with DI water and dry with N_2

Inspect the wafer in an optical microscope for quality

If quality inspection is passed, hard bake at 150C for 2 mins 30 sec

There are a few suggestions at this point for the processor. Watch out for patterns of faint white fringes in between the photoresist mesas under the microscope during the optical inspection. If these fringes are present then the development is not complete and there is still photoresist where these white fringes are. This will interfere with future processing and the success of the devices if all the photoresist between the mesas is not cleared out during the development step. If left on the wafer it will create a micromasking effect that will leave behind residual SiO_2 between the mesas. This will ultimately form a highly resistive black residue in regions of the wafer where the bottom contacts will be formed after the etch step is performed in the Cloey tool. Additionally, once this process is started the processor can not take the wafer out of the photolithography bay area until after the hard bake is completed. Failure to do so will compromise the ability of the photoresist to tolerate HF during the subsequent oxide etch step.

If the device being processing was grown on a Ge wafer it needs to be glued to a Si-wafer carrier dummy for this photolithography process to prevent the Ge wafer from breaking when the mask on the aligner comes into contact with the sample surface. The gluing procedure is as follows:

Rinse the Si dummy wafer with solvents and dry with N_2

Spin HMDS on Si wafer at 500 rpm, 2 sec ramp, 5 sec spin; 3000 rpm, 5 sec ramp, 30 sec spin

Spin AZ-4330 resist onto Si wafer under the same conditions as the HMDS

Place Ge-substrate sample on Si wafer, gently press down at the sample corners

Bake for 2 mins at 100C on a hot plate

Bake in vacuum oven at 80-100C for at least 30 mins

Rinse with solvents and N_2 dry (CAUTION: remember to use a 8-10 PSI N_2 gun)

After the first photolithography is performed and the hard bake is completed it is safe to take the sample into the areas where the cleanroom is illuminated by white light. Next the first SiO_2 etch is performed. This step is designed to selectively etch through the protective oxide layer around the photoresist mesas down to the epilayer sample surface. This will then form mesa patters of photoresist on SiO_2. The etch rate of the SiO_2 in the clean-room provided BOE (buffered-oxide etch solution) that is a diluted 20:1 Ammonium fluoride: Hydrofluoric acid solution is 1.10-1.25 nm/sec. Determine the necessary time to etch through the oxide layer prior to taking the following steps:

Rinse the sample with DI water

Dip sample in 20:1 BOE solution for required time, slightly agitating

Dip sample in DI water and agitate mildly for a few seconds

Thoroughly rinse with DI water and dry with N_2

Inspect sample with an optical microscope for quality

Under the microscope, watch out for signs of photoresist delamination from this step. The lithography processing outlined above is designed to reduce photoresist delamination in HF, however there are always risks that the AZ-3312 on a particular day may be of poor quality. If this happens there will be liquid regions under the microscope that are not fully dried and sitting between the mesas. This is highly undesirable as the longer this residual liquid remains on the surface between the mesa patters, the longer the HF in this liquid is etching at the oxide mesa patterning. If this occurs try repeating a brief oxide etch right away for ~10 sec in the BOE while making sure to aggressively rinse the sample during the DI water rinse steps. If the problem persists to such an extent

that much of the sample has this issue, remove the photoresist and oxide layers completely and restart the processing from step one.

Prior to loading the sample into the tool known as “Cloey” it is a good idea to remove the photoresist from the sample surface so that it does not react with the BCl_3 plasma during etching. The plasma can cause the photoresist to chip off and burn into the surface which irreversibly contaminates the sample, ruining the device. The photoresist may be removed by submerging the sample in 100-200 mL of AZ-400T Stripper at 90-120C for 5-10 minutes. Do not heat AZ-400T above 120C or it may cause the photoresist to caramelize and contaminate the sample. Once this is done, thoroughly rinse the sample surface off with DI water and dry with N_2.

While the photoresist is being removed it is a good idea to begin preparing Cloey for the etch process. This tool is an Oxford M80 RIE (reactive ion etch) instrument. The recipe to use is “GeSn BCl_3 with O_2 clean”. Prior to venting the chamber and loading the sample, verify that the previous user has run the line pump out recipe and at least a 10-15 minute O_2 clean of the chamber has been performed, or make sure that they used a process that exclusively used BCl_3 if they did not clean the chamber. Open the aforementioned recipe and initiate a dummy run without the sample to ensure nominal tool performance. For the dummy run it is recommended that the O_2 clean step of the recipe be ran for an additional 5 minutes and that the BCl_3 etch step be set for at least 5 minutes as well to condition the chamber and to check that the BCl_3 flow rate through the controller is at its mandated level of 50 sccm. After successfully performing the dummy run the chamber may be vented to load the sample. During the live run on the sample set the time on the recipe O_2 clean for 2-3 minutes to remove any residual organics from the

surface that might be left following the photoresist removal in AZ-400T Stripper. The BCl_3 etch time must be known prior to using this tool. Typically Ge etches at 30-35 nm/min with this recipe, however most samples are GeSn and/or GeSiSn alloys that will vary in etch rate depending on the alloy concentration and tool performance on a given day. The general trend is that higher Sn-containing materials etch faster and higher Si-containing materials etch slower. For example, a typical etch rate for 6-8% Sn, GeSn materials is 50-65 nm/min. However by adding 2-4% Si the etch rate decreases to about 40-50 nm/min, respectively. The difficulty with nailing down exact etch rates is due to the fact that Cloey is a very finicky tool. Various issues that I've operated the tool under have been: unstable or too high BCl_3 flow due to mass flow controller issues, failing chamber turbo pumps that cause fluctuations in pressure, and failing RF power supplies that cause the plasma blink off and on. All of these issues affect the etch rate of the recipe on any given alloy material. It is therefore recommended that the processor keep a vigilant eye on the status and condition of this tool so as to be able to adjust accordingly to the various issues that may arise.

Following the etch in Cloey, measure the mesa sidewall profile using the Dektak profilometer in the cleanroom. Be sure to properly subtract the oxide thickness from the profile and that the depth into the target bottom contact layer is deep enough to ensure that there will be no shorts across the devices after the metals deposition. For example, an ideal etch depth into a 800 nm *n*-Ge layer would be 250-400 nm if the plan is to later deposit 20 nm Cr followed by 180-200 nm Au during metallization. This prevents forming a short across the device and keeps the carriers well away from possible interface defects with the substrate at the bottom of the layer. Continuing with the example, let's

say that the initial protective SiO_2 coat was 140 nm, the total thickness of all other layers on top of the 800 nm *n*-contact is 650 nm, and that the expected etch rate of these materials is 60 nm/min. A sensible time to choose for the BCl_3 etch step in this case would be (300 nm + 650 nm)/(60 nm/min) = 15.83 minutes ~ 16 minutes. After running this process it is found that the Dektak measures the total profile thickness of etched material + oxide to be 965 nm. Recalling that the SiO_2 etch rate in Cloey is 3-5 nm/min we can obtain a conservative estimate of the etch depth into the contact layer and the etch rate of the material: depth into contact layer = 965 nm – (140 nm – (3-5 nm/min)×16 min) – 650 nm = 220-255 nm, at 54-57 nm/min. Even though the etch depth into the contact layer is likely slightly below the target range in this case, as long as the total metal thickness (Cr + Au) is less than 200 nm this depth profile will produce a working device. This example also highlights the importance of choosing an appropriate protective oxide thickness in the early stages of processing. If the initial SiO_2 layer is grown too thin for the required etch time, this layer may be removed during the etching. If this happens the entire wafer will start to be uniformly etched by the BCl_3 plasma and the top contact layer may be etched away, ruining the device. In the case of this example we see that there should still be 60-90 nm SiO_2 left on the device mesas.

The next step in the processing is to remove the protective oxide coat and deposit a passivating anti-reflective SiO_2 coat across the entire wafer. To do this, submerge the sample in a 1:10 HF:Methanol solution in a Teflon beaker until all of the oxide is visibly gone. Keep the sample submerged and gently agitate the solution for an additional 60 seconds to make sure all of the oxide is removed, then dip the wafer in a pure methanol solution to quench the HF. Promptly dry with a N_2 gun and load the sample into either the

Oxford PECVD or PlamaQuest RPCVD tools for the oxide deposition. This must be done as quickly as possible to minimize the amount of native oxide that forms on the surface of the wafer under ambient conditions. If the PECVD is used for the SiO_2 deposition there are specific recipes that have been developed for this step: “SiO_2 Slow Dep Hi Strike 350C” and “SiO_2 Slow Dep Hi Strike 250C”. These recipes deposit SiO_2 on group-IV materials at 6.2-6.4 nm/min. The strategy behind these two processes is to strike the plasma with a high power (25W) and then grow the material at a lower power (5W) to achieve the low growth rate necessary for good sidewall passivation. The tool operator must do this manually so it is critical to keep an eye on the process when striking the plasma because the power must be turned down to 5W as soon as possible after the reflected power in the chamber reads 0W (plasma ignited). If PlasmaQuest is used for this step the “SR_Rouck” recipe mentioned previously is used in this case as well.

Since this oxide layer functions as an antireflective coating as well it is important to determine the target SiO_2 thickness prior to growth. The optimal thickness can be calculated using the Igor program “Reflectance_calculator_SOI”. The oxide thickness should be chosen to minimize the reflectance of this layer to photons with energy very near the band gap of the active material in the device. For example, for pure Ge devices the optimal thickness is 270 nm. As the band gap of the active layer material decreases the thickness must be increased such that for 10% Sn, GeSn alloys the optimal thickness is 410 nm. The effect of strain on the band gap should also be taken into consideration before doing this calculation so that the thickness of the oxide is optimally tuned for the real band gap of the material.

After a suitable passivating and antireflective SiO_2 layer is deposited the next step is the second lithography step which will define the metal contact regions on the wafer. For this procedure we keep a stock of AZ-5214 resist, which we use in image reversal mode, in the refrigerator of the clean room on a bottle labeled "Kouvetakis IRPR". This must be restocked on occasion but it is important to only take about half a bottle's worth at a time because the resist is best for processing when it is at room temperature, but needs to be stored at cooler temperatures for longer periods of time. When using the OAI at this step the contact vacuum mode is sufficient to attain the necessary feature resolution. If the EVG is to be used there are 2 recipies that are stored on the software for our purposes: "Jimmy_2nd_Photodiode" which is followed by "Jimmy_Flood". This is because the processing of the AZ-5214 resist involves first a UV exposure with the metals mask followed by a flood exposure with no mask when using it in image reversal mode. The first exposure with the metals mask requires the processor to align the mask to the wafer before making contact between the mask and sample with exposure. It is critical this be done correctly because if the contacts are not placed properly then a short can be made and the devices will not work. It takes time an patience to do a good, proper alignment and experience is really the best teacher in this case. As a beginner it can take up to an hour or more to align a mask to 1 sample so it is important to keep this in consideration when scheduling time on these tools since they may not have time windows that are open for more than 2 hours. The lithography procedure is very similar to that done with the AZ-3312 resist, and as such it too is designed to promote good adhesion of the photoresist to the wafer so that it does not delaminate during subsequent exposure to HF:

Rinse with solvents and dry with N_2

Dehydrate bake on a hot plate at 150C for 1 min 30 sec.

Tape the sample to a quarter piece of blue processing tape

Spin HMDS at 500 rpm, 2 sec ramp, 5 sec spin; 4000 rpm, 5 sec ramp, 30 sec spin

Bake at 150C for 2 mins

Spin AZ-5214 resist under the same conditions as the HMDS

Bake at 95C for 90 sec

Expose to 50 mJ/cm^2 UV light on the OAI or EVG

Post-exposure bake 115C for 60 sec

Flood expose to 200 mJ/cm^2 on the OAI or EVG

Develop in AZ-300 MIF developer for 55 sec

Rinse thoroughly with DI water and dry with N_2

Inspect the wafer in an optical microscope for quality

If quality inspection is passed, hard bake at 115C for 60 sec

If the lithography was done properly, under the optical microscope there should be ring patters of SiO_2 in the photoresist that sit inside and just outside of the circular semiconductor mesas. This oxide will need to be removed to make way for the metals that will be deposited on the areas the oxide currently covers. This etch process is in principle identical to that described previously for the first oxide etch, with the exception being that in this case it has been found that it is safe to assume a 1.5-1.75 nm/sec etch rate. In fact, assuming this rate for this oxide etch step has been found to produce devices that possess significantly lower dark currents (about an order of magnitude lower). This has been found to be the case when processing parallel 12% Sn, GeSn devices using the

1.1 nm/sec vs the 1.5-1.75 nm/sec rates. A plausible explanation as to why this higher etch rate is likely true is because at this step we are clearing out smaller feature sizes, and so the required etch time seems to be less than that required when we were clearing out the broader features between the mesas that takes place earlier in the processing. It is likely that etch times derived using this rate give better dark currents because the surface is not exposed to the HF for a longer period of time, minimizing possible damage and the expansion of surface etch-pit defects. As before, to perform the etch follow these steps:

Rinse the sample with DI water

Dip sample in 20:1 BOE solution for the required time, slightly agitating

Dip sample in DI water and agitate mildly for a few seconds

Thoroughly rinse with DI water and dry with N_2

Inspect sample with an optical microscope for quality

At this point the ring patterns should be the same color the sample surface was prior to processing under the microscope if the oxide has indeed been cleared out. Now the sample is ready for metals deposition. Two tools may be used for this process: an Edwards thermal evaporator (Edwards II) or a Lesker electron beam evaporator (Lesker 3). It is recommended the processor use Edwards II even though it is not as modern as Lesker 3. The advantages of Edwards II however are that the sample can be processed faster and there is not as much competition for time on this tool (Lesker 3 can be booked for 3 weeks in advance at a time). Since switching to Edwards II as the standard metals tool, no devices have been produced using the Lesker 3 tool so I will devote my discussion of metals deposition entirely to the former tool. However, if the user desires to use Lesker 3, a description of this tool's operation can be found in the Appendices of the

dissertations written by Dr. Jay Mathews and Dr. Richard Beeler. Metals that may be deposited in Edwards II are: Au, Ag, Cr, Ge, and Ni. For the contacts on the devices discussed in this dissertation, the metals employed were 15-20 nm Cr followed by 100-200 nm Au. The recommended metals thicknesses to aim for however are 20 nm Cr followed by 190 nm Au to ensure robust contacts that can withstand multiple experiments from the probe tips used for performing I-V and responsivity measurements on the probe station in the Goldwater lab, temperature dependent I-V measurements in the ERC probe station lab, and EL measurements. The cleanroom staff provide the Cr source for this tool so there is no need to order Cr rods. However it will be necessary to periodically order Au pellets for these depositions. Before using this tool be sure to thoroughly clean the walls with a vacuum to make sure no particles fly onto the sample when the chamber is pumped down to high vacuum. Ideally this system deposits metals at pressures below 3×10^{-6} Torr. Check the Cr rod and make sure there is plenty of Cr left on it to deposit the metal that is required. One thing to keep in mind is that the green color on this rod is due to the native oxide. This is undesirable and needs to be burned off thoroughly before exposing the sample to the Cr. Position the tungsten boat containing the Au that will be deposited and remember what positions the Cr and Au are in. It is recommended to begin with the Cr in position for deposition with the shutter in the closed position to block any CrO from getting onto the sample. Load the samples into the chamber and begin pumping as soon as possible after the oxide etch is performed to make sure a native oxide is not formed on the exposed samples. To ensure this is the case it is good to do a quick oxide etch (~5 sec in BOE while following the oxide etch procedure described above) right before loading the sample into the metals tool after inspecting the main etch for

completeness. Allow the tool to pump down below $3x10^{-6}$ Torr before performing the deposition. It is possible to operate the tool at higher pressures (up to $1x10^{-5}$ Torr) if the diffusion pump and/or vacuum sealing is experiencing difficulties, however the user will have to be very cautious and monitor the deposition vigilantly in this case.

When ready to begin metals deposition, first turn up the current on the Cr source slowly until a glow is seen in the chamber. As the deposition is proceeding, use the crystal rate monitor to keep track of the deposition rate and the total film thickness. The pressure should rise significantly (~$4\text{-}7x10^{-6}$ Torr) as the CrO is burned off. Once the pressure drops back to base ($1\text{-}3x10^{-6}$ Torr), deposit at least an additional 5 nm Cr with the shutter closed at 0.1 nm/sec to ensure that all CrO is gone. Slowly adjust the current until the rate is a stable ~0.05 nm/sec and open the shutter to allow Cr to deposit on the sample. Allow this to continue until 15-20 nm Cr has been deposited. Slowly turn the current down and switch the source to the Au boat. Since Au does not form an oxide under ambient conditions, this metal may be deposited directly onto the sample once the rate is stabilized. Again, turn the current up slowly with the shutter closed until a glow is seen inside the chamber and the rate detector shows Au depositing on the walls. Adjust the current until the deposition rate is stable at ~0.1 nm/sec and open the shutter allowing the Au to deposit on the sample surface. When the deposition is done (100-200 nm) close the shutter and turn the current down slowly. Allow the tool to cool for at least 10 minutes before venting the chamber to atmosphere.

After removing the samples from Edwards II, place them in an acetone bath for at least 5 minutes to begin to liftoff the photoresist that is on the sample. This process should selectively remove the remaining photoresist, leaving only the Cr/Au stacks

between widows of SiO_2 that cover the entire sample. To expedite the time required to remove all of the photoresist, the sample may be sonicated for short bursts of 5-15 seconds. Remove the samples from the acetone bath and rinse well with acetone and dry with N_2. Finally, place the samples in one of the Tegal asher tools for 5-10 minutes. These tools ignite oxygen plasmas using RF radiation powers between 200-300 Watts at pressures between 300-400 mTorr which effectively removes all carbon-based contaminants from the chamber, including any residual photoresist on the sample surface. Once this is done the devices are completed and are ready for measurement.

Waveguide Processing Procedure

In order to make waveguides that will be optically pumped for laser measurements, the initial processing follows the same protocols as those for the LEDs just described. To begin processing an optically pumped waveguide device, all of the same processes apply up to the point of depositing the passivation/antireflective SiO_2 coating. The one change in this case is to make the SiO_2 thickness optimal for minimizing the reflectance to the energy of the pump laser photons instead of to the emission wavelength of the active material as was the case for the LEDs. After this is done the samples are removed from the cleanroom and polished in the TEM sample preparation room.

The waveguides are placed in groups across the wafer varying in size from 5-100 um wide by 4 mm long. These are cut from the main wafer using the diamond saw in the TEM sample prep room. First use a diamond pen to cleave the wafers along columns of waveguides. Then glue the column strips face (surface)-down onto a glass slide using the sample prep wax and cut out each individual waveguide packet with the diamond saw

both parallel to the waveguides and perpendicular to the edges. Be sure that the wax covers the entire surface of the sample and that there are no air bubbles within the wax, otherwise particles from the saw water will find their way between the waveguides and these are extremely difficult to remove by standard sonication methods. Let the samples sit in acetone for at least 15 minutes. From this point on only grab the devices along the sides running parallel to the waveguides to avoid scratching the polished ends.

Next use the Allied Multi-Prep tool to polish the ends of the waveguides that are perpendicular to the devices. The aim here is to create a mirror-polished finish that will enable confinement of light in the device, a requirement if stimulated emission is to be achieved. Be sure to align the Allied Multi-Prep before proceeding to polish the ends. It is desired that the polish be perpendicular to the waveguides and if the turntable on the tool is not level it can lead to a polish that is not normal to the devices. There is a special sample holder (Allied High Tech Part No. 15-1010) in the TEM sample prep box that the samples are glued to and mounted onto the tool. As with mounting the sample to the glass slide, secure the sample on the holder face-down using the TEM sample prep wax that adequately covers the whole sample surface. The polish is achieved by applying diamond lapping paper to the waveguide edges normal to the devices. Begin with the 9 μm paper until it is clear under an optical microscope that the paper is grinding away a portion of the waveguides. Then move onto the 3 μm, 0.5 μm, and finish with the 0.1 μm. The typical setting used for this polished is a spin rate of 20 rmp on the table at a pressure of 0.007 mm with the arm moving. As the sample is polished the stage position need to be continually adjusted manually so that the pressure constantly reads 0.007 mm. Typically this takes the form of allowing the reading to drop to 0.003 mm and then increasing the

pressure until it reads 0.010 mm, allowing the process to repeat until the polish for a particular grit of lapping paper is completed. Typically it takes about 30 minutes at each grit level once the waveguides have been reached. Once on the 0.1 μm paper, polish for an additional 30 minutes beyond the necessary 30 to ensure a good mirror-like surface. This must be done on both sides of the waveguide ends normal to the devices.

After polishing the waveguides are cleaned by dipping in acetone and sonicating. The technique that works best for eliminating particles between the waveguides is to grab the waveguide along the sides parallel to the devices and to dip the sample so that it is suspended in the acetone while the medium is under sonication. A few pulses that last for 30 seconds has been found to be sufficient to clean almost all foreign gunk from between the devices introduced during handling in the TEM sample prep room.

At this point the waveguides are taken back into the cleanroom for metallization. There are stainless steel blocks that measure about 1/2-inch on all sides in the main lithography tool kit with a flat tail and a screw hole. These were fabricated in the machine shop at ASU and are the sample holders for the metal deposition. The samples are mounted to the holders using AZ-4330 photoresist. Apply high-temperature eutectic tape to anchor the sample such that ~1/4 of the waveguide length hangs off the end of the holder. The goal here is to deposit metals onto one of the polished ends of the waveguides so be sure the desired polished side is the one that is hanging off the end of the holder. Cover the top of the waveguide with the photoresist and bake the sample on the holder in a vacuum oven for ~60 minutes at 80-100C. Once this is done use the Edwards II tool described previously to deposit no more than 5 nm Cr at 0.5-0.6 A/sec followed by 100-150 nm Ag at 0.8 A/sec. Again, be sure to thoroughly burn off the

native CrO before deposition of the metal. Cr is deposited in this case to act as a whetting layer for the Ag deposition so that the Ag has good adhesion to the Si wafer and Ge-like alloys.

APPENDIX B

OPERATION OF PHOTOLUMINESENCENT AND ELECTROLUMINESENT SYSTEMS

This appendix describes the experimental procedure for acquiring PL and EL data with the liquid nitrogen (LN_2) cooled InGaAs, thermoelectrically (TE) cooled InGaAs, and TE cooled PbS detectors. This appendix will also give details how to configure the apparatus to go between the two experimental techniques and detectors. Details on the parts and fundamental alignment of the system have been described in Appendix C of Dr. Jay Mathew's dissertation and the reader is referred to that text for any details not disclosed here. The spectrometer used on this system has 2 gratings: a 600 grooves/mm blazed at 1000 nm and a 600 grooves/mm blazed at 2000 nm. These are referred to as grating #1 and #2, respectively. To switch the turret between these gratings go to Start > All Programs > Jobin Yvon > Utilities > USBSpectrometerControl. Click initialize. In the section "Wavelength Control" there is a box with a pull-down menu that specifies which grating is currently being used. Using this pull-down box automatically switches between the gratings. For the work presented in this dissertation grating #2 was predominantly used, since it has superior transmission characteristics for longer wavelengths relative to grating #1.

PL Measurements

For PL measurements the wafer is prepared by using rubber cement to glue the sample to a glass slide. The glass slide is then inserted between a row of screws on the sample stage that allows the sample to remain fixed and upright for the duration of the experiment. This is an advance over using double sided tape, which loses its sticking ability over time and is sensitive to humidity. Under this arrangement an experiment can go for as long as the user desires without worrying about the sample shifting position. Once the sample is in place the rest of the apparatus can be prepared for measurement.

Begin by slowly turning the current up on the power supply to the 980 nm laser until the current reads 0.68 A. At this current the output power of the continuous wave laser is ~400 mW. There is a photo-power meter that may be moved directly into the laser path that is calibrated to 1064 nm that will allow the user to verify the laser output power. If the PL data is to be taken with the liquid nitrogen cooled (LN_2) InGaAs detector, set the optical chopper frequency to 191 Hz. If the data is being taken with the thermoelectrically cooled (TE) PbS detector the best frequency to use is 101 Hz. The best frequency to use for the TE InGaAs is 151 Hz. These frequencies are chosen to maximize the signal-to-noise ratio for each of these detectors based on their respective response times.

While turning up the laser and optical chopper, if the LN_2 InGaAs detector is being used to acquire the data it is a good idea to begin pouring liquid nitrogen into the Dewar jacket that surrounds this detector so that it is cooled down by the time data acquisition begins. It typically takes 10-15 minutes for the InGaAs photodiode to equilibrate with the LN_2. Once the optical chopper is running it is safe to turn on the lock-in amplifier. Open the FlourEssence software on the computer. This software controls the spectrometer during the experiment and records the intensity readout from the lock-in which is coupled to the photodetector. At this point all of the electronics are turned on and running.

Continue to prepare for measurement by opening the front and back slits on the spectrometer to their widest positions to maximize the amount of light the system will collect. Open the beam path for the laser and use one of the IR cards in the lab to track where the beam is hitting the sample. Also use the card to check where the reflected

beam of the laser is going after it hits the sample surface. Be sure to wear the laser safety glasses provided when doing this. Ideally the reflected beam should not be going through the collection lens. If it is, the sample stage needs to be readjusted and aligned so that the beam does not go through the collection lens. If the reflected beam is going through the collection lens it will cause the detector to saturate when the laser passes through in 2nd order at 1960 nm. This will damage the detector over time if not remedied. Once it is confirmed that the laser reflection is not going through the collection lens, open the Real Time Control window in the software and set the wavelength to the approximate expected peak maximum for the sample. The sample stage has X and Y micromanipulator adjustments so that the PL signal readout on the lock-in can be maximized at the optimal wavelength. Optimizing the signal in this way is essentially fine-focusing the laser on the sample so that an optimal excitation is occurring. Table VII below lists good wavelengths to use as initial guesses for the peak maximum when aligning $Ge_{1-y}Sn_y$ materials. For ternary $Ge_{1-x-y}Si_xSn_y$ alloys, subtract ~150 nm for every 2% of Si incorporation at the same Sn content. Furthermore, for heavily doped *n*-type materials ($n > 10^{19}$ cm^{-3}), add ~1% Sn to the values listed in the table. Also, bear in mind the strain of the emitting layer. The strains of most samples in this dissertation tended to be residually compressive (0.1-0.4%), but with significant tensile strain, or higher compressive strains the emission will shift noticeably to lower and higher energies, respectively.

TABLE VII: Peak wavelengths of $Ge_{1-y}Sn_y$ materials

Sn Content (y)	Approximate Peak Position (nm)
0.00	1580
0.02	1725
0.04	1850
0.06	2000

0.08	2200
0.10	2400
0.12	2600

A few notes to mention on the experimental technique. Using the lock-in amplifier to readout the signal from the photodetector enables a measurement with very little noise. The operating principle is that the lock-in amplifier uses Fourier analysis to pick out the component at its input that is of the same frequency as the reference provided by the optical chopper. This is why using the optical chopper is crucial: it creates a modulated laser pulse which translates to a modulating signal that is sent by the detector to the lock-in. Essentially the lock-in can be viewed as a very narrow band-pass filter.

The measurement is initiated in the experiment menu. Set the initial and final wavelengths, and specify how many scans to perform. Be sure to set the integration time to at least 5 times the lock-in time constant. Typically a 3 second time constant is used so a 15 second integration time is necessary. Then click on the "Advanced" button and set the readout to μV and the gain to "none". Then begin the measurement.

To switch between detectors, turn off all detector electronics. Replace the plug to the appropriate power supply. The PS-1 power supply is used for the LN_2 InGaAs, but both the TE InGaAs and PbS detectors use the PS/TC-1 supply. Connect the correct BNC cable for the detector being switched to at the A/I port at the front of the lock-in. There are 3 set screws equally distributed around the base of the detector/spectrometer interface. Unscrew these, cap the photodiode and insert the replacement detector as quickly, but also as gently, as possible to avoid getting dust in the spectrometer and to not disturb the overall system alignment. The TE detectors have another jacket they sit in so it is recommended to put this in first, followed by the detector. When switching on the TE

detector power supplies, set the temperature to +10°C at first so that a surge of current does not damage the device. Wait for the status LED to turn from red to green before increasing the current. Once the current gets to 0.6 A the TE detectors should be at -30°C and are ready to collect data.

The final step when switching between detectors is to adjust the set screws and the focusing mirror to optimize the signal. Use the set screws initially to get the detector to sit soundly in the flange. Then adjust the X and Y mirror screws using an Allen wrench. These are diagonal to one another. The third screw that forms the corner between these two screws should never be adjusted.

Assuming the system is in the EL configuration, to switch back to PL remove the L-beam (to be discussed in the next section) and replace the focusing lens, PL sample stage, and collection lens. Set the lock-in back to trigger on an external source. Insert a bulk Ge standard wafer and optimize the intensity in the LN_2 InGaAs detector with the laser at 400 mW. A good intensity to achieve is anywhere between 20-30 mV at 1830 nm. The specific alignment of these three components is discussed in Dr. Mathews's dissertation.

EL Measurements

To switch the system over to perform EL measurements begin by carefully removing the PL sample holder stage, followed by the focusing and collection lenses. Mount the L-shaped optical bridge to the optical bench. Adjust it by hand until it looks visually aligned to send light straight into the focusing lens and subsequently into the spectrometer entrance slit. The L-piece has a removable collection lens at the end that points down at the sample. Unscrew the collection lens and replace it with a red LED.

This LED has been inserted into a screw mount the same size as the collection lens for this purpose. Run the white wires from the Keithley 2602A soucemeter to the pin-outs on the red LED. Be sure to bias the LED correctly. Failing to do so will result in a fried LED. To avoid this, make sure the positive terminal from the Keithley is connected to the longer pin-out wire on the LED while the negative terminal goes to the shorter wire. It is also a good idea to grab a 100 Ω resistor off the shelf and connect that in series with the LED to further protect it. Open the FlourEssence software on the PL computer and the TestScriptBuilder on the I-V computer. Do not put any long pass filters in the optical path and set the spectrometer to 1900 nm (this is the 3rd order transmission of red light). By this point the lock-in must be set to trigger on an internal reference signal since we will not be using a chopper to do this measurement. The default frequency is 50 Hz. This may be adjusted, but all experiments done in this dissertation used this default value. Also, the GBIP cable at the back of the I-V lock-in must be removed and connected to the PL lock-in. This is so the TestScriptBuilder on the I-V computer can "talk" to the lock-in on the PL/EL system. Connect to the lock-in by clicking on the white drop-down arrow in the lower right hand corner of the TestScriptBuilder and select Instrument > Open. This opens a dialog box that should automatically find the GPIB address 26. Click "OK" to connect to the lock-in. Once this is completed a ">TSP" should show up in the dialog box below the program code window.

To begin current pulses into the LED, 3 programs need to activated in succession. The first one initializes the communication pathway. Right click the file Initialize > Run > Run as TSP. Once this is done repeat this same procedure for the files "SetPulse", and "PulseTrain", in that order. The file "Set Pulse" allows the user to set the height of the

square current pulses. For alignment purposes 0.3 A through the red LED should be sufficient. Once signal is reaching the detector, continue to adjust the system until an optimal signal is obtained. The current pulses are killed by flipping a manual switch. If this is not done the current will continue to run in an infinite loop and the user will risk a serious shock. Because the computer that originally ran this program could no longer do so, the complete code to the test script programs to run the EL experiment are given here to avoid lengthy downtimes in the future:

Initialize.tsp:

1. smua.reset()
2. smua.source.rangev=10
3. smua.source.limitv=10
4. smua.source.rangei=0.001
5. smua.source.levelv=0
6. smua.measure.rangev=10
7. smua.measure.rangei=1
8. smua.measure.nplc=0.01
9. smua.measure.autozero=smua.AUTOZERO_ONCE
10. smua.source.output=smua.OUTPUT_ON

SetPulse.tsp:

1. ConfigPulseIMeasureV(smua,0,1.6,6,0.01,0,1,nil,1)
   Order of parameters: output port, bias, level, limit, time on, time off, points, buffer, tag, sync_in, sync_out, sync_in_timeout, sync_in_abort

   Bias=bias level in amps (want this to be 0)
   Level=pulse level in amps (set to desired height)
   Limit=voltage limit in volts
   Time on=pulse width in seconds, make ½ the time of the full cycle
   Time off=pulse off time in seconds
   Points=number of pulse-measure cycles
   Buffer=reading buffer where pulse measurements are stored, if nil, when function is called then no measurement will take place
   Tag=numeric identifier assigned to defined pulse train
   Sync_in=digital I/O trigger input line (not programmed; all syncs not programmed)

This then makes a pulse from SMU-A with 0 A as the base level, 1.6 A as the pulse level, with a 6 V compliance, that is on for 0.01 sec, is off for 0 sec, taking 1 data point, but is nil so no data is stored, tagging as "1"

PulseTrain.tsp:

```
1.  digio.trigger[1].mode=digio.TRIG_RISINGA
2.  digio.trigger[1].clear()
3.  pulseon=0
4.  pulseon=digio.readbit(6)
5.  while (pulseon==1) do
6.          pulsetrigger=digio.trigger[1].wait(5)
7.          if (pulsetrigger==true) then
8.                  InitiatePulseTest(1)
9.          end
10.         digio.trigger[1].clear()
11.         pulsetrigger=false
12.         pulseon=digio.readbit(6)
13. end
14. smua.source.output=smua.OUTPUT_OFF
```

Once the system is aligned, perform an EL measurement by replacing the red LED with the collection lens. Then place a XY manipulator stage on a vertical jack and mount the sample on both of these. When aligning, initially adjust the sample by hand until a significant signal is obtained, then use the XY stage to fine tune the signal. The stage of the sample in the Z-direction is brought as close to the collection lens as possible. This is typically a few cm away from the lens.

The contacts can be made to the sample using the optical microscope at the I-V computer. Be sure not to cover the active area window with one of the contacts and that it is forward biased relative to the Keithley terminals. This means that the positive terminal is connected to the *p*-layer contact of the device. Also, the protective 100 Ω resistor can be removed from the circuit at this time as well. In order to get the highest current density it is desirable to use the smallest devices. However, the smallest devices that practical contacts can be made to are the 300 μm window devices. Thus all the EL experiments

presented in this dissertation were performed on these devices. Set the current to flow through the sample at 0.5 A initially. This is found to be a safe current to start with and it tends to produce a strong enough signal to obtain a good alignment.

The EL measurements proceed in the same fashion as PL measurements. The spectrometer scans over a wavelength range and the lock-in reads out the voltage from the photodiode. One thing to watch out for is arcing of the contacts. If the current gets too high, or if the contact is not very good, the contact will arc. This produces a spark that completely saturates the detector. Furthermore, when the probe tip is lifted off of the pad after this occurs a large chunk of the pad is often removed. This is because the arcing welds the tip and pad metals together. This ruins any opportunity to go back and re-measure the device. Arcing issues typically start occurring around 1.0 A.

APPENDIX C

OPERATION OF GOLDWATER AND ERC MICORPROBE STATIONS

In the following Appendix the operation and configuration of the microprobe stations used to acquire current-voltage (I-V), electrical responsivity, and temperature-dependent I-V (TI-V) data will be described. This will begin with a discussion of the Goldwater station that is used for I-V and responsivity measurements and conclude with the TI-V station in the ERC building.

Goldwater System

The probe station used to acquire all room temperature I-V measurements and responsivity absorption spectra presented in this dissertation were acquired on this system. A detailed description of this system has been provided in the Appendices of Dr. Jay Mathews and Dr. Richard Beeler's dissertations. To take I-V measurements, open the LabView software tab in the lower left corner. The program that runs I-V measurements is called "IV Measurement.vi". Connect the sample up to the Keithley sourcemeter through the BNC to Triaxial cable adapter box. Contacts are made by using the optical microscope and camera above the sample. This signal is sent to the computer allowing the user to make precision contacts to the device using the micromanipulators. The user then inputs the desired start voltage, stop voltage, and step size (typically 0.01 V). The compliance levels are typically set to 100 mA with a range of 5 V. The user then specifies the file directory and name. Taking a measurement with the box "Save data to file?" checked will automatically save the data under the name and directory in the "File Path" box.

To perform a responsivity measurement 2 programs must be utilized. First a spectrum of the lamp power is acquired using the program "MC Spectrum Measurement.vi". Then the measurement is taken on the program "Spectral Response

Measurement.vi”. The methods of calibrating the lamp power, aligning the sample, and doing the measurement have been discussed by Dr. Mathews and Dr. Beeler. The focus of this discussion will be about how to extend the measurement to acquire data beyond 1800 nm.

The photodiode that is used to calibrate the lamp power is a Ge device and so it cannot detect light longer than 1800 nm. This means that technically, the measurement is not possible for wavelengths longer than 1800 nm because the exact power of light hitting the sample is unknown and so the response cannot be converted to A/W. However an *ad hoc* approach has proven useful for extending the range to which these measurements can take place. First, a spectrum of the lamp power is acquired using a 1400 nm long pass filter over the 1400-1800 nm range in the “MC Spectrum Measurement.vi” program, followed by a spectrum of the lamp power using the 980 nm long pass filter covering 1000-1800 nm. By assuming the emission from the lamp follows that of a blackbody, we can extrapolate an approximate correction function that adjusts the power to smoothly match the experimental power at 1800 nm and provides reasonable values of power out to 2300 nm.

In order to perform this extrapolation, an Igor file named “EQELamp_Modeling.pxp” has been written. Load the lamp power files into the Igor program. To roughly correct for the spectrometer response, take the power at 1200 nm and divide by 0.846. This product corresponds to the factors introduced from the spectrometer response at that particular wavelength and the response of the SiO_2 that encases the lamp filament across the whole wavelength range of interest (1 μm-3 μm). Next, fit the wave named “Lamp” (number of points = 261, 1000 nm to 2300 nm in 5 nm

steps) with the function “Blackbody” (parameters: Wavelength, Temperature) by varying the parameter Temperature until the value at 1200 nm corresponds to the calculated one from the previous step. Then multiply the whole function “Lamp” by 0.94 to roughly correct for the SiO_2 response. Copy these calculated lamp powers from 1000 nm to 1800 nm and paste it onto the table. Do the same for the powers covering 1400 nm to 1800 nm. These will be waves “Lamp<N>” and “Lamp<N+1>”. Next, update the wave named “Spec_Res” by entering into the command line: “Spec_Res” = (“Lamp<N>”)/(<Actual Power taken>). In the case of matching data taken with the 1400 nm long pass filter, enter: “Spec_Res_1400” = (“Lamp<N+1>”)/(<Actual Power>). These are in a graph with the function “FitSpec” (parameters: A, B, K, h, lam). Vary the parameters A, B, K, and h in “FitSpec” while holding lam = Wave1023 until the asymptotic behavior of FitSpec matches that of either Spec_Res or Spec_Res_1400, whichever one is of interest. Then enter: “FitSpec = 1/FitSpec”. This has just formed the correction function of the spectrometer and filter. Lastly enter: Lamp = Lamp×FitSpec. Use the values of Lamp beyond 1800 nm as the power values in a .txt file for the responsivity measurement, or save it in an Igor or excel file and use it later after the measurement is performed.

After the sample has been aligned to perform the measurement, open the “Spectral Response Measurement.vi” program. In order to use the extended wavelength range, the number of steps taken in the scan must be set. The default number of 5 nm steps is 161, which is perfect for scans covering 1000 nm to 1800 nm. However, if a scan from 1400 nm to 2300 nm is desired, this value must be changed to 181. To do this, open the program but do not run the software. Go to Windows > Show Block Diagram. This takes the user into the program code itself. There is a for-loop box with a variable “N”

and the number 161 just to the left of it. Change the number to the necessary number of wavelength points needed to conduct the measurement.

Finally, load the files that contain the wavelength and lamp power data to initiate the measurement. Due to the long time it takes to process the lamp power to build the file needed to do this measurement, dummy files exist under the folder "Jimmy" on the desktop that have the wavelengths for scans from 1000 nm to 1500 nm (101 points), 1000 nm to 1900 nm (181 points), and from 1400 nm to 2300 nm (181 points) to get the measurement started right away while the actual lamp power that will be used to analyze the data is worked up as previously described. These dummy wavelength files are titled "Lamp_Spec_1015_Dummy.txt", "Lamp_Spec_1019_Dummy.txt", and "Lamp_Spec_1423_Dummy.txt", respectively. After the data is taken, divide the photocurrent vector by the experimental and extrapolated lamp power to obtain the responsivity in A/W.

<u>ERC Temperature Dependent System</u>

The operation of the TI-V set-up is very similar to that of the Goldwater probe station. Begin by placing the wafer on the chuck and turn on vacuum, lamp, and temperature controller. The latter is located on the left of station. Use the micromanipulators to make contacts to the device. Use the microscope objective and TV screen to make precision contacts to the devices. Due to the software interface with this system, be sure to set up connections so that SMU 2 and 4 are connected to the device. Log into computer and connect to the 4155C source meter in ICV-Lite software. Once this is done, open the ICS-Lite software. The experiment file that is needed is under C-drive > METRICS > ICS > projects > Jimmy > 0_3V_TdepIV. Interface with the

software so that the device under test (DUT) is a diode. The aim is to perform the scans so that the reverse bias current from 0-3 V is measured. So be sure to interface with the software so that the diode is reversed relative to the actual connections. Run a series of measurements from room temperature up to 75°C-80°C taking 5°C steps. Save the data in an excel file.

The aim of the data analysis is to extract the activation energies of the devices. This is done by plotting the natural logarithm of the current at a fixed reverse bias voltage as a function of 1/kT. This is done for several reverse biases ranging from 0.1 V to 2.0 V. Fitting each of these contours with a straight line gives a slope that is equal to the activation energy.

APPENDIX D

CATALOUGE OF GE-SN AND GE-SI-SN DEVICES

This appendix gives a brief account of the devices fabricated following the protocols outlined in Appendix A of this dissertation. What follows is a list of all the devices fabricated during the formation of this dissertation. Each device listed will describe the architecture design of the sample, and note the regions of the sample with the devices that produced the results discussed in the previous chapters. A good convention for describing where a particular device is on the wafer is to use letter/number labels that occur on either side of the TLM pads. There are two rows of devices between sets of TLM pads and labels. In the rows right above the labels half the device sets between the large 3 mm devices will be covered while the devices in the rows directly below the labels are all uncovered. The labels occur directly below the sets of devices in the former case and between the sets of devices in the latter. For example, a 300 μm device that is in the row right above the label F05 is referred to as the F05 300 μm device. Following this convention the 300 μm device that is in the row above this example device and nearest neighbor to the right of the corresponding 3 mm device is referred to as the E05/E06 300 μm device.

Ge *pin* Diodes

Ge_468_nip (A and B) (0% Sn, 0% Si): These devices consist of a 1400 nm thick *n*-Ge layer ($n = 2.0\times10^{19}$ cm^{-3}) grown on a Si(100) wafer doped using $P(GeH_3)_3$, followed by a 800 nm thick *i*-Ge layer, and capped with a 0.3% Sn *p*-GeSn layer that is 260 nm ($p = 5.3\times10^{18}$ cm^{-3}) and 125 nm ($p = 1.1\times10^{19}$ cm^{-3}) thick for wafers A and B, respectively. The *n* and *i*-layers were grown in the GSME reactor while the *p*-layer is grown in the 3-zone CVD. The best performing devices were from the E07 region on the A wafer and the

H07 region on the B wafer. These showed good I-V characteristics, absorption edges, and EL. In Chapter II this device is referred to as sample Ge.

Ge_470_nip_B (0% Sn, 0% Si): This device consists of a 1400 nm thick *n*-Ge layer ($n = 1.9\times10^{19}$ cm^{-3}) grown on a Si(100) wafer doped using $P(SiH_3)_3$, followed by a 800 nm thick *i*-Ge layer, and capped with a 0.3% Sn *p*-GeSn layer that is 135 nm thick with $p = 5.2\times10^{19}$ cm^{-3}. The *n* and *i*-layers were grown in the GSME reactor while the *p*-layer is grown in the 3-zone CVD. The best performing devices were from the F04 and H09 regions. These showed good I-V, absorption edges, and EL.

Ge-Sn *pin* Diodes

GeSnGe_PIN_13 (A and B) (2% Sn): These devices began with a 1065 nm thick *n*-Ge layer ($n = 2.5\times10^{19}$ cm^{-3}) grown on a Si(100) wafer in the GSME reactor. After this *i*-GeSn layers containing 2% Sn were grown in the single-zone CVD on the A and B wafers to thicknesses of 530 nm for A and 375 nm for B. These were capped by 2% Sn *p*-GeSn layers in the 3-zone CVD that are 150 nm thick ($p = 1.2\times10^{19}$ cm^{-3}) for A and 180 nm thick ($p = 1.5\times10^{19}$ cm^{-3}) for B. The best performing devices from the A wafer were in region E4. These showed good I-V curves, absorption edges, and EL. In Chapter II the A wafer is referred to as GeSn2. Sample B was used as a control experiment to test the performance of Ni contacts on Ge-based materials to see if it would improve the performance of the devices that used the Cr/Au metals, which tend to give contact resistivities of 10^{-5}-10^{-4} Ohm-cm^2. There have been reports that a post metals deposition annealing of Ni contacts on *n*-Ge at 600°C improve the contact resistivity to 10^{-7} Ohm-cm^2. In this case it was found that the dark currents increased dramatically after the post

metal deposition anneal, from 8 mA/cm^2 to 40 A/cm^2, and so the process was not switched to Ni contacts.

GeSnGe_PIN_9A (5.3% Sn): This device started with a 1400 nm thick *n*-Ge layer (n = 2.8×10^{19} cm^{-3}) grown on a Si(100) wafer in the GSME reactor. This was followed by the 5.3% Sn *i*-GeSn grown in the single-zone CVD to 440 nm. This was capped by a 4.1% Sn *p*-GeSn layer 150 nm thick (p = 7.9×10^{18} cm^{-3}) grown in the 3-zone CVD. The best region was F05. These devices showed good I-V characteristics, absorption edges, and EL. In Chapter II this sample is referred to as GeSn5.

GeSnGe_PIN_11 (7.0% Sn): This device started with a 1300 nm thick *n*-Ge layer (n = 2.0×10^{19} cm^{-3}) grown on a Si(100) wafer in the GSME reactor. This was followed by the 7.0% Sn *i*-GeSn grown in the single-zone CVD to 250 nm. This was capped by a 3.7% Sn *p*-GeSn layer 175 nm thick (p = 5.4×10^{19} cm^{-3}) grown in the 3-zone CVD. The best region of this device is E05/E06 and showed good I-V characteristics and EL. It is likely that the *i*-layer of this sample is too thin to obtain a good responsivity absorption edge.

GeSnGe_PIN_12 (7.0% Sn): This device started with a 1300 nm thick *n*-Ge layer (n = 2.0×10^{19} cm^{-3}) grown on a Si(100) wafer in the GSME reactor. This was followed by the 7.0% Sn *i*-GeSn grown in the single-zone CVD to 400 nm. This was capped by a 4.0% Sn *p*-GeSn layer 200 nm thick (p = 2.7×10^{19} cm^{-3}) grown in the 3-zone CVD. The best region is D06/D07. These devices showed good I-V characteristics, absorption edges, and EL. In Chapter II this device is referred to as GeSn7.

GeSnGe_60Ap (6.8% Sn): This device started with a 1640 nm thick *n*-Ge layer (n = 1.8×10^{19} cm^{-3}) grown on a Si(100) wafer in the GSME reactor. This was followed by the 6.8% Sn *i*-GeSn grown in the single-zone CVD to 675 nm. This was capped by a 6.6%

Sn *p*-GeSn layer 120 nm thick ($p = 1.2\times10^{19}$ cm^{-3}) grown in the 3-zone CVD. The best region is E06/E07. The devices gave good I-V plots, absorption edges, and EL. In Chapter II this device is referred to as GeSn7-t.

GeSnGe_61Bp (7.0% Sn): This device started with a 1220 nm thick *i*-Ge layer grown on a Si(100) wafer in the GSME reactor. After this the *n*-GeSn contact layer with ~6% Sn is grown 410 nm thick ($n = 2.8\times10^{19}$ cm^{-3}) followed by the 560 nm thick 7.0% Sn *i*-GeSn layer in the single-zone CVD. This is capped by a 6.0% Sn *p*-GeSn layer that is 120 nm thick ($p = 2.4\times10^{19}$ cm^{-3}) in the 3-zone CVD. The best region is G06/G07. These devices gave the very strong EL. This is the fully strain-relaxed GeSn device reported in Chapter II where it is referred to as GeSn7-h.

GeSnGe_51Bp (8.6% Sn): This device started with a 1025 nm thick *n*-Ge layer ($n = 2.5\times10^{19}$ cm^{-3}) grown on a Si(100) wafer in the GSME reactor. This was followed by the 8.6% Sn *i*-GeSn grown in the single-zone CVD to 375 nm. This was capped by a 5.0% Sn *p*-GeSn layer 150 nm thick ($p = 9.1\times10^{18}$ cm^{-3}) grown in the 3-zone CVD. The best devices are in the F05/F06 region. These devices produced good I-V data and EL. The *i*-layer is likely too thin to get a good responsivity reading. In Chapter II this device is referred to as GeSn8.

GeSnGe_53Bp (8.6% Sn): This device started with a 1335 nm thick *n*-Ge layer ($n = 2.1\times10^{19}$ cm^{-3}) grown on a Si(100) wafer in the GSME reactor. This was followed by the 8.6% Sn *i*-GeSn grown in the single-zone CVD to 235 nm. This was capped by a 4.2% Sn *p*-GeSn layer 145 nm thick ($p = 3.2\times10^{19}$ cm^{-3}) grown in the 3-zone CVD. The best devices are in the D07/D08 region. These devices produced good I-V data and EL.

GeSnGe_54Bp (9.4% Sn): This device started with a 1335 nm thick *n*-Ge layer (n = 2.3×10^{19} cm^{-3}) grown on a Si(100) wafer in the GSME reactor. This was followed by the 9.4% Sn *i*-GeSn grown in the single-zone CVD to 300 nm. This was capped by a 2.8% Sn *p*-GeSn layer 115 nm thick ($p = 2.8\times10^{19}$ cm^{-3}) grown in the 3-zone CVD. The best devices are in the G06 region. These produced rectifying I-V plots and EL.

GeSnGe_55Bp (9.5% Sn): This device started with a 1335 nm thick *n*-Ge layer (n = 2.3×10^{19} cm^{-3}) grown on a Si(100) wafer in the GSME reactor. This was followed by the 9.5% Sn *i*-GeSn grown in the single-zone CVD to 425 nm. This was capped by a 3.6% Sn *p*-GeSn layer 150 nm thick ($p = 1.6\times10^{19}$ cm^{-3}) grown in the 3-zone CVD. The best devices are in region H07/H08. These produced rectifying I-V plots.

GeSnGe_56Ap (10.5% Sn): This device started with a 1400 nm thick *n*-Ge layer (n = 2.5×10^{19} cm^{-3}) grown on a Si(100) wafer in the GSME reactor. This was followed by the 10.5% Sn *i*-GeSn grown in the single-zone CVD to 430 nm. This was capped by a 4.4% Sn *p*-GeSn layer 135 nm thick ($p = 1.6\times10^{19}$ cm^{-3}) grown in the 3-zone CVD. The best devices are from region F05. These produced rectifying I-V data and strong EL. In Chapter II this sample is referred to as GeSn10.

GeSnGe_57Bp (11.1% Sn): This device started with a 1340 nm thick *n*-Ge layer (n = 2.2×10^{19} cm^{-3}) grown on a Si(100) wafer in the GSME reactor. This was followed by the 11.1% Sn *i*-GeSn grown in the single-zone CVD to 320 nm. This was capped by a 4.4% Sn *p*-GeSn layer 115 nm thick ($p = 3.8\times10^{19}$ cm^{-3}) grown in the 3-zone CVD. The best devices are from region F04/F05. These showed rectifying IV properties and EL.

GeSnGe_64Ap (11.1% Sn): This device started with a 740 nm thick *n*-Ge layer (n = 1.8×10^{19} cm^{-3}) grown on a Si(100) wafer in the GSME reactor. This was followed by the

11.1% Sn *i*-GeSn grown in the single-zone CVD to 400 nm. This was capped by a 4.8% Sn *p*-GeSn layer 250 nm thick ($p = 8.9\times10^{19}$ cm^{-3}) grown in the 3-zone CVD. The best devices are in region E06/E07. These showed good I-V plots and EL was obtained.

GeSnGe_66Bp (11.9% Sn): This device started with a 675 nm thick *n*-Ge layer ($n = 1.7\times10^{19}$ cm^{-3}) grown on a Si(100) wafer in the GSME reactor. This was followed by the 11.9% Sn *i*-GeSn grown in the single-zone CVD to 360 nm. This was capped by a 6.0% Sn *p*-GeSn layer 275 nm thick ($p = 6.6\times10^{19}$ cm^{-3}) grown in the 3-zone CVD. The best devices are in region F08/F09. These showed diode I-V plots and EL.

GeSnGe_68Bp (12.8% Sn): This device started with a 710 nm thick *n*-Ge layer ($n = 1.8\times10^{19}$ cm^{-3}) grown on a Si(100) wafer in the GSME reactor. This was followed by the 12.8% Sn *i*-GeSn grown in the single-zone CVD to 430 nm. This was capped by a 10.0% Sn *p*-GeSn layer 140 nm thick ($p = 3.4\times10^{19}$ cm^{-3}) grown in the 3-zone CVD. The best devices are in region E05/E06. These gave rectifying diode I-V curves and EL.

GeSnGe_67Bp (13.7% Sn): This device started with a 710 nm thick *n*-Ge layer ($n = 1.8\times10^{19}$ cm^{-3}) grown on a Si(100) wafer in the GSME reactor. This was followed by the 13.7% Sn *i*-GeSn grown in the single-zone CVD to 335 nm. This was capped by a 8.4% Sn *p*-GeSn layer 140 nm thick ($p = 4.0\times10^{19}$ cm^{-3}) grown in the 3-zone CVD. The best devices are in region G08 and show good I-V characteristics. A very weak EL signal was seen in the InGaAs detector, but none in the PbS. This is likely because the peak emission wavelength from this device should be near 3000 nm.

Ge-Sn *pn* Diodes

GeSnGeN_20Ap: This device started with a 1285 nm thick *i*-Ge buffer layer on a Si(100) wafer in the GSME reactor. This was followed by a 6.9% Sn *n*-GeSn layer (n =

4.7×10^{19} cm^{-3}) grown in the single-zone CVD to 560 nm. This was capped by a 5.1% Sn *p*-GeSn layer 130 nm thick ($p = 6.0\times10^{19}$ cm^{-3}) grown in the 3-zone CVD. This device did not produce the desired tunnel current properties or EL.

GeSnGeN_21Ap: This device started with a 975 nm thick *i*-Ge buffer layer on a Si(100) wafer in the GSME reactor. This was followed by a 9.9% Sn *n*-GeSn layer ($n = 3.3\times10^{19}$ cm^{-3}) grown in the single-zone CVD to 360 nm. This was capped by a 8.5% Sn *p*-GeSn layer 165 nm thick ($p = 8.0\times10^{19}$ cm^{-3}) grown in the 3-zone CVD. This device did not produce the desired tunnel current properties or EL.

GeSnGeN_21Bp: This device started with a 920 nm thick *i*-Ge buffer layer on a Si(100) wafer in the GSME reactor. This was followed by a 10.5% Sn *n*-GeSn layer ($n = 1.8\times10^{19}$ cm^{-3}) grown in the single-zone CVD to 360 nm. This was capped by a 8.5% Sn *p*-GeSn layer 125 nm thick ($p = 1.0\times10^{19}$ cm^{-3}) grown in the 3-zone CVD. The best devices are in region E08. This device showed tunnel I-V properties and EL from both the *n* and *p*-layers. In Chapter IV this sample is referred to as Sample C.

GeSnGeN_22Bp: This device started with a 875 nm thick *i*-Ge buffer layer on a Si(100) wafer in the GSME reactor. This was followed by a 9.3% Sn *n*-GeSn layer ($n = 4.8\times10^{18}$ cm^{-3}) grown in the single-zone CVD to 525 nm. This was capped by a 8.6% Sn *p*-GeSn layer 300 nm thick ($p = 2.4\times10^{19}$ cm^{-3}) grown in the 3-zone CVD. The best devices are in region F06/F07. This device showed tunnel I-V properties and very intense EL from the *n*-layer. In Chapter IV this sample is referred to as Sample D.

GeSnGeN_23Bp: This device started with a 780 nm thick *i*-Ge buffer layer on a Si(100) wafer in the GSME reactor. This was followed by a 11.2% Sn *n*-GeSn layer ($n = 2.7\times10^{19}$ cm^{-3}) grown in the single-zone CVD to 325 nm. This was capped by a 10.4% Sn *p*-GeSn

layer 150 nm thick ($p = 3.1\times10^{19}$ cm^{-3}) grown in the 3-zone CVD. This device did not produce the desired tunnel current properties or EL.

GeSnGeN_24Bp: This device started with a 1400 nm thick *i*-Ge buffer layer on a Si(100) wafer in the GSME reactor. This was followed by a 11.9% Sn *n*-GeSn layer ($n = 2.0\times10^{19}$ cm^{-3}) grown in the single-zone CVD to 480 nm. This was capped by a 11.9% Sn *p*-GeSn layer 120 nm thick ($p = 1.8\times10^{19}$ cm^{-3}) grown in the 3-zone CVD. The best region is F06/F07. This device showed tunnel I-V properties and EL.

GeSnGeN_27Ap: This device started with a 760 nm thick *i*-Ge buffer layer on a Si(100) wafer in the GSME reactor. This was followed by a 6.5% Sn *n*-GeSn layer ($n = 1.3\times10^{19}$ cm^{-3}) grown in the single-zone CVD to 450 nm. This was capped by a 3.5% Sn *p*-GeSn layer 100 nm thick ($p = 1.2\times10^{20}$ cm^{-3}) grown in the 3-zone CVD. The best devices are in region F08/F09. These showed tunnel I-V properties and EL from the *n*-layer. In Chapter IV this device is referred to as Sample A.

GeSnGeN_27Bp: This device started with a 750 nm thick *i*-Ge buffer layer on a Si(100) wafer in the GSME reactor. This was followed by a 7.0% Sn *n*-GeSn layer ($n = 9.7\times10^{18}$ cm^{-3}) grown in the single-zone CVD to 460 nm. This was capped by a 4.6% Sn *p*-GeSn layer 100 nm thick ($p = 4.9\times10^{19}$ cm^{-3}) grown in the 3-zone CVD. The best devices are in region C06/C07. These showed tunnel I-V properties and EL from the *n*-layer.

GeSnGeN_28Bp: This device started with a 740 nm thick *i*-Ge buffer layer on a Si(100) wafer in the GSME reactor. This was followed by a 12.3% Sn *n*-GeSn layer ($n = 5.3\times10^{18}$ cm^{-3}) grown in the single-zone CVD to 535 nm. This was capped by a 8.5% Sn *p*-GeSn layer 100 nm thick ($p = 6.3\times10^{19}$ cm^{-3}) grown in the 3-zone CVD. The best devices are in

region G05. These showed tunnel I-V properties and EL from the *n*-layer. In Chapter IV this device is referred to as Sample B.

Ge-Si-Sn *pin* Diodes

Ge495_SiSnp: This device started with a 1425 nm thick *n*-Ge layer ($n = 2.0\times10^{19}$ cm^{-3}) grown on a Si(100) wafer in the GSME reactor. This is followed by a 850 nm thick, 3.3% Sn, 2.3% Si *i*-GeSiSn layer also grown in the GSME. The device is completed by a 200 nm *p*-Ge:Sn layer ($p = 6.6\times10^{19}$ cm^{-3}) in the 3-zone CVD. The best devices are in region D08/D09. These showed good absorption responsivities and EL. The dark currents showed much higher than expected levels at -1V for this composition. This has been attributed to growing the *i*-layer in the GSME directly on the Ge-buffer. Most other devices with *i*-layers grown in the GSME showed the same issue with their reverse bias dark currents.

Ge496_SiSnp: This device started with a 975 nm thick *n*-Ge layer ($n = 2.0\times10^{19}$ cm^{-3}) grown on a Si(100) wafer in the GSME reactor. This is followed by a 800 nm thick, 3.9% Sn, 1.8% Si *i*-GeSiSn layer also grown in the GSME. The device is completed by a 100 nm *p*-Ge:Sn layer ($p = 1.5\times10^{20}$ cm^{-3}) in the 3-zone CVD. The best devices are in region F04/F05. These showed good absorption responsivities and EL. The dark currents showed much higher than expected levels at -1V for this composition.

Ge497_SiSnp: This device started with a 970 nm thick *n*-Ge layer ($n = 2.0\times10^{19}$ cm^{-3}) grown on a Si(100) wafer in the GSME reactor. This is followed by a 440 nm thick, 5.2% Sn, 2.4% Si *i*-GeSiSn layer also grown in the GSME. The device is completed by a 100 nm 1% Sn *p*-GeSn layer ($p = 5.0\times10^{19}$ cm^{-3}) in the 3-zone CVD. The best devices are in region F04/F05. These showed good absorption responsivities and EL. This device was

the only one with an *i*-layer grown in the GSME that showed a reasonable reverse bias dark current level for its composition.

Ge503_SiSnp (A and B): This device started with a 860 nm thick *n*-Ge layer ($n = 2.0\times10^{19}$ cm^{-3}) grown on a Si(100) wafer in the GSME reactor. This is followed by a 270 nm thick, 7.7% Sn, 2.6% Si *i*-GeSiSn layer in the case of the A wafer and a 220 nm thick, 8.0% Sn, 2.6% Si *i*-GeSiSn layer in the case of the B wafer grown in the single-zone CVD. These devices are completed by a 170 nm 3.9% Sn *p*-GeSn layer ($p = 5.0\times10^{19}$ cm^{-3}) for the A wafer and a 120 nm 3.5% Sn *p*-GeSn layer ($p = 5.0\times10^{19}$ cm^{-3}) for the B wafer in the 3-zone CVD. The regions with the best devices are F06/F07 in the case of the A wafer and F05/F06 for the B wafer. Both wafers showed nearly identical rectifying I-V plots and EL. These are too thin to get a good responsivity signal.

Ge511_SiSnp: This device started with a 980 nm thick *n*-Ge layer ($n = 1.8\times10^{19}$ cm^{-3}) grown on a Si(100) wafer in the GSME reactor. This is followed by a 380 nm thick, 6.8% Sn, 3.0% Si *i*-GeSiSn layer also grown in the GSME. The device is completed by a 150 nm 7.0% Sn, 4.0% Si *p*-GeSiSn layer ($p = 1.1\times10^{19}$ cm^{-3}) in the 3-zone CVD. The best devices are in region F06/F07. These showed good absorption responsivities and EL. The dark currents showed much higher than expected levels at -1V for this composition.

Ge513_SiSnp: This device started with a 1040 nm thick *n*-Ge layer ($n = 1.8\times10^{19}$ cm^{-3}) grown on a Si(100) wafer in the GSME reactor. This is followed by a 240 nm thick, 7.3% Sn, 2.7% Si *i*-GeSiSn layer also grown in the GSME. The device is completed by a 100 nm 7.0% Sn, 3.5% Si *p*-GeSiSn layer ($p = 2.6\times10^{19}$ cm^{-3}) in the 3-zone CVD. The best devices are in region F06/F07. These showed good EL. The *i*-layer is too thin to obtain a

good absorption signal. The dark currents showed much higher than expected levels at -1V for this composition.

Ge516_SiSnp: This device started with a 1075 nm thick *n*-Ge layer ($n = 1.9\times10^{19}$ cm^{-3}) grown on a Si(100) wafer in the GSME reactor. This is followed by a 575 nm thick, 5.9% Sn, 2.8% Si *i*-GeSiSn layer also grown in the GSME. The device is completed by a 190 nm 7.0% Sn, 8.0% Si *p*-GeSiSn layer ($p = 8.7\times10^{18}$ cm^{-3}) in the 3-zone CVD. The best devices are in region G07/G08. These showed good EL. The dark currents showed much higher than expected levels at -1V for this composition.

Ge519_SiSnp: This device started with a 880 nm thick *n*-Ge layer ($n = 2.0\times10^{19}$ cm^{-3}) grown on a Si(100) wafer in the GSME reactor. This is followed by a 430 nm thick, 7.0% Sn, 2.3% Si *i*-GeSiSn layer also grown in the GSME. The device is completed by a 140 nm 8.0% Sn, 7.8% Si *p*-GeSiSn layer ($p = 1.7\times10^{19}$ cm^{-3}) in the 3-zone CVD. The best devices are in region D08/D09. These showed good EL. The dark currents showed much higher than expected levels at -1V for this composition.

Ge524_SiSnBp: This device started with a 800 nm thick *n*-Ge layer ($n = 2.0\times10^{19}$ cm^{-3}) grown on a Si(100) wafer in the GSME reactor. This is followed by a 280 nm thick, 9.5% Sn, 2.8% Si *i*-GeSiSn layer in the single-zone CVD. These devices are completed by a 85 nm 7.0% Sn, 3.0% Si *p*-GeSiSn layer ($p = 8.8\times10^{19}$ cm^{-3}) in the 3-zone CVD. The regions with the best devices are F07. This device showed good rectifying I-V properties, responsivity, and EL.

Ge527_SiSnBp: This device started with a 900 nm thick *n*-Ge layer ($n = 1.8\times10^{19}$ cm^{-3}) grown on a Si(100) wafer in the GSME reactor. This is followed by a 450 nm thick, 11.1% Sn, 3.0% Si *i*-GeSiSn layer in the single-zone CVD. These devices are completed

by a 90 nm 6.0% Sn, 6.0% Si *p*-GeSiSn layer ($p = 2.5\times10^{19}$ cm^{-3}) in the 3-zone CVD. The regions with the best devices are F07. This device showed good rectifying I-V properties, responsivity, and EL.

Ge538_SiSnAp: This device started with a 1000 nm thick *n*-Ge layer ($n = 2.1\times10^{19}$ cm^{-3}) grown on a Si(100) wafer in the GSME reactor. This is followed by a 340 nm thick, 9.3% Sn, 5.7% Si *i*-GeSiSn layer in the single-zone CVD. These devices are completed by a 90 nm 6.5% Sn, 6.0% Si *p*-GeSiSn layer ($p = 6.6\times10^{19}$ cm^{-3}) in the 3-zone CVD. The regions with the best devices are E05/E06. This device showed good rectifying I-V properties and EL.

Ge540_SiSnAp: This device started with a 860 nm thick *n*-Ge layer ($n = 1.7\times10^{19}$ cm^{-3}) grown on a Si(100) wafer in the GSME reactor. This is followed by a 315 nm thick, 9.5% Sn, 8.0% Si *i*-GeSiSn layer in the single-zone CVD. These devices are completed by a 400 nm 3.0% Sn, 3.0% Si *p*-GeSiSn layer ($p = 3.5\times10^{20}$ cm^{-3}) in the 3-zone CVD. The regions with the best devices are D06/D07. This device showed good rectifying I-V properties and EL.

Ge541_SiSnBp: This device started with a 860 nm thick *n*-Ge layer ($n = 1.7\times10^{19}$ cm^{-3}) grown on a Si(100) wafer in the GSME reactor. This is followed by a 320 nm thick, 10.5% Sn, 8.5% Si *i*-GeSiSn layer in the single-zone CVD. These devices are completed by a 90 nm 8.5% Sn, 8.5% Si *p*-GeSiSn layer ($p = 1.2\times10^{19}$ cm^{-3}) in the 3-zone CVD. The regions with the best devices are F07/F08. This device showed good rectifying I-V properties and EL.

Ge-Si-Sn *pn* Diodes

At this point there have been no successful ternary *pn* junction diodes. This portion is meant to serve as a reference to show what has been tried and has produced devices that do not show tunnel I-V properties or EL. Other attempts to produce these devices have been to grow the *n*-GeSiSn material in the GSME directly on the *i*-Ge buffer. However there have been issues with doping the materials at the low growth temperatures used during first iteration experiments. The GSME method may still be a viable route, but growths will likely need to be conducted at 260°C or more to activate the dopant precursors.

Ge551_SiSnp: This device started with a 1520 nm thick *i*-Ge buffer layer on a Si(100) wafer in the GSME reactor. This was followed by a 5.5% Sn, 5.5% Si *n*-GeSiSn layer grown in the single-zone CVD to 320 nm. This was capped by a 9.0% Sn, 5.0% Si *p*-GeSiSn layer 105 nm thick grown in the 3-zone CVD.

Ge555_SiSnAp: This device started with a 840 nm thick *i*-Ge buffer layer on a Si(100) wafer in the GSME reactor. This was followed by a 6.0% Sn, 4.5% Si *n*-GeSiSn layer grown in the single-zone CVD to 500 nm. This was capped by a 3.0% Sn, 4.0% Si *p*-GeSiSn layer 175 nm thick grown in the 3-zone CVD.

Ge567_SiSnBp: This device started with a 760 nm thick *i*-Ge buffer layer on a Si(100) wafer in the GSME reactor. This was followed by a 11.5% Sn, 5.0% Si *n*-GeSiSn layer grown in the single-zone CVD to 270 nm. This was capped by a 11.5% Sn, 5.5% Si *p*-GeSiSn layer 80 nm thick grown in the 3-zone CVD.

Ge568_SiSnAp: This device started with a 800 nm thick *i*-Ge buffer layer on a Si(100) wafer in the GSME reactor. This was followed by a 11.0% Sn, 5.0% Si *n*-GeSiSn layer

grown in the single-zone CVD to 380 nm. This was capped by a 12.0% Sn, 6.0% Si *p*-GeSiSn layer 105 nm thick grown in the 3-zone CVD.

Ge569_SiSnAp: This device started with a 750 nm thick *i*-Ge buffer layer on a Si(100) wafer in the GSME reactor. This was followed by a 10.5% Sn, 5.0% Si *n*-GeSiSn layer grown in the single-zone CVD to 500 nm. This was capped by a 7.0% Sn, 5.0% Si *p*-GeSiSn layer 60 nm thick grown in the 3-zone CVD.

APPENDIX E

FITTING AND MODELING PHOTOLUMINESENCE AND ELECTROLUMINESENCE DATA BY LINESHAPES

In this Appendix the fitting procedures for extracting the direct and indirect band gaps from PL and EL experiments will be discussed. As an example each step of the process is shown from the PL spectra for a 4% Sn, GeSn sample that is grown on Ge-buffered Si. After collecting and saving the data as discussed in Appendix B, the analysis of the data begins by correcting for the spectrometer and filter responses. To initiate this process, open the Igor file named “Background_correction.pxp” if the LN_2 InGaAs detector was used to collect the data. If the TE InGaAs was used, open “MicroHR_calibration_USHIO_lamp.pxp”. If the PbS detector was used, open “PbS_lamp_calibration.pxp”. In the window “Sample_Ge391SiSn_A” there are lines of code that need to be executed to correct the data. If this window cannot be found go to Windows > Other Windows and find it in the list that appears on the right. In the other two programs the corresponding windows that will be needed are “Correction_function” for the TE InGaAs and “Notebook0” in the PbS detector’s program. There are lines of code in each of these windows that are executed to correct the PL/EL spectra.

Begin by loading the average of the intensity over all scans and the wavelength range the data was taken over. Plot the data along the y-axis and its wavelengths along the x-axis. In the case of our sample the PL intensity wave is named “PL_23A” and the wavelength wave is “Wave1323”. Adjust the code in the window “Sample_Ge391SiSn_A” so that it reads the following:

```
PL_23A=PL_23A[p]*Correction(Wave1323[p])
PL_23A=PL_23A[p]/Transmission_1400new_comp_SS(Wave1323 [p])
```

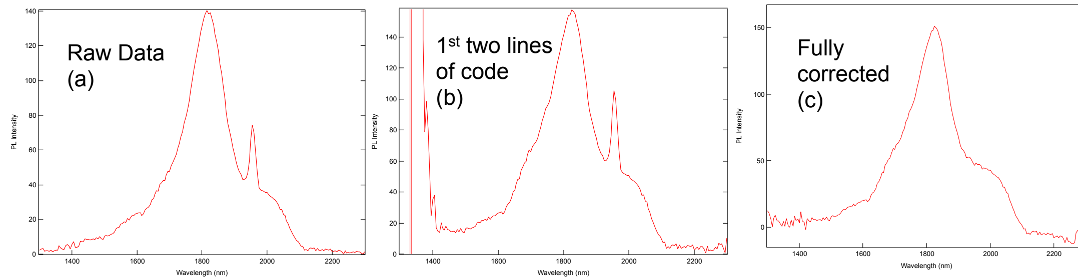

Figure 57: Evolution of the PL/EL data processing. (a) Raw experimental data. (b) Data at an intermediate stage of correction. (c) Fully corrected spectrum.

Depending on which filter was used, the second line of code will need to be adjusted. In this case the code is set for the data taken using the 1400 nm long pass filter. If the 1064 nm long pass filter was used, this entry will need to be changed to read "Transmission_1064_SS". Panels (a) and (b) in Figure 57 demonstrate how the execution of this code changes the spectrum.

There are 2 features of this spectrum we want to subtract off. The laser contribution and the constant background which introduces artificial features in the spectrum after the code is run. To subtract off the laser, go to Analysis > Packages > Multipeak Fitting > Multipeak Fitting 2. Specify the y and x waves in the pop-up dialog box and click "Continue". In the graph that appears on the left draw a box around the portion of the spectrum where the peaks are, right click, and in the options that show up select "Add or Edit Peaks". Another graph will show up. In this new graph draw in the peaks you would like to assign, making sure to place a very narrow Gaussian over the laser signal at ~1960 nm. When this is done have the program fit the profile. If the fit returns a reasonable Gaussian peak for the laser subtract this off by running the final line of code in the "Sample_Ge391SiSn_A" window by adjusting the y-data wave name, the directory to the correct peak that describes the laser contribution, and the wavelength range. Lastly, make a wave called "Bkgd" with the same number of points as the PL data

wave by going to Data > Make Waves. In the window that opens enter "Bkgd" in one of the empty cells and make the number of rows equal to the number of required data points. The default is 128, but to match the number of points in PL_23A we need this value to be 201. Then enter in the command: "SetScale/P x, 1300, 5, Bkgd". This makes it so that the x-values for the wave Bkgd are automatically calculated by Igor (this is actually one of Igor's most convenient and powerful features). In fact, this makes the x-values of the background wave identical to those we have been using for the PL data (Wave1323). To eliminate any artifacts introduced by the first iteration of code, pick out the baseline intensity reading that best matches the raw data if the sample did not emit any light. By inspecting the raw data of panel (a) in Figure 57 we can say in the case of our example sample that the background is about 5 μV. To calculate the background enter the command: "Bkgd=5*Correction(x)/Transmission_1400new_comp_SS(x)". Then perform: "PL_23A=PL_23A-Bkgd". After this the spectrum should appear as it does in the far right in panel (c) of Figure 57. At this point all corrections have been applied, and the laser and background have been subtracted off the spectrum. In the case of the other detectors, this same process is applied in the other programs.

We are now ready to convert the data to the energy scale, and assign the E_0 EMG and E_{ind} Gauss signals. This can be done either in the modeling program, or there is a separate Igor program built just for conversion to the energy scale. Either one will contain the same window with the necessary code to perform the operation. Load in the corrected PL data on the wavelength scale along with the wave that contains the wavelengths of the scan. In the file "PL_Bkgrd.pxp" the window needed is "Notebook0", in the case of the file "Direct_indirect_emission_fit.pxp" the code can be found in the

window “Sample_SnGe3_Ge290”. Input the wavelength wave name and the PL intensity wave name in the first two lines and specify a name for the output wave that will be the intensity along the energy scale. An example is:

```
String /G nm_wave="Wave1323"
String /G int_wave="PL_23A_Int"
String /G energy_wave="PL_Energy_23A"
```

In this case the output wave we will be interested in will be called “PL_Energy_23A”. Execute the next cluster of code directly beneath these first three lines. This essentially converts the wavelengths to energies and makes the intensity signal proportional to the number of photons emitted at a particular energy. The reason this must be done by code is because the experiment uses slits with fixed widths and a spectrometer with a fixed path length. This means that the equal $\Delta\lambda$ steps that are taken during the experiment do not correspond to equal ΔE steps. To remedy this we say that the starting energy of the scan is the direct conversion of the longest wavelength in nm to energy in eV, and that equal energy steps are taken where the width of the step is centered about the average wavelength used during the run. To make this more concrete, in the case of our example the longest wavelength that the spectrum was measured at was 2300 nm. Thus if we make a vector of energies E(n), our 0th entry to this vector, E(0), will be E(0) = (1240 eV-nm)/(2300 nm) = 0.53913 eV. In the case of photons we have:

$$E = \frac{h \cdot c}{\lambda} . \tag{E.1}$$

Differentiating this equation gives:

$$dE = -\frac{h \cdot c}{\lambda^2} d\lambda , \tag{E.2}$$

which for our practical purposes we can approximate to be:

$$\Delta E = -\frac{h \cdot c}{\lambda_{avg}^2} \Delta\lambda \,. \tag{E.3}$$

Applied to our example, $\Delta\lambda$ = 5 nm and λ_{avg} = (1300+2300)/2 nm = 1800 nm. And so ΔE = -0.001914 eV. This means that each entry in our vector must satisfy E(n+1) – E(n) = 0.001914 eV. Thus once we have our output wave it is good to record the starting energy

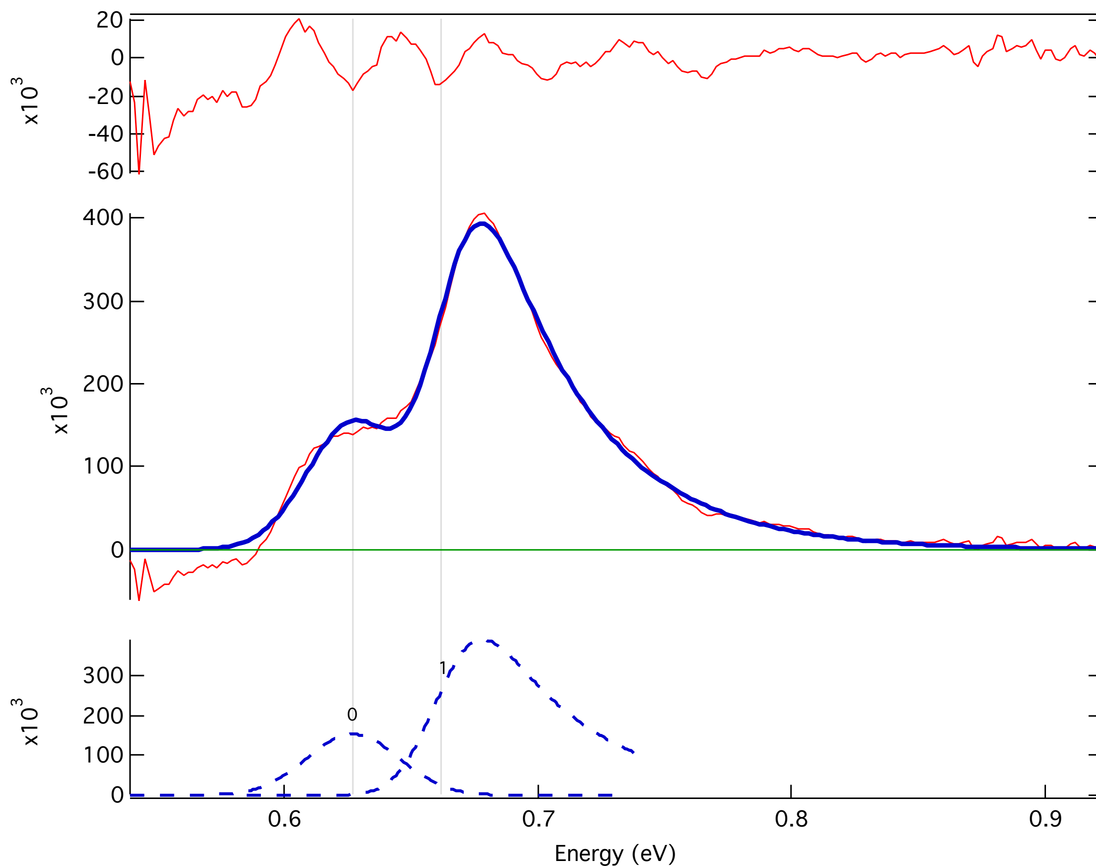

Figure 58: Converged line shape fit to the corrected spectrum plotted along the energy scale. The direct and indirect band gaps are fit by an EMG and Gaussian, respectively.

and the energy step values. For example, this will enable all future analysis to be done very quickly on our data by loading the intensity wave and applying the command:

"SetScale/P x, 0.53913, 0.001914, PL_Energy_23A" without having to keep track of an extra wave that contains the x-axis energy information.

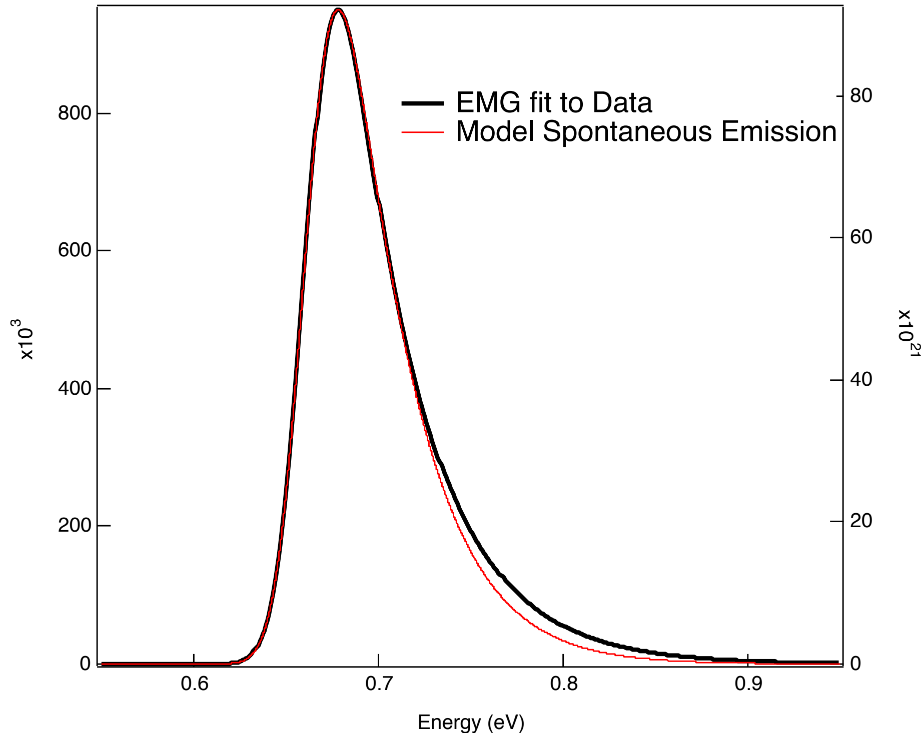

Figure 59: Converged fit of the spontaneous emission model to the shape of the direct gap EMG.

Once this is done we are ready to fit the spectrum with an EMG for the E_0 and a Gaussian for the E_{ind}. To do this, go to Analysis > Packages > Multipeak Fitting > Multipeak Fitting 2. Specify the intensity wave, however at this point the x-values should be simply calculated so click on this option under x-wave. Assign a Gaussian to the lower energy shoulder peak and an EMG to the main peak and use a constant background (typically very close to 0) to perform the fit. Figure 58 is an example of a converged fit following these protocols.

It is good to record the parameters of the peaks fit by these methods in case the fits need to be revisited in the future. Note the position of the Gaussian peak max of the E_{ind} signal. In the program "Direct_indirect_emission_fit.pxp" find the window labeled "Indirect_gap_computation". Part way down this window there are a few lines of code where the energy value of the peak location is entered followed by a location to input the sample strain as well. Running this code then produces the value of E_{ind}.

To extract E_0, the rest of the code in the window "Sample_SnGe3_Ge290" can be used. This code produces a wave called "spontaneous_emission". The goal here is to match the shapes of "spontaneous_emission" and the EMG we have just fit to the raw data. This is accomplished by adjusting the parameters of Si/Sn composition, number of photoexcited carriers, and the peak broadening. From the EMG fit we can obtain a good initial guess of the broadening. This can be found by clicking on the box labeled "Peak Results" once the converged fit is obtained. The broadening value will be very close to the Gauss FWHM value under the EMG results so it is good to use this as a first iteration. The other parameters in the model include sample thickness, doping level, temperature, strain, and the spectrometer resolution. Input the appropriate values for the sample thickness, doping, and strain. The values of temperature are almost always held fixed at 315 K for PL measurements while for EL measurements it is appropriate to vary this slightly to check for consistency of the fit. The spectrometer resolution is never changed. Make a graph with the EMG plotted along one axis and spontaneous emission plotted opposite to the EMG. This normalizes the intensities, which is ok in this case because we are only interested in matching lineshapes. Adjust the parameters of composition, photoexcited carriers, and broadening until the two peaks agree as shown in Figure 59.

When agreement of this level is obtained, record the energy computed from the code. It is also a good idea to record the calculation parameters as well so that the entire fit can be revisited if the need arises.

APPENDIX F

PERMISSIONS FOR REPRINTED MATERIALS

AIP PUBLISHING LLC LICENSE
TERMS AND CONDITIONS

Oct 04, 2015

All payments must be made in full to CCC. For payment instructions, please see information listed at the bottom of this form.

License Number	3722200690492
Order Date	Oct 04, 2015
Publisher	AIP Publishing LLC
Publication	Journal of Applied Physics
Article Title	Ge1−x−ySixSny light emitting diodes on silicon for mid-infrared photonic applications
Author	J. D. Gallagher,C. Xu,C. L. Senaratne, et al.
Online Publication Date	Oct 1, 2015
Volume number	118
Issue number	13
Type of Use	Thesis/Dissertation
Requestor type	Author (original article)
Format	Print and electronic
Portion	Figure/Table
Number of figures/tables	6
Title of your thesis / dissertation	The Optical and Electronic Properties of Ge1-ySny and Ge1-x-ySixSny Materials and Devices for Si-Integrated Optoelectronics
Expected completion date	Nov 2015
Estimated size (number of pages)	250
Total	0.00 USD
Terms and Conditions	

AIP Publishing LLC -- Terms and Conditions: Permissions Uses

AIP Publishing LLC ("AIPP"") hereby grants to you the non-exclusive right and license to use and/or distribute the Material according to the use specified in your order, on a one-time basis, for the specified term, with a maximum distribution equal to the number that you have ordered. Any links or other content accompanying the Material are not the subject of this license.

1. You agree to include the following copyright and permission notice with the reproduction of the Material:"Reprinted with permission from [FULL CITATION]. Copyright [PUBLICATION YEAR], AIP Publishing LLC." For an article, the copyright and permission notice must be printed on the first page of the article or book chapter. For photographs, covers, or tables, the copyright and permission notice may appear with the Material, in a footnote, or in the reference list.
2. If you have licensed reuse of a figure, photograph, cover, or table, it is your responsibility to ensure that the material is original to AIPP and does not contain the copyright of another entity, and that the copyright notice of the figure, photograph, cover, or table does not indicate that it was reprinted by AIPP, with permission, from another source. Under no

AIP PUBLISHING LLC LICENSE
TERMS AND CONDITIONS

Oct 05, 2015

All payments must be made in full to CCC. For payment instructions, please see information listed at the bottom of this form.

License Number	3722280864646
Order Date	Oct 04, 2015
Publisher	AIP Publishing LLC
Publication	Applied Physics Letters
Article Title	Fundamental band gap and direct-indirect crossover in Ge1-x-ySixSny alloys
Author	J. D. Gallagher,Chi Xu,Liying Jiang, et al.
Online Publication Date	Nov 11, 2013
Volume number	103
Issue number	20
Type of Use	Thesis/Dissertation
Requestor type	Author (original article)
Format	Print and electronic
Portion	Figure/Table
Number of figures/tables	5
Title of your thesis / dissertation	The Optical and Electronic Properties of Ge1-ySny and Ge1-x-ySixSny Materials and Devices for Si-Integrated Optoelectronics
Expected completion date	Nov 2015
Estimated size (number of pages)	250
Total	0.00 USD
Terms and Conditions	

AIP Publishing LLC -- Terms and Conditions: Permissions Uses

AIP Publishing LLC ("AIPP"") hereby grants to you the non-exclusive right and license to use and/or distribute the Material according to the use specified in your order, on a one-time basis, for the specified term, with a maximum distribution equal to the number that you have ordered. Any links or other content accompanying the Material are not the subject of this license.

1. You agree to include the following copyright and permission notice with the reproduction of the Material:"Reprinted with permission from [FULL CITATION]. Copyright [PUBLICATION YEAR], AIP Publishing LLC." For an article, the copyright and permission notice must be printed on the first page of the article or book chapter. For photographs, covers, or tables, the copyright and permission notice may appear with the Material, in a footnote, or in the reference list.
2. If you have licensed reuse of a figure, photograph, cover, or table, it is your responsibility to ensure that the material is original to AIPP and does not contain the copyright of another entity, and that the copyright notice of the figure, photograph, cover, or table does not indicate that it was reprinted by AIPP, with permission, from another source. Under no

AIP PUBLISHING LLC LICENSE
TERMS AND CONDITIONS

Oct 04, 2015

All payments must be made in full to CCC. For payment instructions, please see information listed at the bottom of this form.

License Number	3722200412522
Order Date	Oct 04, 2015
Publisher	AIP Publishing LLC
Publication	Applied Physics Letters
Article Title	Electroluminescence from GeSn heterostructure pin diodes at the indirect to direct transition
Author	J. D. Gallagher,C. L. Senaratne,P. Sims, et al.
Online Publication Date	Mar 2, 2015
Volume number	106
Issue number	9
Type of Use	Thesis/Dissertation
Requestor type	Author (original article)
Format	Print and electronic
Portion	Figure/Table
Number of figures/tables	5
Title of your thesis / dissertation	The Optical and Electronic Properties of Ge1-ySny and Ge1-x-ySixSny Materials and Devices for Si-Integrated Optoelectronics
Expected completion date	Nov 2015
Estimated size (number of pages)	250
Total	0.00 USD

Terms and Conditions

AIP Publishing LLC -- Terms and Conditions: Permissions Uses

AIP Publishing LLC ("AIPP"") hereby grants to you the non-exclusive right and license to use and/or distribute the Material according to the use specified in your order, on a one-time basis, for the specified term, with a maximum distribution equal to the number that you have ordered. Any links or other content accompanying the Material are not the subject of this license.

1. You agree to include the following copyright and permission notice with the reproduction of the Material:"Reprinted with permission from [FULL CITATION]. Copyright [PUBLICATION YEAR], AIP Publishing LLC." For an article, the copyright and permission notice must be printed on the first page of the article or book chapter. For photographs, covers, or tables, the copyright and permission notice may appear with the Material, in a footnote, or in the reference list.
2. If you have licensed reuse of a figure, photograph, cover, or table, it is your responsibility to ensure that the material is original to AIPP and does not contain the copyright of another entity, and that the copyright notice of the figure, photograph, cover, or table does not indicate that it was reprinted by AIPP, with permission, from another source. Under no

AIP PUBLISHING LLC LICENSE
TERMS AND CONDITIONS

Oct 05, 2015

All payments must be made in full to CCC. For payment instructions, please see information listed at the bottom of this form.

License Number	3722281448016
Order Date	Oct 05, 2015
Publisher	AIP Publishing LLC
Publication	Journal of Applied Physics
Article Title	Non-radiative recombination in Ge1−ySny light emitting diodes: The role of strain relaxation in tuned heterostructure designs
Author	J. D. Gallagher,C. L. Senaratne,C. Xu, et al.
Online Publication Date	Jun 30, 2015
Volume number	117
Issue number	24
Type of Use	Thesis/Dissertation
Requestor type	Author (original article)
Format	Print and electronic
Portion	Figure/Table
Number of figures/tables	13
Title of your thesis / dissertation	The Optical and Electronic Properties of Ge1-ySny and Ge1-x-ySixSny Materials and Devices for Si-Integrated Optoelectronics
Expected completion date	Nov 2015
Estimated size (number of pages)	250
Total	0.00 USD
Terms and Conditions	

AIP Publishing LLC -- Terms and Conditions: Permissions Uses

AIP Publishing LLC ("AIPP"") hereby grants to you the non-exclusive right and license to use and/or distribute the Material according to the use specified in your order, on a one-time basis, for the specified term, with a maximum distribution equal to the number that you have ordered. Any links or other content accompanying the Material are not the subject of this license.

1. You agree to include the following copyright and permission notice with the reproduction of the Material:"Reprinted with permission from [FULL CITATION]. Copyright [PUBLICATION YEAR], AIP Publishing LLC." For an article, the copyright and permission notice must be printed on the first page of the article or book chapter. For photographs, covers, or tables, the copyright and permission notice may appear with the Material, in a footnote, or in the reference list.
2. If you have licensed reuse of a figure, photograph, cover, or table, it is your responsibility to ensure that the material is original to AIPP and does not contain the copyright of another entity, and that the copyright notice of the figure, photograph, cover, or table does not indicate that it was reprinted by AIPP, with permission, from another source. Under no

AIP PUBLISHING LLC LICENSE TERMS AND CONDITIONS

Oct 04, 2015

All payments must be made in full to CCC. For payment instructions, please see information listed at the bottom of this form.

License Number	3722201034035
Order Date	Oct 04, 2015
Publisher	AIP Publishing LLC
Publication	Applied Physics Letters
Article Title	Compositional dependence of the bowing parameter for the direct and indirect band gaps in Ge1−ySny alloys
Author	J. D. Gallagher,C. L. Senaratne,J. Kouvetakis, et al.
Online Publication Date	Oct 8, 2014
Volume number	105
Issue number	14
Type of Use	Thesis/Dissertation
Requestor type	Author (original article)
Format	Print and electronic
Portion	Figure/Table
Number of figures/tables	3
Title of your thesis / dissertation	The Optical and Electronic Properties of Ge1-ySny and Ge1-x-ySixSny Materials and Devices for Si-Integrated Optoelectronics
Expected completion date	Nov 2015
Estimated size (number of pages)	250
Total	0.00 USD

Terms and Conditions

AIP Publishing LLC -- Terms and Conditions: Permissions Uses

AIP Publishing LLC ("AIPP"") hereby grants to you the non-exclusive right and license to use and/or distribute the Material according to the use specified in your order, on a one-time basis, for the specified term, with a maximum distribution equal to the number that you have ordered. Any links or other content accompanying the Material are not the subject of this license.

1. You agree to include the following copyright and permission notice with the reproduction of the Material:"Reprinted with permission from [FULL CITATION]. Copyright [PUBLICATION YEAR], AIP Publishing LLC." For an article, the copyright and permission notice must be printed on the first page of the article or book chapter. For photographs, covers, or tables, the copyright and permission notice may appear with the Material, in a footnote, or in the reference list.
2. If you have licensed reuse of a figure, photograph, cover, or table, it is your responsibility to ensure that the material is original to AIPP and does not contain the copyright of another entity, and that the copyright notice of the figure, photograph, cover, or table does not indicate that it was reprinted by AIPP, with permission, from another source. Under no

AIP PUBLISHING LLC LICENSE
TERMS AND CONDITIONS

Oct 05, 2015

All payments must be made in full to CCC. For payment instructions, please see information listed at the bottom of this form.

License Number	3722281049015
Order Date	Oct 05, 2015
Publisher	AIP Publishing LLC
Publication	Applied Physics Letters
Article Title	Electroluminescence from Ge1−ySny diodes with degenerate pn junctions
Author	J. D. Gallagher,C. L. Senaratne,P. M. Wallace, et al.
Online Publication Date	Sep 25, 2015
Volume number	107
Issue number	12
Type of Use	Thesis/Dissertation
Requestor type	Author (original article)
Format	Print and electronic
Portion	Figure/Table
Number of figures/tables	5
Title of your thesis / dissertation	The Optical and Electronic Properties of Ge1-ySny and Ge1-x-ySixSny Materials and Devices for Si-Integrated Optoelectronics
Expected completion date	Nov 2015
Estimated size (number of pages)	250
Total	0.00 USD

Terms and Conditions

AIP Publishing LLC -- Terms and Conditions: Permissions Uses

AIP Publishing LLC ("AIPP"") hereby grants to you the non-exclusive right and license to use and/or distribute the Material according to the use specified in your order, on a one-time basis, for the specified term, with a maximum distribution equal to the number that you have ordered. Any links or other content accompanying the Material are not the subject of this license.

1. You agree to include the following copyright and permission notice with the reproduction of the Material:"Reprinted with permission from [FULL CITATION]. Copyright [PUBLICATION YEAR], AIP Publishing LLC." For an article, the copyright and permission notice must be printed on the first page of the article or book chapter. For photographs, covers, or tables, the copyright and permission notice may appear with the Material, in a footnote, or in the reference list.
2. If you have licensed reuse of a figure, photograph, cover, or table, it is your responsibility to ensure that the material is original to AIPP and does not contain the copyright of another entity, and that the copyright notice of the figure, photograph, cover, or table does not indicate that it was reprinted by AIPP, with permission, from another source. Under no

Nov 09, 2015

American Physical Society License Details

This is an Agreement between James Gallagher ("You") and American Physical Society ("Publisher"). It consists of your order details, the terms and conditions provided by American Physical Society, and the payment instructions.

License Number License date Licensed content publisher Licensed content publication Licensed content title

Licensed copyright line Licensed content author Licensed content date Volume number

Type of Use

Requestor type

Format

Portion

Number of charts/graphs/tables/figures

Portion description

Rights for Duration of use

Creation of copies for the disabled

With minor editing privileges

For distribution to

Inthefollowinglanguage(s)

With incidental promotional use

The lifetime unit quantity of new product

The requesting person/organization is:

Order reference number

3741421146946 Nov 03, 2015 American Physical Society
Physical Review (1893-1969)

Intrinsic Optical Absorption in Single-Crystal Germanium and Silicon at 77\ifmmode^\circ\else\textdegree\fi{}K and 300\ifmmode^\circ\else\textdegree\fi{}K

Copyright © 1955, American Physical Society W. C. Dash and R. Newman Aug 15, 1955 99

Thesis/Dissertation Student Print, Electronic
chart/graph/table/figure 1

Figure 2 in my dissertation which shows the absorption coefficient of Ge at 300K and 77K

Main product Life of current edition no

no United States Originallanguageofpublication no

0 to 499 James Gallagher cao2841

https://s100.copyright.com/CustomerAdmin/PLF.jsp?ref=96c646b3-154b-4e1a-bcbe-d1e3e87355a5 Page 1 of 3

RightsLink Printable License 11/8/15 10:26 PM

Title of your thesis / dissertation

Expected completion date

Expected size (number of pages)

Total Terms and Conditions

Terms and Conditions

The Optical and Electronic Properties of Ge1-ySny and Ge1-x-

ySixSny Materials and Devices for Si-Integrated Optoelectronics

Nov 2015 250

0.00 USD

The American Physical Society (APS) is pleased to grant the Requestor of this license a non- exclusive, non-transferable permission, limited to [print and/or **electronic** format, depending on what they chose], provided all criteria outlined below are followed.1. For electronic format permissions, Requestor agrees to provide a hyperlink from the reprinted APS material using the source material's DOI on the web page where the work appears. The hyperlink should use the standard DOI resolution URL, http://dx.doi.org/{DOI}. The hyperlink may be embedded in the copyright credit line.

2. For print format permissions, Requestor agrees to print the required copyright credit line on the first page where the material appears: "Reprinted (abstract/excerpt/figure) with permission from [(FULL REFERENCE CITATION) as follows: Author's Names, APS Journal Title, Volume Number, Page Number and Year of Publication.] Copyright (YEAR) by the American Physical Society."

3. Permission granted in this license is for a one-time use and does not include permission for any future editions, updates, databases, formats or other matters. Permission must be sought for any additional use.4. Use of the material does not and must not imply any endorsement by APS.

5. Under no circumstance does APS purport or intend to grant permission to reuse materials to which it does not hold copyright. It is the requestors sole responsibility to ensure the licensed material is original to APS and does not contain the

copyright of another entity, and that the copyright notice of the figure, photograph, cover or table does not indicate that it was reprinted by APS, with permission from another source.

6. The permission granted herein is personal to the Requestor for the use specified and is not transferable or assignable without express written permission of APS. This license may not be amended except in writing by APS.7. You may not alter, edit or modify the material in any manner.

8. You may translate the materials only when translation rights have been granted.9. You may not use the material for promotional, sales, advertising or marketing purposes. 10. The foregoing license shall not take effect unless and until APS or its agent, Copyright Clearance Center (CCC), receives payment in full in accordance with CCC Billing and Payment Terms and Conditions, which are incorporated herein by reference.11. Should the terms of this license be violated at any time, APS or CCC may revoke the license with no refund to you and seek relief to the fullest extent of the laws of the USA. Official written notice will be made using the contact information provided with the permission request. Failure to receive such notice will not nullify revocation of the permission.12. APS reserves all rights not specifically granted herein.13. This document, including the CCC Billing and Payment Terms and Conditions, shall be

the entire agreement between the parties relating to the subject matter hereof.

Other Terms and Conditions

Questions? customercare@copyright.com or +1-855-239-3415 (toll free in the US) or +1-978-646-2777.

https://s100.copyright.com/CustomerAdmin/PLF.jsp?ref=96c646b3-154b-4e1a-bcbe-d1e3e87355a5 Page 3 of 3

Nov 09, 2015

American Physical Society License Details

This is an Agreement between James Gallagher ("You") and American Physical Society ("Publisher"). It consists of your order details, the terms and conditions provided by American Physical Society, and the payment instructions.

License Number License date Licensed content publisher Licensed content publication Licensed content title

Licensed copyright line Licensed content author Licensed content date Volume number

Type of Use

Requestor type

Format

Portion

Number of charts/graphs/tables/figures

Portion description

Rights for Duration of use

Creation of copies for the disabled

With minor editing privileges

For distribution to

Inthefollowinglanguage(s)

With incidental promotional use

The lifetime unit quantity of new product

The requesting person/organization is:

Order reference number

3741421327780 Nov 03, 2015 American Physical Society
Physical Review B

First-principles electronic structure of Si, Ge, GaP, GaAs, ZnS, and ZnSe. I. Self-consistent energy bands, charge densities, and effective masses

Copyright © 1981, American Physical Society C. S. Wang and B. M. Klein Sep 15, 1981 24

Thesis/Dissertation Student Print, Electronic
chart/graph/table/figure 1

Figure 2 in my dissertation. This figure plots the band structure and density of states in Ge.

Main product Life of current edition no

no United States Originallanguageofpublication no

0 to 499 James Gallagher cao2841_christine

https://s100.copyright.com/CustomerAdmin/PLF.jsp?ref=6b928474-6c28-4684-88cb-b863438d339c Page 1 of 3

RightsLink Printable License 11/8/15 10:27 PM

Title of your thesis / dissertation

Expected completion date

Expected size (number of pages)

Total Terms and Conditions

Terms and Conditions

The Optical and Electronic Properties of Ge1-ySny and Ge1-x-ySixSny Materials and Devices for Si-Integrated Optoelectronics

Nov 2015 250

0.00 USD

The American Physical Society (APS) is pleased to grant the Requestor of this license a non- exclusive, non-transferable permission, limited to [print and/or **electronic** format, depending on what they chose], provided all criteria outlined below are followed.1. For electronic format permissions, Requestor agrees to provide a hyperlink from the reprinted APS material using the source material's DOI on the web page where the work appears. The hyperlink should use the standard DOI resolution URL, http://dx.doi.org/{DOI}. The hyperlink may be embedded in the copyright credit line.

2. For print format permissions, Requestor agrees to print the required copyright credit line on the first page where the material appears: "Reprinted (abstract/excerpt/figure) with permission from [(FULL REFERENCE CITATION) as follows: Author's Names, APS Journal Title, Volume Number, Page Number and Year of Publication.] Copyright (YEAR) by the American Physical Society."

3. Permission granted in this license is for a one-time use and does not include permission for any future editions, updates, databases, formats or other matters. Permission must be sought for any additional use.4. Use of the material does not and must not imply any endorsement by APS.

5. Under no circumstance does APS purport or intend to grant permission to reuse materials to which it does not hold copyright. It is the requestors sole responsibility to ensure the licensed material is original to APS and does not contain the copyright of another entity, and that the copyright notice of the figure, photograph, cover or table does not indicate that it was reprinted by APS, with permission from another source.

6. The permission granted herein is personal to the Requestor for the use specified and is not transferable or assignable without express written permission of APS. This license may not be amended except in writing by APS.7. You may not alter, edit or modify the material in any manner.

8. You may translate the materials only when translation rights have been granted.9. You may not use the material for promotional, sales, advertising or marketing purposes. 10. The foregoing license shall not take effect unless and until APS or its agent, Copyright Clearance Center (CCC), receives payment in full in accordance with CCC Billing and Payment Terms and Conditions, which are incorporated herein by reference.11. Should the terms of this license be violated at any time, APS or CCC may revoke the license with no refund to you and seek relief to the fullest extent of the laws of the USA. Official written notice will be made using the contact information provided with the permission request. Failure to receive such notice will not nullify revocation of the permission.12. APS reserves all rights not specifically granted herein.13. This document, including the CCC Billing and Payment Terms and Conditions, shall be

the entire agreement between the parties relating to the subject matter hereof.

Other Terms and Conditions

Questions? customercare@copyright.com or +1-855-239-3415 (toll free in the US) or +1-978-646-2777.

https://s100.copyright.com/CustomerAdmin/PLF.jsp?ref=6b928474-6c28-4684-88cb-b863438d339c Page 3 of 3

AIP PUBLISHING LLC LICENSE
TERMS AND CONDITIONS

Nov 09, 2015

All payments must be made in full to CCC. For payment instructions, please see information listed at the bottom of this form.

License Number	3744600798676
Order Date	Nov 09, 2015
Publisher	AIP Publishing LLC
Publication	Journal of Applied Physics
Article Title	Ge1−x−ySixSny light emitting diodes on silicon for mid-infrared photonic applications
Author	J. D. Gallagher,C. Xu,C. L. Senaratne, et al.
Online Publication Date	Oct 1, 2015
Volume number	118
Issue number	13
Type of Use	Thesis/Dissertation
Requestor type	Author (original article)
Format	Print and electronic
Portion	Excerpt (> 800 words)
Will you be translating?	No
Title of your thesis / dissertation	The Optical and Electronic Properties of Ge1-ySny and Ge1-x-ySixSny Materials and Devices for Si-Integrated Optoelectronics
Expected completion date	Nov 2015
Estimated size (number of pages)	250
Total	0.00 USD
Terms and Conditions	

AIP Publishing LLC -- Terms and Conditions: Permissions Uses

AIP Publishing LLC ("AIPP"") hereby grants to you the non-exclusive right and license to use and/or distribute the Material according to the use specified in your order, on a one-time basis, for the specified term, with a maximum distribution equal to the number that you have ordered. Any links or other content accompanying the Material are not the subject of this license.

1. You agree to include the following copyright and permission notice with the reproduction of the Material:"Reprinted with permission from [FULL CITATION]. Copyright [PUBLICATION YEAR], AIP Publishing LLC." For an article, the copyright and permission notice must be printed on the first page of the article or book chapter. For photographs, covers, or tables, the copyright and permission notice may appear with the Material, in a footnote, or in the reference list.
2. If you have licensed reuse of a figure, photograph, cover, or table, it is your responsibility to ensure that the material is original to AIPP and does not contain the copyright of another entity, and that the copyright notice of the figure, photograph, cover, or table does not indicate that it was reprinted by AIPP, with permission, from another source. Under no

AIP PUBLISHING LLC LICENSE
TERMS AND CONDITIONS

Nov 09, 2015

All payments must be made in full to CCC. For payment instructions, please see information listed at the bottom of this form.

License Number	3744600304058
Order Date	Nov 09, 2015
Publisher	AIP Publishing LLC
Publication	Applied Physics Letters
Article Title	Fundamental band gap and direct-indirect crossover in Ge1-x-ySixSny alloys
Author	J. D. Gallagher,Chi Xu,Liying Jiang, et al.
Online Publication Date	Nov 11, 2013
Volume number	103
Issue number	20
Type of Use	Thesis/Dissertation
Requestor type	Author (original article)
Format	Print and electronic
Portion	Excerpt (> 800 words)
Will you be translating?	No
Title of your thesis / dissertation	The Optical and Electronic Properties of Ge1-ySny and Ge1-x-ySixSny Materials and Devices for Si-Integrated Optoelectronics
Expected completion date	Nov 2015
Estimated size (number of pages)	250
Total	0.00 USD
Terms and Conditions	

AIP Publishing LLC -- Terms and Conditions: Permissions Uses

AIP Publishing LLC ("AIPP"") hereby grants to you the non-exclusive right and license to use and/or distribute the Material according to the use specified in your order, on a one-time basis, for the specified term, with a maximum distribution equal to the number that you have ordered. Any links or other content accompanying the Material are not the subject of this license.

1. You agree to include the following copyright and permission notice with the reproduction of the Material:"Reprinted with permission from [FULL CITATION]. Copyright [PUBLICATION YEAR], AIP Publishing LLC." For an article, the copyright and permission notice must be printed on the first page of the article or book chapter. For photographs, covers, or tables, the copyright and permission notice may appear with the Material, in a footnote, or in the reference list.
2. If you have licensed reuse of a figure, photograph, cover, or table, it is your responsibility to ensure that the material is original to AIPP and does not contain the copyright of another entity, and that the copyright notice of the figure, photograph, cover, or table does not indicate that it was reprinted by AIPP, with permission, from another source. Under no

AIP PUBLISHING LLC LICENSE
TERMS AND CONDITIONS

Nov 09, 2015

All payments must be made in full to CCC. For payment instructions, please see information listed at the bottom of this form.

License Number	3744600713741
Order Date	Nov 09, 2015
Publisher	AIP Publishing LLC
Publication	Applied Physics Letters
Article Title	Electroluminescence from GeSn heterostructure pin diodes at the indirect to direct transition
Author	J. D. Gallagher,C. L. Senaratne,P. Sims, et al.
Online Publication Date	Mar 2, 2015
Volume number	106
Issue number	9
Type of Use	Thesis/Dissertation
Requestor type	Author (original article)
Format	Print and electronic
Portion	Excerpt (> 800 words)
Will you be translating?	No
Title of your thesis / dissertation	The Optical and Electronic Properties of Ge1-ySny and Ge1-x-ySixSny Materials and Devices for Si-Integrated Optoelectronics
Expected completion date	Nov 2015
Estimated size (number of pages)	250
Total	0.00 USD
Terms and Conditions	

AIP Publishing LLC -- Terms and Conditions: Permissions Uses

AIP Publishing LLC ("AIPP"") hereby grants to you the non-exclusive right and license to use and/or distribute the Material according to the use specified in your order, on a one-time basis, for the specified term, with a maximum distribution equal to the number that you have ordered. Any links or other content accompanying the Material are not the subject of this license.

1. You agree to include the following copyright and permission notice with the reproduction of the Material:"Reprinted with permission from [FULL CITATION]. Copyright [PUBLICATION YEAR], AIP Publishing LLC." For an article, the copyright and permission notice must be printed on the first page of the article or book chapter. For photographs, covers, or tables, the copyright and permission notice may appear with the Material, in a footnote, or in the reference list.
2. If you have licensed reuse of a figure, photograph, cover, or table, it is your responsibility to ensure that the material is original to AIPP and does not contain the copyright of another entity, and that the copyright notice of the figure, photograph, cover, or table does not indicate that it was reprinted by AIPP, with permission, from another source. Under no

AIP PUBLISHING LLC LICENSE
TERMS AND CONDITIONS

Nov 09, 2015

All payments must be made in full to CCC. For payment instructions, please see information listed at the bottom of this form.

License Number	3744600422016
Order Date	Nov 09, 2015
Publisher	AIP Publishing LLC
Publication	Journal of Applied Physics
Article Title	Non-radiative recombination in Ge1−ySny light emitting diodes: The role of strain relaxation in tuned heterostructure designs
Author	J. D. Gallagher,C. L. Senaratne,C. Xu, et al.
Online Publication Date	Jun 30, 2015
Volume number	117
Issue number	24
Type of Use	Thesis/Dissertation
Requestor type	Author (original article)
Format	Print and electronic
Portion	Excerpt (> 800 words)
Will you be translating?	No
Title of your thesis / dissertation	The Optical and Electronic Properties of Ge1-ySny and Ge1-x-ySixSny Materials and Devices for Si-Integrated Optoelectronics
Expected completion date	Nov 2015
Estimated size (number of pages)	250
Total	0.00 USD

Terms and Conditions

AIP Publishing LLC -- Terms and Conditions: Permissions Uses

AIP Publishing LLC ("AIPP"") hereby grants to you the non-exclusive right and license to use and/or distribute the Material according to the use specified in your order, on a one-time basis, for the specified term, with a maximum distribution equal to the number that you have ordered. Any links or other content accompanying the Material are not the subject of this license.

1. You agree to include the following copyright and permission notice with the reproduction of the Material:"Reprinted with permission from [FULL CITATION]. Copyright [PUBLICATION YEAR], AIP Publishing LLC." For an article, the copyright and permission notice must be printed on the first page of the article or book chapter. For photographs, covers, or tables, the copyright and permission notice may appear with the Material, in a footnote, or in the reference list.
2. If you have licensed reuse of a figure, photograph, cover, or table, it is your responsibility to ensure that the material is original to AIPP and does not contain the copyright of another entity, and that the copyright notice of the figure, photograph, cover, or table does not indicate that it was reprinted by AIPP, with permission, from another source. Under no

AIP PUBLISHING LLC LICENSE
TERMS AND CONDITIONS

Nov 09, 2015

All payments must be made in full to CCC. For payment instructions, please see information listed at the bottom of this form.

License Number	3744600516535
Order Date	Nov 09, 2015
Publisher	AIP Publishing LLC
Publication	Applied Physics Letters
Article Title	Compositional dependence of the bowing parameter for the direct and indirect band gaps in Ge1−ySny alloys
Author	J. D. Gallagher,C. L. Senaratne,J. Kouvetakis, et al.
Online Publication Date	Oct 8, 2014
Volume number	105
Issue number	14
Type of Use	Thesis/Dissertation
Requestor type	Author (original article)
Format	Print and electronic
Portion	Excerpt (> 800 words)
Will you be translating?	No
Title of your thesis / dissertation	The Optical and Electronic Properties of Ge1-ySny and Ge1-x-ySixSny Materials and Devices for Si-Integrated Optoelectronics
Expected completion date	Nov 2015
Estimated size (number of pages)	250
Total	0.00 USD

Terms and Conditions

AIP Publishing LLC -- Terms and Conditions: Permissions Uses

AIP Publishing LLC ("AIPP"") hereby grants to you the non-exclusive right and license to use and/or distribute the Material according to the use specified in your order, on a one-time basis, for the specified term, with a maximum distribution equal to the number that you have ordered. Any links or other content accompanying the Material are not the subject of this license.

1. You agree to include the following copyright and permission notice with the reproduction of the Material:"Reprinted with permission from [FULL CITATION]. Copyright [PUBLICATION YEAR], AIP Publishing LLC." For an article, the copyright and permission notice must be printed on the first page of the article or book chapter. For photographs, covers, or tables, the copyright and permission notice may appear with the Material, in a footnote, or in the reference list.
2. If you have licensed reuse of a figure, photograph, cover, or table, it is your responsibility to ensure that the material is original to AIPP and does not contain the copyright of another entity, and that the copyright notice of the figure, photograph, cover, or table does not indicate that it was reprinted by AIPP, with permission, from another source. Under no

AIP PUBLISHING LLC LICENSE
TERMS AND CONDITIONS

Nov 09, 2015

All payments must be made in full to CCC. For payment instructions, please see information listed at the bottom of this form.

License Number	3744600629235
Order Date	Nov 09, 2015
Publisher	AIP Publishing LLC
Publication	Applied Physics Letters
Article Title	Electroluminescence from Ge1−ySny diodes with degenerate pn junctions
Author	J. D. Gallagher,C. L. Senaratne,P. M. Wallace, et al.
Online Publication Date	Sep 25, 2015
Volume number	107
Issue number	12
Type of Use	Thesis/Dissertation
Requestor type	Author (original article)
Format	Print and electronic
Portion	Excerpt (> 800 words)
Will you be translating?	No
Title of your thesis / dissertation	The Optical and Electronic Properties of Ge1-ySny and Ge1-x-ySixSny Materials and Devices for Si-Integrated Optoelectronics
Expected completion date	Nov 2015
Estimated size (number of pages)	250
Total	0.00 USD

Terms and Conditions

AIP Publishing LLC -- Terms and Conditions: Permissions Uses

AIP Publishing LLC ("AIPP"") hereby grants to you the non-exclusive right and license to use and/or distribute the Material according to the use specified in your order, on a one-time basis, for the specified term, with a maximum distribution equal to the number that you have ordered. Any links or other content accompanying the Material are not the subject of this license.

1. You agree to include the following copyright and permission notice with the reproduction of the Material:"Reprinted with permission from [FULL CITATION]. Copyright [PUBLICATION YEAR], AIP Publishing LLC." For an article, the copyright and permission notice must be printed on the first page of the article or book chapter. For photographs, covers, or tables, the copyright and permission notice may appear with the Material, in a footnote, or in the reference list.
2. If you have licensed reuse of a figure, photograph, cover, or table, it is your responsibility to ensure that the material is original to AIPP and does not contain the copyright of another entity, and that the copyright notice of the figure, photograph, cover, or table does not indicate that it was reprinted by AIPP, with permission, from another source. Under no